MODELING THE MECHANICAL BEHAVIOR AND DEFORMED MICROSTRUCTURE OF IRRADIATED BCC MATERIALS USING CONTINUUM CRYSTAL PLASTICITY

A Dissertation
Presented to
The Academic Faculty

by

Anirban Patra

In Partial Fulfillment
of the Requirements for the Degree
Doctor of Philosophy in the
School of Materials Science and Engineering

Georgia Institute of Technology
December 2013

MODELING THE MECHANICAL BEHAVIOR AND DEFORMED MICROSTRUCTURE OF IRRADIATED BCC MATERIALS USING CONTINUUM CRYSTAL PLASTICITY

Approved by:

Dr. David L. McDowell, Advisor
School of Materials Science and
Engineering
Georgia Institute of Technology

Dr. Chaitanya Deo
GWW School of Mechanical Engineering
Nuclear and Radiological Engineering
Program
Georgia Institute of Technology

Dr. Hamid Garmestani
School of Materials Science and
Engineering
Georgia Institute of Technology

Dr. Naresh Thadhani
School of Materials Science and
Engineering
Georgia Institute of Technology

Dr. Ting Zhu
GWW School of Mechanical Enginering
Georgia Institute of Technology

Date Approved: November 14, 2013

ACKNOWLEDGEMENTS

would most certainly have been very boring without them. I would also like to acknowledge the interesting talks with Sankar Narayanan regarding various aspects of this project. I am grateful for the company of my 'non-work' friends as well, who have invariably managed to lighten things up. I especially enjoyed the numerous road trips and cook outs with them during all these years.

Finally, this thesis would not have been possible without the patient support of my entire family. Though they do not quite understand the technicalities of my work, they have always appreciated its importance to me and kept encouraging me throughout. I am sorry for not being with them in their many moments of joy and sorrow over the past few years. I hope that this work is commensurate with their innumerable sacrifices.

TABLE OF CONTENTS

LIST OF TABLES

LIST OF FIGURES

SUMMARY

The mechanical behavior of structural materials used in nuclear applications is significantly degraded as a result of irradiation, typically characterized by an increase in yield stress, localization of inelastic deformation along narrow dislocation channels, and considerably reduced strains to failure. Further, creep rates are accelerated under irradiation. These changes in mechanical properties can be traced back to the irradiated microstructure which shows the formation of a large number of material defects, e.g., point defect clusters, dislocation loops, and complex dislocation networks. Interaction of dislocations with the irradiation-induced defects governs the mechanical behavior of irradiated metals. However, the mechanical properties are seldom systematically correlated to the underlying irradiated microstructure. Further, the current state of modeling of deformation behavior is mostly phenomenological and typically does not incorporate the effects of microstructure or defect densities.

The present research develops a continuum constitutive crystal plasticity framework to model the mechanical behavior and deformed microstructure of bcc ferritic/martensitic steels exposed to irradiation. Physically-based constitutive models for various plasticity-induced dislocation migration processes such as climb and cross-slip are developed. We have also developed models for the interaction of dislocations with the irradiation-induced defects. A rate theory based approach is used to model the evolution of point defects generated due to irradiation, and coupled to the mechanical behavior. A void nucleation and growth based damage framework is also developed to model failure initiation in these irradiated materials. The framework is used to simulate the following

major features of inelastic deformation in bcc ferritic/martensitic steels: irradiation hardening, flow localization due to dislocation channel formation, failure initiation at the interfaces of these dislocation channels and grain boundaries, irradiation creep deformation, and temperature-dependent non-Schmid yield behavior. Model results are compared to available experimental data.

This framework represents the state-of-the-art in constitutive modeling of the deformation behavior of irradiated materials.

CHAPTER 1

INTRODUCTION

1.1   Motivation

In recent years, there has been a renewed interest in nuclear energy as a sustainable and relatively clean source for our present and future energy requirements. Design of nuclear power generation systems is contingent on the development of structural alloys that can withstand extreme stress and temperature loading in the presence of radiation fluxes and corrosive environments over the life of these power generation systems. In particular, the presence of irradiation poses a key challenge in extending the life of these structural materials, which are used in the cladding and core structures of nuclear pressure vessel reactors. Varied and complex radiation-induced phenomena occur over multiple length- and time-scales that degrade the mechanical properties of these materials, and their study is a matter of ongoing research. While significant efforts have been directed towards studying the effects of radiation on microstructure evolution, these microstructural features are seldom systematically correlated to the deformation behavior and mechanical properties at the meso- and macro-scale, especially in terms of constitutive modeling.

Understanding the effect of radiation-induced defects on the dislocation-mediated crystallographic deformation behavior holds the key for modeling and designing 'radiation-resistant' structural alloys for nuclear applications. The present research focuses on understanding these dislocation-defect interaction mechanisms and developing

physically-based continuum constitutive equations at the level of crystal plasticity to model the mechanical behavior and deformed microstructure of irradiated bcc alloys.

1.2   Radiation damage in metallic systems

Radiation damage in metallic crystals is initiated by the 'knock-on' event where an incident energetic particle interacts with a lattice atom and transfers a large part of its kinetic energy to the lattice atom. This transfer of energy results in the creation of the primary knock-on atom (PKA) as the 'excited' lattice atom leaves its lattice site and traverses through the lattice creating more PKAs and accompanying defects. When the PKAs have expended all their energy, they finally terminate as interstitials in the lattice. The physics of radiation damage and defect production has been explained in detail by Was [6].

Material defects created during the radiation damage process include point defect clusters, dislocation loops and networks, voids, bubbles, precipitates, solute segregation at grain boundaries, etc. Interaction of the plasticity-carrying dislocations with the radiation-induced defects alters their deformation behavior and mechanical properties. Primary observed effects include irradiation hardening, plastic flow localization, reduced ductility, and significantly lower strains to failure. Further, the irradiation creep rates are accelerated as compared to thermal creep, and occur at relatively lower homologous temperatures [7]. These effects are generally observed in most metallic systems and are a key concern for the use of structural materials in reactor vessels.

The operating conditions and desired mechanical properties for nuclear structural materials are ever-evolving and there are various classes of materials depending on their

application. The present generation 9-12% Cr ferritic/martensitic steels used as cladding material are expected to operate in the temperature range 300-600ºC and can take radiation doses up to 70-80 dpa (radiation damage measured in average displacements per atom) [8]. These bcc ferritic/martensitic steels have higher swelling resistance and better creep properties than the previous generation fcc austenitic steels [9], and are candidates for fusion and Generation IV fission applications [10]. A summary of the tensile strength and fracture properties of various ferritic/martensitic steels is given by Anderoglu et al. [11]. The present work focuses on modeling the mechanical properties of these bcc ferritic/martensitic steels. While the constitutive equations developed here may be applied to bcc materials in general, we have used Mod 9Cr-1Mo ferritic/martensitic steel as a model material in most of this work.

1.3   Scope of the present research

This research develops a continuum constitutive crystal viscoplasticity framework to model radiation damage in bcc materials over a wide range of deformation and loading histories. While crystal plasticity frameworks for modeling radiation damage have been developed previously [12–15], they generally address only the initial irradiation hardening and the post-hardening flow localization during tensile loading. In the present work, a unified model framework is developed to address: both irradiation hardening and flow localization during post-irradiation quasi-static tensile loading; failure initiation subsequent to plastic flow localization during tensile loading; and in-situ irradiation creep deformation. While separate deformation mechanisms may be dominant in each of these deformation regimes, physically, none of them are expected be mutually exclusive. This

allows us to develop a unified model framework with different deformation mechanisms dominant during different loading regimes. Example applications of the framework to model each of the above phenomena are given separately.

In this crystal plasticity framework, defect densities representative of the substructure (mobile dislocations, immobile dislocations, and irradiation-induced defects), rather than phenomenological hardening variables, are used as internal state variables. Physically-based constitutive equations are developed to model the interactions among these defect variables. Many of these constitutive equations draw on information obtained from lower length- and time-scale simulations (e.g., molecular dynamics, and kinetic Monte Carlo) of the interaction of dislocations with irradiation-induced defects. A major emphasis of this research lies on modeling not just the mechanical properties, but the deformed microstructure as well. This allows us to correlate the observed mechanical behavior to the underlying spatial and temporal substructure evolution. Model results and predictions are compared to available experimental data.

1.4   Organization of the thesis

The modeling tasks described above are organized in this thesis in the following fashion.

Chapter 2 starts with a discussion of the microstructural effects of irradiation and the observed deformation mechanisms. A brief review of the prior constitutive modeling efforts is also given. We then discuss the development of a crystal plasticity framework to model irradiation damage. We start with a description of the internal state variables used in this framework, followed by the finite deformation kinematics of the crystal

plasticity framework. Constitutive equations for the thermally-activated dislocation glide kinetics of double kink nucleation (in bcc metals) and point defect flux-governed dislocation climb are then discussed in the context of a conservative crystal plasticity framework. Rate equations for irradiation-induced point defects and interstitial loops are then developed and coupled with the deformation phenomena. Constitutive equations for dislocation density evolution are also developed. Climb and cross-slip of dislocations is modeled and tied with the deformation kinetics. The framework is used to model irradiation hardening in a Mod 9Cr-1Mo ferritic/martensitic steel during tensile loading. Model predictions are also made for irradiation creep loading at different applied stresses and radiation rates.

Chapter 3 focuses on modeling flow localization in irradiated bcc materials due to dislocation channel formation. Current understanding of the dislocation channeling phenomena in bcc metals is discussed. A phenomenological constitutive equation is developed to model flow localization due to the clearing of irradiation-induced defects along preferred crystallographic planes, allowing subsequent dislocation glide to occur. This constitutive equation is coupled with the existing framework to model the mechanical behavior and deformed microstructure due to dislocation channel formation. Effect of various mesoscopic factors such as initial crystallographic orientation distribution, grain size, radiation dose, and degree of cross-slip on the localization behavior is also studied.

Chapter 4 develops a continuum damage framework to model failure initiation at the interfaces of dislocation channels, subsequent to flow localization. Constitutive equations are developed for the generation of vacancies during inelastic deformation and

coupled to the nucleation and growth of voids by vacancy-mediated processes. The damage framework is coupled with the existing crystal plasticity framework to model failure initiation ahead of a sharp notch. The numerical simulations are used to measure the crack-tip displacements and compute the crack growth resistance. Fracture toughness calculations are also performed for the irradiated specimens.

Chapter 5 models the mechanical behavior and microstructure evolution during irradiation creep deformation. A constitutive model for the absorption of irradiation-induced point defects at grain boundary sinks is developed and coupled with the existing crystal plasticity framework. The creep strain is correlated with the evolution of radiation damage (measured in dpa). The deformed microstructure is studied in terms of the spatial distribution of dislocations and irradiation-induced defects. Effect of varying the grain size on the creep strain rates is also studied.

Chapter 6 develops constitutive equations for modeling non-Schmid yield effects due to dislocation core spreading in bcc metals. Constitutive equations are developed to model the temperature dependence of non-Schmid coefficients based on available experimental data for bcc-iron. Decay of non-Schmid effects with increasing inelastic deformation is also considered in this model. The constitutive equations are used to model the orientation-dependent mechanical behavior of single crystal iron over different temperatures. Model predictions are also made for tension-compression asymmetry in bcc-iron. Implications for irradiation damage and effect of the presence of interstitials near the screw dislocation core on the non-Schmid yield behavior are also discussed.

Finally, Chapter 7 summarizes the novel contributions and major conclusions of this research, along with recommendations for future work.

Note that Chapters 3 through 6 develop models for addressing different aspects of the deformation behavior of irradiated bcc metals. If interested in one specific aspect of the deformation behavior, the reader may refer to that particular Chapter, after an understanding of the constitutive model framework described in Chapter 2. Further, a separate Chapter on literature review has been foregone, since each Chapter has a rather comprehensive literature review pertaining to the topics discussed in that Chapter.

Significant parts of Chapter 2 have been published in Ref. [16]. Major findings of Chapter 3 have appeared in Ref. [17]. The work done in Chapter 4 is presently under review for publication [18]. Major findings of Chapter 6 have also been submitted for publication [19].

CHAPTER 2

A CONSTITUTIVE CRYSTAL PLASTICITY FRAMEWORK FOR MODELING RADIATION DAMAGE IN BCC MATERIALS[1]

2.1   Introduction

The quasi-static tensile behavior of metals subject to radiation damage is typically characterized by an increase in the yield point and decrease of uniform ductility and true strain to fracture. As for creep behavior, the 'irradiation creep' rates have been found to be much higher than the thermal creep rates in virgin materials and occur at relatively lower temperatures. Radiation damage reduces the life of these structural materials used in nuclear applications. Accordingly, research is directed at understanding the mechanisms governing inelastic deformation and improving material performance.

Inelastic deformation of irradiated materials at ambient and intermediate temperatures is essentially a multiscale phenomenon governed by unit processes spanning length scales over more than 15 orders of magnitude and time scales spanning 21 orders of magnitude [20]. Starting with localized shuffling of the lattice due to incident, high-energy, knock-on atoms and radiation cascade-induced defect nucleation and growth [21], and subsequent spatial evolution (migration and clustering) of these point defects [22] and their interaction with dislocations [23,24], this leads to irradiation-induced hardening, and eventually dislocation channeling and flow localization [25]. A multitude

---

[1] Significant parts of this Chapter have appeared in Ref. [16].

of physical phenomena occur in cascade from the atomic length- and timescales to the length- and timescales of engineering structures.

For modeling the mechanical behavior of such bcc ferritic/martensitic structural materials at the scale of microstructure (e.g., individual grains), it is necessary to consider crystallographic deformation mechanisms based on dislocation-defect interactions and their evolution. Continuum constitutive models should rely on information from lower length- and time-scale models of reaction pathways for dislocation nucleation and barrier bypass, and more importantly the point defect-dislocation reaction kinetics for irradiated materials. This Chapter will discuss a mechanism-based internal state variable (ISV) approach coupled with continuum crystal plasticity to model inelastic deformation in bcc materials subjected to radiation damage at ambient and intermediate homologous temperatures under quasi-static and creep loading.

2.2   Background

2.2.1   Microstructural effects of radiation

Irradiation of metals produces a large number of defects (interstitials and vacancies) that affect their mechanical properties. Depending on the type of metal (fcc or bcc), certain distinct microstructural effects can be observed. For fcc metals such as Cu, stacking fault tetrahedra form the majority of the irradiation-induced defects [26]. For bcc metals such as Fe, interstitial loops are the primary observed defect structures [27]. Complex dislocation networks, cavities and precipitates are also observed [28]. Another common feature of irradiated deformed microstructures is the formation of defect-free channels and corresponding plastic flow localization [25,29].

Dislocation networks act as sinks for point defects. Since a high density of dislocations is generated, the effective dislocation sink strength for these defects in irradiated materials is higher than the grain boundary sink strength. Swelling is another phenomenon observed due to the formation of voids in the lattice [30]. Voids provide a neutral sink facilitating diffusion of excess interstitials to the dislocations. Also observed is the biased absorption of interstitials at dislocations, promoting dislocation climb at barriers [31,32]. The focus of the present work is modeling the effect of these defects on the mechanical behavior of the material during and post-irradiation.

At intermediate to elevated homologous temperatures (> 0.3), inelastic deformation becomes strain-rate and temperature sensitive (thermally activated dislocation migration). In addition to glide, dislocation climb also contributes to inelastic deformation at these temperatures [33], particularly in the presence of irradiation-induced defects. This is affected by the non-equilibrium concentration of point defects, allowing dislocations to climb by absorption or emission of point defects. This is commonly referred to as "climb-controlled" creep [33,34].

For irradiated materials, the creep rate is considerably higher than that in thermal creep (of virgin materials) and occurs at much lower temperatures [6]. Deformation mechanism maps show that irradiation creep occurs at homologous temperatures of the order 0.3-0.5 as compared to thermal creep which occurs at homologous temperatures greater than 0.5 [7]. As opposed to thermal creep, which is governed by diffusion-controlled processes, accelerated irradiation creep rate is attributed to the creation of a large number of point defects that promote the growth and migration of defect loops and voids by stress-assisted mechanisms.

2.2.2 Irradiation creep mechanisms

A number of irradiation creep mechanisms have been conjectured, none of which by themselves have been able to explain the deformation behavior of materials over the entire domain of radiation damage. A comprehensive review of the various irradiation creep mechanisms is given by Bullough and Wood [35] and Matthews and Finnis [36].

Brailsford and Bullough [37] suggested that upon the application of external uniaxial stress, interstitial loops are more likely to nucleate on crystallographic planes with preferred orientation, specifically on planes perpendicular to the applied stress; while vacancy loops nucleate parallel to the direction of applied stress. This mechanism (stress induced preferential nucleation, SIPN) ultimately results in elongation of the material along the direction of applied stress. It can be shown that the creep rate in this case is linearly proportional to the applied stress. This model for creep, though supported by some experimental evidence, does not account for all the observed creep behaviors [6]. However, SIPN can be used to account for creep during the transient creep regime when interstitial loops start nucleating.

The stress-induced preferential absorption (SIPA) model for steady-state irradiation creep was originally proposed by Heald and Speight [38] and later quantitatively analyzed by Bullough and Willis [39]. Under the application of external stress, interstitials drift preferentially towards planes perpendicular to the direction of applied stress. The physical basis of this model is that the stress-induced interaction energy between preferentially aligned edge dislocations and interstitials is higher than that between non-aligned dislocations and interstitials for an applied tensile stress. This preferential drift of interstitials facilitates climb of edge dislocations perpendicular to the

plane by absorption of interstitials. The climb contribution to creep strain has been shown to be a linear function of the applied stress and is in reasonable agreement with steady-state creep data for steels [40].

The SIPA mechanism accounts only for climb of edge dislocations by absorption of interstitials under applied external stress. Mansur and Reiley [31,41] suggested that there must be an additional component of creep strain due to the subsequent glide of dislocations on the crystallographic plane, after the edge component of dislocations pinned at interstitials have climbed by SIPA. This climb-enabled glide of dislocations, also known as preferred absorption glide (PAG) has been shown to provide a dominant contribution to the creep strain at lower stresses and low dislocation densities [41].

2.2.3 Summary of prior constitutive modeling efforts

A multitude of phenomenological and physics-based constitutive models have been developed in the past to model plasticity and creep in irradiated materials. A brief review of some of the models is given here.

Ghoniem et al. [42] developed a model for creep (GMA model) based on unit dislocation evolution mechanisms. This model can be integrated with rate theory-based evolution of point defects in irradiated materials. This model has evolution laws for dislocation growth and migration processes, based on the interaction of dislocations with other (point) defects. The GMA model laid a comprehensive framework for linking physical dislocation mechanisms of deformation to the mechanical behavior of materials at high temperatures.

The mechanical behavior of irradiated materials characterized by an initial increase in yield stress has been correlated to the observed microstructural changes and modeled using a dispersed barrier hardening (DBH) model [43,44]. This model tries to establish a direct relation between the change in yield strength and the evolution of defect densities. Singh et al. [45] developed a cascade-induced source hardening (CISH) model wherein the increase in yield strength is interpreted as the added stress necessary to free the grown-in dislocations from irradiation-induced defect loops, thus enabling them to act as Frank-Read sources for dislocation multiplication and initiating plastic deformation.

Arsenlis et al. [12] discussed a continuum dislocation density-based plasticity model for irradiated fcc metals at low homologous temperatures. In this model, the material strength is derived from impediments to dislocation glide in the form of forest dislocations and irradiation-induced defects (stacking fault tetrahedra). The dislocation densities in this model evolve by dislocation multiplication and pair-wise annihilation mechanisms and the defects evolve by shearing of the initially perfect defects by passing dislocations.

Krishna et al. [13] developed a micromechanics-based rate-independent crystal plasticity model to capture the quasi-static tensile behavior of OFHC copper subject to radiation damage. The critical resolved shear stress on each slip system has a square root dependence on the dislocation and defect densities in this model. An evolution law for irradiation-induced defects based on experimental observation of annihilation of these defects, when they are within a prescribed standoff distance of the dislocations [46], was also proposed in this work.

Li et al. [14] developed a multiscale model for predicting irradiation hardening in iron-based alloys. Dislocation dynamics (DD) simulations of interactions between dislocations and irradiation-induced defects were used to compute the average critically resolved shear stress (CRSS) as a function of the defect density in irradiated iron, which was then fed into a phenomenological viscoplastic crystal plasticity framework to model the irradiation hardening and texture evolution. Simulation results were then compared with experiments to establish the hardening behavior as a function of radiation damage (in dpa).

More recently, Barton et al. [15] developed a crystal plasticity framework for modeling strain localization in irradiated iron. The slip system strength in this model evolves as a function of the network dislocation density and a tensor damage variable representative of the 'contact' density between dislocations and irradiation-induced prismatic loops. The crystal plasticity model was calibrated using stress-strain curves of irradiated iron with varying loop densities, obtained from DD simulations. The DD simulations performed by Arsenlis et al. [47] show that elastic interactions of the prismatic loops with gliding dislocations leads to their coarsening and coalescence, until the coarsened loops resemble network dislocations (in virgin, unirradiated materials) in their hardening behavior, thus leading to lower threshold stress for glide within the channels. To account for this flow softening mechanism, Barton et al. [15] developed a phenomenological rule assuming exponential decay of the prismatic loop density.

Most of the models developed to date do not provide a complete description of the underlying dislocation-defect interaction processes at the level of crystal plasticity in irradiated materials. Further, mechanical behavior of bcc metals is governed by more

complex crystallographic deformation mechanisms such as cross-slip of screw dislocations and non-Schmid yield behavior due to dislocation core spreading. To account for all of the above mentioned physical phenomena, a mechanism-based crystal plasticity model is developed for irradiated bcc systems in this Chapter. In the following Sections, the continuum constitutive model is explained and then the model is exercised to qualitatively predict the quasi-static tensile and creep behavior of a bcc ferritic/martensitic steel as a function of irradiation exposure.

2.3   Model description

The following Sections explain the Internal State Variables (ISVs) adopted in this model, the finite deformation kinematics of crystal plasticity, constitutive formulation of inelastic deformation and hardening laws, and the evolution laws of the ISVs.

2.3.1   Defect densities as internal state variables

This work focuses on bcc ferritic/martensitic steels, where interstitial loops are the primary irradiation-induced defects and vacancy loops are not observed (even with transmission electron microscopy) [27]. Interstitial loops are formed in irradiated materials when interstitial-clusters (formed during the displacement cascade) condense onto close-packed planes in the lattice.

Number densities of the interstitial loops, N_i^α, and their mean size, d_i^α, are therefore used as ISVs in this model. They evolve with cumulative irradiation damage, measured in terms of displacements per atom (dpa). It is assumed that all the interstitial

loops are sessile. Furthermore, the dislocation density, ρ^{α}, on each slip system α, comprised of dislocations other than interstitial loops, is also tracked. Along the lines of the work of Estrin and Kubin [48], the dislocation density is additively decomposed into mobile and immobile parts to help capture the transients in plastic flow, i.e., $\rho^{\alpha} = \rho^{\alpha}_M + \rho^{\alpha}_I$, where ρ^{α}_M is the mobile dislocation density and ρ^{α}_I is the immobile dislocation density on slip system α. Apart from the planar and line defects, this model also tracks the concentration of irradiation-induced point defects (interstitials, c_i, and vacancies, c_v) that play an important role in dislocation migration processes. These point defects also evolve with dpa. The evolution of these ISVs is discussed in Section 2.3.3.3.

2.3.2   Finite deformation kinematics

The constitutive crystal plasticity formulation is based on multiplicative decomposition of the deformation gradient tensor, $\boldsymbol{F}$, into the elastic, $\boldsymbol{F}^e$, and inelastic, $\boldsymbol{F}^i$, parts [49,50], i.e.,

$$\boldsymbol{F} = \boldsymbol{F}^e \cdot \boldsymbol{F}^i \tag{2.1}$$

with $\boldsymbol{F}^i$ describing the effects of the inelastic deformation on an undeformed lattice, mapping the reference configuration to an intermediate configuration in which the lattice has the same orientation, and $\boldsymbol{F}^e$ describes the lattice distortion and the rigid body rotation that carries the intermediate isoclinic configuration to the current, deformed configuration. Moreover, $\dot{\boldsymbol{F}}^i = \boldsymbol{L}^i \cdot \boldsymbol{F}^i$, where $\boldsymbol{L}^i$ is the inelastic velocity gradient determined by the crystallographic shearing rates on various slip systems, i.e.,

$$L^i = \sum_{\alpha=1}^{N_s} \dot{\gamma}^\alpha \boldsymbol{m}_0^\alpha \otimes \boldsymbol{n}_0^\alpha \tag{2.2}$$

where $\boldsymbol{m}_0^\alpha$ and $\boldsymbol{n}_0^\alpha$ are unit vectors corresponding to the slip and slip plane normal directions in the reference (or intermediate) configurations, $\dot{\gamma}^\alpha$ is the shearing rate on slip system α, and N_s is the total number of slip systems.

2.3.3 Constitutive model

2.3.3.1 Elastic deformation

For infinitesimal lattice deformation, the elastic Green strain tensor, $\boldsymbol{E}^e = (1/2)\left(\boldsymbol{F}^{eT} \cdot \boldsymbol{F}^e - \boldsymbol{I}\right)$, is related to the second Piola–Kirchhoff (PK) stress tensor in the intermediate configuration by $\boldsymbol{S} = \boldsymbol{C} : \boldsymbol{E}^e$, where $\boldsymbol{C}$ is the fourth rank elasticity tensor of the lattice. The PK stress tensor, $\boldsymbol{S}$, is related to the Cauchy stress, $\boldsymbol{\sigma}$, in the current configuration by $\boldsymbol{S} = \det\left(\boldsymbol{F}^e\right)\boldsymbol{F}^{e-1} \cdot \boldsymbol{\sigma} \cdot \boldsymbol{F}^{e-T}$. The resolved shear stress on a slip plane is given by Schmid's law, i.e.,

$$\tau^\alpha = \boldsymbol{m}^\alpha \cdot \boldsymbol{\sigma} \cdot \boldsymbol{n}^\alpha = \frac{1}{\det\left(\boldsymbol{F}^e\right)}\boldsymbol{m}_0^\alpha \cdot \boldsymbol{S} \cdot \boldsymbol{n}_0^\alpha \tag{2.3}$$

where $\boldsymbol{m}^\alpha$ and $\boldsymbol{n}^\alpha$ are the unit vectors corresponding to the slip and slip plane normal direction in the current configuration.

2.3.3.2 Inelastic deformation

Inelastic deformation in crystalline materials is governed by dislocation migration on close-packed slip planes with preferred orientations. This is represented at the

continuum level in terms of the crystallographic shearing rate for each slip system. The physical picture of inelastic deformation can be visualized as follows: mobile dislocations glide on preferred slip planes and get pinned at barriers, which in this case are primarily in the form of interstitial loops and immobile dislocations. Parts of the pinned mobile dislocation segments then climb by absorbing point defect clusters, allowing the unpinned dislocation segments to glide further. There are therefore two contributions to the crystallographic shearing rate, one due to thermally-activated glide of dislocation segments and the other due to climb of the edge component of dislocations, assisted by preferred absorption of interstitials.

2.3.3.2.1 Dislocation glide

Dislocation glide in bcc metals is governed by the thermally-activated double kink nucleation mechanism. The local, short-range barriers to dislocation glide (e.g., Peierls barrier) can be overcome by thermal fluctuations, while the long-range barriers with higher activation energy for bypass, due to the presence of immobile dislocations and interstitial loops (in this case), cannot be readily overcome by thermal fluctuations. Kothari and Anand [51] formulated a law for the dislocation glide velocity using a Kocks-type activation enthalpy term [52], i.e.,

$$
v_g^\alpha = \begin{cases} l_g \upsilon \exp\left(-\dfrac{\Delta F_g}{kT}\left(1-\left(\dfrac{\left|\tau^\alpha\right|-s_a^\alpha}{s_t^\alpha}\right)^p\right)^q\right) \text{sgn}\left(\tau^\alpha\right); & for \left|\tau^\alpha\right| > s_a^\alpha \\ 0; & for \left|\tau^\alpha\right| \le s_a^\alpha \end{cases}
$$

(2.4)

where l_g is the glide distance between barriers, υ is the cooperative attempt frequency of dislocation glide, ΔF_g is the activation energy barrier in the absence of external applied

stress, k is the Boltzmann constant, T is the absolute temperature, s_a^α is the athermal barrier resistance, s_t^α is the thermal barrier resistance, and p and q are parameters used to model the shape of the activation enthalpy curve.

Based on a dispersed barrier hardening model [43,44,53], the athermal slip resistance, s_a^α, due to long-range interactions of dislocations with interstitial loops and dislocations on other slip systems depends on the dislocation densities, defect loop sizes and corresponding number densities, i.e.,

$$s_a^\alpha = Gb\sqrt{\sum_{\zeta=1}^{N_s} q_\rho A^{\alpha\zeta} \rho^\zeta + q_i N_i^\alpha d_i^\alpha} \tag{2.5}$$

where q_ρ is the dislocation barrier strength, q_i is the interstitial loop strength, and $A^{\alpha\zeta}$ is the matrix of slip system dislocation interaction coefficients. We neglect here any long-range directional contribution to s_a^α (e.g., slip system back stress), as an approximation in view of the propensity for SIPA and screw dislocation cross-slip. It is noted that Bauschinger effects can still arise due to the spatial heterogeneity of yielding associated, for example, with the orientation distribution of grains (cf. [54]). Further, the effect of non-Schmid stresses in constricting the screw dislocation core in bcc materials [55–60] has also been neglected in the constitutive formulation and examples in this Chapter. It is expected that increase in interstitial concentration in irradiated materials will further hinder the constriction of dislocation cores, leading to a more pronounced effect of core spreading. Models to address these non-Schmid stresses are discussed in Chapter 6.

The thermal slip resistance, s_t^α, for bcc materials is typically governed by the (high) Peierls lattice resistance, τ_p, i.e., $s_t^\alpha = \tau_p$.

2.3.3.2.2 Dislocation climb

Climb in irradiated materials is driven by interaction of edge dislocation segments with the local non-equilibrium concentration of point defects (interstitials and vacancies). Climb can occur either by interstitial or vacancy trapping at the edge dislocation core. The climb rate is thus governed by the flux of interstitials and vacancies near the core of the edge dislocation segment. The dependence of dislocation climb velocity on the flux of point defects to and from the core is given as [41]

$$v_c^\alpha = \frac{\Omega}{b}\left(z_i^\alpha D_i c_i - z_v^\alpha D_v c_v\right) \tag{2.6}$$

where Ω is the atomic volume, z_i^α, z_v^α are the interstitial and vacancy capture efficiencies (defined as fraction of the total available point defects absorbed) of the dislocations perpendicular to the slip plane, respectively, and D_i, D_v are the effective interstitial and vacancy diffusivities, respectively. Here, c_i, c_v are the previously mentioned bulk interstitial and vacancy concentrations, respectively. Physically, the capture efficiencies, z_i^α and z_v^α, are affected by the atomic sites around a dislocation core available for the respective point defect absorption. The first term in the above expression represents the climb rate due to interstitial trapping and the second term represents the drag due to vacancy trapping at the dislocation core.

It has been further suggested that the interstitial capture efficiency, $z_i \propto \sigma/E$, where σ is the uniaxial stress and E is the Young's modulus [41]. Extending this to a crystal plasticity framework, we use $z_i^\alpha = z_i^0\left(\sigma_c^\alpha/E\right)$, where $\sigma_c^\alpha = \boldsymbol{n}^\alpha \cdot \boldsymbol{\sigma} \cdot \boldsymbol{n}^\alpha$ is the resolved stress normal to the slip plane; σ_c^α corresponds to the climb component of the

Peach-Koehler force on a dislocation [61]. The coefficient, z_i^0, in the above expression is assumed to be constant over all stress and temperature ranges. This expression reflects the dependence of interstitial capture efficiency on stress, thus differentiating between dislocations that are aligned and those that are not aligned to the stress direction (SIPA). Note that this expression also gives the direction in which dislocation climb occurs, namely $\boldsymbol{n}^\alpha$. A similar expression follows for vacancy capture efficiency, i.e.,

$$z_v^\alpha = z_v^0 \left(\sigma_c^\alpha / E \right).$$

The bias for absorption of interstitials as compared to vacancies (due to the preferential mutual interaction fields of interstitials with dislocations) will be accounted for in the coefficient, z_i^0, having a higher value than z_v^0. For simplicity, interaction of point defects with either edge or screw type of dislocations has not been explicitly differentiated in the present formulation. Note that all of the interactions mentioned in this Section are those with edge dislocations. As mentioned earlier, interactions of point defects with screw dislocations will lead to a more pronounced dislocation core spreading effect. Future work will focus on modeling these interactions based on input from atomistics.

2.3.3.2.3 *Crystallographic shearing rate due to climb and glide*

Since dislocation climb occurs perpendicular to the slip plane, it does not contribute to inelastic strain in the same manner as dislocation glide. Further, climb by itself is a non-conservative process; hence modeling this in a crystal plasticity framework is not straightforward. Based on the physical picture of inelastic deformation presented earlier, glide on the slip plane is assisted by climb events which enable dislocations to

overcome the barriers to glide in the domain of lower (insufficient) stresses. Climb is accompanied by migration of mobile dislocations via absorption of point defects. A schematic of this mechanism is shown in Fig. 1. Hence, there is a contribution of climb to the crystallographic shearing rate, in addition to the glide contribution of mobile dislocations. The inelastic shear strain on a slip plane due to glide of mobile dislocations is given by the Orowan equation [62], i.e.,

$$\gamma^\alpha = \rho_M^\alpha b l_g \tag{2.7}$$

where l_g is the average distance swept by glide dislocations on the slip plane. Taking derivative of this equation with respect to time leads to the expression for inelastic shearing rate, i.e., $\dot{\gamma}^\alpha = \rho_M^\alpha b v_g^\alpha + \dot{\rho}_M^\alpha b l_g$. The first term of this expression represents the shearing rate due glide, i.e., $\dot{\gamma}_g^\alpha = \rho_M^\alpha b v_g^\alpha$, and can be calculated from Eq. (2.4), if ρ_M^α is known. The second term is assumed here to represent the contribution to the crystallographic shearing rate due to climb, $\dot{\gamma}_c$, and is generally negligible in the quasi-static regime at lower homologous temperatures or for virgin (unirradiated) materials at moderate to high levels of mobile dislocation density. However, it is significant in the SIPA regime, when dislocation glide becomes increasingly difficult due to the presence of sessile interstitial loops which dominate the landscape of obstacles, and elevated temperatures result in higher diffusivities of point defects.
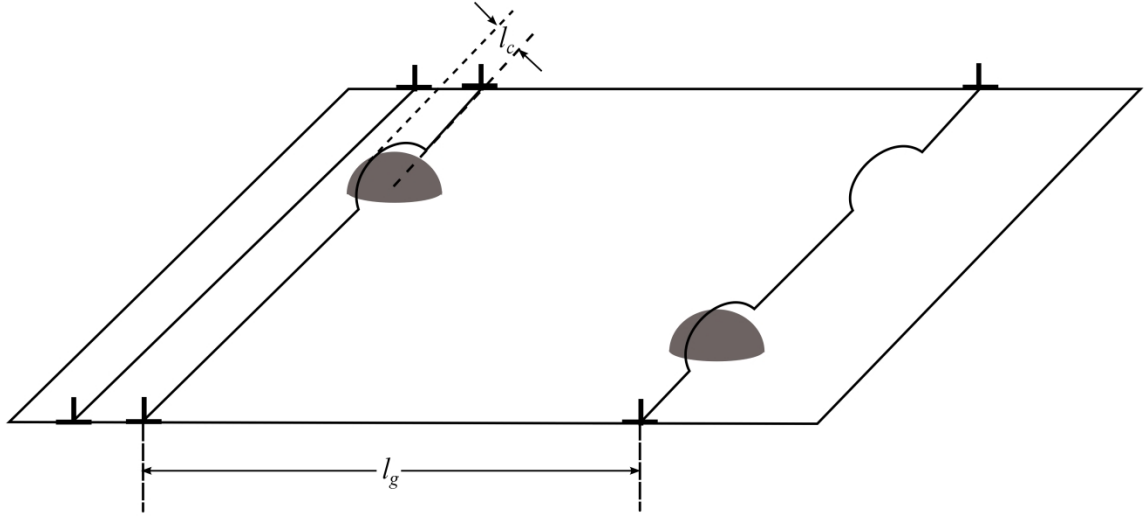
Figure 1. A dislocation on a slip plane climbs across a barrier of height, l_c, and is free to glide to the next obstacle; l_g is the slip distance after which another such barrier is encountered.

The frequency of dislocation climb events reckoned in terms of the population of mobile dislocations is given by $f_c^\alpha = v_c^\alpha / l_c$, where v_c^α is the mean climb velocity of mobile edge segments and l_c is the average distance climbed. The corresponding rate of migration of mobile dislocations passing barriers due to climb is therefore given by $f_c^\alpha \rho_M^\alpha$. Accordingly, we can write the contribution to the crystallographic strain rate due to climb as a function of the migration rate of mobile dislocations, i.e.,

$$\dot{\gamma}_c^\alpha = f_c^\alpha \rho_M^\alpha b l_g = \frac{v_c^\alpha}{l_c} \rho_M^\alpha b l_g \qquad (2.8)$$

The total crystallographic shearing rate on slip system α is therefore given as

$\dot{\gamma}^\alpha = \dot{\gamma}_g^\alpha + \dot{\gamma}_c^\alpha = \rho_M^\alpha b v_g^\alpha + \dot{\gamma}_c^\alpha$.

2.3.3.3 Substructure evolution

This Section deals with the evolution of point, line and planar defects, which constitute the substructure of the material. The evolution equations for all defects are in the form of rate equations, with individual terms representing specific physical mechanisms of defect generation, depletion, and recovery. First we will consider point defects, and then move on to interstitial loops, followed by dislocations. The models presented here offer a continuum scale statistical representation of the mechanisms governing evolution of these defects as a collective ensemble, and is limited in applicability to perhaps the lesser of 10 times the mean dislocation spacing or $10 \; l_g$ in minimum scale.

2.3.3.3.1 Point defects

Point defects are generated due to continuous, sequential collisions of incident high-energy radiation-induced particles with lattice atoms during radiation, knocking atoms off their respective lattice sites and creating interstitial-vacancy pairs. A part of the interstitial and vacancy population recombines over time to regenerate ordered lattice arrangement. Some point defects are subsequently absorbed by the mobile dislocations to form interstitial loops, while others are absorbed by network (immobile) dislocations. Radiation-induced point defects thus evolve by the following competing processes: defect pair creation by collisions between incident high-energy particles and lattice atoms, defect pair recombination, and defect absorption by dislocations. It is assumed for simplicity that the point defects are homogeneously distributed within the material and there are no spatial concentration gradients. The corresponding local rate equations for interstitial and vacancy concentrations are thus given as

$$\dot{c}_i = K_0 - K_{iv}c_ic_v - \sum_\alpha K_{is}^\alpha \left(\rho_M^\alpha + \rho_I^\alpha \right) c_i \qquad (2.9)$$

$$\dot{c}_v = K_0 - K_{iv}c_ic_v - \sum_\alpha K_{vs}^\alpha \left(\rho_M^\alpha + \rho_I^\alpha \right) c_v \qquad (2.10)$$

where K_0, K_{iv} are the defect pair creation and recombination rates, respectively,

$K_{is}^\alpha = \left| z_i^\alpha \right| D_i$ is the interstitial-sink (dislocation) reaction rate coefficient, $K_{vs}^\alpha = \left| z_v^\alpha \right| D_v$ is

the vacancy-sink (dislocation) reaction rate coefficient. Note that the rate of defect

absorption at mobile dislocation sinks (per slip system) also corresponds to the flux of

point defects causing climb of mobile dislocations (cf. Section 2.3.3.2.2). Implications

will be explained in the next Section. The defect pair creation and recombination rates are

assumed to be constant over the entire deformation process. This formulation is based on

a standard rate theory approach used previously to model the evolution of point defects

[63,64].

2.3.3.3.2 Interstitial loops

Rate equations for the evolution of interstitial loops have been developed in the

past, which are based on distributing the loop population into different size classes

[65,66]. A rate theory-based model for similar conditions of loop growth due to

dislocation climb was developed by Semenov et al. [67], again using a distribution of the

dislocation loops with different size classes. Implementation of such models in a crystal

plasticity framework is deemed impractical.

Here we propose a simple model, assuming that interstitial loops are formed when

the mobile edge dislocation segments climb by absorbing point defect clusters. It follows

that the climb rate of mobile dislocations will yield the rate of formation of interstitial

loops, while the absorption rate of point defects at dislocations will yield the growth rate

of the loops. All interstitial loops on slip plane α are assumed to be of mean size d_i^α. It

is also assumed that all loops are planar and approximately circular in shape. Recall that

in Section 2.3.3.2.3, the rate of migration of mobile edge dislocations due to climb is

given by $\dot{\rho}_{c\lim b}^\alpha = \left(|v_c^\alpha|/l_c \right) \rho_M^\alpha = |\dot{\gamma}_c^\alpha|/bl_g$. This population of mobile dislocation segments

grows into interstitial loops by absorption of interstitials. Conserving the total line length

of mobile dislocations involved in climb, we arrive at $\pi \dot{N}_i^\alpha d_i^\alpha = \dot{\rho}_{c\lim b}^\alpha$. The rate of

creation of new interstitial loops is therefore given by

$$\dot{N}_{i,c\lim b}^\alpha = \frac{1}{\pi d_i^\alpha} \frac{|\dot{\gamma}_c^\alpha|}{bl_g} \tag{2.11}$$

The dependence of interstitial loop size as a function of the number of interstitials

absorbed per loop is not entirely known. In this model, the areal growth rate of the planar

loops is assumed to be a linear function of the number of interstitials absorbed per loop.

As will be shown later, this assumption gives a reasonable estimate of the loop size

evolution, at least for low radiation doses. From Section 2.3.3.3.1, the rate of absorption

of interstitials per slip system is given as $K_{is}^\alpha \rho_M^\alpha c_i$. Hence, if we know the number of

interstitials, i^0, required to form a loop of area, A_i^0, the average areal growth rate of N_i^α

loops can be given as

$$\dot{A}_i^\alpha = \frac{1}{N_i^\alpha} \frac{A_i^0}{i^0} K_{is}^\alpha \rho_M^\alpha c_i \tag{2.12}$$

Furthermore, $A_i^\alpha = \frac{\pi}{4} d_i^{\alpha 2}$. This leads us to the growth rate for the size of interstitial

loops, i.e.,

$$\dot{d}^{\alpha}_{i,growth} = \frac{2}{\pi} \frac{A_i^0}{i^0} \frac{K_{is}^{\alpha} \rho_M^{\alpha} c_i}{N_i^{\alpha} d_i^{\alpha}} \tag{2.13}$$

The parameters i^0 and A_i^0 need to be estimated from experimental data. Note that vacancy loops could be formed by a similar mechanism. However, the diffusivities of vacancies are much lower than that of interstitials, leading to a comparatively lower absorption rate at dislocations. These loops are therefore relatively smaller than the corresponding interstitial loops and do not cause considerable impediment to glide. Hence, for simplicity, we do not track the evolution of vacancy loops in our simulations. The absorption of vacancies at dislocations is however accounted for in Eq. (2.10).

The models discussed here are essentially based on creation-exchange relations, with defects being created, recombined, or transformed from one type to another. For simplicity, we have neglected considering the full character of transport relations (defect concentration gradients and fluxes). We will comment on implications of this idealization in later discussion.

2.3.3.3.3 Dislocation densities

This Section discusses the evolution of the mobile and immobile components of dislocation densities on each slip system. Various laws have been proposed to statistically represent the substructure evolution for specific deformation processes. Here we extend these laws to model inelastic deformation in irradiated bcc materials.

Dominant mechanisms governing substructure evolution in bcc irradiated materials can be listed as follows: generation of new dislocations from pre-existing dislocation segments ($\dot{\rho}^{\alpha}_{mul}$), migration of mobile dislocations by cross-slip ($\dot{\rho}^{\alpha}_{cs}$) and climb ($\dot{\rho}^{\alpha}_{climb}$), mutual annihilation of mobile dislocations ($\dot{\rho}^{\alpha}_{mutual}$), trapping of mobile

dislocations at barriers, rendering them immobile ($\dot{\rho}^{\alpha}_{trap}$), and dynamic recovery of immobile dislocations by thermally activated processes ($\dot{\rho}^{\alpha}_{dyn}$). Each of these mechanisms is explained next.

Multiplication of mobile dislocations

The rate of formation of new dislocation segments is a function of the area swept on the slip plane by gliding mobile dislocations. This relation proposed by Essmann and Mughrabi [68] is of the form

$$\dot{\rho}^{\alpha}_{mul} = \frac{k_{mul}}{bl_d}\left|\dot{\gamma}^{\alpha}\right| \qquad (2.14)$$

where l_d is the average line length of the dislocation segment and k_{mul} is a material constant. Further, l_d is inversely related to the current mobile dislocation density, i.e., $l_d \approx 1\left/\sqrt{\sum_{\varsigma}\rho^{\varsigma}_M}\right.$. Thus, we can write the rate of formation of mobile dislocations as

$$\dot{\rho}^{\alpha}_{mul} = \frac{k_{mul}}{b}\sqrt{\sum_{\varsigma}\rho^{\varsigma}_M}\left|\dot{\gamma}^{\alpha}\right| \qquad (2.15)$$

Cross-slip of mobile screw dislocations

Cross-slip of screw dislocations is a prominent process in bcc metals, because of the existence of several slip planes on to which a screw dislocation with a unique Burgers vector can migrate. Cross-slip helps bypass barriers to glide and reduce internal stresses in the material. At low temperatures, a <111> type screw dislocation may spread to three {110} and three {112} slip planes. At higher temperatures, six more {123} planes come into the picture for a given slip direction. This kind of dislocation migration along a specific slip direction, but spread across multiple slip planes, is commonly referred to as wavy slip. A simple stochastic model for cross-slip is proposed here. Cross-slip of screw

dislocations in bcc materials is known to occur by the double kink mechanism [69]. Cross-slip is a thermally activated process; the probability that a screw dislocation will cross-slip to another slip plane ζ is proportional to:

$$P^{\zeta} \propto \exp\left(-\frac{\left(\tau^{*}-\left|\tau^{\zeta}\right|\right)V_{a}}{kT}\right) \tag{2.16}$$

where τ^{*} is the critical activation stress for double kink nucleation, V_{a} is the corresponding activation volume [70], and τ^{ζ} is the resolved shear stress on slip system ζ.

Consider a subset Ψ of slip systems, such that the slip direction is the same for all slip systems in subset Ψ. The probability of cross-slip is calculated on each of the slip planes belonging to Ψ. It is assumed that all screw dislocations belonging to Ψ will then cross-slip to the plane ζ having the highest probability, i.e., $P^{\zeta} = \max\left(P^{\alpha}\right) \forall \alpha, \zeta \in \Psi$. Accordingly, we calculate the associated dislocation annihilation rate on slip system α of subset Ψ as

$$\dot{\rho}_{cs}^{\alpha} = -k_{cs}\exp\left(-\frac{\left(\tau^{*}-\left|\tau^{\zeta}\right|\right)V_{a}}{kT}\right)\rho_{M}^{\alpha}\left|\dot{\gamma}^{\alpha}\right| \tag{2.17}$$

where k_{cs} is a material constant. This would result in additional dislocations on slip system ζ accumulating from the rest of the slip systems of subset Ψ, i.e.,

$$\dot{\rho}_{cs}^{\zeta} = -\sum_{\alpha \in \Psi, \alpha \neq \zeta}\dot{\rho}_{cs}^{\alpha} = \sum_{\alpha \in \Psi, \alpha \neq \zeta}k_{cs}\exp\left(-\frac{\left(\tau^{*}-\left|\tau^{\zeta}\right|\right)V_{a}}{kT}\right)\rho_{M}^{\alpha}\left|\dot{\gamma}^{\alpha}\right| \tag{2.18}$$

Note that slip plane ζ with the highest probability for cross-slip also corresponds to the highest absolute resolved shear stress, i.e., the slip plane that is most favorably

oriented with respect to the imposed stress state. Dislocation glide on slip plane ζ would thus be comparatively easier.

Climb of mobile dislocations

As mentioned earlier, climb is associated with the migration of mobile dislocations. The model for dislocation climb was given in Section 2.3.3.2.3, and the associated rate of migration of mobile dislocations is of the form

$$\dot{\rho}^{\alpha}_{c\lim b} = \frac{|\dot{\gamma}^{\alpha}_c|}{bl_g} \tag{2.19}$$

Mutual annihilation of mobile dislocations

Mutual annihilation of edge dipoles and mobile screw dislocation segments with opposite Burgers vectors occurs when dislocation segments lie within a critical capture radius, R_c [71], i.e.,

$$\dot{\rho}^{\alpha}_{mutual} = \frac{2R_c}{b} \rho^{\alpha}_M |\dot{\gamma}^{\alpha}| \tag{2.20}$$

The factor of two accounts for the fact that two dislocations with opposite Burgers vectors are annihilated as a result of this mechanism.

Trapping of mobile dislocations

Mobile dislocations get trapped at barriers on the slip plane and the corresponding dislocation segments are immobilized. For the case of irradiated materials, these barriers are in the form of dislocation networks (forest interactions) and interstitial loops. Based on a statistical model for trapping [72,73], the dislocation trapping rate is given by

$$\dot{\rho}^{\alpha}_{trap} = \frac{1}{b\lambda^{\alpha}} |\dot{\gamma}^{\alpha}| \tag{2.21}$$

where λ^α is the effective free path of dislocation trapping on slip system α. Since this expression gives a rate for immobilization of mobile dislocations, the immobile dislocation density would increase at the same rate. The effective free path is generally estimated as the harmonic mean of individual barrier free paths [74], i.e.,

$$\frac{1}{\lambda^\alpha} = \frac{1}{\lambda_{dis}^\alpha} + \frac{1}{\lambda_{int}^\alpha} \tag{2.22}$$

where λ_{dis}^α and λ_{int}^α are the mean free paths of the dislocation networks and interstitial loops, respectively. For dislocations, the mean free path has an inverse dependence on the square root of the defect density [73]. The effective free path can therefore be written as

$$\frac{1}{\lambda^\alpha} = \beta_\rho \sqrt{\rho^\alpha} + \beta_i \sqrt{N_i^\alpha d_i^\alpha} \tag{2.23}$$

where β_ρ and β_i are associated material constants.

Dynamic recovery of immobile dislocations

Dynamic recovery of immobile dislocations due to thermally activated processes is considered in a single rate expression [75], i.e.,

$$\dot{\rho}_{dyn}^\alpha = k_{dyn} \rho_I^\alpha \left| \dot{\gamma}^\alpha \right| \tag{2.24}$$

where k_{dyn} is a material constant. Assembling terms, the defect densities and sizes evolve by the following relations:

$$\dot{\rho}_{M,evolution}^\alpha = \dot{\rho}_{mul}^\alpha - \dot{\rho}_{cs}^\alpha - \dot{\rho}_{c\lim b}^\alpha - \dot{\rho}_{mutual}^\alpha - \dot{\rho}_{trap}^\alpha \tag{2.25}$$

$$\dot{\rho}_{I,evolution}^\alpha = \dot{\rho}_{trap}^\alpha - \dot{\rho}_{dyn}^\alpha \tag{2.26}$$

$$\dot{N}_i^\alpha = \dot{N}_{i,c\lim b}^\alpha \tag{2.27}$$

$$\dot{d}_i^\alpha = \dot{d}_{i,growth}^\alpha \tag{2.28}$$

Some parameter estimation is required in these evolution models to fit the experimental data. Note that the interaction of dislocations with interstitial loops has been considered only in terms of its contribution to the hardening behavior (Eq. (2.5)), and trapping of immobile dislocations thus rendering them immobile (Eq. (2.23)). Physically, the interaction of interstitial loops with glide dislocations is expected to reduce the density of the loops and cause flow localization along dislocation channels [29,76–78]. Models to capture this effect will be discussed in Chapter 3.

2.4   Model implementation

The constitutive model developed herein is applied to model the quasi-static tension and creep responses of a Mod (modified) 9Cr-1Mo steel. Mod 9Cr-1Mo steel is a ferritic/martensitic steel that has potential high temperature nuclear applications, such as the cladding in fast reactors. The material is subject to considerable radiation damage in these applications.

2.4.1   Parameter estimation

Temperature dependence of the elastic constants is taken from Ref. [79]. Apart from the elastic constants, not much material-specific data are available for estimating the model parameters. Mod 9Cr-1Mo steel contains mostly ferritic and martensitic phases. This steel derives its strength primarily from lath martensite, which has a body centered tetragonal (bct) crystal structure. Subsequent tempering leads to a tempered martensite phase which is essentially body centered cubic [80]. Moreover, tempering of this microstructure also leads to breakup of the martensite laths [81], generally wider lath

structures and less heterogeneity in terms of the distribution of grains [82]. In the present work it is assumed that the material has a uniform bcc crystal structure with 48 slip systems. A uniform grain size is also assumed to simplify the model implementation.

Model parameters relying on actual physical data were estimated from the corresponding values of (bcc) alpha-Fe. The Burgers vector magnitude is that of bcc-Fe, $b = \left(\sqrt{3}/2\right)a_0$, where $a_0 = 0.2866$ nm is the lattice parameter of bcc-Fe [83]. Model parameters were calibrated to fit the experimental stress-strain response of virgin (unirradiated) material and then used to simulate tensile test behavior under irradiation. The following explains the rationale behind choosing specific parameter values. The values of all the parameters are listed in Table 1.

2.4.1.1 Dislocation glide

Ashby [84] suggested the activation energy for dislocation glide, ΔF_g, to be of the order of $0.5Gb^3$ for irradiated materials. In our calculations, the activation energy was estimated to be $0.35Gb^3$ based on fit to available experimental tension test data. Further, the shape parameters, p and q, of the enthalpy curve should lie in the range $0 < p < 1$, $1 < q < 2$. The values, $p = 0.28$, and $q = 1.34$, adopted for bcc-Ta by Kothari and Anand [51] are found to fit our data reasonably. Temperature and strain rate dependence of the cooperative attempt frequency for dislocation glide, υ, is not exactly known, but it is typically of the order $\upsilon \approx 10^{10} - 10^{11}$ s^{-1}. Further the mobile dislocation density $\rho_M^\alpha \approx 10^7$ mm^{-2}, and the mean dislocation glide distance $l_g \approx 15 - 20$ nm. Accordingly, the pre-exponential factor, $\dot{\gamma}_0 = \rho_M^\alpha b l_g \upsilon$, for the dislocation glide relation,

$\dot{\gamma}_g^\alpha = \rho_M^\alpha b v_g^\alpha = \dot{\gamma}_0 v_g^\alpha / (l_g \upsilon)$, is assumed to have a constant value of 4.0×10^5 s^{-1} in our simulations.

In this work, the Peierls barrier stress has been assumed to be constant over all simulation temperatures and strain rates. Although this may not hold over the entire temperature regime, predictions are limited by lack of experimental data beyond 400 K for bcc-iron. Beyond 400 K, although the dependence of flow stress is not expected to be dominated by the Peierls barrier, it is also unlikely that the flow stress will be entirely independent of the Peierls barrier. As suggested in the literature [85], a value of 390 MPa has been used for the Peierls barrier.

The barrier strengths for dislocations, q_ρ, and interstitial loops, q_i, were calibrated to the experimental data and found to have the values $q_\rho = 0.3$, $q_i = 0.4$. These values are reasonably close to the barrier strengths used by Arsenlis et al. [12] for irradiated fcc-Cu. The coefficients of dislocation interaction ($A^{\alpha\zeta}$) among all the 48 slip systems in bcc are not as well characterized as for fcc crystals. We have used a value of $A^{\alpha\alpha} = 1.0$ for the self-interaction coefficient and $A^{\alpha\xi}(\xi \neq \alpha) = 0.2$ for the latent interaction coefficient. This is based on the assumption that the strongest resistance to glide on a slip plane will be offered by dislocations on the plane itself, and latent interaction offers a relatively weaker resistance. This value of latent interaction coefficient is of the same order as that predicted by Queyreau et al. [86] for different types of interactions and dislocation junction formations in alpha-Fe, based on DD simulations.

2.4.1.2   Dislocation climb

Estimation of dislocation climb parameters requires knowledge of the diffusivities of self-interstitial atoms (SIAs) and vacancies in the material. Point defect diffusivities depend on the migration energies of the respective defects, i.e.,

$$D_p = D_{p,0} \exp\left(-\frac{E_p^m}{kT}\right) \tag{2.29}$$

where E_p^m is the migration energy and $D_{p,0}$ is the diffusion constant of point defect type p. The corresponding values for SIAs and vacancies are based on MD simulations for bcc-Fe performed by Mendelev and Mishin [87]. The proportionality constants for interstitial and vacancy capture efficiencies, z_i^0 and z_v^0, were estimated from fit to experimental data. It has however been suggested in rate theory calculations performed by Stoller et al. [88] that the capture efficiency for self-interstitials is roughly 1.2 times that for vacancies, and this ratio is maintained in our calculations. The average dislocation glide distance between two barriers, l_g, is estimated (from the mean free path of the dislocations) to be 15 nm. This value is assumed to be constant in our simulations, since the average glide distance remains in the same range for dislocation densities evolving over the entire deformation domain. Further, the average dislocation climb distance l_c is assumed to be $3b$. This is reasonable considering the fact that the barriers to glide present in the form of planar loops and dislocation networks, can be overcome by climbing a few atomic planes with respect to the slip plane. This would have been different for the case of larger obstacles, such as precipitates, where the climb distance would be much higher.

2.4.1.3 Evolution of defects

2.4.1.3.1 Point defects

The defect pair creation rate, K_0, is a function the incident radiation flux and the probability of atomic displacement due to radiation. Consequently, K_0 depends on the energy of the incident particles (neutrons, ions, etc.). The underlying physics is beyond the scope of the current work. However, based on calculations done in [6], it is estimated that K_0 is typically of the order $10^{12} - 10^{13}$ mm^{-3}s^{-1} for neutron irradiation in steels. In our simulations, a value of $K_0 = 2.5 \times 10^{12}$ mm^{-3}s^{-1} is used for the creep tests, unless specified otherwise. It has been suggested that in the high temperature, high sink (dislocations) density regime, contribution of the defect pair recombination rate, K_{iv}, is negligible compared to the other evolution terms in the rate equations [6]. This term is therefore set to zero in our simulations.

2.4.1.3.2 Interstitial loops

As mentioned earlier, the areal growth rate of interstitial loops is assumed to be a linear function of the interstitials absorbed per loop. Marian et al. [89] characterized the self-interstitial loops in bcc iron and found that a 4 nm loop contains 91 SIAs. Though the number of interstitials per loop has been found to be lower for larger (> 10 nm) loops, it is reasonable to assume this ratio to be constant over a limited range of cumulative radiation damage. Accordingly, a value of $i^0 = 91$ and $A_i^0 = 12.57$ nm^2 is used in our simulations. These approximations can be appropriately modified for higher dpa levels.

Table 1. Model parameters for Mod 9Cr-1Mo steel.

Parameter	Value	Meaning
E, ν	207300 – 64.58(T[K] -273) MPa, 0.3	Elastic constants
a_0	0.2866 nm	Lattice parameter
ΔF_g, p, q, $\dot{\gamma}_0$	$0.35Gb^3$, 0.28, 1.34, $4.0 \times 10^5 \mathrm{s}^{-1}$	Flow rule parameters
τ_p, q_ρ, q_i, $A^{\alpha\alpha}$, $A^{\alpha\varsigma}\left(\varsigma \neq \alpha\right)$	390 MPa, 0.3, 0.4, 1.0, 0.2	Hardening parameters
z_i^0, z_v^0, Ω, l_g, l_c	1.2×10^{-4}, 1.0×10^{-4}, b^3, 1.5 nm, $3b$	Dislocation climb parameters
K_{iv}, A_i^0, i^0	0, 12.57 nm^2, 91	Point defect and interstitial loop evolution parameters
$D_{i,0}$, $D_{v,0}$, E_i^m, E_v^m	5.34×10^{-2} $\mathrm{mm}^2\mathrm{s}^{-1}$, 7.87×10^{-1} $\mathrm{mm}^2\mathrm{s}^{-1}$, 0.15 eV, 0.6 eV	Diffusivities and migration energies
k_{mul} (quasi-static), k_{mul} (creep), k_{dyn}, R_c, β_ρ, β_i	0.143, 1.02, 329.5, 1 nm, 0.36, 0.3	Dislocation evolution parameters
k_{cs}, τ^*, V_a	8.0×10^3, $0.004G$, $20b^3$	Cross-slip parameters

2.4.1.3.3 Dislocation densities

Dislocation evolution parameters in the model required were calibrated to fit the experimental stress-strain curves as the precise quantitative evolution behavior of these substructure variables is not known.

The dislocation multiplication model is essentially a phenomenological rule based on experimental observations of the growth of dislocation loops [68]. It has been found from our simulations that the dislocation multiplication constant k_{mul} should have a higher value in creep tests as compared to quasi-static tension tests. A higher multiplication rate in creep tests is needed to account for the reduction in dislocation density due to climb of mobile dislocations by absorption of point defects. As will be explained later, it is assumed that point defects due to radiation are produced dynamically in the material only during the creep tests (i.e., continuous irradiation), and accordingly the dislocation multiplication rate needs to be higher in these simulations. The dislocation multiplication constant used for tension tests has a value $k_{mul} = 0.143$ which is in the same range as the value used by Evers et al. [90], i.e., $k_{mul} = 0.1$, for similar simulations of polycrystalline Cu. For the creep tests, however, a higher value of $k_{mul} = 1.02$ is used. Higher values of the constant are also justified by the elevated temperatures at which creep experiments are performed, leading to a higher rate of multiplication of mobile dislocations.

To the best of our knowledge there are no quantitative studies on the evolution rate of dislocations due to cross-slip, in a statistical sense. Hirthe and Lothe [69] calculated the critical stress, τ^*, required by a dislocation for double kink nucleation and this was plotted as a function of the dislocation line length, l_d, in the work of Rhee et al.

[70]. Given an average mobile dislocation density of $\approx 2 \times 10^7 - 3 \times 10^7$ mm^{-2} per slip system, $l_d \approx 100b - 150b$. The calculations of Rhee et al. show that in this range $\tau^* \approx 0.004G$. In the present model we have used the above value, assuming it to be constant over the entire range of dislocation densities. Further, the activation volume for cross-slip is assumed to be $V_a = 20b^3$. Estimation of the amount of cross-slip on each slip system in a polycrystal ensemble is not exactly trivial and the value of the material constant, k_{cs}, has been calibrated such that the rate of cross-slip is comparable to the other dislocation evolution mechanisms at higher stresses and elevated temperatures.

For the mutual annihilation of dislocations, a capture radius, $R_c = 1$ nm, is used. This value is of the same order as that used by Arsenlis et al. [12] for irradiated fcc copper ($R_c = 8.5b$). The trapping coefficients for dislocations and interstitial loops and the dynamic recovery constant are calibrated based on fit to the experimental data.

2.4.2 Measure of radiation damage

Radiation damage is conventionally measured in terms of cumulative effective displacements per atom (dpa) in the material based on the flux of incident particles. Calculation of the effective atomic displacements is however infeasible in the present model, in a continuum sense. Quantitative measure of radiation damage is therefore done in the present model using a correlation for interstitial loop density and size to the cumulative dpa damage based on experimental observations. Deo et al. [53] proposed a square root dependence on cumulative dpa for similar materials for both the loop density and size, i.e.,

$$N_i = A \cdot \text{dpa}^{-1/2} \qquad\qquad (2.30)$$

$$d_i = B \cdot \text{dpa}^{-1/2} \qquad\qquad (2.31)$$

where $A = 5 \times 10^{13}\,\text{mm}^{-3}$ and $B = 3.7 \times 10^{-6}\,\text{mm}$. The same is used in our simulations. Note that this is an empirical relation fit to experimental observations of the variation of loop density and size over a limited range of dpa damage, and will not hold for high (> 10 dpa) or very low (< 1 dpa) radiation doses. Further, the interstitial loops are assumed to be uniformly distributed in the material. Effects of irradiation temperature, material depth from irradiated surface, etc. are neglected here as beyond the scope of the present work.

2.5   Results and discussion

2.5.1   Quasi-static tension tests

Three-dimensional displacement-controlled simulations were performed using the finite element program ABAQUS [91] on 125 cubic grain ensembles, with 30 μm sized grains that have random crystallographic orientation distribution. The constitutive equations were implemented using the User MATerial subroutine (UMAT) in ABAQUS. Periodic boundary conditions were enforced in all directions; implying that displacements on opposite boundaries are tied to each other [92].

It is assumed that all tensile test samples are pre-irradiated and there is no concurrent radiation damage during the tension tests. This is reasonable considering the fact that samples are generally irradiated at the rate of $\approx 10^{-6} - 10^{-5}\,\text{dpa-s}^{-1}$; radiation damage over the time-scales of the tension tests (≈1000 s) will be negligible compared to the damage already accumulated. In this work, simulation results are compared to the

experimental data for Mod 9Cr-1Mo steel from Ref. [2]. It has been confirmed from experiments that Mod 9Cr-1Mo steel has very high dislocation densities of the order $\approx 10^7 - 10^8$ mm^{-2} [82,93]. Further, additional dislocations are generated in the material during the course of irradiation. Accordingly, initial dislocation densities of $\rho_M^0 = 2 \times 10^7$ mm^{-2} and $\rho_I^0 = 3 \times 10^7$ mm^{-2} are assumed on all 48 slip systems.

Tension tests were conducted at a strain rate of 10^{-4} s^{-1}. The results were calibrated with experimental data [2]. Figure 2 compares simulation results for true stress-strain behavior with experimental data. A reasonable fit for the stress-strain curves was obtained over various temperatures and radiation dose histories with a single set of parameters, up to and just beyond the point of material softening.
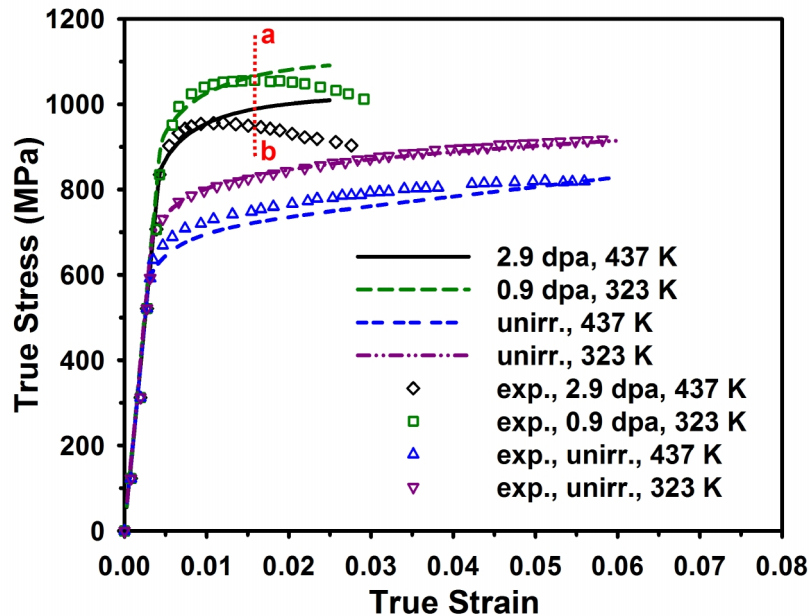
Figure 2. Comparisons of simulations calibrated to experimental stress-strain curves over a range of temperatures and dpa damage. Experimental data from [2]. Experimental data for true stress not corrected for necking. Dotted red line a-b indicates the strain up to which simulated stress-strain behavior for the irradiated samples can be reliable.

Beyond this point, however, the simulated stress-strain curves for the irradiated material have a less negative slope than the corresponding experimental results, and the simulated stress-strain curves appear to be diverging. Moreover, only the engineering stress-strain data were reported for the experiments, so conversion of the data past the point of diffuse necking instability is not reasonable for the virgin material. However, for the irradiated material, the post peak softening behavior in experiments has contributions both from the *material* softening associated with interplay of dislocations with irradiation-induced defects and attendant dislocation substructure evolution <u>and</u> the geometric softening due to the onset of diffuse necking. In the present formulation, interaction of dislocations with irradiation-induced defects has been addressed only in terms of irradiation hardening (cf. Eq. (2.5)), which contributes to the observed increase in initial yield stress. Beyond this, interaction of the irradiation-induced defects with glide dislocations is expected to cause a reduction in the density of the defects and create paths for easy dislocation glide [47,78]. Models to capture this *material* softening effect are discussed in Chapter 3.

Simulations regarding radiation dose-, temperature-, and strain rate-dependence of the tensile test behavior were also performed to parametrically explore model predictions. Results are shown in Figs. 3, 4, and 5, respectively. As expected, the initial yield stress increases with increasing radiation doses. The flow stress decreases with increasing test temperatures, and increases with increasing strain rates. Also note that at higher strain rates the increase in flow stress is not as pronounced. This is due to the fact that the strain rates used in these tests are still close to the quasi-static (strain-rate independent) regime.
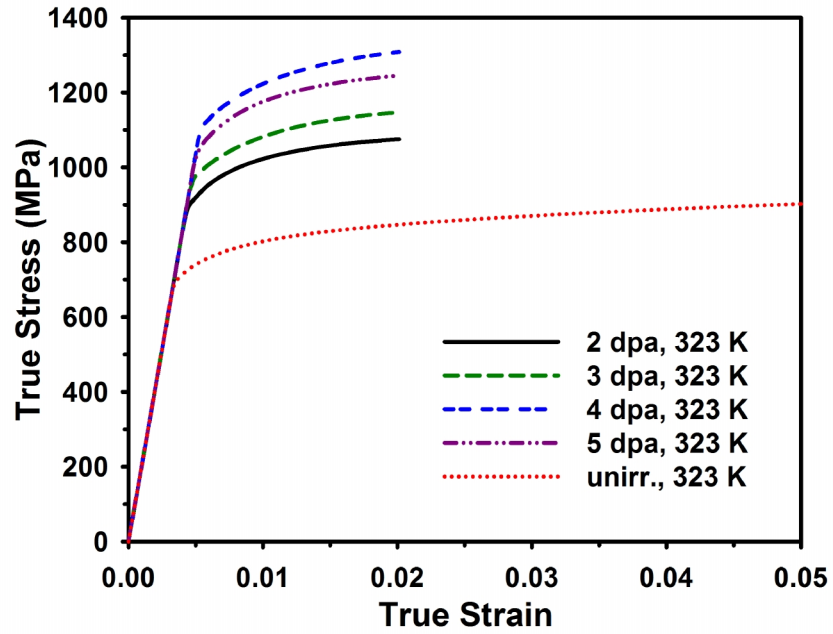
Figure 3. Effect of radiation dose on the stress-strain response.
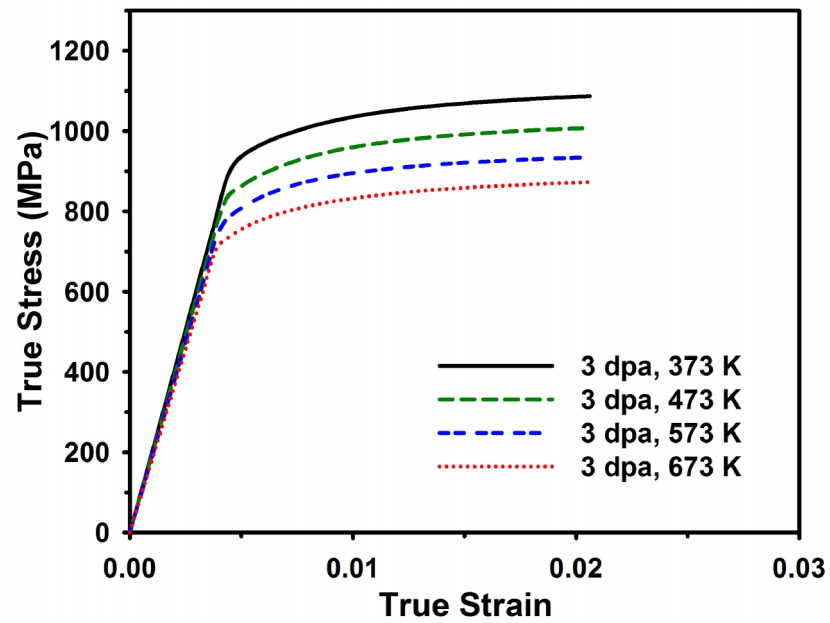
Figure 4. Effect of temperature on the stress-strain response.
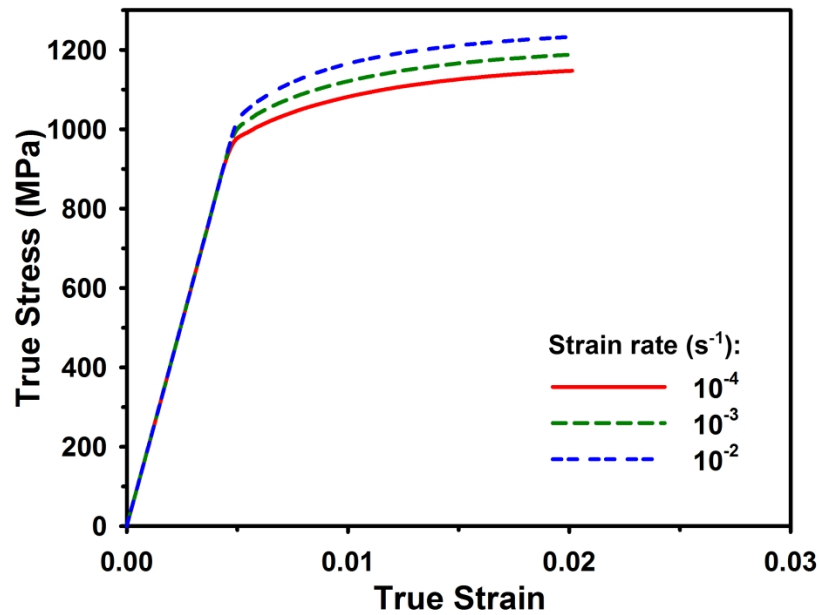
Figure 5. Effect of strain rate on the stress-strain response of the material loaded in tension at 323 K **after being irradiated to** 3 dpa.

2.5.2 Creep tests

Creep simulations are computationally intensive due to the significantly longer time-scales of these tests (100-1000 h). In this work, accelerated creep simulations were performed over shorter durations of time (20-30 h) to explore initial trends of the model under creep loading. They are accelerated in the sense that the rate of absorption of point defects, and consequently the climb rates of mobile dislocations are higher in our simulations. Three-dimensional stress-controlled simulations were performed on 27 grain ensembles with 30 μm cubic grains and random crystallographic orientation distribution. Periodic boundary conditions were used on the lateral (side) faces of the ensemble. All degrees of freedom were restricted on the top face. The bottom face was initially loaded in tensile stress to the requisite level, and the stress was then held constant for the desired duration of time.

It is assumed that the material has no prior deformation history, and has only mobile dislocations. Mobile dislocations will eventually be trapped and become immobile. Dislocation loops are also formed from the mobile dislocations. An initial dislocation density $\rho_M^0 = 1.0 \times 10^8 \, \text{mm}^{-2}$ was assigned to each slip system. An initial concentration of $c_i^0 = 1.0 \times 10^{13} \, \text{mm}^{-3}$, and $c_v^0 = 1.0 \times 10^{13} \, \text{mm}^{-3}$ was used for the interstitials and vacancies, respectively. The initial point defect concentrations used are higher than the corresponding equilibrium concentrations (in the absence of irradiation). High initial concentrations have been used to avoid numerical instabilities in the simulations. Given the fact that the defect pair production rate is high during irradiation, these initial concentration levels used will be reached within seconds of the start of irradiation in actual experiments.

Simulations were performed over a range of stress, temperature and radiation damage rates. To the best of our knowledge, there is currently no representative experimental data in the literature to validate our simulation results. Predictive trends are consistent with expectations. Figure 6 shows the total strain evolution over time for different defect pair production rates. Of course, creep strain dominates after the initial loading portion. Simulations show that the creep rate depends linearly on the defect pair production rate. Based on the correlation between loop density and dpa levels in Eq. (2.30), the average radiation damage rate was found to be $1.05 \times 10^{-5} \, \text{dpa-s}^{-1}$, and the corresponding average creep rate was $3.65 \times 10^{-8} \, \text{s}^{-1}$ at 160 MPa true stress and 773 K for $K_0 = 2.5 \times 10^{12} \, \text{mm}^{-3} \text{s}^{-1}$. For the same stress and temperature conditions, when the defect production rate was increased to $K_0 = 5.0 \times 10^{12} \, \text{mm}^{-3} \text{s}^{-1}$, the radiation damage rate was

found to be $2.12 \times 10^{-5} \, \text{dpa-s}^{-1}$, and the corresponding creep rate was $7.31 \times 10^{-8} \, \text{s}^{-1}$. For $K_0 = 1.25 \times 10^{12} \, \text{mm}^{-3} \text{s}^{-1}$, the radiation damage rate was found to be $5.15 \times 10^{-6} \, \text{dpa-s}^{-1}$, and the corresponding creep rate was $1.57 \times 10^{-8} \, \text{s}^{-1}$.
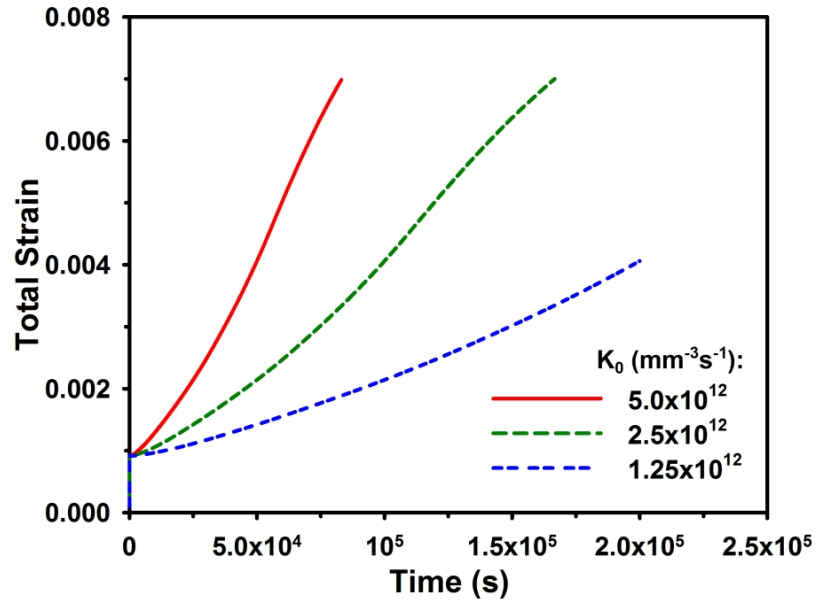
Figure 6. Total strain evolution over time for different defect pair production rates. The material was loaded to $160 \, \text{MPa}$ **in stress control at** $773 \, \text{K}$ **.**

Figure 7 shows the evolution of total strain over time for different true stress levels. The creep rate is initially dominated by SIPA. In the later stages however the creep rates start increasing. In the steady state creep regime, the mobile and the immobile dislocation evolution processes compete against each other, until the mobile dislocation density starts decreasing at a higher rate. This reduces the athermal slip resistance and facilitates dislocation glide, leading to higher creep rates during the later stages of deformation.
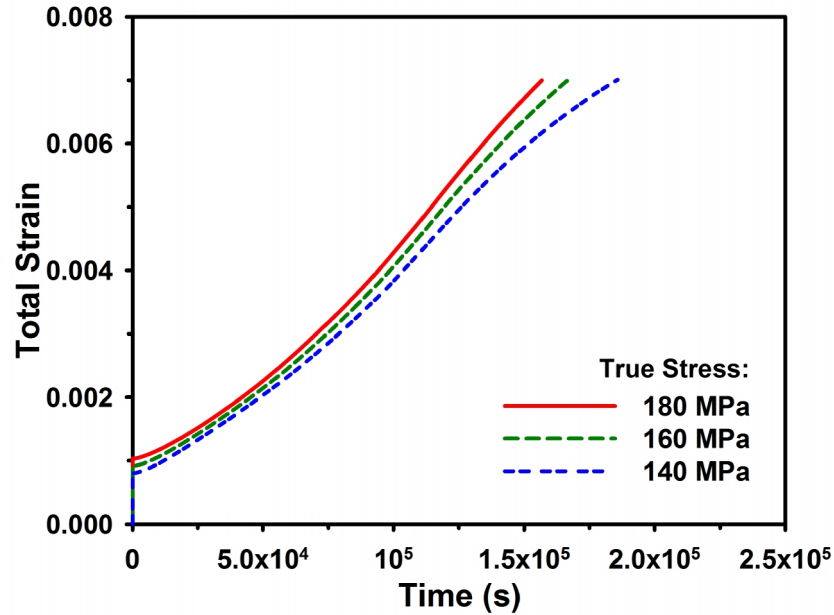
Figure 7. Total strain evolution over time for different stresses under creep loading at 773 K **.** $K_0 = 2.5 \times 10^{12}\,\text{mm}^{-3}\text{s}^{-1}$ **in these simulations.**

Figure 8 shows the evolution of defects (dislocation densities, areal interstitial loop density) during creep as a function of the total strain. The mobile and immobile dislocation evolution trends are (qualitatively) similar to those predicted by Magnusson et al. [94] for thermal creep. Note that the equilibrium vacancy concentration at 773 K is approximately $3.5 \times 10^9\,\text{mm}^{-3}$; as expected, the present vacancy concentration is of substantially non-equilibrium character. The mobile dislocation density decreases with increasing strain; and the immobile and areal interstitial loop densities increase with increasing creep. The areal interstitial loop density is however several times higher than the immobile dislocation density. This is due to the accumulation of defects associated with the radiation damage phenomena. Our simulations have also shown that the mobile dislocation densities decrease to very low levels on certain slip planes. The resolved

normal stress, σ_c^{α}, is higher on these planes, leading to a more rapid migration of mobile

dislocations from them via absorption of point defects.
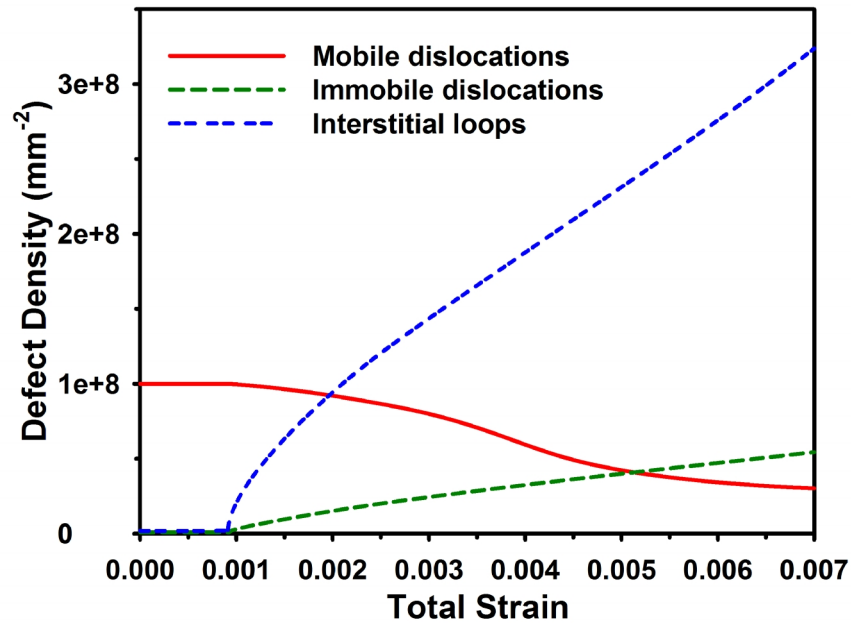
Figure 8. Average dislocation densities and areal interstitial loops density (per slip system) as a function of total strain. Initial threshold indicated loading of the sample in stress, before the constant stress creep regime has begun. The material was loaded to 160 MPa **at** 773 K **.** $K_0 = 2.5 \times 10^{12}$ mm^{-3}s^{-1} **in these simulations.**

Figure 9 shows the evolution of point defects during creep as a function of the

total strain. Qualitative trends compare well with the mean field rate theory calculations

of Stoller et al. [88], at least initially. In the calculations of Stoller et al., a constant

dislocation density was used. Note that they used a more complex rate theory formulation

for point defect evolution, with terms accounting for additional mechanisms.

The spatial evolution of effective inelastic strain and defect substructure during

irradiation creep deformation is discussed in detail in Chapter 5.
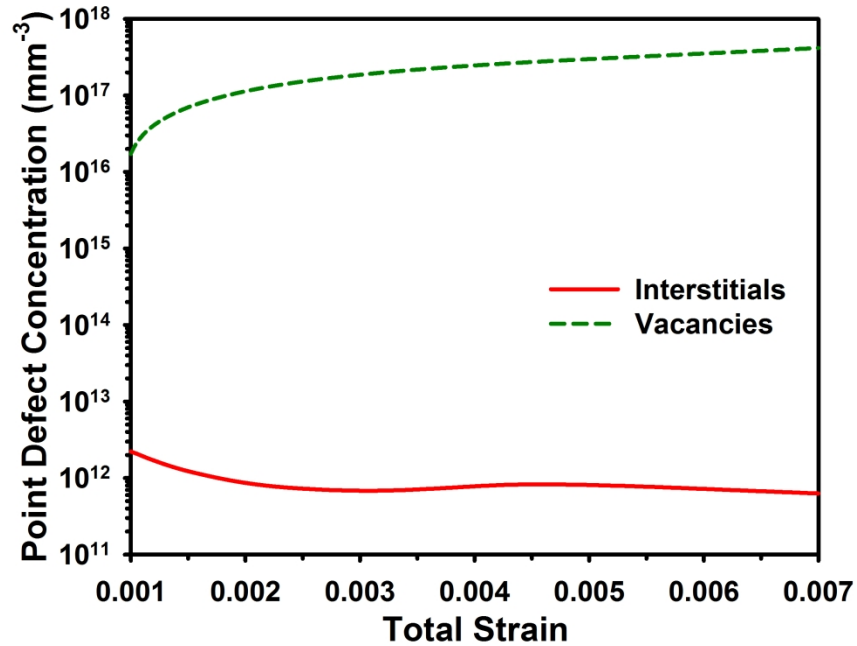
Figure 9. Average point defect concentrations as a function of total strain. Loading conditions same as in Fig. 8.

2.6   Summary

A mechanism-based ISV continuum crystal plasticity model has been formulated to simulate the inelastic behavior of irradiated bcc structural materials. Statistically representative continuum models have been developed for cross-slip and climb of dislocations and growth of interstitial loops. A rate theory-based approach has been used to model the point defect evolution during radiation. The model was used to predict the quasi-static tensile behavior and creep behavior of Mod 9Cr-1Mo ferritic/martensitic steel. Reasonable calibration with available experimental quasi-static loading data for the initial hardening response was achieved and behavioral trends were predicted for creep loading. Most of the material parameters used in the model are based on physical constants and data. This mesoscale model provides a framework for bridging simulations

49

across multiple length- and time-scales by drawing on information from various atomistic and kinetic Monte-Carlo simulations of radiation damage. The constitutive model has been proposed for bcc metals; however, it can be easily applied to other systems by making necessary modifications of the evolution mechanisms and relevant crystallography.

This Chapter lays the foundations of continuum framework to model the deformation behavior of irradiated bcc materials over a range of loading and radiation histories. The following Chapters will apply the framework to model these deformation histories, with necessary model modifications.

CHAPTER 3

MODELING LOCALIZED DEFORMATION DUE TO

DISLOCATION CHANNEL FORMATION[2]

3.1   Introduction

The mechanical behavior of bcc ferritic/martensitic steels is significantly influenced by radiation damage, with effects including an increase in yield point, decrease in uniform ductility and considerably lower true strain to fracture [2,95–98]. Failure in these materials is governed by heterogeneous localized deformation due to the formation of dislocation channels, wherein majority of the inelastic strain is localized [29,76,77]. As a result, irradiated materials fail at relatively lower strains compared with virgin materials. In fact, the formation of dislocation channels and the resulting localized deformation is not just a feature of these ferritic/martensitic steels, but is observed in all irradiated metallic systems [99–102]. Research is therefore directed at understanding the physical mechanisms underlying these processes and the factors influencing them.

This Chapter focuses on modeling localized deformation in irradiated bcc materials using a mesoscale crystal plasticity model. A physics-based continuum constitutive framework was developed in Chapter 2 to model the quasi-static tensile and creep behavior of irradiated bcc metals. This framework is applied here to model the mechanical response and microstructure evolution resulting from heterogeneous localized

---

[2] Significant parts of this Chapter have appeared in Ref. [17].

deformation in irradiated bcc ferritic/martensitic steels. Necessary modifications are made to the existing constitutive model to capture the localization behavior.

3.2   Background

The microstructure of as-irradiated bcc metals is typically characterized by defect clusters and dislocation loops (primarily interstitial-type) [27,103,104]. On being subjected to tensile deformation, cellular structures of dislocations are observed at low radiation doses (< 0.2 dpa) [78]. However, at larger radiation doses, the deformed microstructure changes drastically and is dominated by the formation of dislocation channels, associated with the <111>{110}- and <111>{112}-type slip systems in bcc crystals [29,78,99,105]. These dislocation channels are typically depleted of irradiation-induced defects and dislocation debris [106,107], though they might not be entirely free of defects [78,108]. The channels are generally found to be oriented along the direction of maximum resolved shear stress in the material, e.g., at 45° to the loading axis for uniaxial tension [78]. The channels are ~ 50-200 nm wide [29,78,109,110] and the spacing between channels is ~1.5-5 μm [78]. It has been found that the channels are formed more densely near the fracture surfaces as compared to the uniformly strained bulk; the average spacing between channels differs by an order of magnitude in these regions [78].

The mechanical behavior of these materials is governed primarily by the dislocation-defect interactions. Irradiation leads to an increase in yield strength of the materials. This is due to the presence of irradiation-induced point defect clusters and dislocation loops, posing as added obstacles in the path of glide dislocations that carry

inelastic deformation. More importantly, there is a severe decrease in ductility and engineering strain to failure in these irradiated materials. This observed behavior has been correlated to the formation of defect-depleted dislocation channels mentioned above. It has been suggested [105] that pinning of dislocation sources at (stronger) irradiation-induced defects leads to stress concentration and restricted flow in the material. When the dislocations are eventually unpinned, higher resolved shear stresses allow them to sweep through and annihilate the barriers, hence creating defect-depleted channels [111]. Subsequent glide of dislocations through these 'cleared' channels becomes easier, leading to flow softening and localization of inelastic deformation along the channels [104], finally resulting in failure at relatively lower bulk strains [112].

Physical mechanisms involved in the annihilation of defects by mobile glide dislocations are still a matter of ongoing research. In situ transmission electron microscopy (TEM) and molecular dynamics (MD) simulations are primarily used for this purpose. It has been found that screw dislocations are more effective at annihilating irradiation-induced defects and have higher mobility within the channels as compared to edge dislocations in fcc metals [107,113]. It is noted that majority of the defect annihilation studies have been performed for fcc metals and alloys. Studies of the interaction of dislocations with defect clusters in fcc metals (primarily vacancy type stacking fault tetrahedra, SFT) show that the SFTs can either be sheared by or absorbed into the gliding dislocations [114–118]. The SFTs can also be partially unfaulted on interaction with screw dislocations which spontaneous cross-slip on the face of the SFTs [119]. Interstitial type Frank loops interacting with screw dislocations have been found to be transformed into helical turns, which pin the dislocation lines [120,121]. When the

dislocations are eventually unpinned at higher stresses, they carry the helical turns along with them, leading to progressive clearing of dislocation channels [120,121]. Similar phenomena have also been suggested for the interaction of SFTs with screw dislocations [119].

In bcc metals, plastic deformation is non-trivial due to the inherent non-planar nature of the $1/2\langle111\rangle$ screw dislocation cores, manifesting in the form of non-associative plastic flow, tension-compression asymmetry, and temperature-dependent screw dislocation mobility [122–125]. Consequently, the study of defect (primarily interstitial loop) annihilation mechanisms in bcc structures is much more difficult, and is also material-dependent. Experimental observations of post-deformed samples of irradiated Fe-9Cr alloy [126] suggest that removal of irradiation induced-$\langle100\rangle$ interstitial loops occurs by continued interaction with $1/2\langle111\rangle$ screw dislocations based on the reaction: $[100]+1/2[\bar{1}11]=1/2[111]$. Subsequent transformation of the resultant loops into screw dislocations with the same Burgers vector leads to a microstructure typical of the unirradiated deformed specimens. MD simulations of temperature-dependent reactions between $1/2\langle111\rangle$ screw dislocations and $\langle100\rangle$ interstitial loops in bcc iron [127] have suggested that the absorption of loops by screw dislocations results in the formation of glissile helical turns at elevated temperatures. This could lead to potential reactions of the gliding helical turns with other radiation induced-defects, resulting in their growth or shrinkage, ultimately contributing to dislocation channel formation. MD studies of edge dislocations interacting with self-interstitial atom (SIA) loops have also suggested other potential defect annihilation mechanisms via loop

absorption into the dislocations [128,129]. A recent dislocation dynamics (DD) study of irradiated bcc-Fe [47] suggests that transition to localized deformation occurs at a critical density of the irradiation-induced defects (prismatic loops), below which deformation is mostly homogeneous. It was suggested [47] that flow localization along dislocation channels is a two-step process: initial coarsening of the prismatic loops on their interaction with glide dislocations, followed by 'transformation' of these coarsened prismatic loops into structures that are indistinguishable from network dislocations (in unirradiated materials). As a result, flow resistance along these regions is greatly reduced due to transformation of the prismatic loops to the 'apparent' network dislocations, allowing inelastic deformation to localize. While this might be a possible mechanism to account for flow localization along dislocation channels, further experimental evidence is needed to confirm its exclusivity.

As can be seen, modeling the localization phenomena in irradiated materials is rather complicated due to the nature of dislocation-defect interactions involved; it has been mostly limited to MD (mentioned above) and DD studies [25,47,120,121,130–132]. There is also an issue associated with the inherent length scale (~ hundred nm) of the problem. On one hand, coarse-grained calculations need to capture the underlying physics of phenomena occurring at lower length scales; on the other hand, lower scale atomistic studies of such large polycrystalline ensembles over the time frame of a few hundred seconds are impractical. Nonetheless, MD simulations are vital in understanding the defect evolution and individual physical mechanisms at the atomic scale and extracting information for higher scale simulations. Although providing an effective method to model this phenomenon at intermediate length scales, DD simulations are

limited in applicability to very small sample sizes and are therefore inadequate for predicting the overall mechanical properties of the bulk. Further, constitutive assumptions are still involved in the dislocation-dislocation interactions in DD simulations. A mechanism-based mesoscale constitutive crystal plasticity continuum framework with adequate phenomenological treatment of the underlying deformation processes (including a suitable description of the defect annihilation mechanism, yet to be fully resolved) at lower scales can address the aforementioned scale issues. Moreover, it can be used to study the effect of factors such as crystallographic orientation, grain size, etc. on the localization behavior.

A defect density-based crystal plasticity framework was developed to simulate the mechanical behavior of irradiated bcc materials in Chapter 2. Evolution laws for dislocations and interstitial loops (produced due to radiation in bcc materials) were tied to the inelastic deformation behavior. In addition, rate theory calculations were used to model the evolution of irradiation-induced point defects. However, the constitutive framework did not attempt to model the localization behavior observed in irradiated metals loaded in tension. In this Chapter, a phenomenological model is developed to account for the observed localization due to interaction of irradiation-induced defects with glide dislocations. The framework is used to model the mechanical response and deformed microstructure of an irradiated ferritic/martensitic steel loaded in tension.

3.3   Model description

The continuum crystal plasticity model accounts for the climb-enhanced glide of mobile dislocations trapped in the field of immobile dislocations and irradiation-induced

interstitial loops, at the level of slip systems. Dislocation densities, both mobile (ρ_M^α) and immobile (ρ_I^α), number densities of the sessile interstitial loops (N_i^α), and interstitial loop sizes (d_i^α) are used as ISVs in the model, the evolution of which affect the hardening behavior of slip system α. It is assumed that all the interstitial loops are planar and circular in shape. In addition, point defects, i.e., interstitials (c_i) and vacancies (c_v) (generated during irradiation and present thereafter) are tracked using rate theory calculations. As described in Chapter 2, physically-consistent models are used for the evolution of defect densities.

In this Chapter, we develop a phenomenological model for reduction in density of the interstitial loops, to account for the observed flow softening behavior.

3.3.1 Defect annihilation model

Using insights from MD simulations for fcc Ni, Rodney et al. [133] developed a micromechanical model that asserts 'absorption' by glide dislocations within a critical capture radius of irradiation-induced defects. However, they assumed that the defects would be absorbed uniformly, without any consideration for preferential slip on favorably oriented planes. A critical capture radius for defect absorption has also been employed in DD simulations of fcc metals by Ghoniem et al. [46,131]. Using this information, Krishna et al. [13] recently developed a constitutive model for defect annihilation in fcc metals. Their model considered dependence of the defect annihilation rate on both the defect density and dislocation density, as compared to Rodney et al. [133] where absorption rate is dependent only on the defect density. Further, Krishna et al. [13] used a

crystal plasticity framework and also accounted for dependence of the annihilation rate on the crystallographic shearing rate.

Before describing our defect annihilation model, it is again emphasized that the mechanisms of defect annihilation in bcc metals are less well understood and quantified than those in fcc metals (cf. Section 3.2). Assuming that a similar concept of critical capture radius would hold for bcc metals, we have formulated a phenomenological model for the annihilation rate with dependence on both mobile dislocation density, ρ_M^α, and areal loop density, $N_i^\alpha d_i^\alpha$. Accordingly, the depletion rate of areal loop density on any slip system α is given as

$$\dot{N}_{i,ann}^\alpha d_i^\alpha = -\frac{R_{ann}}{b}\left(N_i^\alpha d_i^\alpha\right)^c \left(\rho_M^\alpha\right)^{1-c}\left|\dot{\gamma}^\alpha\right| \tag{3.1}$$

where R_{ann} is the capture radius of annihilation and c is the exponent of the areal loop density such that the product of areal loop density term and mobile dislocation density term on the right hand side of Eq. (3.1) has the units of dislocation/areal loop density. This leads us to the annihilation rate of interstitial loop number density as

$$\dot{N}_{i,ann}^\alpha = -\frac{1}{d_i^\alpha}\frac{R_{ann}}{b}\left(N_i^\alpha d_i^\alpha\right)^c \left(\rho_M^\alpha\right)^{1-c}\left|\dot{\gamma}^\alpha\right| \tag{3.2}$$

Rodney et al. [133] also suggested that the capture radius would increase with increasing loop sizes. Accordingly, the capture radius, R_{ann}, is varied as a function of the current loop size, d_i^α, in this framework, and the areal loop density exponent, c, is also varied to study their effect on the localization behavior. Both these parameters are also used for calibrating simulation results to experimental stress-strain data for irradiated specimens.

Recent dislocation dynamics studies of irradiated Fe [47] have suggested that reduction in flow stress may simply be due to transformation of these loops into ordinary network dislocations (without any annihilation/absorption of the loops), thus reducing their resistance to dislocation glide and promoting localization. While this assertion may be valid, this does not rule out the 'absorption' of irradiation-induced defects by mobile dislocations as observed by others (cf. Section 3.2). With continued physical insights, appropriate modification to the phenomenological relation given in Eq. (3.2) may be made to account for this mechanism in the future. Nevertheless, our constitutive model in its present form accounts for the reduction in loop density, and consequent reduction in flow stress, enabling us to study localization as a function of other mesoscopic factors, such as crystallographic orientations, loop density, etc.

The updated rate of evolution of interstitial loop density (modified from Eq. (2.27)) is thus given as

$$\dot{N}_i^\alpha = \dot{N}_{i,climb}^\alpha + \dot{N}_{i,ann}^\alpha \tag{3.3}$$

Note that mobile dislocations also get (statistically) trapped at the interstitial loop barriers and 'transform' to immobile dislocations. This is modeled using the last term in Eq. (2.25).

3.4　Model implementation

3.4.1　Model parameters

The constitutive model was used to simulate the tensile behavior of Mod 9Cr-1Mo steel. This steel has good radiation resistance and high temperature properties. Ferrite and martensite constitute the main phases of Mod 9Cr-1Mo steel, which derives its strength from the lath martensite microstructure. Moreover, the crystal structure of the subsequently tempered martensite phase is closer to body-centered cubic than body-centered tetragonal [80]. Thus, we have assumed the material to have a uniform bcc structure with 48 slip systems. The majority of the parameters in this model require estimation from physical constants. For Mod 9Cr-1Mo steel, however, not much physical data are available apart from the elastic constants. Since, it has primarily ferritic and martensitic phases, most of the parameters are estimated from available data for bcc-iron. The rationale behind selecting specific values has already been explained in detail in Section 2.4.1 and the corresponding values given in Table 1 in Chapter 2.

Experimental studies of the microstructure of Mod 9Cr-1Mo steel have estimated a high density of dislocations of the order $10^7 - 10^8 \, \text{mm}^{-2}$ [82,93]. Based on this, the initial density of mobile dislocations is assumed to be $\rho_M^0 = 2 \times 10^7 \, \text{mm}^{-2}$ and that of $\rho_I^0 = 3 \times 10^7 \, \text{mm}^{-2}$ is assumed for immobile dislocations on all 48 slip systems in our simulations.

In this Chapter, a parametric study of the cross-slip model and its effects on localization behavior has been performed. An analytical solution for the critical activation stress for cross-slip, τ^*, is given by Hirth and Lothe [69]. The value of τ^* depends on the average dislocation line length. Given an average dislocation density of

$1 \times 10^7 - 5 \times 10^7 \, \text{mm}^{-2}$ per slip system, the average dislocation line length $\approx 100 - 200b$. Corresponding to this dislocation line length, τ^* was estimated to be $\approx 0.004G$ from Rhee et al. [70]. The same value was used in all our simulations. The activation volume for cross-slip was assumed to be $V_a = 20b^3$. The value of the material constant, k_{cs}, was varied to study its effect on the microstructure evolution.

3.4.2 Loading and boundary conditions

The 3D constitutive model was implemented in the finite element program ABAQUS [91] using the User MATerial (UMAT) subroutine. Simulations were performed using generalized plane strain elements along with the 3D crystallography, effectively treating a network of cubic grains (square cross-section in the plane) as columnar with random orientation distribution. Finite elements (FEs) with linear interpolation and reduced integration were used.

Quasi-static tension tests were simulated on the polycrystalline ensembles. A schematic of the loading and boundary conditions is shown in Fig. 10. The bottom edge of the 2D simulation box was constrained along the loading direction, and the center of the bottom edge was constrained in all degrees of freedom to prevent rigid body rotation. The side edges of the simulation box were traction-free. Note that traction-free surfaces are valid boundary conditions only for loading samples to relatively small strains ($\sim$ 4-5% strains in the present case). Displacement-controlled tensile loading was applied on the top edge at a prescribed strain-rate of $1 \times 10^{-4} \text{s}^{-1}$ in all simulations.
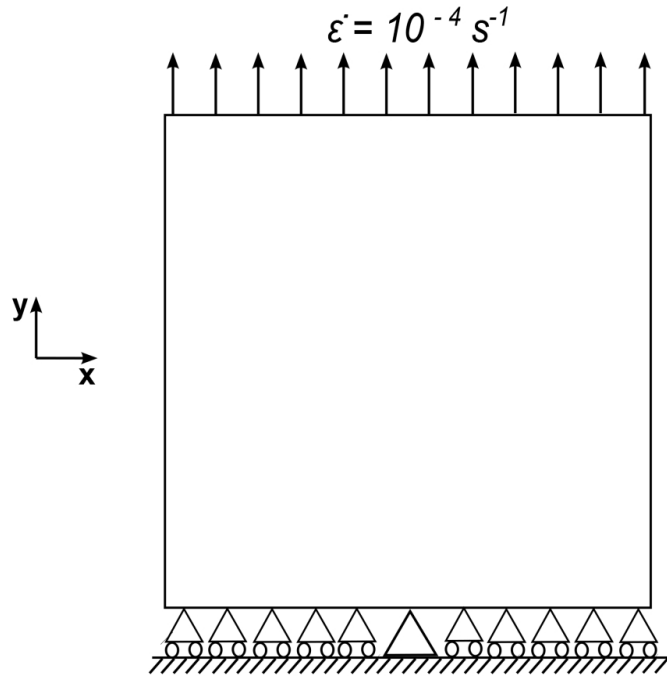
Figure 10. Schematic of loading and boundary conditions applied to the simulation box.

3.5 Results and discussion

Post-irradiation tension tests were performed on 25 square-shaped, randomly oriented, 5 μm-sized grains, unless mentioned otherwise. Post-irradiation tension tests are those for which the material is loaded in a normal (no radiation) environment following irradiation to a certain dpa damage level. The presence of prior radiation damage leads to dislocation channel formation and inelastic strain localization during these tensile tests. Note that in-reactor tension test (concurrent radiation and deformation with little or no prior radiation history) studies on bcc-Fe and Fe-Cr alloys by Singh et al. [134] found that deformation is homogeneous and dislocation channels are not formed. However, in-reactor tension test studies on Cu and CuCrZr alloys [135] did find the formation of dislocation channels, though yield drop and plastic instability was not observed in the

associated mechanical behavior. These experiments suggest that channel formation and plastic instability is strain rate- and radiation dose-dependent.

The following Sections will first consider the simulated mechanical response of the material, and then describe the simulated deformed microstructure in terms of the evolution of effective inelastic strain, mobile dislocation density, and interstitial loop density.

3.5.1 Mechanical behavior

Certain model parameters were calibrated to match the experimental engineering stress-strain data for Mod 9Cr-1Mo steel [2]. The model was first fit to the virgin specimen data using the parameter values given in Table 1. Values of $k_{cs} = 2.0 \times 10^4$, $R_{ann} / d_i^\alpha = 3.0$ and $c = 0.85$ for the cross-slip and flow softening models were then used to match the model results to the irradiated specimen data. Figure 11 shows the simulated stress-strain curves and the corresponding experimental data for various loading and irradiation histories. A reasonable fit is obtained for all cases, to 3-4% engineering strain for irradiated specimens, and 5-6% engineering strain for virgin specimens. Note the change in the stress-strain response of the irradiated specimens as a result of the additional defect annihilation model (Eq. (3.2)) from the initial stress-strain curves shown previously in Fig. 2. For irradiated specimens, the initial localization behavior is dominated primarily by material softening instabilities due to formation of dislocation channels. At higher strains, geometric softening instabilities are expected to set in, which the current simulation meshes and boundary conditions do not address; only material instabilities are captured. For virgin specimens, no material softening instabilities are

present for the simulated mechanical response. The softening observed in the experimental stress-strain curves of the virgin specimens is dominated by geometric instability due to diffuse necking.

For the post-irradiation tensile tests simulated here, diffusion gradients were neglected in the point defect rate equations (Eqs. (2.9), (2.10)). This is a valid assumption given the fact that there is no concurrent irradiation and the overall point defect concentrations are low in the material. However, for the case of in-reactor tension tests (cf. [134,135]), with concurrent irradiation, the diffusion gradients cannot be neglected, and will play a role in the evolution of the deformed microstructure. Future work will focus on modeling these experiments.
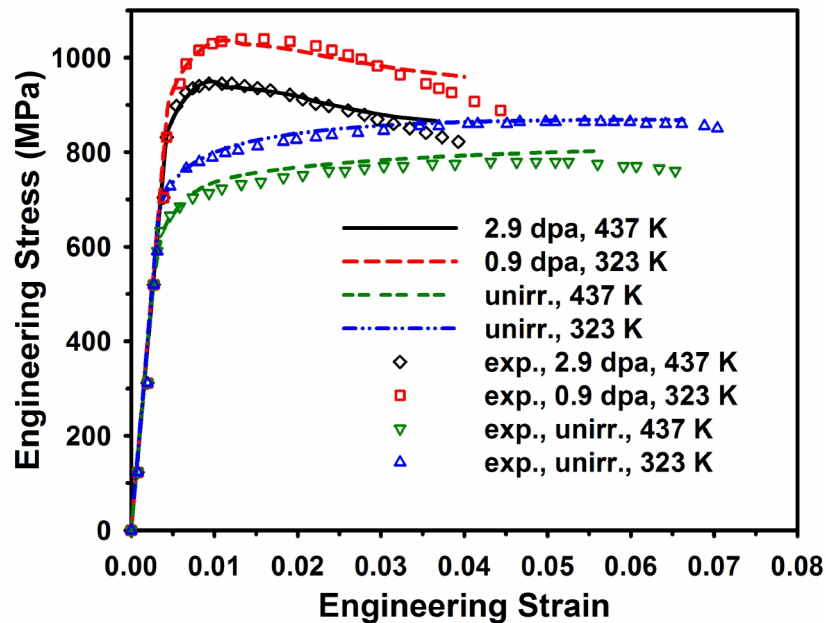
Figure 11. Comparison of simulated stress-strain curves (solid and dotted lines) calibrated to experimental data (open symbols). Experimental data from Maloy et al. [2].

The objective of the present modeling is to determine the localization patterns and how they relate in terms of spatial frequency and orientation to the larger scale polycrystalline grain structure. The simulation results presented in Fig. 11 were carried out using finite elements with a mesh size of 200 nm. This mesh size is selected as the minimum size which serves as a compromise between a converged polycrystal stress-strain response and the lower limit of the continuum field approximation of continuously distributed dislocations (cf. [136]). The current dislocation mechanism-based constitutive framework admits interpretation of the dislocation spacing in channels and allows for estimation of continued channel refinement and enhanced strain localization without having to explicitly resolve the fields below the minimum mesh size of 200 nm. Even if the measured channel width is below this scale, the net shear strain is comparable at the mesoscale (e.g., grain scale) in both cases. At a resolution of 200 nm element size, each finite element would contain ~2-4 dislocations per slip system (for a given dislocation density $\sim 5 \times 10^7 - 10^8 \, \mathrm{mm}^{-2}$). A finer mesh would effectively have less than one dislocation per element. This provides a lower limit on the element size for purposes of a statistical ensemble representation.

Effect of element size on the inelastic part of the stress-strain response was analyzed by coarser mesh simulations for the case of 2.9 dpa radiation damage at 437 K (Fig. 12). It was found that the mechanical response of the material depends somewhat on the uniform element size. Using the same set of parameters, a reasonable fit to the experimental stress-strain curve was obtained for all element sizes, at least until geometric instabilities set in later on. However, note that the drop in stress due to localization instabilities is much larger when using a coarse mesh. This is because

localized deformation takes place over a relatively larger volume of the coarse mesh, thus contributing to the (volume averaged) stress response more significantly. Convergence was achieved in the peak stress and initial localization regime for element sizes approaching 200 nm. An element size of 200 nm will be used in the following simulations, unless specified otherwise. A finer mesh would also lead to significantly higher computational times. Even with a mesh size of 200 nm, the simulations took $\approx$ 100 h to reach 4% applied strain on 24 CPU cores (2.2 GHz AMD Opteron) running in parallel.
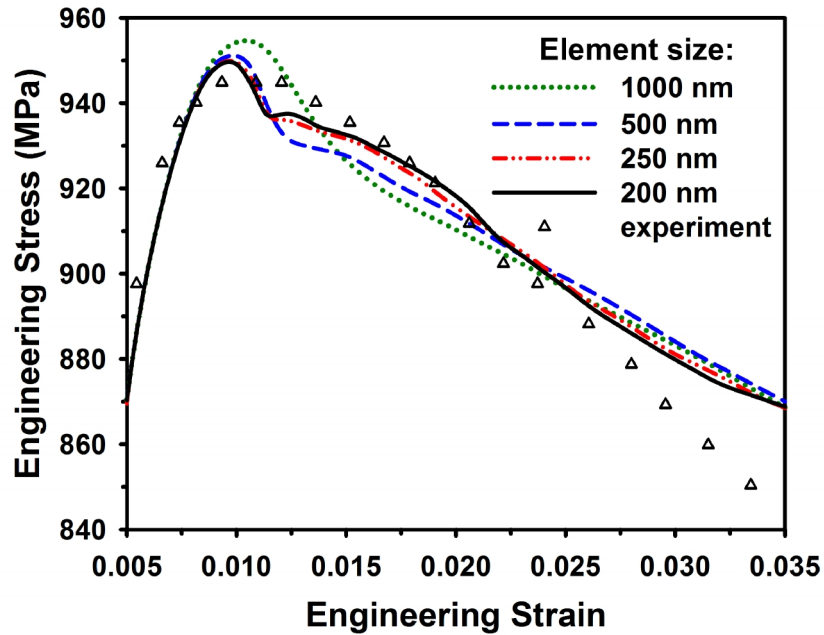
Figure 12. Effect of element size on the inelastic part of the stress-strain curves for the material loaded at $437\,K$ **after irradiation to** $2.9\,dpa$**. Open triangles indicate the corresponding experimental data.**

Finally, these simulations were performed using 5 μm-sized grains. This was done to homogenize the effect of random initial crystallographic orientations on the deformation behavior, and still use a relatively small simulation cell size (with a very fine

mesh). We have verified using larger grain simulations that grain size effects on the yield strength and hardening behavior are not noticeable. In the present form of model there are no scale effects to reflect this. However, the element size and the grain size affect localization behavior in terms of the dislocation channel width and the channel spacing, respectively. These effects will be discussed in detail in Section 3.5.6.

3.5.2   Microstructure evolution

3.5.2.1   Evolution of inelastic strain

The microstructure of irradiated materials loaded in tension is dominated by the formation of defect-depleted dislocation channels. This results in highly localized deformation along narrow shear bands. To visualize this phenomenon, the distribution of effective inelastic strain was plotted after tensile deformation to 2% engineering strain in Fig. 13(a), and subsequently 4% engineering strain in Fig. 13(b).
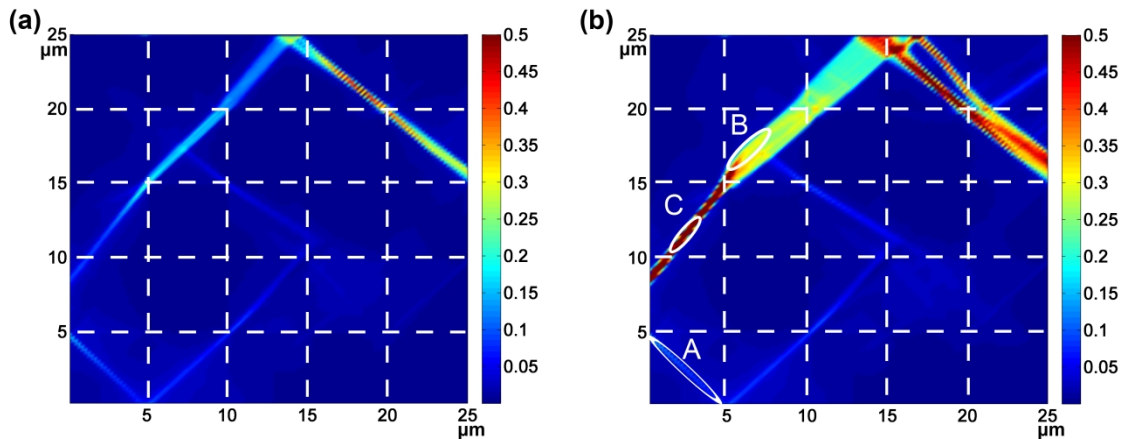
Figure 13. Distribution of effective inelastic strain for material loaded in tension at $437 \, \text{K}$ **after (a)** 2% **, and (b)** 4% **applied engineering strain. The material was irradiated to** $2.9 \, \text{dpa}$ **prior to tensile loading. Dotted lines overlaid indicate grain interfaces. See text for description of regions A, B, and C.**

The sample was tested at 437 K, following irradiation to 2.9 dpa. Values of $k_{cs} = 2.0 \times 10^4$, $R_{ann} / d_i^\alpha = 3.0$ and $c = 0.8$ were used for the cross-slip and defect annihilation parameters, respectively. Regions A, B and C marked in Fig. 13(b) indicate the microstructure evolution during the stages of dislocation channel formation. These regions will be discussed later in the context of defect evolution.

As shown in Fig. 13, intense shear bands, with inelastic strains as high as ≈ 0.7, are formed when the average engineering strain in the bulk is much lower (≈ 0.02-0.03). The shear bands (due to channels) are about 200-500 nm and the average spacing between the bands is of the order of 10 μm. The dislocation channel width is over-predicted by a factor of 2-4 as compared to the experimental results of Zinkle and Singh [78]. Also, the inelastic strain values in our simulations are lower than the experimentally measured shear strains (~1.0-5.0) [99,137]. As mentioned in the last Section, the 200 nm mesh size in these simulations facilitated applicability of the mechanism based continuum approach at or above the scale of mean dislocation spacing in the channels, which allows us to consider a polycrystalline ensemble with a number of grains, addressing issues such as the effects of microstructure on channel formation and spacing. Presently, discrete dislocation mechanics models, also a continuum theory that introduces dislocation lines within a lattice, are not sufficiently advanced to consider the large scale of polycrystals (such approaches are typically used to model dislocation substructure formation), to address dislocation interactions with grain boundaries, or to consider in a robust way the problem of numerous dislocation interactions with irradiation induced defects, including effects of local lattice rotations within shear bands (cf. [120,131,132,138]). Since the net shear strain at the polycrystal level due to localized

plasticity is essentially the same regardless of channel width, the product of the inelastic shear strain within the channel and the channel width should be more or less invariant; in the present case of a 200 nm minimum channel width, the computed localized plastic shear strains should be multiplied by a factor of roughly 4 to project the inelastic shear strain levels in the actual channels with 50 nm width, for example. This is indeed within the window of reported values of localized inelastic strain on the order of 2-3.

Inelastic strain evolution in the microstructure (Figs. 13(a) and 13(b)) suggests that multiplication of channels occurs during later stages of deformation; not all channels are formed simultaneously. Further, the channels grow at different rates; those oriented along favorable slip planes grow preferentially. Also, as expected, the inelastic strain in channels increases as the applied engineering strain goes from 2% to 4%. The widening of channels from Fig. 13(a) to Fig. 13(b) might be an artifact of FE simulations given the present assignment of uniform initial defect density. In experiments, channel widening with increasing applied strains is seldom observed in majority of the metals, and it is believed that the channels, once formed during the initial stages, allow all the applied deformation to localize within them. Introduction of a non-uniform distribution of initial defect density, in conjunction with softening, has been shown (cf. [139]) to provide enhanced sharpening of shear bands in alpha-Ti using a crystal plasticity continuum formulation, and may play a similar role in the present case (cf. Section 3.5.7 for the effect of non-uniform initial defects on channel width). However, in an experimental study by Byun et al. [140], evidence of the formation of channels at different points in time was shown for bcc vanadium. They also showed evidence of widening and bifurcation channels, attributing this to multiple cross-slip of screw dislocations within

the channels in bcc vanadium. Note that the present model framework considers the (rate-dependent) cross-slip mechanism; widening and bifurcation of channels observed in our simulations are in part due to cross-slip (discussed in detail in Section 3.5.4). From a continuum perspective, it is intuitive that if a 'soft' channel cannot accommodate all the applied deformation, it has to widen. Cross-slip offers a possible mechanism to this end.

The constitutive framework assumes a homogeneous local material, i.e., neglects gradients of strain or (line, point) defect densities in the material. Generally, heterogeneous localized deformation is associated with gradients (discussed in detail in Section 3.5.8), and has contributions from both material and geometric instabilities, leading to mesh dependence in FE simulations. However, as has been demonstrated, the present framework accounting only for local 'constitutive' material softening due to dislocation channel formation is able to qualitatively capture both the microstructure evolution and mechanical behavior of irradiated materials. Heterogeneous localized deformation, in the present case, is a consequence of spatial correlations of crystallographic orientations of the grains. Dislocation channels form along favorably oriented slip planes, which have achieved higher resolved shear stresses to annihilate the defects. Further, geometric instabilities are not dominant, at least during the early stages of localization (< 4% engineering strain for the present material). Experiments suggest that these irradiated specimens fail at ≈ 6-8% engineering strain [2]. At such low strain levels, geometric softening effects, though present during the later stages of localization behavior, might not be significant.

3.5.2.2   Substructure evolution

To understand the underlying physical processes governing dislocation channel formation, it is instructive to observe the defect evolution in the material. Figs. 14(a) and 14(b) show the distribution of the mobile dislocation density, ρ_M, and interstitial loop density, N_i (averaged over all slip systems), respectively, corresponding to the effective inelastic strain shown in Fig. 13(b). Based on the regions A, B and C marked in each of the Figs. 13(b), 14(a) and 14(b), three different stages of microstructure evolution can be identified during dislocation channel formation.

I. *Incipient channel formation*

Region A marks the incipient stages of channel formation, when interstitial loops have just started getting annihilated. The mobile dislocation density is slightly lower than the bulk average, as trapping of mobile dislocations by interstitial loops has rendered them immobile.

II. *Defect depletion*

Once the mobile dislocations are subject to sufficient driving force (resolved shear stress), they start annihilating the interstitial loops. As a result, the interstitial loop density is depleted to lower values than the bulk average in region B. Many of the mobile dislocations are still getting trapped at barriers due to the immobilization process, the rate of which has increased due to continual accumulation of immobile dislocations contributing to statistical trapping of the mobile dislocations.

III. *Flow localization*

Finally, the flow resistance is lowered due to depletion of interstitial loop density to very low values in region C. As a result, easier dislocation glide leads to large inelastic

strain in this region. The mobile dislocation density is replenished to relatively high values by dislocation multiplication processes in the defect-depleted channels as a result of enhanced inelastic deformation.

Average values of the mobile dislocation density, interstitial loop density and inelastic strain in the three regions are summarized in Table 2. The interstitial loop density shown in Fig. 14(b) and reported in Table 2 is averaged over all 48 slip systems. Generally, localization takes place on just a few slip systems, on which majority of the interstitial loops get depleted. Hence, the plotted slip system averaged loop density, also accounting for interstitial loops on slip systems for which localized deformation has not taken place, does not diminish to very low values in the dislocation channels, and differs from the bulk average loop density by a factor of less than 2. In reality, channels are depleted of the majority of the irradiation-induced defects (interstitial loops in the present case), if not entirely cleared [78,108]. Irrespective of this, the stages of microstructure evolution during dislocation channel formation would remain the same.
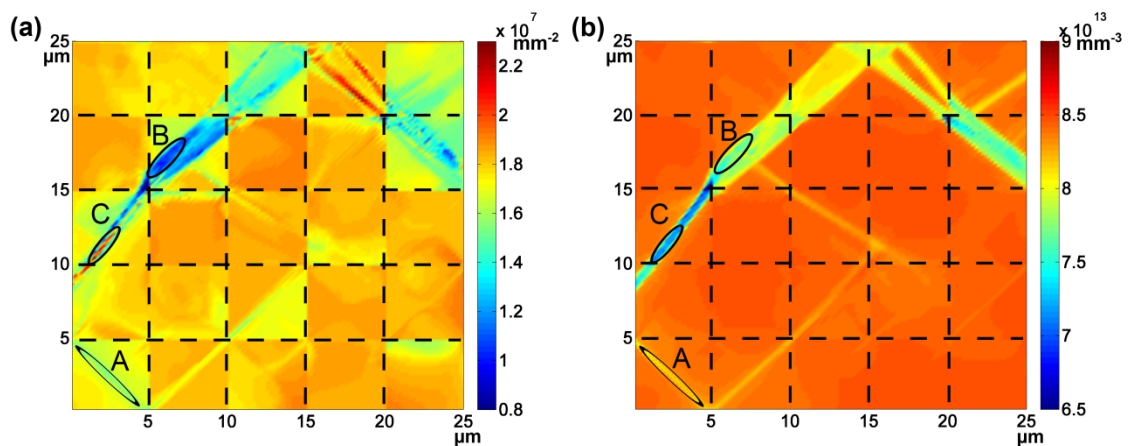
Figure 14. Distribution of (a) mobile dislocation density, and (b) interstitial loop density corresponding to the effective inelastic strain in Fig. 13(b). See text for description of regions A, B and C.

Recent TEM studies of the migration of dislocations through a field of irradiation-induced defects by Briceño et al. [141] offer valuable insights regarding the dislocation-defect interactions just prior to localization. The modeled substructure evolution is in agreement with the TEM observations, i.e., mobile dislocations get trapped in a field of defects, thus rendering them immobile, followed by percolation of dislocations through the field as a result of annihilation of defects. They also suggested that pumping of mobile dislocations takes place via sources not induced by irradiation, and percolation of the dislocations by defect annihilation only enhances their activation. This is consistent with our constitutive model, i.e., dislocation multiplication takes place irrespective of the irradiation-induced defect field (1st term in Eq. (2.25)), and annihilation of defects only leads to enhanced dislocation migration and larger inelastic strain.

Table 2. Average values of mobile dislocation density, interstitial loop density, and inelastic strain during the different stages of dislocation channel evolution, based on regions marked in Figs. 4(b), 5(a) and 5(b).

Region	Stage	Mobile dislocation density (mm^{-2})	Interstitial loop density (mm^{-3})	Effective inelastic strain
A	Incipient channel formation	1.6×10^7	8.0×10^{13}	0.10
B	Defect depletion	1.1×10^7	7.7×10^{13}	0.30
C	Flow localization	2.1×10^7	6.7×10^{13}	0.70
Bulk	---	1.8×10^7	8.5×10^{13}	0.04

3.5.3 Effect of radiation dose on localization

Experimental studies by Sharp [137] and more recently by Jiao et al. [108] show that the inelastic strain in channels (experimentally interpreted in terms of the height of channels) increases with increasing dpa damage (increasing loop size and density). The same was observed in our simulations as the radiation dose was increased from 1 dpa to 2.9 dpa. The measured values of maximum inelastic strain in the channels are given in Table 3. All simulations were performed with the same initial microstructures (crystallographic orientation distributions). As seen in Table 3, the maximum inelastic strain in channels increases with increasing dpa dose. In fact, the simulated maximum inelastic strain was found to scale linearly with the radiation dpa dose at both 2% and 4% engineering strains (Fig. 15). Note that we have assumed a square root dependence of the interstitial loop density and size on dpa dose (Eqs. (2.30), (2.31)). This suggests that maximum inelastic strain in the channels also has a square root dependence on the interstitial loop density and size.

Note that the linear dependence of maximum inelastic strain in channels as a function of dpa dose emerges from our simulations using the same initial microstructures and the assumption of an initially uniform defect distribution. In physical experiments, it is highly unlikely that different samples with different dpa dose histories would have the same initial microstructures; linear dpa dependence has not been reported experimentally. Interestingly, if one were to plot the surface slip band (correlated to dislocation channels in the interior, cf. [142]) heights as a function of the corresponding neutron dose fluxes at the same extension levels reported for irradiated single crystal copper in the table in Ref. [137], it is found that the slip band height does have a near-linear dependence on the

neutron dose flux for the limited reported data. However, more systematic experiments are needed to address this issue and verify our model predictions.

Table 3. Maximum inelastic strain in channels as a function of radiation dose, engineering strain, k_{cs}, R_{ann} and c. Material was loaded in tension at $437\ \text{K}$. The same initial microstructure was used in all simulations.

Radiation dose (dpa)	k_{cs}	R_{ann}/d_i^{α}	c	Engineering strain	Maximum inelastic strain in channels
1	2.0×10^4	3.0	0.8	2%	0.117
				4%	0.303
2	2.0×10^4	3.0	0.8	2%	0.266
				4%	0.479
2.9	2.0×10^4	3.0	0.8	2%	0.392
				4%	0.598
2.9	2.0×10^6	3.0	0.8	2%	0.359
				4%	0.446
2.9	2.0×10^8	3.0	0.8	2%	0.252
				4%	0.345
2.9	2.0×10^4	2.5	0.8	2%	0.360
				4%	0.620
2.9	2.0×10^4	3.5	0.6	2%	0.099
				4%	0.287
2.9	2.0×10^4	3.5	0.8	2%	0.401
				4%	0.575
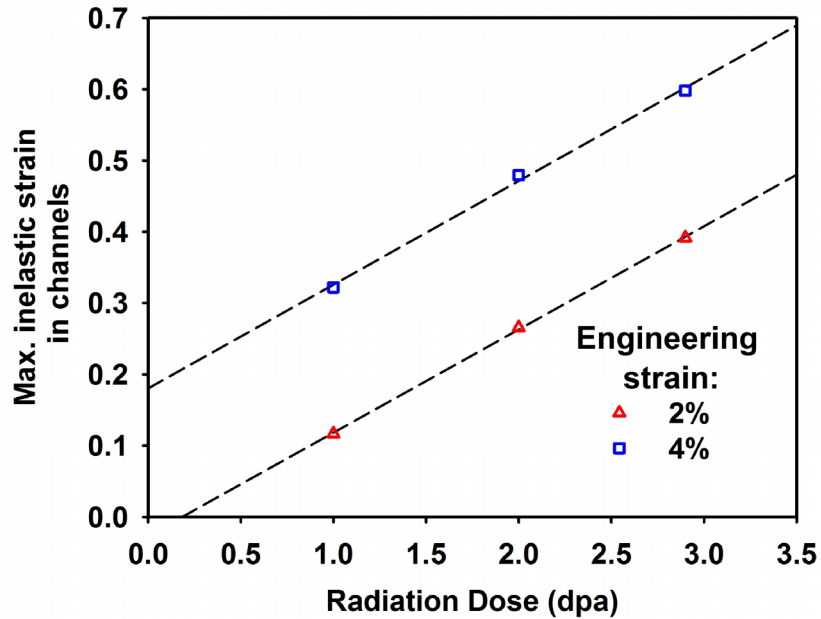
Figure 15. Maximum inelastic strain in dislocation channels as a function of dpa dose after tensile loading to 2%**, and** 4% **engineering strains at** $437\,\mathrm{K}$**.**

Maximum inelastic strain in the channels given in Table 3 depends strongly on the initial crystallographic orientation distributions in the material. For example, using a different initial (random) crystallographic orientation distribution, maximum inelastic strain in the channels is as high as 1.198 at 4% engineering strain, 2.9 dpa radiation dose and 437 K (using $k_{cs} = 2.0 \times 10^4$, $R_{ann} / d_i^{\alpha} = 3.0$ and $c = 0.8$).

3.5.4 Effect of degree of cross-slip on localization

The role of cross-slip in the localized deformation of irradiated materials is not yet completely understood. DD simulations by Diaz de la Rubia et al. [25] showed that cross-slip during defect annihilation plays a role in dislocation channel formation. They proposed that double cross-slip of screw dislocations (during their interaction with

irradiation-induced defects) back to the slip plane from which they initially started contributes to large inelastic strains and hence the localization process. These observations were consistent with TEM studies by Robach et al. [107], which verified the role of cross-slip in the formation and clearing of dislocation channels.

In the present work, we performed a parametric study of the cross-slip model described in Section 2.3.3.3. The estimation procedure for the cross-slip activation stress, τ^*, was mentioned earlier. Here, we vary the cross-slip constant, k_{cs}, and study the resulting localization behavior. The simulated samples were irradiated to 2.9 dpa and then loaded in tension at 437 K. Figs. 16(a) and 16(b) show the effect of increasing k_{cs} on the evolution of effective inelastic strain. The corresponding interstitial loop density evolution is shown in Figs. 16(c) and 16(d), respectively. All parameters except k_{cs} remain same in both these simulations. Further, we started out with the same initial crystallographic orientation distribution in both cases. Values of maximum inelastic strains in the channels as a function of k_{cs} are summarized in Table 3.

As the degree of cross-slip (k_{cs}) is increased from Fig. 16(a) to Fig. 16(b), the channels spread over a wider region and have lower localized inelastic strains. Cross-slip offers a way for mobile dislocations within the channels to bypass slip on planes which have higher flow resistance (due to higher interstitial loop density). As a result, mobile dislocations have migrated to planes with lower interstitial loop densities; lesser interstitial loops are annihilated by mobile dislocations in the localized region during the subsequent loop annihilation process. Therefore, increasing cross-slip results in a relative higher loop density within the channels. This is reflected in the (slip system averaged) interstitial loop density plots shown in Figs. 16(c) and 16(d). As a result of lesser

interstitial loops getting annihilated, the flow resistance is relatively higher with increasing degree of cross-slip, though it is still lower than regions in the immediate vicinity (where no defect annihilation has occurred). However, stress gradients (with the neighboring regions) are now smeared, thus resulting in the formation of wider and more diffuse shear bands.
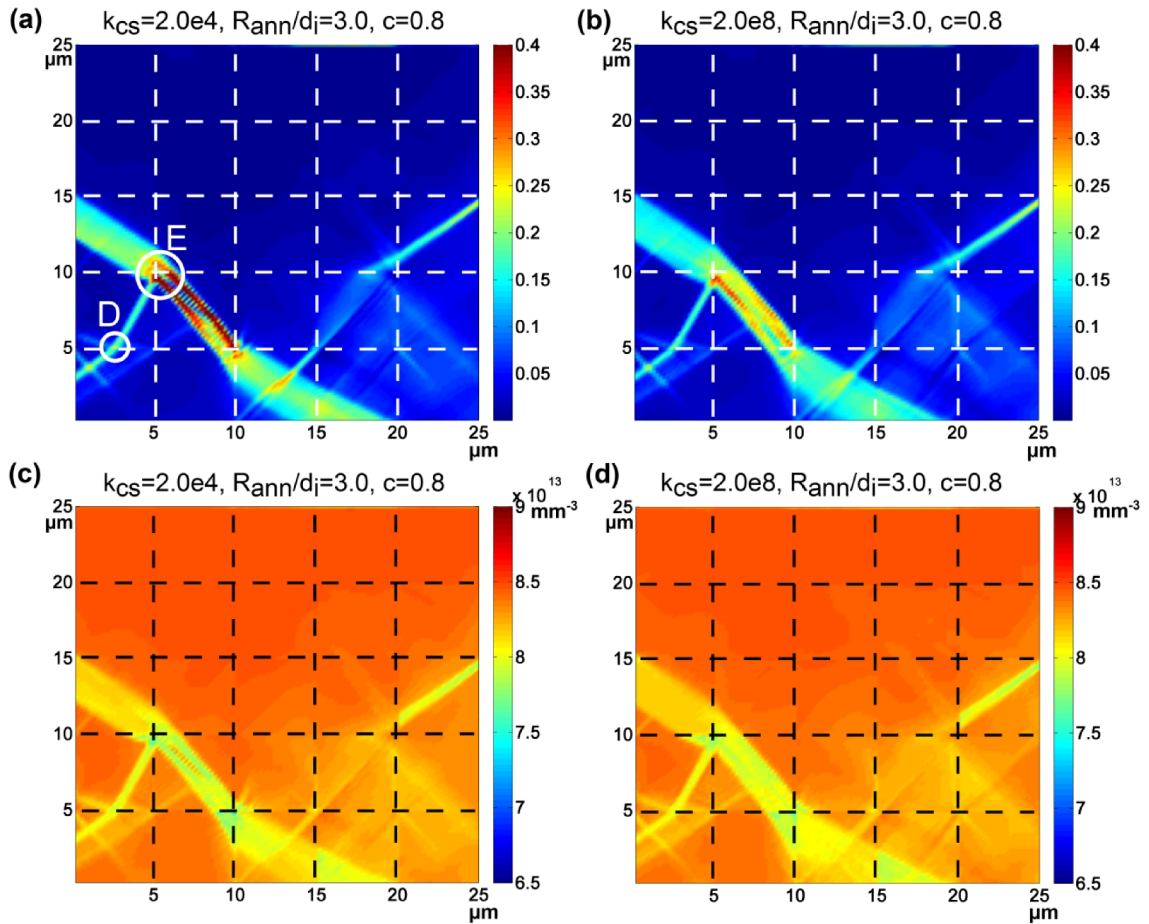
Figure 16. (a), (b): Effect of degree of cross-slip (k_{cs}) on the distribution of effective inelastic strain for material loaded in tension to 4% engineering strain at $437\,\mathrm{K}$, after being irradiated to $2.9\,\mathrm{dpa}$ damage. (c), (d): Distribution of interstitial loop density corresponding to the effective inelastic strain shown in (a) and (b) respectively. See text for description of regions D and E.

There are no quantitative studies to compare the simulated effect of the degree of cross-slip on localization behavior. However, the current parametric study suggests that cross-slip assists in the formation of wider dislocation channels. Cross-slip is a material dependent phenomenon; the tendency to cross-slip depends on the stacking fault energy, availability of slip planes, etc. In fact, it was observed in a set of experiments performed on irradiated copper and copper-aluminum alloys [143,144] that the low stacking fault energy alloys do not show channel formation. It was observed that for the low stacking fault energy alloys, glide is confined to only a few slip planes [144] as cross-slip to other planes is much more difficult. This precludes any cleared channel formation. Nevertheless, more detailed studies are needed to find a physical basis for choosing the values of k_{cs} and τ^*, perhaps from MD simulations.

The spatial orientation of dislocation channels depends not just on the loading direction, but also on the crystallography. As also seen in experiments [145], our simulations clearly suggest that not all dislocation channels are formed along the maximum resolved shear stress plane (diagonal 45° direction to the vertical loading axis, in the present case); dislocation channels are formed along off-diagonal directions as well. The spatial orientation of dislocation channels depends on the availability of favorable slip planes within a grain. Experimental studies of dislocation channel formation in bcc-vanadium [140] also suggest the same, where it was seen that the channels within a single grain are spatially oriented along multiple directions that are coincident with the favorable crystallographic slip planes. This was attributed to cross-slip [140].

The structure of grain boundaries is not explicitly accounted for in this model. However, it is known that grain boundaries can act as points of localized stress concentration. This results in a multiaxial stress state and leads to reorientation and bifurcation of dislocation channels. The same was observed in our simulations at the interface between grains where the crystallographic orientations change, for example, in the regions marked D and E in Fig. 16(a). This is in agreement with experimental observations of reorientation and bifurcation of dislocation channels in bcc materials [78,140]. Further, we have assumed a uniform grain structure to simplify the model implementation in our simulations. It is expected that the presence of laths and carbide precipitates in the martensitic microstructure may lead to sites of stress concentration and promote localization (effect of stress concentration on localization is studied in detail in Chapter 4).

3.5.5 Parametric study of defect annihilation model

A parametric study of the defect annihilation model and its effect on the localization behavior is presented here. In this phenomenological model (Section 3.3.1), R_{ann} represents the critical capture radius around a mobile dislocation within which interstitial loops will be annihilated during glide. R_{ann} was varied as a function of the current interstitial loop size, d_i^α. The exponent of interstitial loop term, c, in Eq. (3.2) was also varied.

Figures 17(a)-(c) show the effective inelastic strain in the material for different combinations of R_{ann} and c. Comparison of corresponding engineering stress-strain

curves to the experimental data is shown in Fig. 17(d). These simulations again represent

a material irradiated to 2.9 dpa damage and then loaded in tension to 4% engineering

strain at 437 K. Note that the same initial crystallographic orientation distributions were

used as for the cross-slip simulations. Values of maximum inelastic strain in the channels

as function of R_{ann} and c are summarized in Table 3.
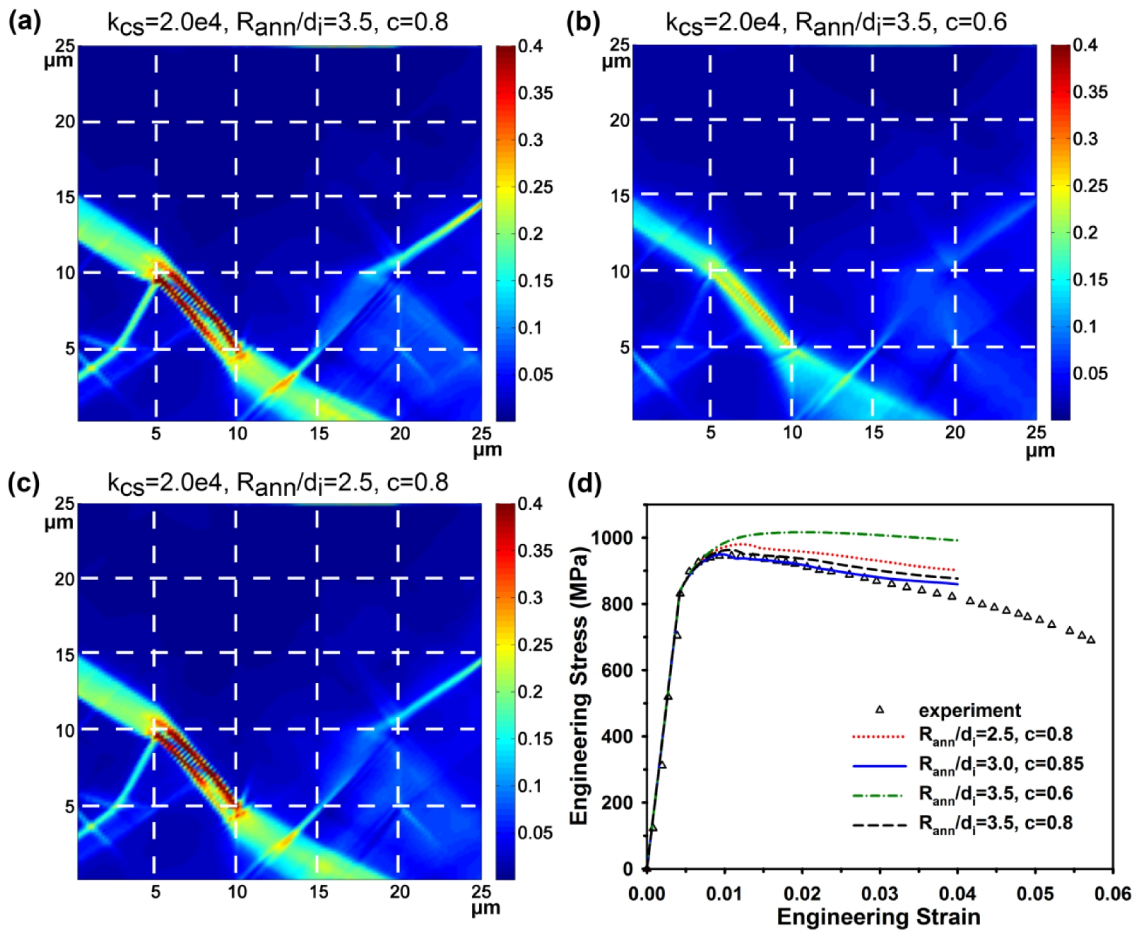
Figure 17. (a-c): Effect of R_{ann} and c on the distribution of effective inelastic strain in a material loaded in tension to 4% **engineering strain at** $437\,\text{K}$**, after being irradiation to** $2.9\,\text{dpa}$**. (d): Corresponding effect on the stress-strain curves.**

It is found that neither R_{ann} nor c have a major effect on the channel width. However, the localized inelastic strains and the stress-strain responses are greatly affected. It is observed from Table 3 that as R_{ann} is increased from 2.5 d_i^α to 3.5 d_i^α (for $c = 0.8$), the maximum inelastic strain in channels increases monotonically at 2% engineering strain but decreases monotonically at 4% engineering strain. This suggests that higher R_{ann} promotes annihilation of defects initially, so that less number of defects are left in the localized region during subsequent deformation. Consequently, localization is accelerated initially with increasing R_{ann}, but is slowed down later. The parameter c has a more drastic effect on the localization behavior. It is observed that as c is decreased from 0.8 to 0.6 (for $R_{ann} = 3.5 \, d_i^\alpha$), the localized strains decrease to negligible levels. This implies that the phenomenological rule given in Eq. (3.2) needs to be weighted higher in terms of the current interstitial loop density than the current dislocation density, for localization to occur.

Comparison of the stress-strain curves for different values of the defect annihilation parameters indicates that quite evidently c has a more pronounced effect on the flow stress. The engineering stress decreases by $\approx$ 150 MPa at 4% engineering strain as c is increased from 0.6 to 0.8 (for $R_{ann} = 3.5 \, d_i^\alpha$). However, as R_{ann} increases from 2.5 to 3.5 (for $c = 0.8$), the flow stress decreases by $\approx$ 20 MPa. Note that the effect of degree of cross-slip (k_{cs}) on the stress-strain curves is not as pronounced (difference in engineering stress values < 10 MPa for any given strain, as k_{cs} is increased from 2×10^4 to 2×10^6). This is because cross-slip only aids in migration of dislocations to slip planes with lower resolved shear stresses, and does not contribute to the defect annihilation

82

process; mobile dislocations still need sufficient levels of resolved shear stress to annihilate the defects.

Figure 16(a) shows the effective inelastic strain plot for $R_{ann}/d_i^\alpha = 3.0$ and $c = 0.8$, other parameters remaining same. Given other parameters, $R_{ann} = 3.0\ d_i^\alpha$ and $c = 0.85$ results in the best fit to the experimental stress-strain curve in the present case. Of course, this is not the only exhaustive data set for the model parameters; other combination of parameter values might also yield a good fit to the experimental data. However, the given data set serves the present objective of qualitative parametric analysis of the constitutive model.

3.5.6   Scale and geometry effects

Effects of length scale and geometry on the localization behavior were studied by varying the grain size, aspect ratio, and dimensions of the simulation cell. These simulations were performed on larger samples. A relatively coarser mesh (500 nm element size) was used in this case to avoid significantly higher computational times resulting from larger samples with highly resolved meshes; however, by keeping the element size fixed as grain size is varied, the physical scale associated with minimum channel width is established as an a priori assumption of the otherwise local FE analysis. Figure 18 shows the effective inelastic strain in the material for different grain sizes and geometries. All samples were irradiated to 2.9 dpa and then loaded in tension along the vertical axis to 4% engineering strain at 437 K. Values of $k_{cs} = 2.0 \times 10^4$, $R_{ann} = 3.0\ d_i^\alpha$ and $c = 0.8$ were used in these simulations.

Figures 18(a) and 18(b) show the effective inelastic strain in a sample with 100 grains of size 5 μm, and 25 grains of size 10 μm, respectively. From simulations, the channel width is not affected by increasing the grain size from 5 μm to 10 μm. However, the corresponding average channel spacing increases from ≈ 10 μm to ≈ 20 μm, indicating that it is dominated by nearest neighbor grain orientation/misorientation effects. For the inelastic strain shown in Fig. 18(b), the same initial crystallographic orientations were used as for Figs. 13 and 14. However, the grain size is double that of the value used earlier. It is observed that the relative spatial arrangement of dislocation channels in Fig. 18(b) is the exact same as that observed in Fig. 13(b). This suggests that dislocation channel orientation and distribution is dependent only on the crystallographic orientations in the material. Further, the spacing between channels is a function of the grain size.

There are two dominant material length scales governing the physics of the localization phenomena. First, the mean free path of mobile dislocations, $l_d \propto 1/\sqrt{\rho_M}$, relates to the area swept out on the glide plane, bl_d (cf. [68], [16]), by mobile dislocations which annihilate the interstitial loops. Subsequent to defect annihilation, the rate of formation of new mobile dislocations (and hence l_d) governs the width of the channels during the third stage of localization (cf. Section 3.5.2.2, region C in Fig. 14(a)). Arsenlis et al. [47] suggested a similar mechanism governing the characteristic width of dislocation channels. Note that for the present case, $l_d \approx 200-225$ nm (given a mobile dislocation density of $2.0-2.5 \times 10^7 \, \text{mm}^{-2}$ along the channels, cf. Table 2). If the FE mesh size is larger than l_d, then channel formation is regularized by the specified mesh size. In

any case, the FE mesh should not reduce below l_d as this is considered as the limit of the continuum field approximation. Hence, the channel width is controlled by the greater of l_d and the mesh size in these simulations. As discussed earlier, the dislocation mechanism-based constitutive framework admits interpretation of the dislocation spacing in channels and allows for estimation of continued channel refinement and enhanced strain localization without having to explicitly resolve the fields below the minimum mesh size of 200 nm in the present case.

A second material length scale is the characteristic grain size, which governs the spacing between dislocation channels via heterogeneous triggering of localization. Hence, the channel spacing increases with increasing grain size. This length scale is explicitly modeled in the initial microstructure of the simulated material.

We note that an additional length scale, the diffusion length for interstitials and vacancies, plays a role at very low stress levels and strain rates at elevated temperatures; this may provide additional regularization and coarsening of the channel localization.

Effect of geometry on the channel formation was studied by varying the aspect ratio of the simulation cell. The effective inelastic strain for two such cases is shown in Figs. 18(c) and 18(d). A grain size of 5 μm was used. Formation of multiple dislocation channels is observed along the longer dimension in both cases. The average channel width and spacing are not affected by changing the aspect ratio of the simulation cell from a square sample to a rectangular (oblate/prolate) sample. This confirms that the localization behavior observed in the present simulations is not an artifact of the geometry and boundary conditions in the simulations; rather, it correlates with the

intergranular heterogeneities in the material, notably triggered by grains favorably oriented for slip.
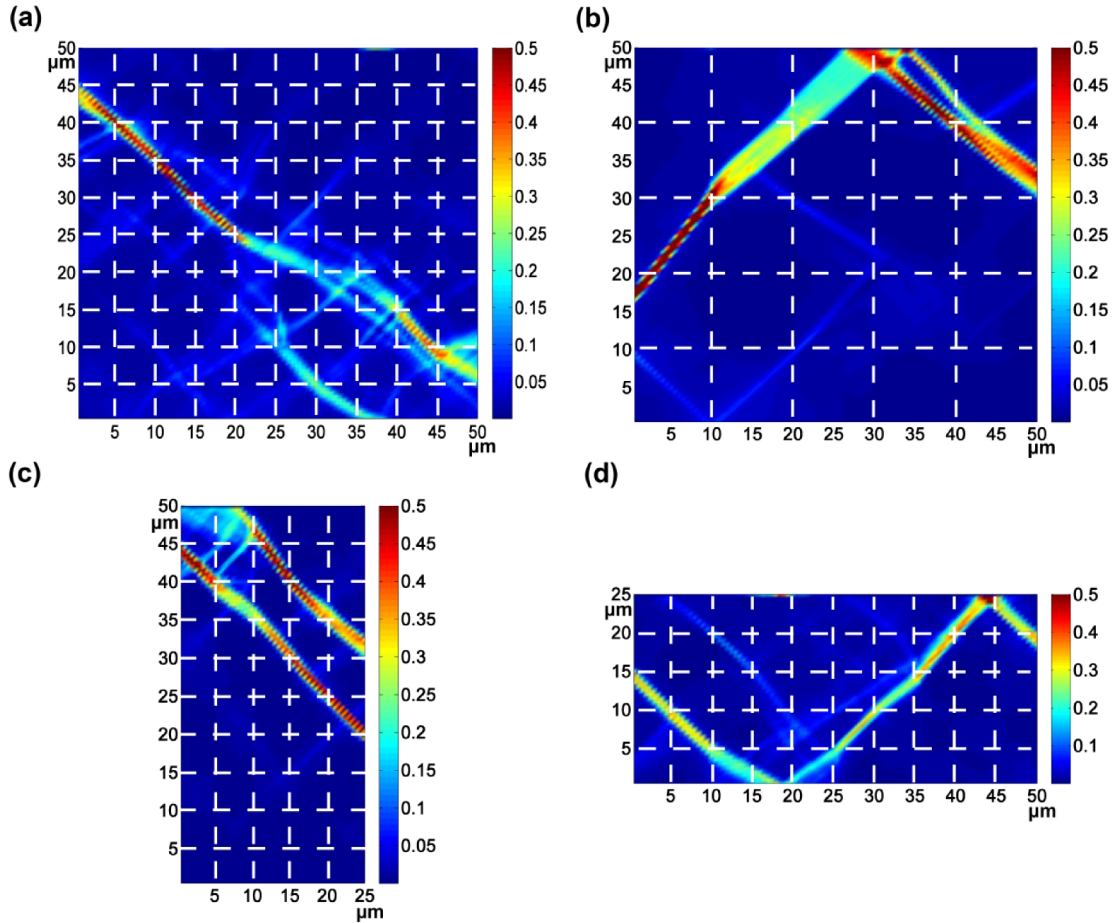
Figure 18. Effect of increasing the grain size from (a) $5\,\mu m$ **to (b)** $10\,\mu m$ **for the same simulation cell size, and (c), (d): effect of simulation cell aspect ratio on the distribution of effective inelastic strain for samples loaded vertically in tension to** 4% **engineering strain at** $437\,K$**, after being irradiated to** $2.9\,dpa$**.**

3.5.7 Effect of random defect density on channel width

Until now, we have assumed that initially the irradiation-induced defects are distributed uniformly in the material. This is an assumption to simplify the model

implementation. Physically, it may be expected that the defects are not distributed uniformly. For example, the density of defects may be higher near the irradiated surface. Further, the interstitial loop density may also vary for each slip system, depending on the crystallographic planes on which the interstitial loops are formed. These considerations are beyond the scope of the present continuum framework. However, it has been found earlier [139] that a non-uniform defect density helps to regularize (inhibit) the width of the shear bands and sharpen the degree of localization within them.
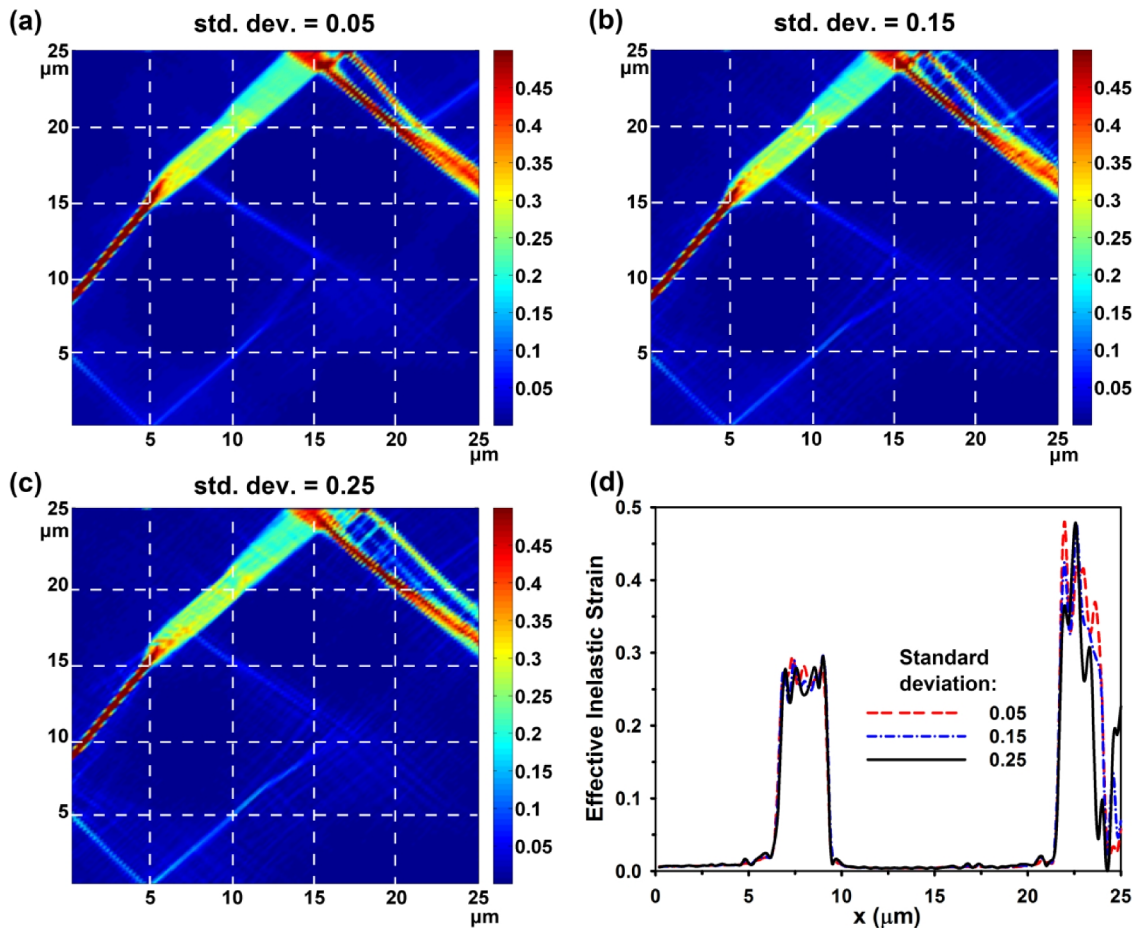
Figure 19. (a-c): Distribution of effective inelastic strain for different degrees of scatter of the spatially non-uniform initial interstitial loop density. (d): Effective inelastic strain profile along a horizontal section at $y = 18\ \mu m$ in the material.

We performed simulations in which each material point in the simulation cell was assigned a random interstitial loop density, with the interstitial loop density having a scatter based on normal (Gaussian) distribution. These simulations were performed with increasing degree of scatter, i.e., standard deviation of the normal distribution was increased from 0.05 to 0.25. The same initial crystallographic orientation was used in all cases. Figures 19(a)-(c) show the distribution of effective inelastic strain in the material with different degrees of scatter. Figure 19(d) shows the corresponding effective inelastic strain profile along a horizontal section of the material at $y = 18\,\mu m$, where y represents the vertical direction.

The overall localization patterns are qualitatively similar in all three microstructures, suggesting that the initial crystallography primarily governs the spatial distribution of localization. As the standard deviation increases from 0.05 to 0.25 in Figs. 19(a)-(c), regions of micro-texture (in terms of inelastic strain) are observed. Slip localization, in the present case, takes place along multiple parallel paths due to trickling of mobile dislocations through the non-uniform defect field, thus giving rise to the observed micro-texture. Further, Fig. 19(d) shows that the inelastic strain profile is jagged along the localized deformation regions. This suggests that the 'apparent' shear bands in Figs. 19(a)-(c) are in fact composed of multiple localization pathways (or dislocation channels). The width of each of these channels is limited by the element size (200 nm) and varies from 200-400 nm (i.e., 1-2 elements). Due to their spatial proximity, interaction and coalescence of localization pathways may also contribute to the 'apparent' widening of dislocation channels discussed in Section 3.5.2.1, in addition to the cross-slip mechanism. As discussed in Zbib and Aifantis [146], if the spacing

between two shear bands is less than a characteristic length scale, they may coalescence into one. More importantly, the inelastic strain pattern at $x \approx 22\ \mu m$ in Fig. 19(d) clearly shows that as the degree of scatter increases, the localization profile becomes sharper, i.e., the inelastic deformation has a higher to tendency to localize within a single dislocation channel. In other words, scatter in the initial defect density helps regularize the dislocation channel width.

3.5.8 Non-local model considerations

We have reiterated throughout this Chapter that mesh dependence of the local constitutive framework stipulates that the dislocation channel width is inevitably governed by the minimum FE size. While a non-local constitutive framework seems to be the obvious approach to address this mesh dependence issue and model the inherent physical length scale, there are problems associated with the scale at which the dislocation channeling phenomena occurs.

As mentioned in Section 3.5.6, the dislocation channel width is governed by the mean free path of mobile dislocations, $l_d \propto 1/\sqrt{\rho_M}$, which trickle through the field of interstitial loops. This length scale may be accounted for by considering gradients of either the dislocation density or the inelastic strain. Aifantis and co-authors [146–151] have derived analytical conditions for the instability of a perturbed viscoplastic solid (localization is a type of material instability) by considering higher order gradients of either of these state variables in the evolution of flow stress. Based on linear and non-linear stability analyses of a simplified solid, they derived solutions for the size (width) and periodicity (spacing) of the localized regions. A similar gradient-based constitutive

model may be used in our spatially resolved numerical finite element calculations to model the inherent length scale of localization. Though computationally intensive, this method is not entirely unfeasible.

However, as mentioned earlier, the length scale governing dislocation channel width is coincidental with the lower limit of continuum field approximation of continuously distributed dislocations (cf. [136]) in the present case. This stipulates that the minimum mesh size be of the order of 100-200 nm in our continuum field finite element calculations. Even if we were to use a gradient-based non-local model, it would be physically unreasonable to use a mesh resolution much further below 200 nm. Hence, there is no significant advantage gained by using non-local continuum plasticity equations to model dislocation channels. In our simulations, the mesh size serves as the length scale governing dislocation channel width.

3.5.9 Various forms of flow localization models

In this work, we have used a phenomenological constitutive equation for interstitial loop annihilation that allows flow localization to occur along crystallographically favored directions. This simple constitutive model is based on the concept of annihilation/absorption of interstitial loops within a critical capture radius, R_{ann}, of the gliding mobile dislocations. Different forms of capture radius-based annihilation criterion were earlier proposed in Refs. [13,131,133]. On the other hand, Barton et al. [15] proposed a contact density based tensor representation of the irradiation-induced defects and a phenomenological decay of the contact density along pathways with coincident defect- and dislocation glide-planes, thus allowing localization

to occur. Arsenlis et al. [12] considered shearing of the irradiation-induced defects on their interaction with dislocations as a possible mechanism of dislocation-defect interaction. This model was shown to cause flow softening for certain values of the associated strength sensitivity coefficient, while hardening in other cases. More recently, Po and Ghoniem [152] assumed a simple linear decay of the irradiation-induced defects based on collision (or interaction) of these defects with the gliding dislocations.

All of these models (including the one developed in the present Chapter) have tried to address the observed flow localization in irradiated metals with varying degrees of success. In all these models, reduction in the irradiation-induced defect density is identified as the means to reduce flow stress and promote localization. Further, the role of crystallography in allowing localization to occur along preferential directions was considered only in Refs. [13,15,152] and the present work. This is especially important in view of the experimental observations of dislocation channel formation only along preferential slip planes [78]. Another consideration in modeling flow localization is the presence of a heterogeneous spatial distribution of irradiation-induced defects in the material. Not only is this a more physical representation of the irradiation phenomena, but it has also been shown to promote localization [152] and regularize the dislocation channel width (in the present work).

Uncertainties in these models, for example, associated with the various constitutive model forms, distribution functions of the heterogeneous density of irradiation-induced defects, crystallographic orientation distribution, etc. need to be quantified and their effect on the macroscopic mechanical response studied. This will

help identify the suitable flow localization model for predicting the material properties in engineering problems. We leave this to future work.

3.6 Summary

A continuum crystal plasticity framework has been used to model the localization behavior in irradiated bcc ferritic/martensitic steels, and results compared to available experimental data. Our simulations have been able to qualitatively capture majority of the microstructure evolution characteristics observed in experiments. The validity of the cross-slip model and its effect on the widening of dislocation channels in irradiated bcc materials has been examined. Effect of the defect annihilation model on lowering the flow stress and widening of dislocation channels has been studied. The cross-slip model and the flow softening model are essential to simulate the deformed microstructure of irradiated bcc metals and control the degree of localization in terms of the width of the dislocation channels.

It has been found that the maximum inelastic strain in channels is a linear function of the radiation dpa dose for the same initial crystallographic orientation distribution of grains. It has also been found that the localization behavior depends strongly on the crystallographic orientation distribution of grains. Further, the dislocation channel width is controlled by the mean free path of dislocations, l_d, and the channel spacing is controlled by the grain size. These parameters define the characteristic length scales in the localization phenomena in tensile deformation of irradiated metals.

Finally, it is imperative to note the differences between prior FE-based continuum modeling of flow localization in irradiated materials and the present work. Most of the

prior FE modeling efforts [153–155] have explicitly modeled dislocation channels in the material, i.e., explicitly embedded 'softer' shear bands in a 'harder' matrix. In contrast, we started out with a bulk consisting of uniformly distributed irradiation-induced defects and let the microstructure evolve according to constitutive rules based on the physics of the material behavior under mechanical loading. Shear bands (dislocation channels) with higher accumulated inelastic stains (and lower defect densities) were found to form implicitly in the microstructure as a result of the "constitutive" material softening effects triggered by intergranular heterogeneity, combined with the flow softening arising from annihilation of irradiation-induced defects. More recently, Barton et al. [15] and Po and Ghoniem [152] have modeled flow localization in irradiated metals using continuum constitutive equations. As in our model, both these works have used phenomenological descriptions of the reduction in density of the irradiation-induced defects, thus allowing localization pathways to form. Interestingly, Po and Ghoniem [152] also found that shear localization is promoted by using a heterogeneously distributed initial density of irradiation-induced defects.

The present modeling approach serves the objective of parametric exploration of the underlying mechanisms governing localized deformation, and relating these to the deformation behavior expected for various mechanical and material loading histories (e.g., in-reactor tensile tests with continued generation of point defect clusters). Future work will focus on modeling these experiments.

CHAPTER 4

MODELING THE EFFECT OF FLOW LOCALIZATION ON

FAILURE INITIATION AHEAD OF A SHARP NOTCH

4.1   Introduction

Failure in irradiated alloys correlates with the flow localization along dislocation channels. Dislocation channels have been found to be more densely spread near the fracture surfaces, where the channel spacing decreases by more than an order of magnitude from that in the uniformly deformed region [78]. In terms of mechanical properties, the fracture toughness has been found to universally decrease with increasing radiation dose under quasi-static loading [2,44,96,156]. Fracture has been found, in many cases, to propagate along the 'faceted' interfaces of dislocation channels with the uniformly deformed bulk [112,157]. Further, intergranular cracks have been found to initiate at the intersections of dislocation channels and grain boundaries [158]. Inability of the grain boundaries (GBs) to accommodate highly localized strains from dislocation channels has been suggested as one of the dominant factors contributing to irradiation-assisted intergranular stress corrosion cracking [159].

These experimental observations motivate the present study of flow localization and failure initiation ahead of a sharp notch in irradiated bcc materials by coupling crystal plasticity with nucleation and growth of damage. A void nucleation and growth-based continuum damage framework is developed in this Chapter and coupled to the existing defect density-based crystal plasticity framework to explore dislocation channel patterns,

and void nucleation and growth in the regions of high stress triaxiality ahead of the notch. Effects of loading rate and temperature on failure initiation are studied. The framework is also used to predict the crack growth resistance and fracture toughness of irradiated specimens.

4.2   Background

4.2.1   Flow localization and ductile failure in irradiated metals

Failure in irradiated metals is triggered, in many cases, by plasticity mismatch at the interface of dislocation channels with the uniformly deformed bulk. The fracture surface of a ferritic/martensitic Eurofer-97 steel, irradiated at 300ºC, shows evidence of transgranular 'zigzag' fracture, and the dimples associated with ductile failure become more shallow with increasing radiation dose, suggesting pathways of localized shear, in particular [112]. The 'zigzag' fracture pattern suggests an arbitrary crack path along intertwined dislocation channels in the deformed material. It was proposed [112] that plasticity mismatch, at the interface of the 'hard' matrix and the 'soft' dislocation channel, promotes void nucleation, growth and coalescence, ultimately resulting in failure. It was also found [112] that the crack resistance of the quasi-statically loaded irradiated material degrades significantly as compared to the unirradiated material. This was attributed to the occurrence of mixed mode (Mode I + II) fracture ahead of the crack tip. However, the crack resistance was found to increase under dynamic loading and was comparable to that of the virgin, unirradiated material.

Observation of 'shallow' ductile fracture was also reported for irradiated 9Cr-1Mo martensitic steel at both room temperature and at 250ºC, along with evidence of

secondary cracks, which were not present in the unirradiated specimens [160]. Further, evidence of limited-ductility 'channel' fracture with separation of fracture surfaces along localized-shear dislocation channel paths has been found in 304 stainless steel [157], 321 austenitic steel [156], and 308 and 316 stainless steel [161] at elevated temperatures and high radiation doses. Fracture surfaces show relatively flat facets along dislocation channels that intersect and are intertwined with other channels [157], akin to the 'zigzag' fracture [112] mentioned earlier, but without any dimples. This 'channel' fracture mechanism may be considered as a limiting case of transgranular ductile failure along dislocation channels in irradiated metals with little or no dimple formation.

Note that failure in irradiated materials does not always occur by ductile fracture. Although the quasi-static fracture toughness of metals has been universally found to decrease as a result of radiation, the failure mode is temperature dependent, with brittle cleavage fracture occurring at low test temperatures [3] and an increase in the apparent ductile-brittle transition temperature (DBTT) with increasing radiation [6,162,163]. In a recent study [164], it has been shown that the irradiation temperature has a dominant effect on the fracture toughness, as opposed to irradiation dose, in the regime of moderate to high radiation doses (3-148 dpa). Brittle fracture was observed when the ferritic/martensitic HT9 steel was irradiated at temperatures below 400ºC, while ductile fracture was observed when the irradiation temperature was higher [164].

4.2.2 Models for void nucleation and growth

Ductile failure occurs by nucleation, growth and coalescence of voids subsequent to significant plastic deformation in metals [165]. In unirradiated metals, nucleation of

voids generally occurs at the interfaces of second phase particles and inclusions. In the absence of second phase particles, voids may nucleate by the condensation/clustering of vacancies in regions of high plastic deformation [166]. Under the influence of high plastic strain and hydrostatic stress (developed due to plastic instability during tensile loading, for example), these voids grow rapidly and coalesce, thus forming macroscopic flaws or cracks.

The physics of void nucleation has been studied using the classical theory of heterogeneous nucleation at interfaces (GBs, inclusions) [167–172]. In these studies, it is implicitly assumed that the driving force for void nucleation is derived from the condensation of supersaturated vacancies (cf. [170,173]), while not explicitly tracking the vacancy concentration in the material. The energy barrier and critical radius for void nucleation was calculated given the applied normal stress and interfacial energy at GBs and second phase particles [167,168], and also considering local internal stresses due to the presence of voids [170]. A major conclusion from all these calculations was that high local stress concentration, more specifically high tensile normal stresses, are necessary for voids to nucleate. Based on experimental observations of voids in 304 stainless steel under creep loading [171], it was also concluded that many of the voids were formed in the material prior to mechanical loading, possibly during primary forming processes, thus bypassing the requirement for the presence of high stress concentration for voids to nucleate.

It should be noted that majority of the studies mentioned here concern intergranular fracture under quasi-static tensile or creep loading. In the context of the present problem, heterogeneous void nucleation is of interest because localization of

deformation along dislocation channels in irradiated materials leads to the formation of interfacial regions with plasticity mismatch within the grains. In the regions of high stress concentration (e.g., ahead of a sharp notch or crack-tip), nucleation and growth of voids would presumably be promoted at such interfaces, ultimately leading to transgranular 'zigzag' fracture [112] or 'channel' fracture [157].

The problem of void growth has received much attention in the past, especially in the context of correlating void growth with macroscopic applied stress and plastic strain. The mechanics of void growth is generally studied using/extending models developed most notably some 30-40 years ago [174–179]. The influence of stress triaxiality and plastic strain on the growth rate of an isolated cylindrical void was first studied by McClintock [174]. Analytical solutions of the growth of an isolated spherical void in a perfectly plastic material by Rice and Tracey [175] showed an exponential dependence of the growth rate on the stress triaxiality ratio. Gurson [176] considered material softening as a result of void growth and developed a void porosity-dependent, and hydrostatic stress-dependent plastic potential function for a cell containing a void. This model was further extended to a periodic array of cells containing voids in a hardening material by Tvergaard [177,178] and later modified by Tvergaard and Needleman [179] to account for void coalescence once a critical porosity is reached. More recently, models for the micromechanics of void growth and coalescence have also been developed and compared to experiments by Benzerga and co-authors [180–182]. A review of the current advances in continuum modeling of void phenomena (growth and coalescence) and associated implications for fracture is given by Besson [183].

However, these models are mostly phenomenological in nature and focus on strain-driven growth. Void growth by vacancy diffusion mechanisms has also been studied [166,167,184–191]. It is generally agreed [166,187,188,190,191] that vacancy surface diffusion and GB diffusion (where present) are the dominant mechanisms contributing to void growth in a supersaturated field of vacancies, as may arise in the case of irradiated metals. Among these studies, the work of Cuitiño and Ortiz [166] is of particular interest in that it employs a dislocation density based crystal plasticity framework to model vacancy supersaturation and void growth in fcc metals subject to plastic deformation.

In this Chapter, a continuum damage framework is developed to model heterogeneous nucleation and growth of voids due to condensation of vacancies formed by excessive inelastic deformation. The damage framework is coupled with the existing dislocation density crystal plasticity framework to study flow localization and failure initiation ahead of a sharp notch in irradiated bcc metals.

4.3 Model description

The constitutive model framework considers the following physical phenomena:

(a) inelastic deformation of bcc materials in the field of irradiation-induced defects (primarily interstitial loops) that evolve with inelastic strain,

(b) vacancy supersaturation in the regions of localized inelastic deformation along dislocation channels,

(c) void nucleation by condensation/clustering of supersaturated vacancies in the regions of stress concentration, further promoted along dislocation channel interfaces (via plasticity mismatch with the surrounding interior) and GBs,

(d) void growth via diffusional transport of vacancies from the bulk to the void surface under the influence of multi-axial stress.

These phenomena principally account for the decrease in ductility and eventual failure of irradiated metals. While the flow localization associated with channel formation is modeled using the existing crystal plasticity framework, constitutive equations for items (b)-(d) above are developed in this Chapter, and coupled to the crystal plasticity model in terms of the field of vacancies in the material. Note that the ferritic/martensitic steels modeled in this work have high swelling resistance; voids/vacancy loops are not generally observed post-irradiation, even with transmission electron microscopy [27]. Accordingly, it is assumed here that no voids are formed due to irradiation; rather they are assumed to form by vacancy condensation subsequent to inelastic deformation.

4.3.1 Crystal plasticity framework

The coupled crystal plasticity-damage framework uses the void number density, N_V, and the corresponding mean void radius, r_V, as state variables, in addition to the ISVs defined earlier. Note that while the dislocation densities, ρ_M^α and ρ_I^α, and the interstitial loop density, N_i^α, and loop size, d_i^α, are defined at the level of slip systems, N_V, r_V, and the interstitial, c_i, and vacancy concentrations, c_v, are defined at the

mesoscale. Constitutive equations for the finite deformation crystal plasticity framework (item (a) above) were developed in Chapters 2 and 3.

In this Section, we will briefly summarize the cross-slip and dislocation dipole annihilation models and the corresponding rate of vacancy generation due to inelastic deformation (item (b) above).

4.3.1.1   Vacancy supersaturation due to inelastic deformation

Cuitiño and Ortiz [166] developed a model for vacancy formation due to inelastic deformation in a dislocation density based crystal plasticity framework for fcc materials. They assumed that intersection jogs, formed during dislocation glide and cross-slip, leave behind a trail of vacancies during their subsequent motion. The formation of vacancies by edge dislocation dipole annihilation during cyclic deformation of fcc metals was also modeled by Repetto and Ortiz [192] to predict fatigue crack initiation. Based on similar concepts, we assume that vacancies are formed by cross-slip of dislocations, and by mutual annihilation of dipoles within a critical capture radius of the associated glide dislocations.

The cross-slip model [16] assumes that mobile screw dislocations from slip system α migrate to slip plane χ, which has the lowest stress-biased activation energy barrier, $\left(\tau^* - \left| \tau^\chi \right| \right) V_a$, amongst all possible slip systems $\alpha \in \Theta$, such that all slip systems of subset Θ have the same Burgers vector direction. Here, τ^* is the critical activation stress for double-kink nucleation, τ^χ is the resolved shear stress on slip system χ and V_a is the activation volume for cross-slip. Accordingly, the rate of migration of mobile screw dislocations from slip system α is given as

$$\dot{\rho}_{cs}^{\alpha} = -k_{cs} \exp\left(-\frac{\left(\tau^* - |\tau^\chi|\right)V_a}{kT}\right)\rho_M^\alpha |\dot{\gamma}^\alpha| \tag{4.1}$$

where k_{cs} is a material constant, k is Boltzmann's constant, T is absolute temperature, and $\dot{\gamma}^\alpha$ is the crystallographic shearing rate on slip system α. The corresponding rate of accumulation of mobile screw dislocations on slip system χ with the lowest activation barrier for cross-slip is given by

$$\dot{\rho}_{cs}^\chi = -\sum_{\alpha \in \Theta, \alpha \neq \chi} -\dot{\rho}_{cs}^\alpha = \sum_{\alpha \in \Theta, \alpha \neq \chi} k_{cs} \exp\left(-\frac{\left(\tau^* - |\tau^\chi|\right)V_a}{kT}\right)\rho_M^\alpha |\dot{\gamma}^\alpha| \tag{4.2}$$

This migration rate, when multiplied by the Burgers vector, b, and the average line length of mobile dislocations, $l_M^\alpha \approx 1/\sqrt{\rho_M^\alpha}$, gives the number of migration events per unit time. The corresponding rate of vacancy generation due to cross-slip is obtained as the product of the migration events per unit time with the atomic density $N_0 = 1/\Omega$, i.e.,

$$\dot{c}_v^\alpha\big|_{cs} = N_0 b l_M^\alpha |\dot{\rho}_{cs}^\alpha| = \frac{b l_M^\alpha}{\Omega} k_{cs} \exp\left(-\frac{\left(\tau^* - |\tau^\chi|\right)V_a}{kT}\right)\rho_M^\alpha |\dot{\gamma}^\alpha| \tag{4.3}$$

where Ω is the atomic volume.

Mutual annihilation of mobile dislocation dipoles within a critical capture radius, R_c, of the gliding mobile dislocations is accounted for by the relation [68,71,192]

$$\dot{\rho}_{mutual}^\alpha = -\frac{2R_c}{b}\rho_M^\alpha |\dot{\gamma}^\alpha| \quad , \tag{4.4}$$

where the factor of two accounts for the fact that two mobile dislocations with opposite Burgers vectors are annihilated via this mechanism. The total number of mutual annihilation events per unit time is obtained as half the product of the mutual dislocation

annihilation rate with the Burgers vector and the capture radius, i.e., $bR_c \left| \dot{\rho}_{mutual}^{\alpha} \right| / 2$ [68,192]. Following a similar procedure as in Eq. (4.3), the corresponding vacancy generation rate is given as

$$\dot{c}_v^{\alpha} \Big|_{mutual} = N_0 \frac{bR_c}{2} \left| \dot{\rho}_{mutual}^{\alpha} \right| = \frac{R_c^2}{\Omega} \rho_M^{\alpha} \left| \dot{\gamma}^{\alpha} \right| \tag{4.5}$$

The factor of two here avoids double counting of the dislocation annihilation events. The total vacancy generation rate due inelastic deformation on all slip systems is thus given as

$$\dot{c}_v \Big|_{in} = \sum_{\alpha, \alpha \neq \chi} \dot{c}_v^{\alpha} \Big|_{cs} + \sum_{\alpha} \dot{c}_v^{\alpha} \Big|_{mutual} \tag{4.6}$$

As a result, the total vacancy evolution rate (given in Eq. (2.10)) is modified to reflect the vacancy generation rate due to inelastic deformation, i.e.,

$$\dot{c}_v = K_0 - K_{iv} c_i c_v - \sum_{\alpha} K_{vs}^{\alpha} \left(\rho_M^{\alpha} + \rho_I^{\alpha} \right) c_v + \dot{c}_v \Big|_{in} \tag{4.7}$$

where K_0, K_{iv} are the defect pair creation and recombination rates, respectively, and K_{vs}^{α} is the vacancy-dislocation reaction rate coefficient. Except for $\dot{c}_v \Big|_{in}$, the other terms in Eq. (4.7) will be dominant mainly under concurrent irradiation.

4.3.2 Damage framework

A continuum damage approach is used to model the evolution of an isotropic damage variable, ϕ, in the material. Using the concept of effective stress, i.e., $\tilde{\sigma} = \sigma / (1 - \phi)$, and the strain equivalence principle (cf. [193]), the elastic stiffness of the damaged material is given as

$$\tilde{C} = (1 - \phi) C \tag{4.8}$$

where C is the elastic stiffness of the undamaged material and $\tilde{\sigma}$ is the effective stress in the damaged material. Here, ϕ is the volume fraction of voids. In what follows, the voids are assumed to be spherical in shape, and their volume number density, N_V, and mean radius, r_V, are used as ISVs in this damage framework.

4.3.2.1 Void nucleation model

Based on the classical theory of void nucleation due to vacancy condensation, the steady state nucleation rate of voids that are each composed of j vacancies is given as [6,173]

$$\dot{N}_V^j = Z\beta_j N_V^p \exp\left(-\frac{\Delta G_j}{kT}\right) \tag{4.9}$$

where Z is the dimensionless Zeldovich factor, β_j, is the rate of impingement of vacancies on a void nucleus having j vacancies, N_V^p is the number of potential nucleation sites, and ΔG_j is the Gibbs free energy change associated with the formation of a void nucleus having j vacancies. A relation between the radius, r_V, of the void and the number of vacancies, j, in the void can be obtained by equating their respective volumes, i.e.,

$$\frac{4\pi}{3}r_V^3 = j\Omega \Leftrightarrow r_V = \left(\frac{3j\Omega}{4\pi}\right)^{1/3} \tag{4.10}$$

where Ω is the volume of a single vacancy. An implicit assumption, of course, is that the voids are composed only of vacancies; there are no gas atoms present within the voids. Accordingly, the free energy change associated with the formation of a spherical void

104

composed of j vacancies under the influence of local tensile hydrostatic stress, σ_H, is given as

$$\Delta G_j = -j\sigma_H \Omega + (4\pi)^{1/3}(3j\Omega)^{2/3}\Delta\Upsilon = -\left(\frac{4\pi}{3}r_V^3\right)\sigma_H + \left(4\pi r_V^2\right)\Delta\Upsilon \qquad (4.11)$$

where $\Delta\Upsilon$ is the associated interfacial energy change, and is given as the difference between the surface energy of new void surfaces created and the surface energy of interfaces annihilated as a result of void formation. The present framework considers both heterogeneous void nucleation at the dislocation channel-induced plasticity mismatch interfaces and homogeneous void nucleation in the homogeneously deformed grain interiors; $\Delta\Upsilon$ would vary accordingly depending on whether the nucleation site is at a dislocation channel interface or a GB interface ($\Delta\Upsilon = \Delta\Upsilon_{het}$), or in the homogeneous interior ($\Delta\Upsilon = \Delta\Upsilon_{hom}$). The critical number of vacancies, j^*, required to form a void nucleus of radius, r_V^*, is obtained from the stationary point of ΔG_j, i.e.,

$$\frac{\partial \Delta G_j}{\partial j} = 0 \Rightarrow j^* = \frac{32\pi}{3\Omega}\left(\frac{\Delta\Upsilon}{\sigma_H}\right)^3 \Leftrightarrow r_V^* = \frac{2\Delta\Upsilon}{\sigma_H} \qquad (4.12)$$

and the associated critical free energy change is

$$\Delta G^* = \frac{16\pi}{3}\frac{\Delta\Upsilon^3}{\sigma_H^2} \qquad (4.13)$$

The non-equilibrium Zeldovich correction factor, Z, accounts for fluctuations between the subcritical and supercritical nuclei [169], and is given by [6,173]

$$Z = \left(-\frac{1}{2\pi kT}\left[\frac{\partial^2 \Delta G_j}{\partial j^2}\right]_{j^*}\right)^{1/2} \qquad (4.14)$$

105

The impingement rate of vacancies on the void nucleus, β_j, depends on the probability of finding vacancies within an atomic layer, $\Omega^{1/3}$, of the void surface, i.e., $\left(4\pi r_V^2\right)\Omega^{1/3}\big/\Omega$, and the jump frequency of vacancies, given by $D_v\big/\Omega^{2/3}$ [169]. Here, D_v is the vacancy diffusivity. Accordingly, the impingement rate is given as

$$\beta_j = \frac{4\pi r_V^2}{\Omega^{2/3}}\frac{D_v}{\Omega^{2/3}} \tag{4.15}$$

From Raj and Ashby [167], the number of potential nucleation sites per unit volume, N_V^p, is related to the available volume for void nucleation. Hence, it depends on the damage parameter, ϕ, and the current volume, $j\Omega$, of the void nucleus, i.e.,

$$N_V^p = \frac{1-\phi}{j\Omega} \tag{4.16}$$

As a result of nucleation of voids due to vacancy condensation, the vacancy concentration in the material is depleted. Based on the steady state void nucleation rate given in Eq. (4.9) and the critical number of vacancies required to nucleate the voids given in Eq. (4.12), the corresponding mean field vacancy absorption rate is given by

$$\dot{c}_v\big|_V^n = j^*\dot{N}_V^{j^*} \tag{4.17}$$

This framework tracks the number density and radii of voids at each material point. However, as a result of simultaneous nucleation and growth events, there would exist a distribution of void sizes at any instant of time. Keeping track of such a void size distribution for each material point in a crystal plasticity framework is computationally expensive, given that the slip system-ISVs must be tracked as well. Hence, we track only the average void radius at each material point, which is calculated by conserving the volume of the pre-existing and newly nucleated voids, i.e.,

$$\langle r_V \rangle_t = \frac{\left(\left(\dot{N}_V \big|_t \Delta t \right) r_V \big|_t^3 + N_V \big|_{t-1} \langle r_V \rangle_{t-1}^3 \right)^{1/3}}{\dot{N}_V \big|_t \Delta t + N_V \big|_{t-1}} \tag{4.18}$$

where subscripts t and $t-1$ in the above equation refer to values of the variable at the respective time steps, Δt is the time interval between these time steps, and values within $\langle \ \rangle$ represent mean values of the respective variables. For brevity, the average void radius at the current time step, $\langle r_V \rangle_t$, will be simply referred to as r_V in the following Sections, unless mentioned otherwise.

Note that effect of the presence of interstitials on void nucleation and growth is neglected in the present work. This is reasonable given the fact that interstitials, though present due to prior irradiation, may be neglected in comparison to the significantly larger number of vacancies generated during inelastic deformation.

4.3.2.2   Void growth model

As mentioned earlier, surface diffusion is one of the dominant mechanisms contributing to void growth (in the absence of GB diffusion). Void growth may also be reaction rate controlled (cf. [6]). Reaction rate controlled processes are those in which no macroscopic concentration gradients of the reactants exist; rather, these processes are governed by the 'sink strengths' of the respective reactants. Initially when $r_V \leq 1\,\mathrm{nm}$, void growth may be reaction rate limited [6]. As the voids increase in size, the growth rate is controlled by the diffusive flux of vacancies from the surrounding material. As outlined in Was [6], a mixed void growth rate equation may be used to reflect contributions from each of these mechanisms. However, for simplicity, we focus on modeling just diffusion controlled void growth. This is reasonable given the fact that

initial reaction rate controlled void growth in the field of supersaturated vacancies will be swift, and diffusion controlled growth is the rate limiting step (a similar assumption has also been made in [166,191,194]). Note that void growth is further accelerated in the regions of heavy inelastic deformation due to vacancy pipe diffusion along dislocations [166,192,195].

From Was [6], assuming steady state diffusion in an infinite field of vacancies, the absorption rate of vacancies for void growth is calculated using a standard rate theory approach, i.e.,

$$\dot{c}_v\big|_V^g = 4\pi r_V D_v N_V \left(c_v - c_v^V\right) \ ; \ c_v > c_v^V \tag{4.19}$$

where c_v^V is the vacancy concentration at the void surface. This expression is obtained by solving the steady state diffusion of vacancies to a spherical void lying within a larger spherical shell, which is an infinite vacancy source. Applying conservation to the vacancy change rate within voids, the equivalent expression for uniform growth rate of voids is given by [6]

$$N_V \dot{V}_V = N_V \left(4\pi r_V^2 \dot{r}_V\right) = \dot{c}_v\big|_V^g \Omega \Rightarrow \dot{r}_V = \frac{\Omega}{r_V} D_v \left(c_v - c_v^V\right) \ ; \ c_v > c_v^V \tag{4.20}$$

The vacancy concentration at the void surface, c_v^V, is a function of the force balance between the external tensile hydrostatic stress, σ_H (promoting growth), and the inward pressure due to surface tension, $2\gamma_V/r_V$ (resisting growth). Following a similar procedure as in Was [6], c_v^V as a function of the net resultant force due to surface tension and hydrostatic stress, is given by

$$c_v^V = c_v^0 \exp\left(\frac{\Omega}{kT}\left(\frac{2\gamma_V}{r_V} - \sigma_H\right)\right) = \frac{1}{\Omega}\exp\left(-\frac{E_v^f - TS_v^f}{kT}\right)\exp\left(\frac{\Omega}{kT}\left(\frac{2\gamma_V}{r_V} - \sigma_H\right)\right) \quad (4.21)$$

where c_v^0 is the equilibrium vacancy concentration, E_v^f is the vacancy formation energy, S_v^f is the vacancy formation entropy, and γ_V is the interfacial energy associated with creation of a new void surface. Note that this expression also gives the dependence of the void growth rate, $\dot{r}_V$, on σ_H. A higher value of σ_H would lower c_v^V, thus increasing $\dot{r}_V$ (from Eq. (4.19)), and vice-versa.

As mentioned earlier, vacancy diffusion is accelerated along dislocations (pipe diffusion) in the regions of excessive inelastic deformation. Based on the pipe diffusion model, the vacancy diffusion coefficient in the grain interior is a function of the dislocation density in the material, and is given as [195]

$$D_v = D_v^l + b^2 \left(\sum_\alpha \rho^\alpha\right) D_v^\rho \quad (4.22)$$

where D_v^l is the vacancy lattice diffusion coefficient, and D_v^ρ is the vacancy pipe diffusion coefficient.

Note that the present framework models only the initial stages of failure due to diffusion-driven void growth. It is expected that strain-driven void growth and coalescence will dominate in the later stages. Strain-driven void growth may be modeled using the Rice and Tracey model [175], for example. Further, our model assumes that the voids are spherical in shape. Ellipsoidal void growth is generally expected at high stress triaxialities with a dominant principal stress (cf. [183]), and has been studied in Gologanu et al. [196], for example. Future work may address these issues.

Before moving further, it should be noted that the presence of voids is expected to cause additional resistance to the glide of dislocations. Accordingly, this is accounted by modifying the dispersed barrier hardening model for athermal slip resistance of dislocations (Eq. (2.5)) to the following form:

$$s_a^\alpha = Gb\sqrt{\sum_{\zeta=1}^{N_s} q_\rho A^{\alpha\zeta} \rho^\zeta + q_i N_i^\alpha d_i^\alpha + q_V N_V r_V} \qquad (4.23)$$

where q_V is the void barrier strength. Note that while dislocations and interstitial loops are expected to resist dislocation glide at the level of slip systems, voids are not associated with a particular slip system and resist glide on all slip systems.

4.3.2.3   Modeling simultaneous void nucleation and growth

Void nucleation and growth are competitive and complementary processes. Initially, when there is little or no damage in the material, void nucleation would obviously occur preferentially over void growth. However, with increasing damage, void growth takes preference over nucleation as potential nucleation sites decay in number (modeled using Eq. (4.16)). A simple strategy is implemented here to model void nucleation and growth, decomposing it into a two-step process. It is assumed that following inelastic deformation, void nucleation occurs if possible. Criteria for critical void nucleation are outlined in the algorithm given in Fig. 20. Subsequent to nucleation, void growth is allowed to occur according to Eq. (4.20). Though this is a deterministic treatment of the problem of simultaneous void nucleation and growth, the nucleation rate is slowed down at higher damage values due to the lack of potential nucleation sites according to Eq. (4.16). Figure 20 presents the detailed algorithm for modeling void nucleation and growth and coupling it to the crystal plasticity framework.
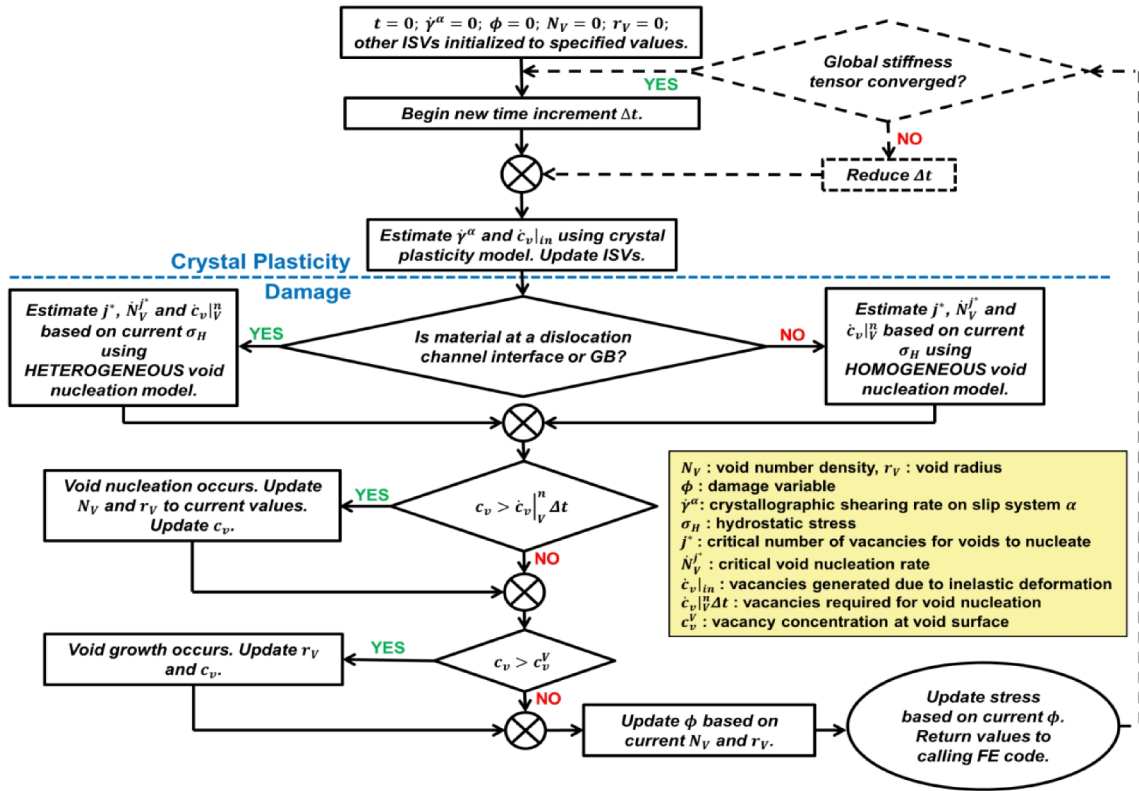
Figure 20. Algorithm for integration of void nucleation and growth-based damage model. Dashed black lines indicate operations performed by calling FE code.

4.4   Model implementation

4.4.1   Loading and boundary conditions

The 3D constitutive model is implemented in the FE program ABAQUS [91] as a User MATerial (UMAT) subroutine. Generalized plane strain elements are used along with fully 3D crystallography and the described constitutive model. The elements employ linear interpolation and reduced integration.

A single deep edge notch with semi-circular tip is created at mid-height on the side of a 800-800 μm simulation cell. A schematic of the loading and boundary

conditions is shown in Fig. 21(a). Regions in the immediate vicinity of the notch are modeled using the (incremental) coupled crystal plasticity-damage material behavior described in Section 4.3. The microstructure (courtesy Dr. J. Padbidri, Georgia Tech) is generated using an approximate Dirichlet (weighted Voronoi) tessellation achieved by packing of (randomly oriented) polygonal grains with Gaussian size distribution (25 μm mean size), through random sequential addition. Deformation plasticity model with Ramberg-Osgood hardening behavior is assigned to the outer region (shaded in green) in Fig. 21(a). Based on the dimensions of the respective regions indicated in Fig. 21(a), a representative simulation cell has ~ 45 grains in the crystal plasticity domain enveloping the notch root. Different notch depths and radii are used in the simulations; these values are specified where needed.
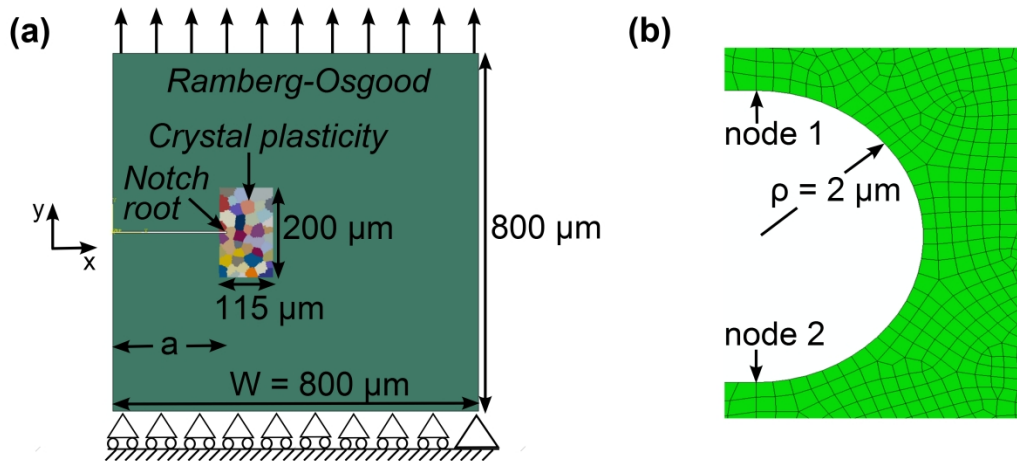
Figure 21. (a): Schematic of loading and boundary conditions. (b): Representative mesh ahead of a notch root of radius, $\rho = 2 \, \mu m$, having a minimum mesh size of 200 nm.

The bottom edge of the 2D simulation cell is constrained along the loading direction, and the far right node of the bottom edge is constrained in both x and y degrees

of freedom (to prevent rigid body rotation). Displacement-controlled tensile loading is applied on the top edge in the y direction (remote applied straining), and the side edges of the simulation cell are traction-free. The simulation cell is loaded at quasi-static strain rate (10^{-4} s^{-1}), unless mentioned otherwise.

The simulation cell is freely meshed in ABAQUS using quadrilateral and triangular elements. A mesh size of 200 nm is used in the crystal plasticity zone in regions in the immediate vicinity and up to 5 μm away from the notch, with radially increasing mesh size up to 4 μm in the crystal plasticity zone, and up to 15 μm in the Ramberg-Osgood zone. A typical simulation cell has ≈ 15,000 elements in the crystal plasticity zone, ≈ 5,000 elements in the Ramberg-Osgood zone. With this mesh density, the simulations take ≈ 80 h to reach 0.7% applied strain on 24 CPU cores (2.2 GHz AMD Opteron) running in parallel. A representative mesh ahead of a deep notch with radius, $\rho = 2$ μm, is shown in Fig. 21(b). This sharp notch effectively represents a crack.

Following Refs. [197,198], the crack tip displacement (CTD) computed as the net displacement between nodes 1 and 2 labeled in Fig. 21(b), is used to characterize the driving force for fracture. The CTD relates to the J-integral for stationary crack growth (cf. [165,199]), and is often used to quantify fracture. Also note that $CTD = \sqrt{CTOD^2 + CTSD^2}$. Thus, CTD is able to characterize failure under mixed mode (Mode I and Mode II) loading. Here, $CTOD$ is the crack tip opening displacement, and $CTSD$ is the crack tip shear displacement.

4.4.2   Algorithm for identifying dislocation channel interface and GB elements

An essential step in modeling void nucleation and growth in the present framework is identifying whether a material point is in the homogeneously deformed bulk, dislocation channel interface, or at a GB. This is implemented in our FE simulations in the following fashion:

(a) A list of nearest neighbor elements is stored that lie within a cutoff radius, $1.5d$ (d is the characteristic length of the material point, defined as the square root of the area of the respective element), of the centroid of the element in question.

(b) At each time step, the difference in effective inelastic strain, ε_{eff}^{i}, between the neighboring elements is computed. If the difference is greater than 0.05, and ε_{eff}^{i} is lower in the present FE than its neighbor, then the material point is at a dislocation channel interface.

(c) If the neighboring element belongs to a different grain, the material point is at a GB.

(d) If none of the above conditions are satisfied, the material point lies within the uniformly deformed bulk.

4.4.3   Non-local vacancy concentration at interface elements

This simple framework identifies interface elements along dislocation channels and GBs in the material. Heterogeneous void nucleation and growth processes are expected to be more prolific at these interface elements. Physically, the vacancy population at material points contiguous to the 'interface' should also contribute to the nucleation and growth of voids. This is implemented in our framework by taking a non-local estimate of the vacancy concentration at the interface elements. Using the nearest

neighbor list computed in Section 4.4.2, the non-local vacancy concentration, $\left.c_v\right|_{nl}^i$, at the interface element is calculated as the element area-weighted sum of vacancy concentration over all nearest neighbors, including the vacancy concentration at the interface element. If void nucleation and/or growth occurs at the interface element, vacancy concentration in the neighboring elements is depleted proportional to their contribution to $\left.c_v\right|_{nl}^i$.

4.4.4 Damage estimation

The crystal plasticity and damage framework outlined here employs 3D crystallography and 3D constitutive equations. However, as explained in Section 4.4.1, the polycrystalline simulations are performed using generalized plane strain FEs, effectively treating polyhedral grains as columnar (polygonal cross-section in the plane). We employ a commonly used microstructure scaling relation, which relates the mean areal density, $\langle x^A \rangle$, of convex-shaped particles to the volume density, x^V, according to the relation

$$\langle x^A \rangle = \langle D \rangle x^V \tag{4.24}$$

where $\langle D \rangle$ is the mean caliper diameter of the particle, to find the areal density (N_V^A) of voids across the material cross-section. Further, using Cavalieri's principle, the volume fraction of voids, V_V, is equal to the average area fraction of voids, A_A (cf. [200]). Thus, the damage variable, ϕ, measuring the volume fraction of voids, is given as

$$\phi = V_V = A_A = \frac{N_V^A \pi r_V^2}{A_0} = \frac{(2 r_V N_V) \pi r_V^2}{A_0} \tag{4.25}$$

where A_0 is the cross-sectional area of the initially undeformed material.

4.4.5 Model parameters

The framework is used to simulate the deformation behavior of Mod 9Cr-1Mo steel loaded in quasi-static tension. This steel has good radiation resistance and high temperature properties. The microstructure of Mod 9Cr-1Mo steel is mainly comprised of ferrite and martensite phases. It is assumed that the crystal structure of the subsequently tempered martensite phase is body-centered cubic (cf. [80]). Accordingly, the material is assigned a uniform bcc crystal structure with 24 slip systems (12 {110}-type and 12 {112}-type). To save computational costs, deformation along the 24 {123} bcc slip systems is neglected for the example applications presented in this Chapter.

The crystal plasticity model was calibrated earlier [16,17] to match the experimental engineering stress-strain data of Mod 9Cr-1Mo steel [2] for different radiation and temperature histories. In addition to the parameter estimation described in Chapter 2, the void barrier strength, q_V, is assumed to have a value of unity. This follows the experimental observation that voids are the strongest obstacles in the path of gliding dislocations [44].

The damage model adds only four new parameters to the framework: E_v^f, S_v^f, D_v^p, and $\Delta\Upsilon$. The vacancy formation energy, E_v^f, and entropy, S_v^f, are taken from [87]. Studies have shown [201,202] that the pipe diffusion coefficient, D_v^p, is ~3-4 orders of magnitude higher than the lattice diffusion coefficient in bcc-Fe at elevated temperatures, and even higher at low and intermediate temperatures. Accordingly, we assume that

$D_v^\rho = 10^4 D_v^l$. The interfacial energy change associated with homogeneous void nucleation is $\Delta\Upsilon_{hom} = \gamma_V = 1.95 \text{ Jm}^{-2}$ [69], where γ_V is the surface energy of the material. The exact value of $\Delta\Upsilon_{het}$ is not entirely known. From [69], the grain boundary interfacial energy of Fe, $\gamma_{GB} \approx 0.78 \text{ Jm}^{-2}$. Assuming that the energy of a dislocation channel interface is the same, the interfacial energy change associated with heterogeneous nucleation of a spherical void at an interface (in Eq. (4.12)) is ideally given by $\Delta\Upsilon_{het} = \gamma_V - \gamma_{GB}/4$. This expression accounts for the fact that a void of surface area, $4\pi r_V^2$, with interfacial energy, γ_V, is created by destroying a dislocation channel interface (or GB) of area, πr_V^2, with interfacial energy, γ_{GB} ($4\pi r_V^2$ is already factored out in the corresponding term in Eq. (4.12)). Substituting values of the respective parameters into the above expression, $\Delta\Upsilon_{het} \approx 1.75 \text{ Jm}^{-2}$. This value of $\Delta\Upsilon_{het}$ is too high to allow spherical void nucleation even at peak stress for stress triaxialities on the order of 3-3.5. Note that an assumption of spherical voids is used here just to simplify the constitutive equations; the voids are seldom spherical in nature. This is because a spherical shape has the highest contact angle (90°) at the void-GB interface (cf. [167]), and is the least energetically favorable. Contact angle-based shape factors of voids of various shapes and their effect on void nucleation and growth at different temperatures has been studied in detail by Raj and Ashby [167]. Based on their analysis of void nucleation at grain interfaces, plausible void-interface contact angles lie in the range 0°-37° for Cu, meaning that the nucleated voids are essentially prolate spheroids with a high degree of eccentricity. The surface and interfacial energies of Fe are in the same range as Cu, allowing us to extrapolate these results to the present case. Using the shape factors given

in [167] and the contact angles mentioned above, $\Delta \Upsilon_{het} \leq 0.33$ Jm^{-2} for Fe. Note that the surface and interfacial energy values reported above are generally measured at $T > 1000$ K. These values increase with decrease in temperature; at intermediate temperatures of 400-600 K, the calculated value of $\Delta \Upsilon_{het}$ would be even higher. Accordingly, we have used a value of $\Delta \Upsilon_{het}$ in the range $0.32 - 0.38$ Jm^{-2} in our simulations. Effects of this parameter on damage initiation and the computed CTD are studied in Section 4.5.3.

As mentioned in Section 4.4.1, Ramberg-Osgood hardening behavior is assumed for the material far away from the notch in the context of a deformation plasticity model. Separate sets of Ramberg-Osgood model parameters, for different loading (temperature, strain rate and radiation dose) histories, were generated by fitting to the stress-strain response from the respective crystal plasticity simulations of smooth specimens with 125, randomly oriented cubic grains of 30 μm size, deformed uniaxially up to 1.5% engineering strain.

4.5   Results and discussion

Post-irradiation tension test simulations are performed on the notched specimens at different test temperatures and loading rates. The following Sections will first consider inelastic deformation and vacancy generation in the vicinity of the notch, and then describe the damage behavior.

4.5.1 Channel formation and vacancy supersaturation

Figure 22 shows the distribution of effective inelastic strain and the corresponding vacancy concentration ahead of a circular notch of radius, $\rho = 2\ \mu m$, with notch depth, $a = 250\ \mu m$, in the material irradiated to 2.9 dpa and then strained normal to the notch to 0.7% remote applied engineering strain at 550 K. $\Delta \Upsilon_{het} = 0.38\ \mathrm{Jm}^{-2}$ in these simulations. Figure 22(a) shows that the deformation is primarily localized in a single grain ahead of the notch. As mentioned earlier, localization of deformation occurs via reduction in density of the irradiation-induced defects along these channels, thus reducing the flow stress. This has been modeled phenomenologically in Eq. (3.2) as a function of the interacting defect density and mobile dislocation density (cf. Chapter 3 for detailed description of the localization mechanism). Multiple, intertwined channels are formed in the regions of stress concentration in the immediate vicinity of the notch. Reorientation and bifurcation of channels at GBs is also observed. The spacing between channels here is much lower than computed previously for the case of localization in smooth specimens in Chapter 3. This is in agreement with experimental observation of higher density of dislocation channels near the fractured surface as compared to uniformly deformed regions [78]. We also found earlier in Chapter 3 that the dislocation channel spatial patterns are strongly dependent on the crystallography of the material. The width of modeled dislocation channels is limited by the minimum mesh size at 200 nm, and is larger than the experimentally observed channel width of 50-200 nm [29,78,109,110]. Further, the localized inelastic strain in channels (~ 0.6-1.4) is lower than that seen in experiments (~ 1.0-5.0) [99,137]. However, we have verified that the simulated net localization of shear strain in the stress-strain response of polycrystalline, smooth

specimen ensembles is comparable to experiments, and the product of the channel width

with the localized strain within channels is more or less invariant (cf. [17]). A finer mesh

may be used to achieve the experimentally observed channel widths and localized strains,

albeit at the cost of significantly increased computational times. For the present

qualitative study of dislocation channel patterns and failure initiation ahead of the notch

root, a mesh resolution of 200 nm is deemed sufficient.
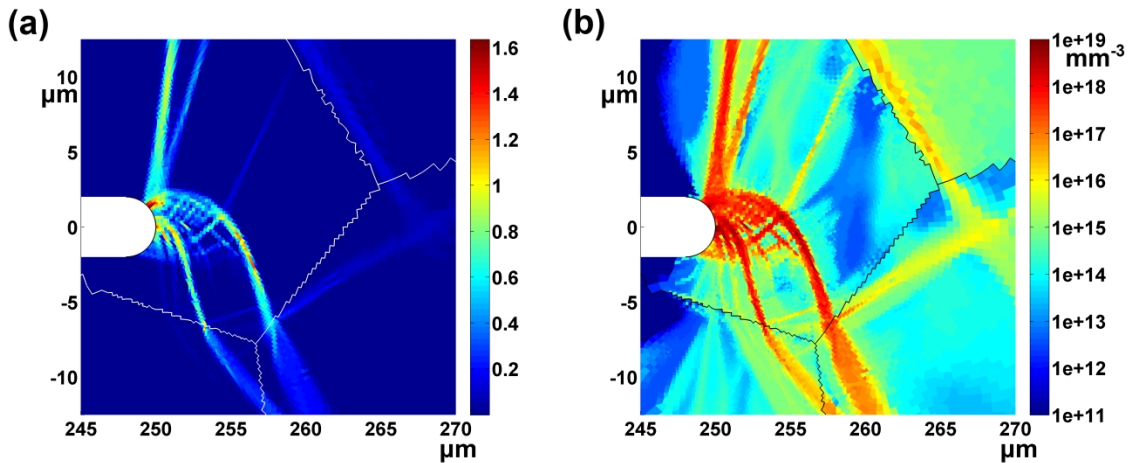
Figure 22. Distribution of (a): effective inelastic strain, and (b): vacancy concentration ahead of the notch after 0.7% **applied strain. Grain boundaries are rendered. The material was irradiated to** 2.9 dpa **prior to tensile loading at** 550 K **.**

Figure 22(b) shows that the vacancy concentration increases by ~ 3-4 orders of

magnitude in the regions of localized deformation, thus facilitating void nucleation and

growth. The vacancy generation due to inelastic deformation has contributions from both

dislocation cross-slip and annihilation of dislocation dipoles. We have verified that the

vacancy contribution from these respective mechanisms is of the same order of

magnitude using the model parameters specified in Table 1. As will be shown later, this

vacancy concentration is in general sufficiently high to promote void nucleation and

growth even at GBs ahead of the notch root, where localized deformation is not that prevalent.

4.5.2   Damage evolution

Figure 23 shows the distribution of voids (Fig. 23(a): number density, 23(b): radius) corresponding to the effective inelastic strain distribution shown in Fig. 22(a). Void nucleation and growth is observed at multiple regions along the dislocation channel interfaces. In some cases, voids nucleate on both sides of a dislocation channel, for example in the regions A and B marked in Fig. 23(a). The nature of void activity within the grain is consistent with the experimentally observed, faceted 'zigzag' fracture [112] along localized shear pathways. Strain-driven void growth and coalescence (not modeled here) would ultimately lead to transgranular fracture along these failure routes. Further, void activity is also prevalent at the intersection of dislocation channels with GBs ahead of the notch root. As mentioned earlier, incompatibility of highly localized strains along dislocation channels at their intersection with GBs is known to contribute to intergranular stress corrosion cracking in irradiated materials [159]. Note that the interfacial energy change associated with heterogeneous void nucleation was assigned to be the same for nucleation at both dislocation channel interfaces and GBs, i.e., $\Delta\Upsilon_{het} = 0.38$ Jm^{-2}.

Figure 23(a) shows that the density of voids goes up to 10^7 mm^{-3}, and the void radius up to 1 μm in Fig. 23(b). Correlating the void radius distribution to the vacancy concentration in Fig. 22(b), it is found that the void radius is higher in regions of higher vacancy concentration. The void radius is in general higher along dislocation channel

121

interfaces, compared to GBs. This is because the vacancy concentration is higher along the dislocation channel interfaces than GBs.
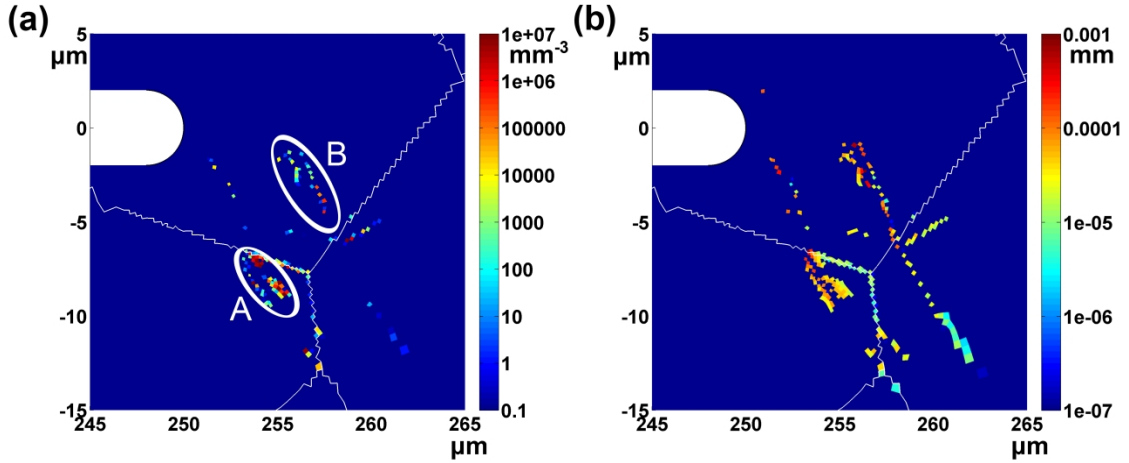
Figure 23. Distribution of (a): void number density, and (b): void radius corresponding to the effective inelastic strain in Fig. 22(a). See text for discussion of regions A and B.

The evolution of damage (volume fraction of voids) for the same microstructure is shown in Fig. 24. Figure 24(a) shows the evolution of total damage with applied strain. This is calculated as the total area-weighted damage over all elements in a semi-circular region of 25 μm radius ahead of the notch root, i.e.,

$$\left(\phi\right)_t = \frac{\sum_i \phi_i A_i}{\sum_i A_i} \tag{4.26}$$

where A_i is the area of the ith FE. The corresponding damage distribution at 0.45%, 0.55%, and 0.70% strain is shown in Figs. 24(b), 24(c), and 24(d), respectively.
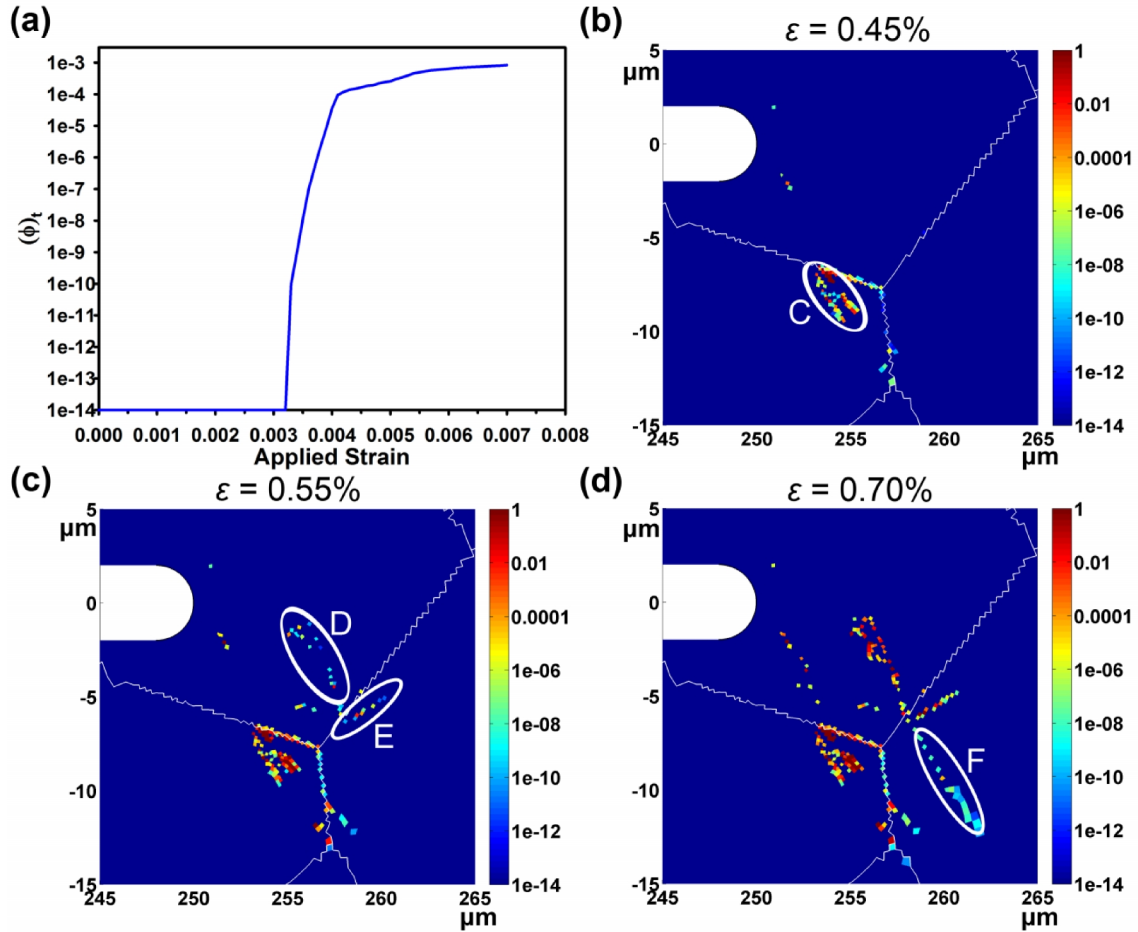
Figure 24. (a): Evolution of total area-weighted damage (in a semi-circular region of radius $25\,\mu\text{m}$ **ahead of the notch) with applied strain. (b), (c), (d): Distribution of damage in the material after (b)** 0.45% **, (c)** 0.55% **, and (d)** 0.70% **applied strain, respectively. See text for discussion of regions C, D, E and F.**

As seen in Fig. 24(a), damage initiates first at $\approx 0.32\%$ applied remote strain in the present case. The evolution of damage is however not uniform; change in damage rate with applied strain is observed. This is associated with damage propagation along new region(s), and can be correlated to the corresponding damage distribution plots. Initially failure propagates mainly along the region C marked in Fig. 24(b). At 0.55% strain, damage is also found to propagate along the new regions D and E marked in Fig. 24(c). With further applied deformation, failure is again initiated along region F marked in Fig.

24(d). Decrease in the damage rate, for example in the range 0.4-0.5% applied strain in Fig. 24(a), is due to relative saturation of damage in region C, and consequently its inability to accommodate the applied deformation, promoting failure elsewhere.

Note that a maximum damage of 0.65 is allowed in each element. Excessive element distortion beyond this damage level leads to convergence issues in our simulations. A higher order FE may be used to address this problem, but with increased computation costs. Even if damage were allowed to occur up to the maximum possible value of 1.0, a similar, but delayed, damage pattern may be expected.

4.5.3 Parametric study of $\Delta \Upsilon_{het}$

Figure 25(a) shows the evolution of $(\phi)_t$ with applied strain for three different values of $\Delta \Upsilon_{het}$. The material was irradiated to 2.9 dpa and then loaded at 550 K. A notch of $\rho = 0.5\,\mu\text{m}$ and $a = 300\,\mu\text{m}$ was used in all these simulations. Further, the same initial microstructure was used for all cases. Note that the simulation for $\Delta \Upsilon_{het} = 0.32\ \text{Jm}^{-2}$ failed to converge beyond 0.2% applied strain.

As expected, damage initiates earlier with a lower value of $\Delta \Upsilon_{het}$. Inspection of the deformed microstructure (not shown here) suggests that the damage initiation patterns are similar in all three cases, albeit delayed in time with increasing $\Delta \Upsilon_{het}$. A lower value of $\Delta \Upsilon_{het}$ allows failure to initiate prematurely at GBs (provided the hydrostatic stress is sufficient for void nucleation). This is because strain localization within a dislocation channel needs to be high enough such that the difference in ε_{eff}^i with the neighboring

element exceeds 0.05, for an 'interface' to be created in our simulations (cf. Section 4.2). In the early stages of localization this might not be the case, allowing (aphysical) premature void nucleation at GBs for lower values of $\Delta\Upsilon_{het}$.

$\Delta\Upsilon_{het}$ may be used as a parameter to calibrate our simulations to experiments. For example, if the critical value of damage were to be pre-defined as $(\phi)_t|_c = 1.0 \times 10^{-4}$ (say), the *CTD* (or fracture toughness) corresponding to $(\phi)_t|_c$ can be computed for different values of $\Delta\Upsilon_{het}$ and compared to experiments. Figure 25(b) shows the computed *CTD* for different $\Delta\Upsilon_{het}$ at $(\phi)_t|_c = 1.0 \times 10^{-4}$. As $\Delta\Upsilon_{het}$ increases, $(\phi)_t|_c$ is found to occur at higher *CTD*. The *CTD* corresponding to $\Delta\Upsilon_{het} = 0.38 \text{ Jm}^{-2}$ is found to occur closest to the point of intersection of the 5% secant line (from the origin with linear elastic loading slope) with the load-displacement curve. Experimentally, intersection point of the 5% secant line with the load-displacement curve is generally used to estimate the critical fracture toughness (cf. [165]). Using $\Delta\Upsilon_{het} = 0.32 \text{ Jm}^{-2}$ or 0.35 Jm^{-2}, the computed *CTD* was found to be much lower. Hence, a value of $\Delta\Upsilon_{het} = 0.38 \text{ Jm}^{-2}$ is used for the rest of our simulations.

It can be seen from the damage evolution plots in Figs. 24(a) and 25(a) that $(\phi)_t|_c = 1.0 \times 10^{-4}$ roughly indicates the point at which 'stable' damage propagation begins. As will be shown in Section 4.5.7, this value is in agreement with the critical damage corresponding to the computed fracture toughness.
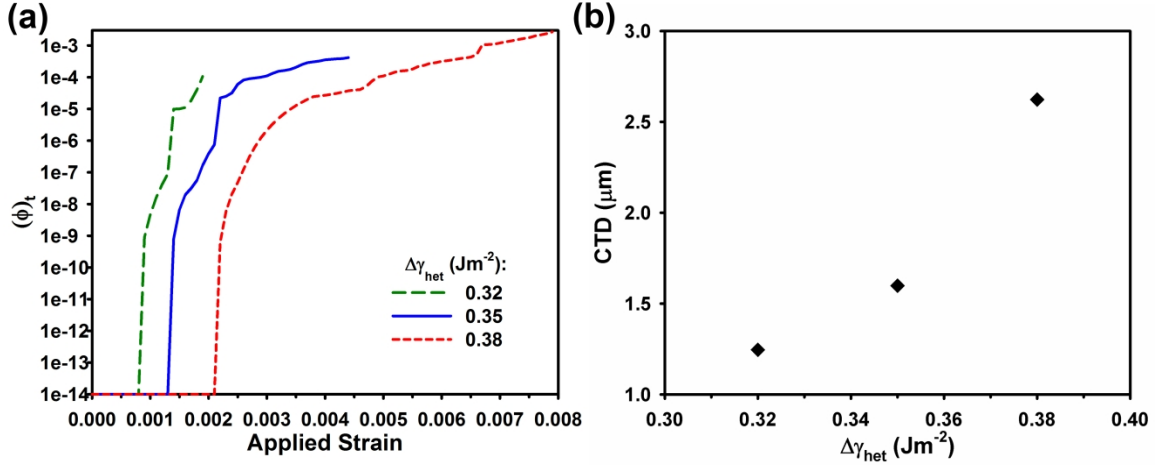
Figure 25. (a): Evolution of total area-weighted damage with applied strain for different values of $\Delta \Upsilon_{het}$. (b): Computed CTD as a function of $\Delta \Upsilon_{het}$ at $(\phi)_t\big|_c = 1.0 \times 10^{-4}$.

4.5.4 Crack growth resistance

The framework developed here is used to estimate the crack growth resistance in terms of the CTD of a stationary crack (sharp notch) of increasing crack length for monotonic remote loading. A circular notch of $\rho = 0.5\,\mu m$ was placed at increasing depths in the range 50-400 μm within the material. The dimensions of the crystal plasticity zone, loading and boundary conditions remain the same as shown in Fig. 21(a). The material was loaded to 0.5% remote applied engineering strain at a quasi-static strain rate of 10^{-4} s^{-1} at 550 K. The material response was found to be just at or beyond the point of intersection of the 5% secant line with the load-displacement curve at 0.5% engineering strain, in all cases. Further, damage initiation was observed in all the irradiated microstructures.

Figure 26 shows the computed CTD of the 2.9 dpa irradiated specimens with increasing crack length, compared to the simulations of the corresponding CTD for

virgin (no irradiation) specimens. As expected, a monotonic, "R curve" behavior is seen for both the irradiated and virgin specimens. Further, the crack growth resistance of the irradiated material is lower than that of the corresponding virgin material in all cases. This agrees with experimental observations regarding the effect of irradiation on crack growth resistance under quasi-static loading for another ferritic/martensitic steel [112], suggesting a loss in tearing resistance with increasing radiation dose.
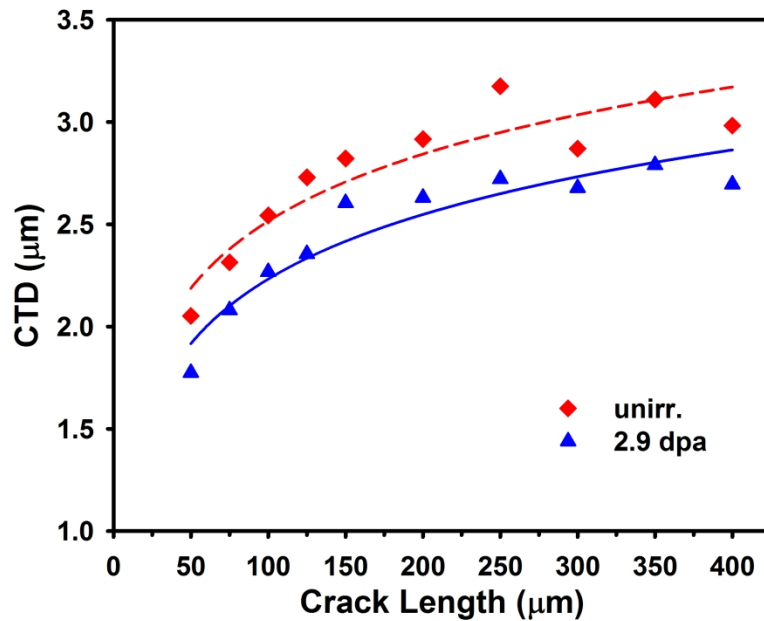
Figure 26. Crack growth resistance of irradiated material compared to that of the virgin material, computed in terms of the *CTD* of stationary cracks of increasing lengths.

Note that we are not modeling crack growth explicitly in our simulations, rather we are measuring the *CTD* of stationary cracks of increasing crack lengths at a given strain to measure the crack growth resistance. Strictly speaking, the R curve must also reflect potential toughening effects during crack growth, e.g., plastic deformation in the

wake of the crack. These effects are not captured in the present work. Explicit crack growth needs to be modeled to capture these phenomena.

A comparison of the deformed microstructures (loaded to 0.5% remote applied engineering strain) for the 2.9 dpa irradiated and virgin specimens for $a = 200\,\mu\text{m}$ is shown in Fig. 27. Figures 27(a) and 27(c) show the distribution of inelastic strain for the irradiated and the virgin material, respectively. The corresponding damage distribution is shown in Figs. 27(b) and 27(d), respectively. The same grain distribution and initial crystallography was used in both cases. As expected, no dislocation channels are observed in the virgin specimen; the inelastic strain localization is typical of a plane strain, small-scale yielding (cf. [165,203]). Further, no damage is observed in the virgin specimens. Physically, failure may initiate in the regions of stress concentration at second phase particles and inclusions (microstructural features not considered here) in the unirradiated specimens. This may lead to even higher *CTDs* than computed for the virgin specimens in our simulations. In the context of the present constitutive equations, a lower value of $\Delta\Upsilon_{het}$ may be used to initiate failure at GB interfaces in the virgin specimens.

The irradiated microstructure, in contrast, shows failure initiation along interfaces, both dislocation channels and GBs, in the vicinity of the notch. These heterogeneous interfaces provide paths for 'easy' crack propagation in the irradiated material, thus degrading the crack growth resistance. Though not supported by explicit experimental results, Chaouadi [112] suggested a similar mechanism to be responsible for degradation in the crack growth resistance of irradiated materials. FE simulations of void growth at bi-material interfaces [204] have shown that void growth is more prolific at the interfaces as compared to that in a homogeneous material. This further asserts that the

experimentally observed degradation in crack growth resistance of irradiated specimens is due to 'accelerated' void nucleation and growth processes at the dislocation channel interfaces, as modeled in our simulations. Note that the stress levels ahead of the notch are higher in the irradiated material (higher flow stress due to irradiation hardening) than the virgin material. Higher stress promotes void nucleation according to the constitutive relations given in Eqs. (4.9)-(4.13), all other conditions remaining the same.
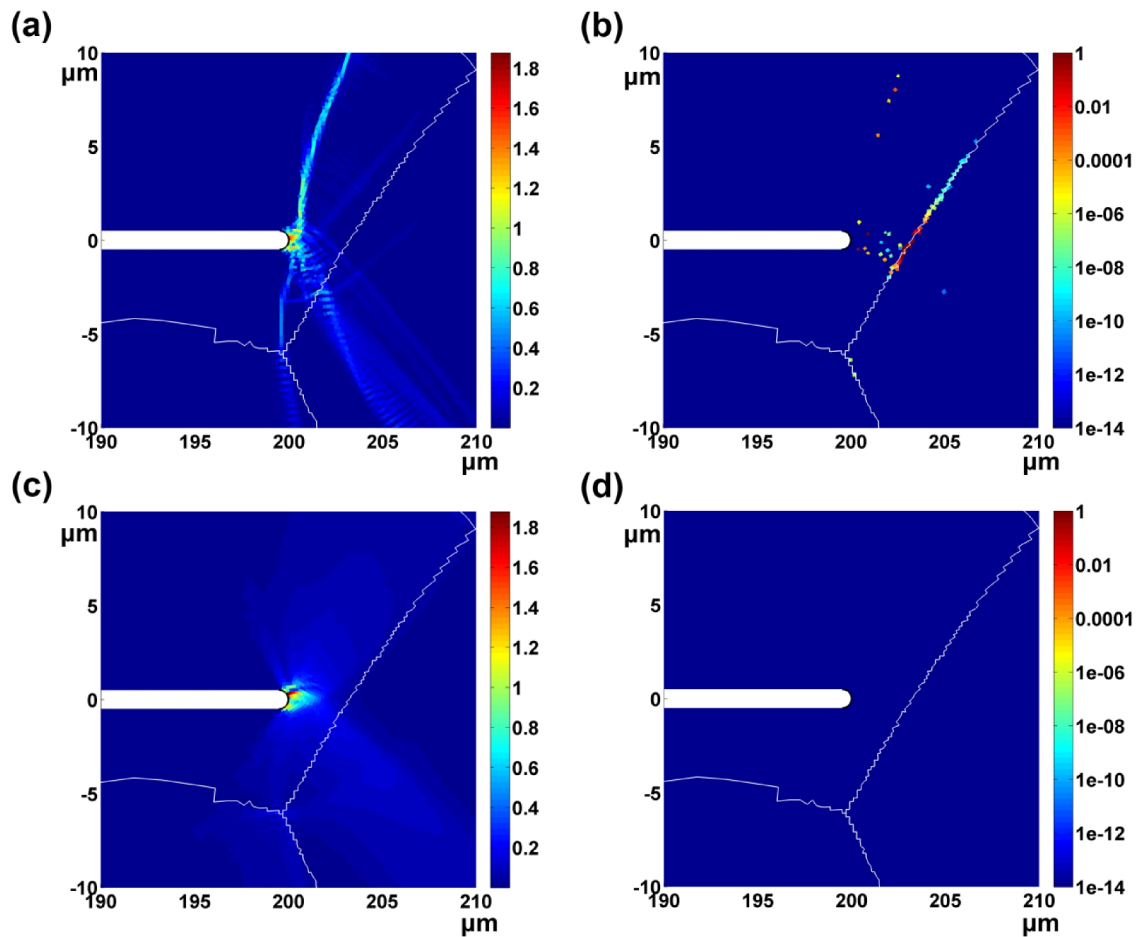
Figure 27. Distribution of effective inelastic strain for (a): irradiated (to 2.9 dpa), and (c): virgin specimens loaded to 0.5% strain at 550 K. (b), (d): Distribution of damage corresponding to the microstructures in (a), and (c), respectively.

4.5.5 Strain rate effects

Figure 28(a) shows the effective inelastic strain distribution ahead of a 300 μm deep notch loaded at a strain rate of 1.0 s^{-1}. The same microstructure loaded at a strain rate of 10^{-4} s^{-1} is shown in Figure 28(b). The material was irradiated to 2.9 dpa and then deformed to 0.49% strain at 550 K in both cases. It can be seen that the level of localization is lower at higher strain rate and the dislocation channels are not fully developed. In contrast, parts of the quasi-statically loaded microstructure are already in the post-localization, softening regime. Note that the material is modeled using a viscoplastic flow rule (cf. Eq. (2.4)). Rate effects in limiting 'viscous' inelastic dissipation may lower the extent of localization in the material loaded at 1.0 s^{-1}. We have also verified from the stress-strain curves that the material loaded at higher strain rate has a higher hardening rate (with respect to inelastic strain). It has been shown earlier [205] that localization is accommodated less readily at higher hardening rates. As a result, formation of dislocation channel 'interfaces' and subsequent failure initiation is delayed at higher strain rates. Further, void nucleation and growth, as modeled here, are diffusion-controlled processes. Diffusion time scales are much lower than the time scales of inelastic deformation, especially for the material loaded at 1.0 s^{-1}; fewer voids would nucleate and grow (i.e., less damage) over the time scale of inelastic deformation at this loading rate. From simulations, ϕ_t was found to be 1.54×10^{-6} for the material loaded at 1.0 s^{-1}, and 1.02×10^{-4} for the quasi-statically loaded material, after 0.49% applied strain. This may be used to interpret the experimentally observed increase in crack growth resistance of the irradiated material under dynamic loading [112]. Since the material loaded at higher strain rate has lower damage, its tearing resistance would be higher.
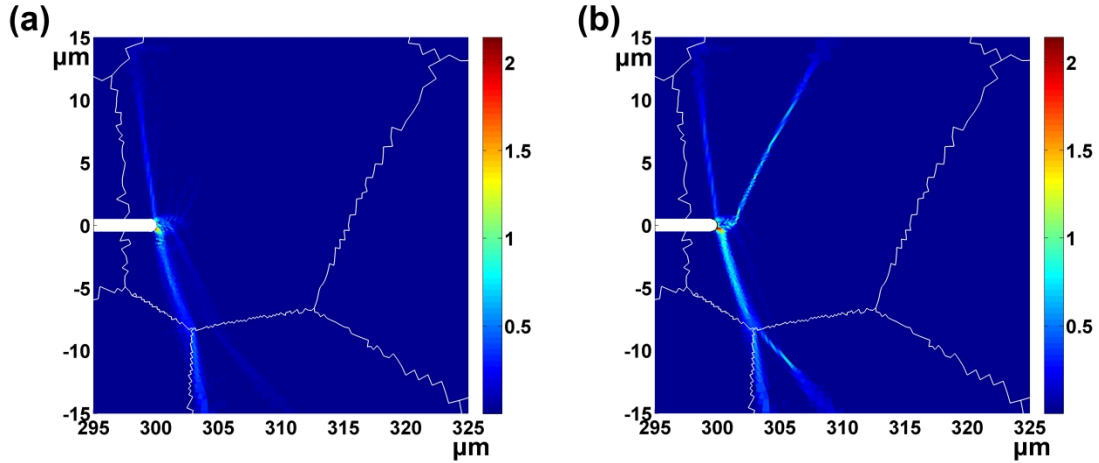
Figure 28. Comparison of effective inelastic strain distribution for specimen irradiated to 2.9 dpa **and then loaded in tension at a strain rate of (a):** 1.0 s^{-1}**, and (b):** 10^{-4} s^{-1}**, to** 0.49% **strain at** 550 K **.**

4.5.6 Temperature effects

Figure 29(a) shows the evolution of total area-weighted void number density, $\left(N_V\right)_t$, for three different test temperatures. The corresponding evolution of total area-weighted void radius, $\left(r_V\right)_t$, is shown in Fig. 29(b). $\rho = 2$ μm and $a = 250$ μm in all these simulations. The same initial microstructure as in Figs. 22 and 23 was used for all three cases. The material was loaded in tension, after irradiation to 2.9 dpa. $\left(N_V\right)_t$ and $\left(r_V\right)_t$ were computed using a similar procedure described for $\left(\phi\right)_t$ in Section 4.5.2. Note that the simulation failed to converge beyond 0.5% strain for the 600 K case.

As can be seen in Fig. 29(a), voids nucleate earlier in the material loaded at higher temperatures. However, the evolution of $\left(N_V\right)_t$ is not intuitive beyond the point of failure initiation. The rate of evolution of void number density is higher at higher temperatures due higher thermal 'activation' of void nucleation, as modeled in Eq. (4.10). Inspection

of the deformed microstructure (not shown here) revealed roughly the same failure patterns in all three cases, albeit at lower applied strains for the materials loaded at higher temperatures. It can also be seen that $(N_V)_t$ for the material loaded at 437 K is initially lower, but exceeds that for material loaded at 550 K after $\approx 0.55\%$ applied strain. This is because the material at lower temperature has relatively higher flow stress, resulting in lower activation energy for void nucleation (cf. Eq. (4.13)). Another reason for this is also due to the fact that the void radius of the material loaded at 437 K is much lower than that at 550 K (Fig. 29(b)), meaning less overall damage. In order to accommodate the incompatible deformation, failure initiation takes place via higher void nucleation rate at 437 K.
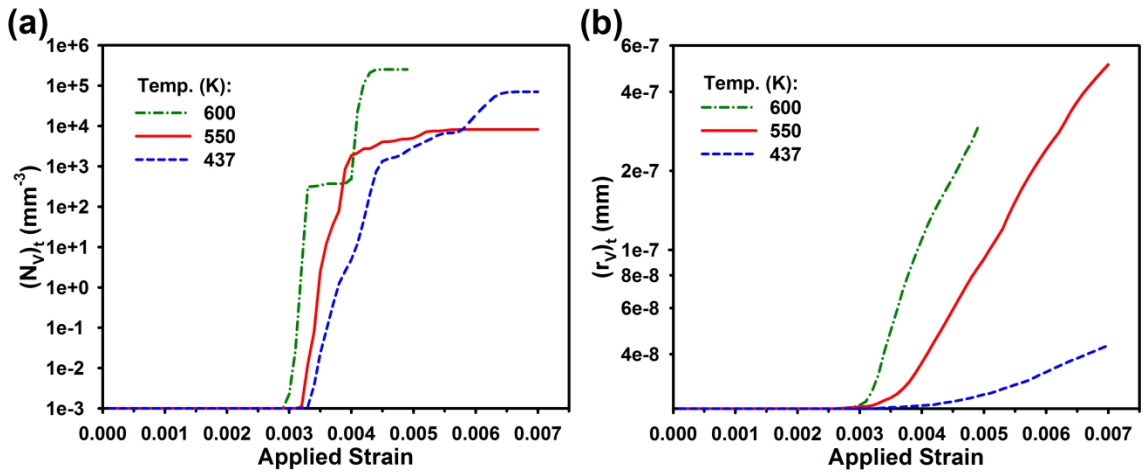
Figure 29. Evolution of (a): total area-weighted void number density, and (b): total area-weighted void radius as a function of temperature.

Figure 29(b) shows that the evolution of void radius is near-monotonic at all temperatures; the rate of change of void radius is higher at higher temperatures. This is because void growth, as modeled here, is governed solely by thermally-activated

diffusion kinetics. Void nucleation, on the other hand, is dependent both on the material stress levels and the loading temperature. The void radius is much lower at 437 K than the higher loading temperatures, indicating a change in failure mechanism from ductile 'zigzag' fracture [112] to limited ductility 'channel' fracture [157] in the temperature range 437-550 K. Note that $\Delta\Upsilon_{het}$ was assumed to be temperature invariant in these simulations. However, $\Delta\Upsilon_{het}$ may be expected to increase with decrease in temperature, further lowering the rate of void nucleation and growth.

4.5.7 Fracture toughness calculations

In the limit of small-scale yielding, the stress intensity factor, K, in terms of the CTD, is given as [165]

$$K = \sqrt{m\sigma_{YS}\left(CTD\right)E'} \qquad (4.27)$$

where m is a dimensionless constant dependent on the stress state ($m = 2$ for plane strain), σ_{YS} is the yield stress, and $E' = E/\left(1-v^2\right)$ for plane strain. As mentioned earlier, the intersection of the 5% secant line with the load-displacement curve is generally used to assess the critical fracture toughness, K_c, in experiments. We adopt a similar procedure in the present work, computing the CTD at the point of intersection of the 5% secant line with the load-displacement curve, and calculating K_c using Eq. (4.27). Based on the true stress-true strain curve of Mod 9Cr-1Mo steel irradiated to 2.9 dpa (not presented here), $\sigma_{YS}|_{550\ K} \approx 725\ \text{MPa}$ at $T = 550\ \text{K}$. Similarly, $\sigma_{YS}|_{437\ K} \approx 750\ \text{MPa}$, and $\sigma_{YS}|_{600\ K} \approx 710\ \text{MPa}$.

The values of K_c calculated for different notch depths and radii are listed in Table 4. There is a large discrepancy in the value of K_c between simulations and that measured in experiments. However, note that the experiments used a much larger notch radius, ρ. In general, the measured K_c is known to decrease with decreasing ρ for both metals [206–208] and ceramics [209–211]. The same was observed in our simulations, when ρ was decreased from 2 μm to 0.5 μm. It has also been suggested that K_c scales linearly with $\rho^{1/2}$, beyond a threshold notch root radius [207,210]. See Refs. [212,213] for analytical model to explain this effect. As shown in Fig. 30, if we were to extrapolate the simulated K_c as a function of $\rho^{1/2}$ for $a/W = 0.5$, the predicted K_c at $\rho = 60-80\,\mu m$ is consistent with the experimental values. Possible reasons of slightly lower values of K_c reported in experiments may be due to higher radiation doses and lower test temperatures (reflecting in lower ductility). Also note that the experimental notch root radii are larger than the grain size (≈ 25 μm). At these notch root radii, intergranular interactions may homogenize and mitigate the effect of grain level heterogeneity on the fracture toughness that are observed for sub-grain size notch root radii, for example in the present simulations. Further, fracture toughness has also been found to vary with irradiation temperature [164]. These effects are beyond the scope of the present work and not considered here.
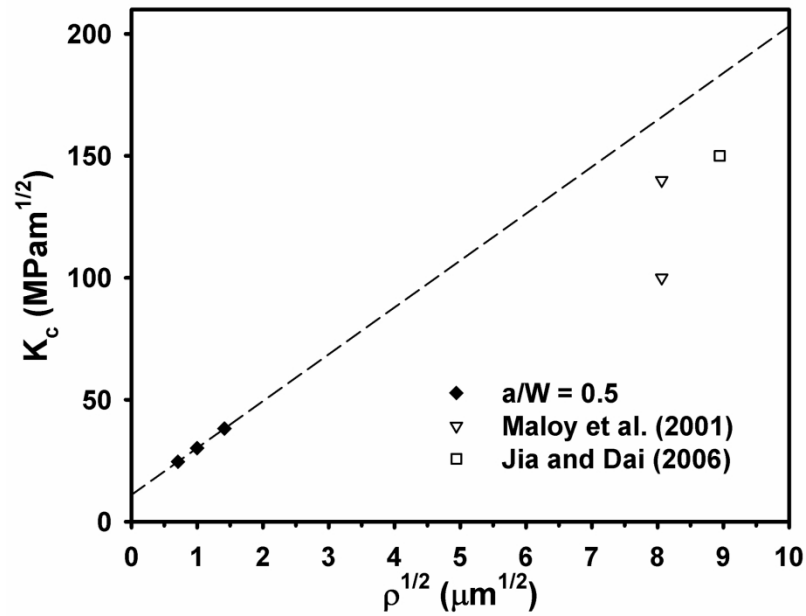
Figure 30. K_c, **as a function of** $\rho^{1/2}$, **extrapolated to the experimental notch radii. Experimental data from [2,3].**

It can be seen from Table 4 that the value of $(\phi)_t$ at critical fracture toughness is in the range $10^{-5} - 10^{-4}$ at 550 K. We have shown earlier in Section 4.5.3 that this value roughly corresponds to the stable damage propagation regime. In terms of classical fracture mechanics, the driving force for fracture, K, overcomes the material resistance, K_c, at this critical $(\phi)_t$ to allow stable crack propagation. Further, $(\phi)_t$ decreases with decrease in temperature, indicating a decrease in ductility. $(\phi)_t$ may thus be used as an indicator of the material's fracture behavior in the present framework.

Table 4. Fracture toughness calculations for different notch radii, ρ, and notch depths, a. $W = 800\ \mu m$ is the width of the specimens.

Radiation dose (dpa)	T (K)	ρ (µm)	a/W	$(\phi)_t$	CTD (µm)	$K_c(\mathrm{MPa}\sqrt{\mathrm{m}})$
2.9	550	0.5	0.3125	2.44×10^{-5}	2.35	26.61
2.9	550	0.5	0.375	2.11×10^{-5}	2.21	25.84
2.9	550	0.5	0.4375	1.03×10^{-4}	2.00	24.58
2.9	550	0.5	0.5	3.29×10^{-5}	2.01	24.60
2.9	550	1.0	0.5	1.05×10^{-5}	3.01	30.15
2.9	550	2.0	0.5	1.86×10^{-5}	4.83	38.18
2.9	550	1.0	0.3125	1.97×10^{-4}	3.27	31.41
2.9	550	2.0	0.3125	1.48×10^{-4}	5.41	40.40
2.9	437	2.0	0.3125	1.1×10^{-9}	5.12	40.74
2.9	600	2.0	0.3125	4.18×10^{-4}	5.50	39.97
3.0	323-433	~ 65	0.5	-	-	100-140[1]
4.3	523	~80	0.5	-	-	≈ 150[2]

[1] Ref. [2], [2] Ref. [3].

4.6   Summary

A void nucleation and growth based continuum damage framework has been developed and coupled with an existing crystal plasticity framework, to model failure initiation in irradiated bcc materials. Constitutive equations for vacancy generation via cross-slip and dislocation dipole mechanisms (during inelastic deformation) have been developed. Void nucleation has been modeled using a classical nucleation theory, while void growth is modeled using a diffusion-controlled mechanism. The framework has been used to model vacancy supersaturation along dislocation channels, and void nucleation and growth along these dislocation channel interfaces and GBs at high stress triaxialities. Our simulations have been able to capture the microstructural evolution characteristics of the transgranular 'zigzag' failure mechanism [112] at intermediate temperatures. Further, the crack growth resistance of the irradiated notched specimens has been found to be lower than that of the corresponding virgin specimens. The extent of localization and damage (in the irradiated microstructures) was found to decrease with increase in the loading rate. The effect of temperature on the evolution of void number density and radius has also been studied. There is a discrepancy between the irradiated specimen fracture toughness measured from simulations and from experiments. However, when the simulated fracture toughness values are extrapolated to the experimental notch root radii, they are consistent with the values measured from experiments.

The simulated failure initiation is strongly sensitive to the value of the interfacial energy change, $\Delta \Upsilon_{het}$, for heterogeneous void nucleation at dislocation channel interfaces and GBs. As has been demonstrated, this parameter may be used to calibrate the simulations to experimental results, in terms of the measured crack tip displacement

137

and/or critical fracture toughness. Insights from atomistic simulations of the interfacial phenomena may also be used to refine the estimation of this parameter, for example its temperature dependence. Further, the value of $\Delta\Upsilon_{het}$ adopted here is used to study failure initiation ahead of sharp notches having radii in the range 0.5-2 μm. At lower stress triaxialities (larger notch root radii), this value of $\Delta\Upsilon_{het}$ may be too high to allow any void nucleation. Future work will address these issues by performing detailed parametric studies of the effect of notch geometry on failure initiation. Future work can also incorporate strain-driven void growth mechanisms in this framework, to model failure over larger applied strains.

Defect-tolerant design of structures used in nuclear applications often relies on the fracture toughness master curve of the material used (cf. [214]). This framework (calibrated to experiments) may be used to construct such master curves for various loading histories. Further, the framework developed here is pretty general and may be applied to simulate void nucleation and growth-mediated failure for other deformation histories (no irradiation) as well, for example, at slip band interfaces during cyclic loading, or at second phase interfaces, etc. in different material systems.

CHAPTER 5

MODELING IRRADIATION CREEP DEFORMATION

5.1 Introduction

Irradiation creep deformation of metallic systems is accelerated (in comparison to conventional thermal creep) due to the creation of point defects that promote the growth and migration of defect loops and voids by stress-assisted mechanisms. Further, irradiation creep occurs at relatively lower homologous temperatures [7]. Irradiation creep has been correlated to the volumetric changes and swelling observed in structural metals [36,194]. While ferritic/martensitic steels (materials modeled in this work) are generally known to have good swelling resistance at elevated temperatures [10,11], irradiation creep can still contribute to the creation and growth of defect loops. Subsequent glide of dislocations through the field of these irradiation-induced defect loops is impeded.

This Chapter focuses on modeling the mechanical behavior and microstructure evolution during irradiation creep deformation. The crystal plasticity framework developed in Chapter 2 is modified to account for absorption of radiation-induced point defects at grain boundary (GB) sinks, in addition to the dislocation sinks considered earlier. The framework is used to simulate the substructure in terms of dislocation densities, interstitial loop densities, and point defect concentrations. The effect of radiation rate, applied stress, and grain size on the creep behavior is studied. A parametric study of the GB sink model is also performed. The creep strain is also correlated to the in-situ radiation damage (measured in dpa).

5.2   Background

The microstructure of metals undergoing irradiation creep deformation is characterized by the formation of defect loops, dislocation pileups and subgrain boundaries [215,216]. Deformation mechanism maps indicate that irradiation creep generally occurs at relatively lower homologous temperatures of the order ≈ 0.3-0.5 as compared to thermal creep (in virgin materials) which occurs at homologous temperatures greater than 0.5 [7]. This is attributed to the presence of non-equilibrium concentration of irradiation-induced point defects that allow accelerated migration and growth of defect loops under the application of external stress. The evolution of loops is initially prolific, with saturation reached at higher dpa doses [217]. In order to account for the stress anisotropy, the evolution of strain and defects was correlated [215] to the stress-induced preferential absorption (SIPA) model [31,41]. Again, the SIPA model was not able to account for the entire deformation all by itself [217]. As mentioned in Section 2.2.2, glide of dislocations subsequent to their climb (by SIPA) also needs to be accounted for. Further, it was found [215] that a threshold radiation dose must be reached after which irradiation creep commences. The creep strain rate (with respect to dpa rate) has also been found to be a near-linear function of the applied stress [218]. Studies also suggest [219] that a transition stress level exists beyond which the creep exponent changes from unity to a higher value.

A review of the irradiation creep mechanisms was given in Section 2.2.2. Without going into the details, it is again emphasized that SIPA and preferential absorption glide (PAG) of dislocations are the dominant mechanisms contributing to irradiation creep, at

140

least in the steady state regime. We have modeled the same using the climb-enhanced glide mechanism in Section 2.3.3.2.3.

The constitutive model developed in Chapter 2 did not account for the absorption of radiation-induced point defects at GBs. While this assumption may be valid for certain cases of pure metals and single crystals, point defect-GB interactions go hand-in-hand with the radiation-induced solute segregation effects observed in alloys [6]. For example, irradiation has been found to cause depletion of Cr, and enrichment of Ni and Si at the GBs in stainless steels [220]. Since atomic transport is generally accompanied by a parallel point defect transport (interstitial or vacancy, depending on the direction), the fluxes of these solute atoms are often related to the point defect fluxes [6]. We do not model the effects of radiation on solute segregation explicitly, but we consider point defect absorption at GBs in this Chapter and study its effect on the inelastic deformation characteristics near GBs during creep loading.

5.3   Model description

The finite deformation crystal plasticity framework developed in Chapter 2 models the following ISVs: mobile dislocation density, ρ_M^α, immobile dislocation density, ρ_I^α, interstitial loop density, N_i^α, interstitial loop size, d_i^α, at the level of slip system α, as well as the interstitial, c_i, and vacancy concentration, c_v, at the mesoscopic (integration point) level.

Constitutive equations for the evolution of slip system level ISVs are defined in Chapter 2, while those for the point defect evolution are modified here to account for

absorption at GB sinks. Specifically, Eqs. (2.9) and (2.10), representing the rate of evolution of interstitials, $\dot{c}_i$, and vacancies, $\dot{c}_v$, are modified to the following form:

$$\dot{c}_i = K_0 - K_{iv}c_ic_v - \sum_\alpha K_{is}^\alpha \left(\rho_M^\alpha + \rho_I^\alpha \right)c_i - k_{iGB}^2 D_i c_i \tag{5.1}$$

$$\dot{c}_v = K_0 - K_{iv}c_ic_v - \sum_\alpha K_{vs}^\alpha \left(\rho_M^\alpha + \rho_I^\alpha \right)c_v - k_{vGB}^2 D_v c_v \tag{5.2}$$

where K_0, K_{iv} are the defect pair creation and recombination rates, respectively, $K_{is}^\alpha = \left| z_i^\alpha \right| D_i$ is the interstitial-dislocation reaction rate coefficient, $K_{vs}^\alpha = \left| z_v^\alpha \right| D_v$ is the vacancy-dislocation reaction rate coefficient, k_{iGB}, k_{vGB} are the GB sink strengths for interstitials and vacancies, respectively, and D_i, D_v are the interstitial and vacancy diffusivities, respectively. Here, $z_x^\alpha = z_x^0 \left(\sigma_c^\alpha / E \right)$ is the point defect capture efficiency of defect type x, $\sigma_c^\alpha = \boldsymbol{n}^\alpha \cdot \boldsymbol{\sigma} \cdot \boldsymbol{n}^\alpha$ is the resolved stress normal to the slip plane α with unit normal direction, $\boldsymbol{n}^\alpha$, E is the Young's modulus, and z_x^0 is a material constant (assumed to be temperature-indepedent). While the rest of the terms were defined earlier in Chapter 2, the sink strength, k_{xGB}, represents the tendency of the GB to absorb point defect x [6,221]. Physically, k_{xGB}^{-1} represents the distance travelled by the point defect x in the GB before it gets absorbed [6].

In the present work, we use a spatially resolved mesh to solve for the point defect rate equations and also couple them with the crystallography-dependent deformation behavior. Note that in our model implementation, $k_{xGB} = 0$ when the material point is not at a GB. This is in contrast with coarse-grained mean field rate theory calculations, where an average value of GB sink strength has to be assumed. While these are useful for

studying the time evolution of ISVs and associated properties, spatial correlation is beyond the scope of the mean field rate theory calculations. The procedure for identifying GB elements is explained later.

It is again emphasized that we have neglected the full character of transport relations with defect gradients and fluxes in the present formulation. Physically, point defect fluxes would exist from the grain interior to the GBs, more so in the presence of radiation-induced segregation. In the presence of defect gradients, the point defect evolution equations will have the following form:

$$\dot{c}_i = K_0 - K_{iv}c_ic_v - \sum_\alpha K_{is}^\alpha \left(\rho_M^\alpha + \rho_I^\alpha\right)c_i - k_{iGB}^2 D_i c_i + \nabla \cdot \left(D_i \nabla c_i\right) \qquad (5.3)$$

$$\dot{c}_v = K_0 - K_{iv}c_ic_v - \sum_\alpha K_{vs}^\alpha \left(\rho_M^\alpha + \rho_I^\alpha\right)c_v - k_{vGB}^2 D_v c_v + \nabla \cdot \left(D_v \nabla c_v\right) \qquad (5.4)$$

where the last term in each equation represents the respective diffusive flux due to spatial concentration gradients. The flux terms are expected to be non-negligible in the regions of high concentration gradients, for example near the irradiated surfaces of metals, in the regions of solute segregation, etc. Incorporating these defect gradients requires non-local continuum modeling. We leave this to future work.

5.4   Model implementation

5.4.1   Loading and boundary conditions

The 3D constitutive model was implemented in the finite element program ABAQUS [91] using the User MATerial (UMAT) subroutine. 2D finite elements with linear interpolation and reduced integration were used. Generalized plane strain finite elements were used along with 3D material crystallography. Grains with in-plane square

cross-section were used, thus effectively simulating a network of cuboidal grains. The grain size is specified where needed. Random initial crystallographic orientations were assigned to all the grains.

Creep tests with concurrent irradiation were simulated on the polycrystalline ensembles. Figure 31 shows a schematic of the loading and boundary conditions. A 2D square-shaped simulation cell of side 175 μm was used in all simulations. The bottom edge of the 2D simulation cell is constrained along the loading direction, and the center of the bottom edge constrained in all degrees of freedom to prevent rigid body rotation. The side edges are traction-free. Stress-controlled loading is applied to the top edge. The applied tensile stress is ramped up to the desired level at an effective strain rate of 10^{-4} s^{-1}, and then the stress is held constant for the desired amount of time.
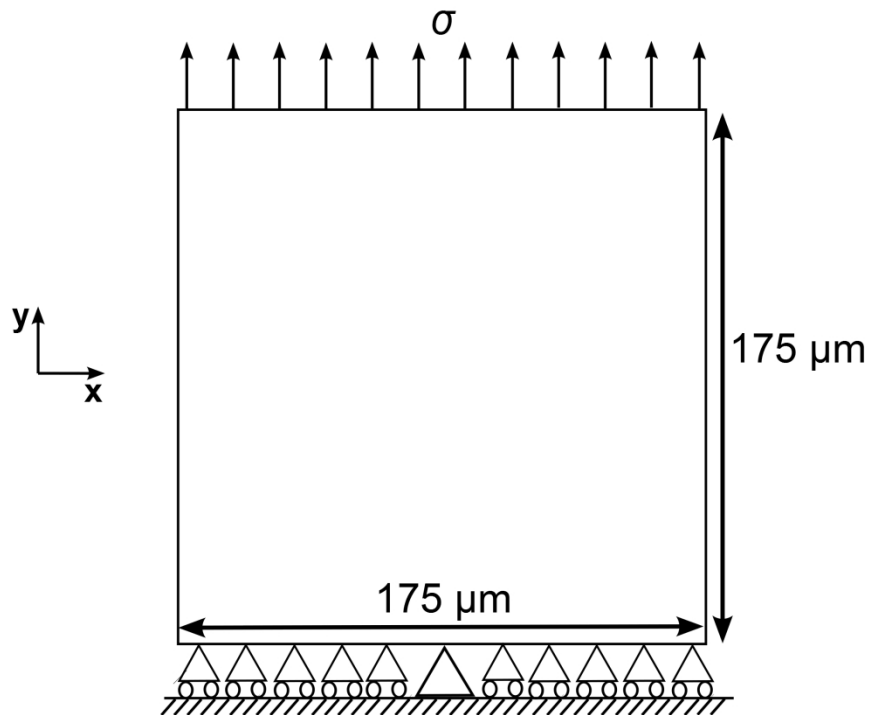
Figure 31. Schematic of stress-controlled loading and boundary conditions.

This model differentiates between a GB and grain interior; elements with first nearest neighbors belonging to a different grain are assigned as GB elements. We have used a regular mesh in our simulations, with uniform mesh size. The thickness of the GB element is thus governed by the mesh size. We will comment on implications later.

5.4.2 Model parameters

The constitutive model was used to simulate the creep response of Mod 9Cr-1Mo ferritic/martensitic steel. A uniform bcc crystal structure with 48 slip systems is assumed. It is assumed that the dislocation population is entirely mobile at the beginning of the simulation with an initial dislocation density of $\rho_M^0 = 1.0 \times 10^8$ mm^{-2} on each slip system. This dislocation density is of the same order as that observed in experiments [82,93]. It is assumed that there are no immobile dislocations or interstitial loops present initially. Further, an initial concentration of $c_i^0 = c_v^0 = 1.0 \times 10^{10}$ mm^{-3} was used for both the interstitials and vacancies. As explained in Chapter 2, though the initial point defect concentrations may be expected to be lower in the actual material, the high irradiation rate (in terms of K_0) ensures that the specified initial concentrations would be reached momentarily subsequent to the start of irradiation in physical experiments.

Model parameters for the constitutive framework are given in Section 2.4.1. The GB absorption model adds two new parameters, k_{iGB} and k_{vGB}, to the framework. It was suggested [221] that $k_{xGB}^2 \approx 10^7 - 10^9$ mm^{-2} for a mean grain size > 10 μm and defect type x. Physically, the GB sink strength for interstitials and vacancies may be expected to be different. However, there is no data in the literature to indicate their relative magnitudes.

We have assumed that the GB sink strengths for interstitials and vacancies have the same magnitudes. We have also performed a parametric study of the effect of GB sink strength on creep strain evolution in Section 5.5.3. In the rest of this Chapter, we have used a value of $k_{xGB}^2 = 5.0 \times 10^9$ mm^{-2} for both interstitials and vacancies. While this is on the higher side of the above mentioned range of the GB sink strength, it allows us to isolate the effect of GB sinks on the irradiation creep behavior.

5.5   Results and discussion

Creep simulations with concurrent irradiation were performed on 49 square-shaped, randomly oriented, 25 μm-sized grains, unless specified otherwise. An initial stress hold was applied for 3 h before the start of irradiation (point defect generation) in all cases. This allows the applied stress to equilibrate before irradiation-induced deformation begins. The material was loaded at 773 K in all cases. A uniform mesh size of 2.5 μm was used in these simulations, thus having 10 elements along the length of each grain. The peripheral elements of each square grain are assigned as GB elements, thus effectively assigning a GB thickness of 2.5 μm. The following Sections will first consider the simulated mechanical response of the material, and then discuss the microstructure evolution in terms of the effective inelastic strain, dislocation and interstitial loop densities, and interstitial concentrations.

5.5.1 Mechanical behavior

Figure 32(a) shows the evolution of strain as a function of time for different irradiation rates (in terms of the defect pair generation rate, K_0) at an applied stress of 160 MPa. The corresponding instantaneous strain rates are plotted in Fig. 32(b). The same initial (random) crystallographic orientation distribution was used in all cases. The strain rate goes up with increase in K_0; higher K_0 promotes faster generation of point defect pairs (according to Eqs. (5.1), (5.2)), and corresponding higher dislocation climb rate (Eq. (2.6)) and interstitial loop creation rate (Eq. (2.11)). At a total strain of 0.0016 (near steady-state), the instantaneous strain rate is: $2.69\times10^{-9}\,\mathrm{s}^{-1}$ for $K_0 = 1.0\times10^{12}\,\mathrm{mm}^{-3}\mathrm{s}^{-1}$, $5.34\times10^{-9}\,\mathrm{s}^{-1}$ for $K_0 = 2.0\times10^{12}\,\mathrm{mm}^{-3}\mathrm{s}^{-1}$, $2.23\times10^{-8}\,\mathrm{s}^{-1}$ for $K_0 = 5.0\times10^{12}\,\mathrm{mm}^{-3}\mathrm{s}^{-1}$, and 3.27×10^{-8} for $K_0 = 10.0\times10^{12}\,\mathrm{mm}^{-3}\mathrm{s}^{-1}$. Based on these data, the instantaneous strain rate was found to scale almost linearly as a function of K_0.
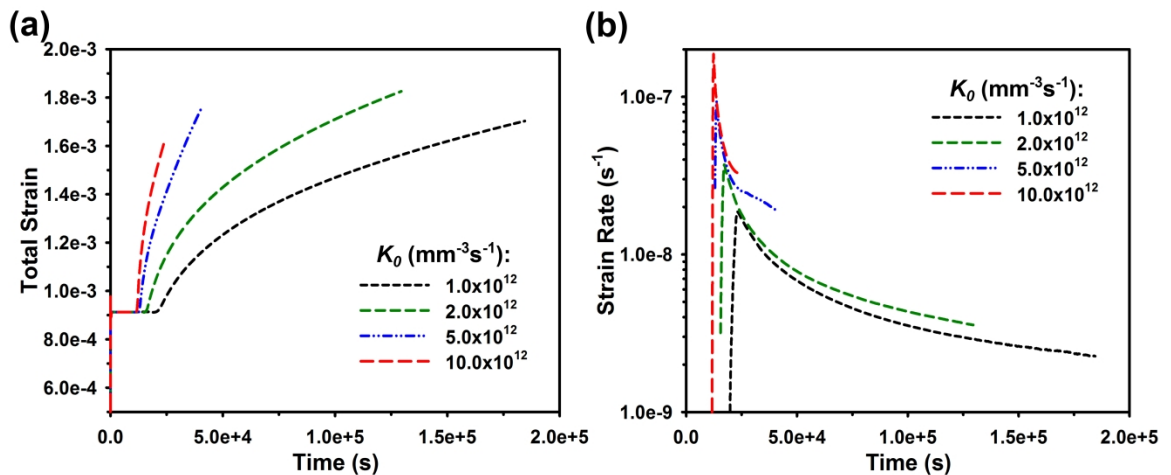
Figure 32. (a): Evolution of total strain as a function of time for different K_0, (b): evolution of instantaneous strain rate corresponding to the strain evolution in (a).

More interestingly, it is observed in Fig. 32(a) that following the initial stress hold period of 3 h, irradiation creep does not begin at the same instant for the different radiation rates. Irradiation creep begins earlier for the material irradiated at higher K_0. This suggests that a radiation threshold needs to be reached before irradiation creep commences. Such a radiation dose threshold has been observed in experimental studies of irradiation creep in 304 and 316 stainless steels [215,222].

Correlation with the evolution of average interstitial loop density (Fig. 33(a)) and loop size (Fig. 33(b)) suggests that this radiation dose threshold is associated with the initial generation of interstitial loops and saturation of the average interstitial loop size. Note that the evolution rate of loop size, $\dot{d}_i^\alpha$, depends on the rate of absorption of interstitials by climbing mobile dislocations and is a linear function of the interstitial concentration, c_i (cf. Eq. (2.13)). As observed in Fig. 9 in Chapter 2, c_i saturates following the initial transients, leading to saturation of d_i^α, as well. It is noted that the loops are expected to grow in size with increasing radiation. Evolution of multiple size classes of loops at a material point may be used to capture this experimentally observed effect in a rate theory model (e.g. [217]). A size class based model allows for transport of point defects from one size class to the next by diffusion-mediated absorption/emission of point defects. However, these calculations are computationally intensive, especially so in the context of the present spatially resolved finite element crystal plasticity framework, where the ISVs have to be resolved at the slip system level.

The interstitial loop density, on the other hand, increases monotonically as a function of time. The creation rate of interstitial loops, $\dot{N}_i^\alpha$, is proportional to the climb

rate, $\dot{\gamma}_c^\alpha$ (cf. Eq. (2.11)), and hence has a similar evolution trend as the creep strain. Deo et al. [53] suggested a square root dependence of the interstitial loop density on the radiation dpa level, i.e.,

$$N_i = A \cdot \mathrm{dpa}^{1/2} \tag{5.5}$$

where $A = 1.0 \times 10^{15} \, \mathrm{mm}^{-3}$ for low radiation levels (< 1 dpa). While this phenomenological relation was proposed to correlate the 'post-irradiation' interstitial loop density with the dpa level, we have used this relation to estimate the in-situ dpa level during the irradiation creep simulations. Given that the physics of defect pair production is beyond the scope of the present continuum framework, this is the only feasible way of estimating radiation dpa levels during our irradiation creep simulations.
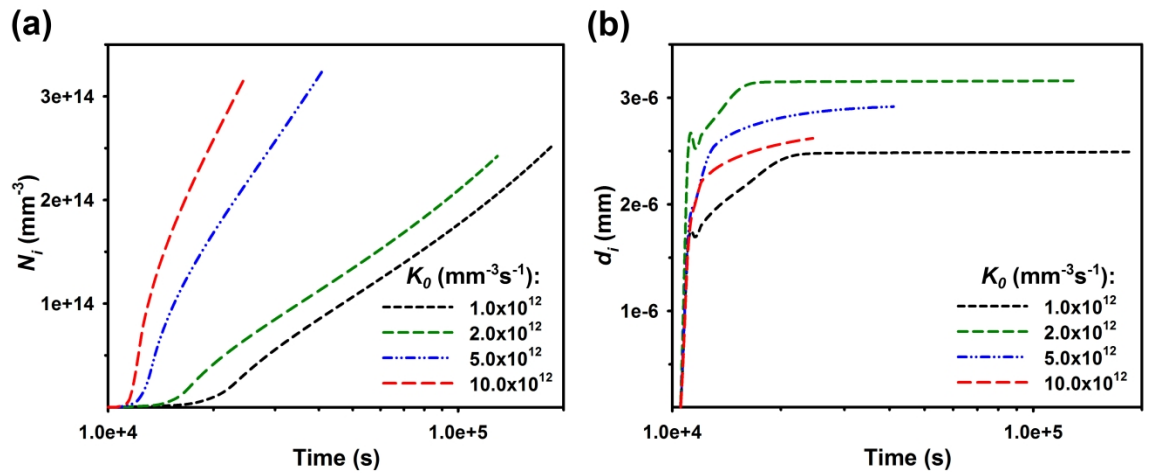
Figure 33. Evolution of (a): average interstitial loop density, and (b): average interstitial loop size as a function of time for different radiation rates.

Figure 34(a) shows the evolution of radiation dpa level with time. The radiation dpa is found to increase linearly with time for all radiation rates, subsequent to the initial stress hold period. This observation has two implications. First, this suggests that the

phenomenological relation in Eq. (5.5) is estimating the qualitative radiation damage trends correctly as the dpa level is expected to increase linearly with time for a constant radiation rate. While this validates the qualitative estimation of radiation damage in our simulations, the exact value of the pre-multiplication factor, A, in Eq. (5.5) needs to be determined from irradiation creep experiments for quantitative predictions. More importantly, this asserts that the constitutive model given in Eq. (2.11) is indeed capturing the qualitative physics of interstitial loop creation during irradiation creep, since a linear dpa evolution rate is never prescribed in our simulations, rather it emerges from the simulation results. A caveat of estimating radiation dpa using this procedure is that there is no way to measure the initial threshold dpa required for irradiation creep deformation to commence. Given that this threshold dpa is expected to be very small, this should not affect the correlation of steady state irradiation creep with dpa level. Presumably, another problem with estimating radiation damage in this manner is that the dpa damage rate is not solely a function of the defect pair production rate, K_0. The measured dpa damage rate is expected to change if one or more of the other loading conditions and material variables change.

In any case, the radiation dpa rate was measured to be: 3.9×10^{-7} dpa$\cdot$s^{-1} for $K_0 = 1.0 \times 10^{12}$ mm^{-3}s^{-1}, 5.1×10^{-7} dpa$\cdot$s^{-1} for $K_0 = 2.0 \times 10^{12}$ mm^{-3}s^{-1}, 3.61×10^{-6} dpa$\cdot$s^{-1} for $K_0 = 5.0 \times 10^{12}$ mm^{-3}s^{-1}, and 7.94×10^{-6} dpa$\cdot$s^{-1} for $K_0 = 10.0 \times 10^{12}$ mm^{-3}s^{-1} using Eq. (5.5). This suggests that the radiation dpa level is not a linear function of K_0. Again, the physics of point defect generation due to energetic particle flux is beyond the scope of the present continuum framework. See Was [6] for a discussion of the dependence of dpa rate on the displacement cross-section, particle flux, energy of the incident particles.
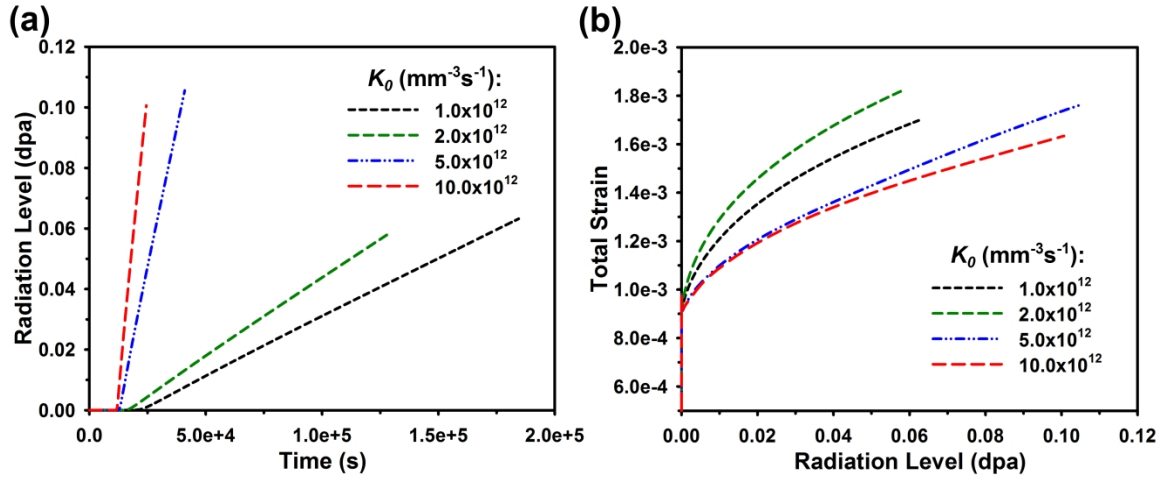
Figure 34. (a): Evolution of radiation dpa **level as a function of time using Eq. (5.5), (b): evolution of total strain as a function of radiation** dpa **level for different** K_0**.**

Regardless, the purpose of this exercise is to correlate the evolution of strain (and other properties, as well) to the radiation dpa level during irradiation creep deformation. For example, Fig. 34(b) shows the evolution of total strain as a function of the average dpa level. The initial strain at zero radiation level indicates the strain accumulated during initial loading of the material to the desired stress. The reason for highest strain rate (with respect to dpa) at $K_0 = 2.0 \times 10^{12}\,\text{mm}^{-3}\text{s}^{-1}$ is not intuitively evident. Correlating this to the loop size evolution in Fig. 33(b), the defect pair generation rate of $K_0 = 2.0 \times 10^{12}\,\text{mm}^{-3}\text{s}^{-1}$ is such that the density of mobile dislocations that have climbed produced the largest loops (in size) by absorbing interstitials. At higher K_0, a greater number of interstitial loops is generated such that less interstitials are available per interstitial loop formed (cf. Eq. (2.12)). At lower K_0, the interstitial concentration in the material is lower, and consequently the growth rate of the interstitial loops is also lower.

151

5.5.2 Deformed microstructure

5.5.2.1 Spatial distribution of inelastic strain

Figure 35 shows the distribution of effective inelastic strain in the material loaded at an applied stress of 160 MPa at 773 K. Following the initial stress hold of 3 h, the material was irradiated at a rate of $K_0 = 5.0 \times 10^{12} \, \text{mm}^{-3}\text{s}^{-1}$ for ≈ 10 h. The total strain in the material is ≈ 0.00176.
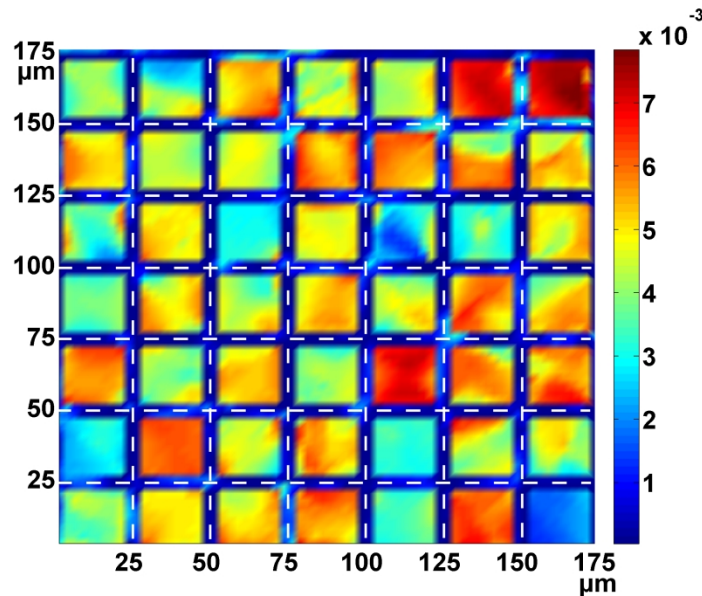
Figure 35. Distribution of effective inelastic strain in the material loaded at an applied strain of $160 \, \text{MPa}$ **at** $773 \, \text{K}$ **. The material was irradiated at** $K_0 = 5.0 \times 10^{12} \, \text{mm}^{-3}\text{s}^{-1}$ **for** $\approx 10 \, \text{h}$ **. Dotted lines overlaid on the mesh indicate GBs.**

Depending on the initial crystallographic orientation, the level of deformation varies within each grain interior. However, significantly less deformation is observed at the GBs (regions adjacent to the dotted lines overlaid in Fig. 35). According to the model described in Section 5.3, GBs act as sinks for point defects. Relatively lower

concentration of point defects is available for absorption by the deformation-carrying mobile dislocations in regions near GBs; inelastic deformation is inhibited near the GB regions.

Mesh size serves as the length scale that limits the thickness of the GB point defect sink regions and the inelastic deformation characteristics near GB regions in our local framework. A non-local constitutive formulation may be more appealing in this scenario, where the length scale associated with GB point defect sinks is intrinsically modeled in the constitutive equations, rather than pre-determined to be a function of the mesh size (as in present simulations). Physically, the material length scale associated with GB point defect absorption should relate to the distance travelled by point defect x in the GB before it gets absorbed, k_{xGB}^{-1} (cf. Section 5.3). However, the mesh size (= 2.5 µm) is significantly larger than k_{xGB}^{-1} ($\approx$ 30-300 nm) in our simulations. Hence, the mesh size serves as the model parameter that determines the degree of point defect absorption near GB regions. Consequently, the macroscopic deformation behavior is expected to change as a function of the mesh size. A finer mesh would allow for lower absorption at the GB regions due lesser relative thickness of the GBs. However, computational times were found to increase significantly using a mesh size lower than this (for a mesh size of 2.5 µm and simulation cell size of 175x175 µm, the creep simulations would take $\approx$ 250 h to reach a total strain of $\approx$ 0.0017 on 16, 2.2 GHz AMD Opteron CPU cores running in parallel). We have therefore limited our mesh size to 2.5 µm. Future work may address these mesh sensitivity issues.

5.5.2.2   Substructure

Figures 36(a)-(d) show the distribution of substructure in terms of the (slip system averaged) mobile dislocation density, immobile dislocation density, interstitial loop density, and the interstitial concentration, respectively, corresponding to the effective inelastic strain plot in Fig. 35.

The mobile dislocation density is in general lower in the grain interior as compared to the GB regions. This is because mobile dislocations are absorbed and 'transformed' to interstitial loops in the grain interior, where the interstitial concentration is relatively higher. In contrast, the 'transformation' of mobile dislocations to interstitial loops is limited at the GBs due to the lack of interstitials, thus resulting in higher mobile dislocation density near the GBs.

A part of the mobile dislocation density is also transformed to immobile dislocations via dislocation trapping events (cf. Section 2.3.3.3.3). The rate of mobile dislocation trapping and consequent formation of immobile dislocations is higher in the grain interior, since the deformation is higher. In contrast, the average immobile dislocation density is lower at the GBs. A similar spatial evolution pattern is also observed for the interstitial loop density. This again can be explained by the contrast in deformation and resulting transformation of mobile dislocations to interstitial loops in the grain interior versus the GBs. Spatial evolution of dislocations and interstitial loops is dependent on the availability of interstitials for absorption by mobile dislocations, thus creating interstitial loops. Since GB sinks absorb all the point defects near the grain edges, the interstitial concentration is significantly lower in these regions. The interstitial concentration in the grain interior varies proportional to the amount of deformation

154

within the grains. Note that the substructure and inelastic deformation is more or less uniform within the grains; no localization is observed within the grains. This is in contrast to quasi-static tensile loading, where flow localization is observed along narrow dislocation channels (cf. Chapter 3). It is noted that the radiation dpa levels are significantly higher in the localized microstructures considered earlier. As observed in Arsenlis et al. [47], a radiation threshold may exist beyond which inelastic deformation is no longer homogeneous and localization commences.
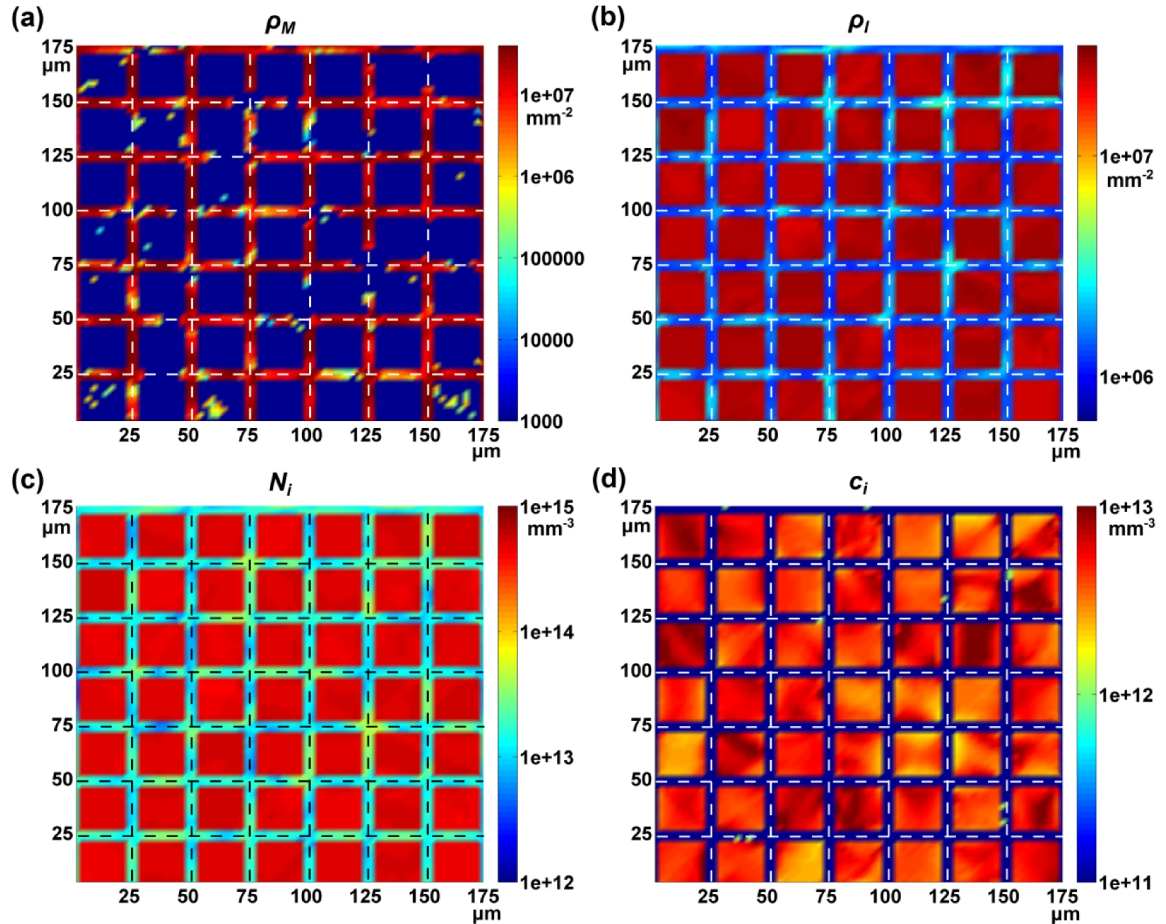
Figure 36. Distribution of (a): mobile dislocation density, (b): immobile dislocation density, (c): interstitial loop density, and (d): interstitial concentration corresponding to the inelastic distribution plot in Fig. 35.

5.5.3 Parametric study of GB sink model

We performed a parametric study of the GB sink model by varying the GB sink strengths, k_{iGB}^2 and k_{vGB}^2, and studying their effects on creep strain evolution. The defect pair generation rate was $K_0 = 2.0 \times 10^{12} \, \text{mm}^{-3} \text{s}^{-1}$ in the material loaded to 160 MPa applied stress at 773 K in all cases. Keeping all other parameters constant, the GB sink strength was varied from $5.0 \times 10^8 \, \text{mm}^{-2}$ to $5.0 \times 10^{10} \, \text{mm}^{-2}$. We also considered a case with no GB sinks present, i.e., $k_{iGB}^2 = k_{vGB}^2 = 0$. Figure 37(a)-(c) shows the deformed microstructure for three different GB sink strengths at ≈ 0.00157 total strain. Figure 37 (d) compares the creep strain evolution w.r.t. time for the different sink strengths. It is more intuitive to compare the strain evolution w.r.t. time than dpa since the damage rate measured in terms of $\text{dpa} \cdot \text{s}^{-1}$ will not be the same for all cases in our simulations (different average interstitial loop density evolution for different cases).

The deformed microstructure shows that there is significant deformation at the GBs for the microstructure with zero sinks. As the sink strength increases, the amount of inelastic strain along the GBs decreases. Note that all three microstructures are compared at the same total strain. In order to accommodate the total applied deformation, the degree of deformation in the grain interior is higher for the microstructures with non-zero sink strengths. The strain evolution plot in Fig. 37(d) shows that the strain rate (w.r.t. time) increases as the GB sink strength decreases and more deformation is transferred across the GBs. Further, the strain evolution is identical for the sink strengths $5.0 \times 10^9 \, \text{mm}^{-2}$ and $5.0 \times 10^{10} \, \text{mm}^{-2}$. This suggests that for $K_0 = 2.0 \times 10^{12} \, \text{mm}^{-3} \text{s}^{-1}$, majority of the point defects are absorbed by GBs having sink strengths $5.0 \times 10^9 \, \text{mm}^{-2}$ and higher.
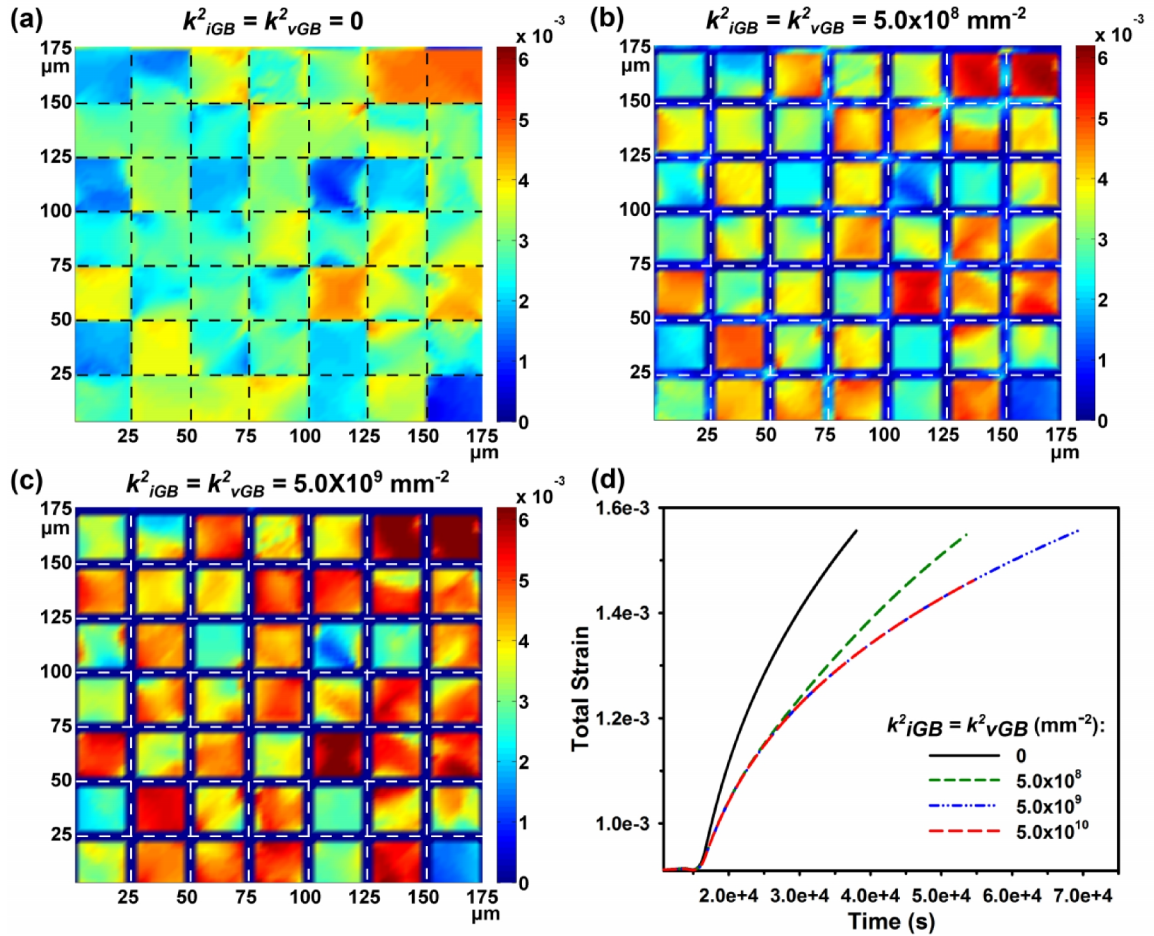
Figure 37. (a-c): Distribution of effective inelastic strain for three different GB sink strengths. Dotted lines overlaid on the mesh indicate grain interfaces. (d): Evolution of strain as a function of time for different GB sink strengths.

Since GB sinks lower the irradiation creep rate, it might seem beneficial to engineer materials with higher sink strengths. However, note that we have not accounted for the point defects once they are absorbed at GBs. Physically, these point defects, especially vacancies, might contribute to intergranular failure via void nucleation and growth processes at the GBs. Further, incompatibility of strain at the GBs might also accelerate these failure processes. As mentioned earlier, point defect absorption at GBs is also associated with radiation-induced segregation (cf. [6]), which is again detrimental

for the material's fracture resistance. In addition, we have not considered high temperature GB diffusional creep in the present constitutive framework. A model considering all these physical phenomena may be used to estimate the optimal amount of GB sink strength that would prolong the material's life in irradiation environments.

5.5.4 Grain size effect

The effect of GB sinks on the creep strain evolution was also studied by varying the density of GBs. Keeping the simulation cell dimensions constant, we performed three separate simulations with 196 grains of 12.5 μm size, 49 grains of 25 μm size, and 25 grains of 35 μm size, respectively. The same element size of 2.5 μm was used in all cases. Random initial crystallographic orientation distribution was assigned in all three cases. $K_0 = 5.0 \times 10^{12} \, \text{mm}^{-3}\text{s}^{-1}$ was used. The material was loaded to ≈ 0.0016 total strain at an applied stress of 160 MPa at 773 K.

Figure 38 shows the evolution of strain with time for different grain sizes. As the density of GBs increases (i.e., grain size decreases), the creep strain rate decreases. This is because GBs inhibit the transfer of deformation. The grain interior, which is expected to deform at similar rates in all cases, has to be crept longer to achieve the same amount of deformation for the smaller grain sizes (higher density of GBs). Decrease in irradiation creep rate with decreasing grain size was also observed in experiments during in-reactor stress relaxation of Zr alloys [223,224]. This is in contrast to conventional creep (in the absence of irradiation) where creep rates generally increase with decrease in grain size. We have also neglected diffusional creep at interfaces in the present framework. It is interesting to note that since irradiation creep can occur at lower homologous

temperatures, perhaps there is a range of temperature in which one might see decreasing creep rate with decreasing grain size, although at higher temperatures intergranular diffusional creep would again begin to dominate.
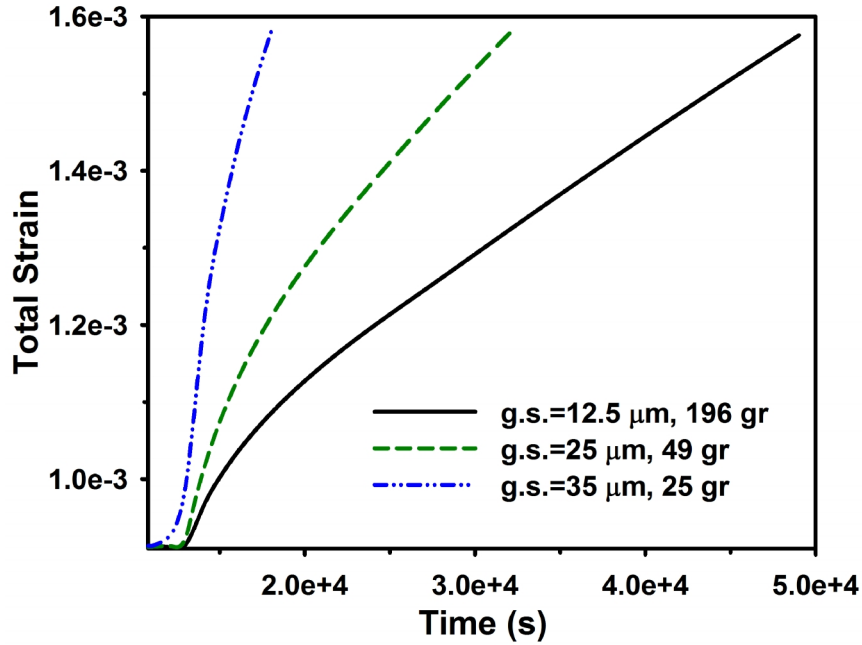
Figure 38. Evolution of creep strain as a function of time for different grain sizes in a simulation cell having the same dimensions.

5.5.5 Irradiation creep compliance

Assuming a linear stress dependence, the creep rate as a function of stress is given by [225]

$$\varepsilon' = B_0\sigma + \varepsilon'_0 \tag{5.6}$$

where ε' is the strain rate per dpa rate (measured in dpa^{-1}), B_0 is the creep compliance (measured in $dpa^{-1}MPa^{-1}$), σ is the stress (measured in MPa), and ε'_0 is the strain offset

at zero stress (measured in dpa^{-1}). Irradiation creep simulations were performed at three different applied stresses (80 MPa, 160 MPa, and 240 MPa) for $K_0 = 2.0 \times 10^{12}\,\text{mm}^{-3}\text{s}^{-1}$ and $K_0 = 5.0 \times 10^{12}\,\text{mm}^{-3}\text{s}^{-1}$. The irradiation temperature was 773 K in all cases. The in-situ radiation dpa level was calculated using Eq. (5.5) and correlated to the total strain. ε' was measured in the steady-state creep regime.
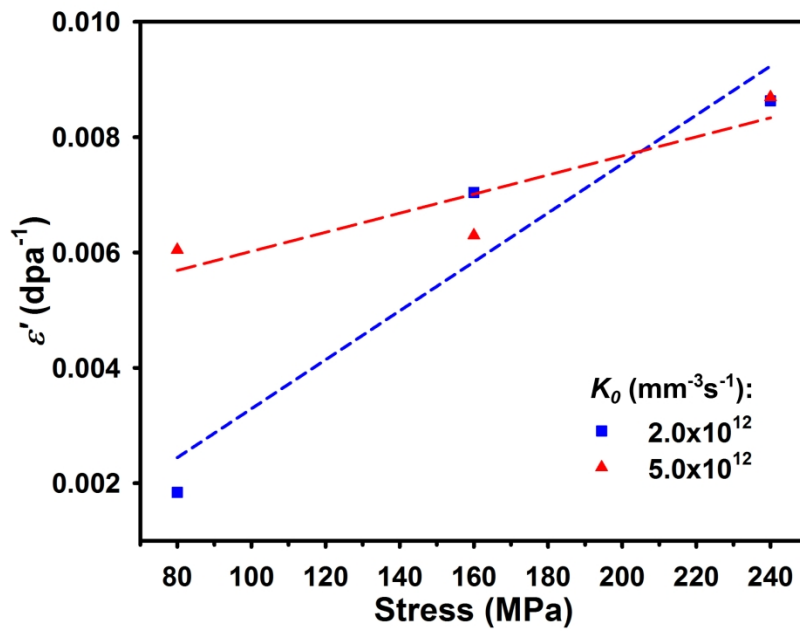
Figure 39. Creep rates as a function of stress for different radiation rates.

Figure 39 shows the variation of ε' with applied stress for different K_0. ε' increases with increase in applied stress. A linear regression fit of ε' (w.r.t. stress) was used to compute the creep compliance. From simulations, $B_0 = 4.24 \times 10^{-5}\,\text{dpa}^{-1}\text{MPa}^{-1}$ for $K_0 = 2.0 \times 10^{12}\,\text{mm}^{-3}\text{s}^{-1}$, and $B_0 = 1.65 \times 10^{-5}\,\text{dpa}^{-1}\text{MPa}^{-1}$ for $K_0 = 5.0 \times 10^{12}\,\text{mm}^{-3}\text{s}^{-1}$. B_0 is of the same order of magnitude as that seen in experiments for oxide dispersion

strengthened ferritic steels at similar temperatures [225], but higher by a factor of 2-4. Xu and Was [216] performed irradiation creep experiments on a similar 9Cr-1Mo steel at 773 K. While they did not measure the creep compliance, they did measure the creep rate, ε', at 160 MPa. Again, the creep rates predicted from our simulations are of the same order of magnitude, but higher by a factor of ~ 3-4. The simulated radiation damage rates are similar to their dpa rates. In our model, the absorption efficiency of interstitials at dislocations, z_i^α, and the GB sink strength, k_{iGB}, may be calibrated to fit the creep strain rates and dpa rates to experiments.

5.6   Summary

The constitutive framework developed in Chapter 2 was used to model the mechanical behavior and deformed microstructure during stress-controlled creep loading with concurrent irradiation. A GB sink model was used to account for the absorption of point defects at GBs. The framework was used to correlate the creep strain with the in-situ radiation dpa level for different defect pair generation rates. The substructure was studied in terms of the evolution of interstitial loop densities and sizes. While the interstitial loop densities increase monotonically with ongoing radiation, the loop sizes were found to saturate following the initial transients. The creep strain rate was found to increase with decreasing density of GBs and lower GB sink strengths. Decreasing irradiation creep rate with decreasing grain size has also been observed in experiments during in-reactor stress relaxation of Zr alloys [223,224]. Irradiation creep rates and creep compliances were measured from simulations and compared to available experimental

data for similar ferritic/martensitic steels. They were found to be of the same order of magnitude, but slightly higher than the experimental values.

This framework may be used to study the effect of various microstructural parameters (grain size, density of GBs, GB sink strengths, etc.) on the irradiation creep rates. Model predictions may be used to guide the engineering of structural materials with optimal irradiation creep properties. Future work needs to address the incorporation of spatial point defect gradients in a computationally feasible manner in order to capture the material physics more accurately. Models for failure initiation due to the absorption of point defects and radiation-induced segregation at GBs may also be developed as an extension of this work. High temperature GB-enhanced diffusional creep and void growth effects on creep also need to be considered to make this framework more robust.

CHAPTER 6

CONSTITUTIVE EQUATIONS FOR MODELING NON-SCHMID

EFFECTS IN SINGLE CRYSTAL BCC-IRON

6.1   Introduction

Until now, we have discussed deformation mechanisms in irradiated bcc metals at intermediate and elevated temperatures. While these mechanisms would also extend to the low temperature deformation behavior, non-Schmid effects are expected to be dominant in bcc metals at low temperatures. At these temperatures, inelastic deformation in bcc metals is characterized by complex slip modes. It has been argued that initial yield is governed by core spreading of the ½ <111> screw dislocations that leads to non-Schmid yield behavior [60,226]. Atomistic simulations at relatively high stresses show that the core structure of the screw dislocation in bcc crystals is not confined to its slip plane but splits into several planes of the <111> zone, significant of which are the {110} family of planes [227,228]. This core spreading effect has been argued to severely limit the mobility of screw dislocations in bcc metals; the dislocation core must again constrict for it to glide. In contrast to Schmid law, the yield stress depends not only on the resolved shear stress on the primary slip system, but also on stress components of the secondary 'non-glide' slip systems (necessary for the dislocation core to constrict) in these crystals [57,125,229,230]. Further, plastic flow is non-associative, meaning that the yield surface and plastic flow potential are not identical [58,122,125,231]. Tension-compression asymmetry is an additional manifestation of a non-Schmid formulation, particularly in

terms of initial yield stress. Dislocation core spreading and non-Schmid effects have been discussed in connection with the majority of the bcc metals at low temperatures, observed for example, in Fe [1,232,233], Mo [230,231,234,235], Nb and Nb-Mo alloys [236–238], Ta and Ta-Re alloys [239].

The present work pursues this line of modeling non-Schmid effects for bcc-Fe at low and ambient temperatures. Constitutive equations are incorporated in a previously developed dislocation density based crystal plasticity framework for bcc metals [16] to model the mechanical behavior of Fe single crystals over a range of crystallographic orientations and temperatures, fitting to available experimental data. While the effect of irradiation damage on the non-Schmid yield behavior is not entirely clear (not much research has been done in this area), we will comment on possible effects.

6.2   Background

To account for the influence of non-Schmid stress components on initial yield, Qin and Bassani [57] proposed a first order approximation for the critical yield stress, τ_{cr}, as a linear combination of the resolved shear stress and the non-Schmid stresses on slip system α, i.e.,

$$\tau_{cr} = \tau^{\alpha} + \sum_{i=1}^{N_{ns}} a_i \tau_i^{\alpha} \qquad (6.1)$$

where τ^{α} is the resolved shear stress on slip system α, a_i is the non-Schmid coefficient corresponding to the ith non-Schmid stress component, τ_i^{α}, and N_{ns} is the total number of non-Schmid stress components. Based on atomistic simulations of an isolated ½

<111> screw dislocation on the {110} slip plane in Mo and W [230], for bcc crystals this yield criterion has the form:

$$\tau_{cr} = \boldsymbol{m}^\alpha \cdot \boldsymbol{\sigma} \cdot \boldsymbol{n}^\alpha + a_1 \boldsymbol{m}^\alpha \cdot \boldsymbol{\sigma} \cdot \boldsymbol{n}^\alpha_{ns} + a_2 \left(\boldsymbol{n}^\alpha \times \boldsymbol{m}^\alpha \right) \cdot \boldsymbol{\sigma} \cdot \boldsymbol{n}^\alpha + a_3 \left(\boldsymbol{n}^\alpha_{ns} \times \boldsymbol{m}^\alpha \right) \cdot \boldsymbol{\sigma} \cdot \boldsymbol{n}^\alpha_{ns} \qquad (6.2)$$

where $\boldsymbol{\sigma}$ is the current stress state, $\boldsymbol{m}^\alpha$ and $\boldsymbol{n}^\alpha$ are unit vectors corresponding to the slip direction and the slip plane normal on slip system α, $\boldsymbol{n}^\alpha_{ns}$ is the unit vector of the 'non-glide' plane on which the screw dislocation core was initially spread, and, a_1, a_2 and a_3 are coefficients that can be fit to the atomistically/experimentally determined yield stress for the bcc single crystal loaded in different orientations. From left to right, the terms on the RHS of Eq. (6.2) represent the conventional resolved (Schmid) shear stress along the slip plane, the resolved shear stress along the 'non-glide' plane, the resolved stress normal to the primary slip plane, and the resolved stress normal to the 'non-glide' plane, respectively. For the case of a conventional Schmid-type yield formulation, only the resolved shear stress on the primary slip plane is considered, i.e., $a_1 = a_2 = a_3 = 0$.

In recent years, a number of continuum crystal plasticity frameworks have incorporated non-Schmid effects in bcc crystals at low homologous temperatures [233,240–243]. These frameworks generally rely on the aforementioned non-Schmid coefficients (or its variants) to capture asymmetric yield behavior observed in bcc crystals. With the exception of Lim et al. [243], the non-Schmid coefficients used in these crystal plasticity models are generally assessed using molecular statics simulations performed at 0 K. However, experimental studies of single crystal bcc metals suggest that the contribution of non-Schmid stresses to the yield stress diminishes with increasing temperature. For example, studies on single crystal Fe [1] show that as the temperature is increased from 143 K, deviation of yield from Schmid's law decreases monotonically and

becomes almost negligible at 295 K. Based on comparison to experiments, Lim et al. [243] showed that while the non-Schmid stresses are dominant in the yield behavior of single crystal Ta at 77 K, they are not so significant at 273 K and 300 K. Chen and co-authors [244,245] also derived an atomistically based macroscopic yield criterion and an orientation-dependent Peierls potential for kink-pair nucleation on screw dislocations in bcc-Fe. In their bottom-up model, effects of temperature on diminishing the twinning-antitwinning asymmetry and tension-compression asymmetry are captured by the Peierls potential itself. Temperature dependence of the non-Schmid coefficients thus needs to be considered in the expression for yield in constitutive models that employ this kind of non-Schmid formulation.

It should also be noted that the non-Schmid coefficients derived from atomistics are based on simulations of an isolated screw dislocation in the lattice, meaning that the yield stress is simply the lattice frictional resistance that needs to be overcome to initiate glide of an isolated screw dislocation; dislocation-dislocation interactions are not considered. Also, the yield criterion does not provide any information about the evolution of non-Schmid stresses past the point of initial yield. In the presence of the long range field of other dislocations, the contribution of non-Schmid stresses may be expected to diminish beyond the point of initial yield, more so because dislocation glide (plastic flow) is governed primarily by the Schmid stresses. These effects are not generally considered in the continuum crystal plasticity models mentioned above.

The present work develops constitutive equations for yield in bcc-Fe, accounting for the temperature dependence of non-Schmid coefficients (based on results from available experiments), and the evolution of non-Schmid stresses with inelastic

166

deformation. These equations are coupled with existing models for thermally-activated dislocation glide kinetics and used in the crystal plasticity framework developed in Chapter 2 to model the orientation and temperature dependence of yield and inelastic flow in single crystal Fe. Some of the constitutive equations presented in Chapter 2 are restated here as they have different implied meanings. A top-down modeling approach is presented, with model parameters based entirely on available experimental data from laboratory scale coupons. Much experimental and modeling work still remains to resolve the complexity of dislocation mobility and initial yield phenomena in bcc crystals. Alternative explanations may be offered and pursued for orientation dependence and rate dependence of initial yield in bcc crystals that relates to complex dislocation kink pair phenomena that govern kinetics at low applied stress levels and finite temperature without resorting to the core spreading argument and non-Schmid effects in Eq. (6.2) (i.e., $a_1 = a_2 = a_3 = 0$, cf. [246]). This line of reasoning would require that tension-compression asymmetry arise more from cooperative mesoscale (many body) manifestations of the intrinsic twinning/anti-twinning asymmetry of the orientation dependent Peierls stress of bcc crystals. The distinction and validity of these two very different frameworks for mobility of screw dislocations in bcc crystals will take more time to fully resolve. In the present work, we consider available experimental data to explore the temperature dependence and consistency of the formulation based on non-Schmid effects.

6.3   Temperature dependence of non-Schmid coefficients

As mentioned earlier, inelastic deformation in bcc crystals occurs due to the glide of ½<111> screw dislocations via kink pair formation on the {110} family of planes. The 'non-Schmid' plane corresponding to each of the possible slip systems in bcc crystals is given in Gröger et al. [230]. It should be noted that the present work deals with modeling the deformation of bcc crystals at low homologous temperatures, in particular room temperature and below. There are contradictory claims in the literature regarding the nature of active slip systems in bcc-Fe at these temperatures. Although the majority of the studies [233,247–249] concluded that elementary slip occurs via kink-pair formation on the {110} plane at room temperature and below, Brunner and Diehl [250,251] deduced that while this is true at temperatures below 250 K, kink-pair formation occurs on the {112} plane at temperatures above 250 K. Nonetheless, it has been found [247,249,252] that slip on the {112} plane is a combination of elementary slip steps on {110} planes. In the present work, we assume that {110} planes are the primary slip planes in bcc-Fe. Further, in order to account for the twinning/anti-twinning asymmetry observed in bcc crystals (cf. [238]), forward and backward slip has been explicitly accounted for in Ref. [230] by considering the positive and negative slip directions as separate slip systems. Thus, in place of the 12 {110} <111> slip systems, we now have 24 slip systems considering both the positive and negative slip directions. The non-Schmid planes corresponding to these slip systems are also given in Ref. [230].

The Schmid and non-Schmid stresses (on each slip system) scale linearly as a function of the uniaxial stress, proportional to the respective Schmid and 'non-Schmid' factors. At yield, the slip system with the highest Schmid factor is activated; 'non-

Schmid' factors corresponding to the loading orientation can be easily obtained for this activated slip system. Orientation-dependent variation of the uniaxial yield stress may thus be used to estimate the parameters, a_1, a_2, a_3, and τ_{cr}, simultaneously either by solving a system of linear equations corresponding to each orientation for Eq. (6.2), or using a regression analysis. However, this naïve method predicted aphysical values of the parameters when fitted to relevant experimental data. For example, τ_{cr} was predicted to be negative or extremely small ($\tau_{cr} \leq 0.05\sigma_Y$) in many cases, which is not possible; typically τ_{cr} is of the same order as σ_Y (here σ_Y is the yield stress). Further, a_1 was predicted to be negative in certain cases. As explained in [243], a_1, accounting for the twinning/anti-twinning asymmetry [230,235,238], should be non-negative in order to account for higher resolved shear stress along the anti-twinning direction. To avoid these anomalies, we determine a_1 separately by the procedure described below, and then solve for the rest of the parameters, a_2, a_3, and τ_{cr}, simultaneously.

Given the threefold symmetry of a ½<111> screw dislocation in the bcc crystal (cf. [235] and references therein), orientation dependence of the yield stress about ±30° of one reference slip plane of the {110} family is sufficient to determine the non-Schmid coefficients and may be applied to all slip planes. Note that ±30° correspond to the two {112} planes adjacent to a {110} plane along which twinning/anti-twinning asymmetry is observed.

The parameter a_1 may be estimated by fitting the yield stress, σ_Y, on the maximum resolved shear stress plane (MRSSP) measured as a function of the angle, χ, which the MRSSP makes with the reference (110) slip plane about which the orientation

dependence is measured (cf. [229,230,232]). This may be mathematically expressed as [229,232]

$$\sigma_Y = \frac{\sigma^0}{\cos\chi + a_1 \cos\left(\chi + \pi/3\right)} \tag{6.3}$$

where σ^0 is a material constant. Note that this expression is a simplified form of Eq. (6.2) obtained by combining τ_{cr}, and the a_2 and a_3 terms into σ^0. Transformation of the yield rule from the slip system tensorial description in Eq. (6.2) to the angular (i.e., χ) dependence in Eq. (6.3) is a consequence of the bcc crystal symmetry and definition of the slip systems and corresponding non-Schmid slip planes [230].

Spitzig and Keh [1] performed experimental studies of the temperature dependence of the proportional limit stress in uniaxial tension, σ_{pl}, as a function of χ about the $\left(\bar{1}01\right)$ slip plane in single crystal Fe. These values, extracted from Fig. 5 in Ref. [1], are given in Table 5. Assuming $\sigma_Y \approx \sigma_{pl}$, a_1^T is estimated for different temperatures by fitting the experimental data in Table 5 to Eq. (6.3) using a least squares regression method, and is given in Table 5. The superscript T on a_1^T denotes the respective temperature. Based on the fit, a_1^T is found to decrease monotonically as the temperature is increased from 143 K to 295 K. Molecular statics simulations [232,233] have estimated that $a_1^{0K} = 0.61$. From calculations, $a_1^{250K} \approx 0.07 a_1^{0K}$ and $a_1^{295K} \approx 0.06 a_1^{0K}$. This verifies that twinning/anti-twinning asymmetry, though present, is significantly diminished at room temperature for Fe. Compiling the values of a_1^T estimated over different temperatures, the variation of a_1^T as a function of T is shown in Fig. 40. Least square fit

of these data points to an exponential decay function is also shown in Fig. 40, and has the following form:

$$a_1^T = 0.0106 + 2.3311\exp(-0.0162T); \quad 143\ \text{K} \le T \le 298\ \text{K} \tag{6.4}$$

Table 5. Least squares fit of non-Schmid coefficient, a_1, to the experimentally measured variation of σ_{pl} as a function of χ (from [1]) for different temperatures using Eq. (6.3).

T (K)	χ (°)	$\sigma_{pl}/\sigma_{pl}(\chi=0°)$	a_1^T	$\sigma^0/\sigma_{pl}(\chi=0°)$
143	-24	1.02	0.2407	1.125
	0	1		
	10	1.05		
	20	1.15		
195	-24	1.04	0.1154	1.05
	0	1		
	10	1.03		
	20	1.08		
250	-24	1.08	0.0414	1.02
	0	1		
	10	1.03		
	20	1.05		
295	-24	1.08	0.0363	1.015
	0	1		
	10	1.02		
	20	1.04		

Note that the value of $\sigma_{pl}/\sigma_{pl}(\chi = 0°)$ at $\chi = \pm 30°$ was also reported for all temperatures in Ref. [1]. However, these data points did not give good fit to Eq. (6.3) for $T = 143$ K and $T = 195$ K. Hence, these data points were excluded from the estimation of a_1^T for all temperatures. As mentioned earlier, Eqs. (6.2) and (6.3) give the orientation dependence of yield on non-Schmid stresses to a first order approximation; higher order stress terms may be needed for fitting the non-Schmid coefficients over the entire range (even at $\chi = \pm 30°$). Similar problems were also encountered when estimating a_1 from molecular statics results (cf. [232]).
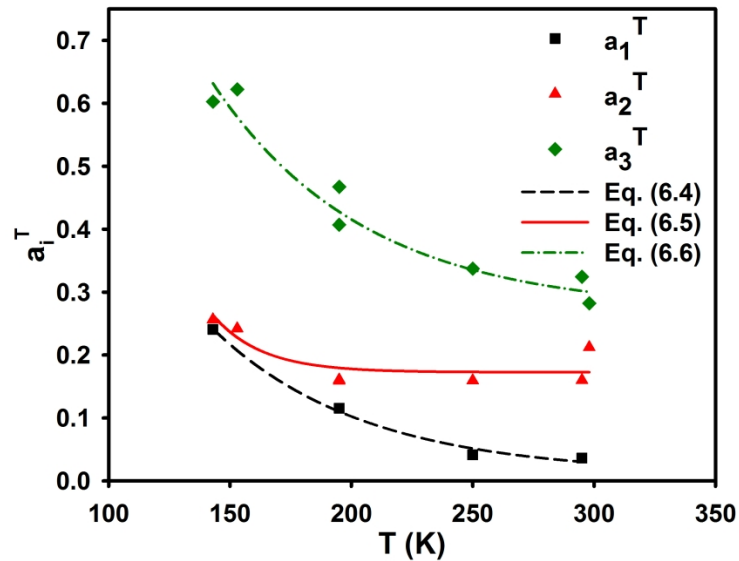
Figure 40. Variation of non-Schmid coefficients with temperature.

Having determined a_1^T, we are now left with three parameters: τ_{cr}^T, a_2^T, a_3^T. Using the values of orientation-dependent yield stress, these parameters are estimated by solving a system of linear equations corresponding to different orientations for Eq. (6.2).

Two sets of temperature-dependent non-Schmid parameters were obtained based on two different sets of experimental data for bcc-Fe [1,253]. These values are reported in Table 6 and plotted as a function of temperature in Fig. 40. Note that the same value of a_1^T (from Eq. (6.4)) was used in both these calculations.

Except for the value of a_2^T in the temperature range 295-298 K, the calculated values of a_2^T and a_3^T are comparable from both experimental data sets at similar temperatures, though the non-Schmid coefficients calculated from Ref. [253] are generally higher than that calculated from Ref. [1]. This might be due to the fact that the lower yield stress was reported in Ref. [253], while the proportional limit stress was reported in Ref. [1]. In terms of deformation, the point of proportional limit occurs prior to the lower yield point. Physically, the non-Schmid stresses are considered to assist in constricting the (already spread) screw dislocation cores for glide to initiate (i.e., yield to occur) in bcc crystals. Full constriction of the dislocation cores might not have occurred at proportional limit, thus reflecting in slightly lower non-Schmid contributions as compared to that at the lower yield point.

It can be seen from Table 6 that both a_2^T and a_3^T decrease with increase in temperature, and start saturating in the range 250-298 K (similar to a_1^T). However, the contribution of these non-Schmid components to yield is still significant at room temperature, in contrast to the near-negligible contribution of the twinning-antitwinning asymmetry component. Temperature dependence of a_2^T and a_3^T, fit to exponential decay functions, are given in Eqs. (6.5) and (6.6), respectively.

$$a_2^T = 0.1727 + 108.9126 \exp(-0.0496T); \ 143 \text{ K} \le T \le 298 \text{ K} \tag{6.5}$$

$$a_3^T = 0.2699 + 3.5454 \exp(-0.0160T); \quad 143 \text{ K} \leq T \leq 298 \text{ K} \qquad (6.6)$$

From atomistic simulations [233], $a_2^{0K} = 0.23$ and $a_3^{0K} = 0.55$. These values are marginally lower than the calculated corresponding non-Schmid parameters at 143 K. Physically, these non-Schmid components represent the contribution of shear stresses perpendicular to the slip direction in constricting the distorted dislocation core [230]. Calculated values of these coefficients from (isolated dislocation) atomistic simulations might have been lower because dislocation-dislocation interactions in distorting the core are not accounted for in the atomistic simulations. Unlike a_1^T, both a_2^T and a_3^T are not negligible at 250 K and 295 K. Physically, this means that resolved stresses normal to the Schmid and the 'non-glide' plane still contribute to the constriction of screw dislocation cores (for glide to initiate) at ambient temperatures.

Table 6. Estimate of a_2^T and a_3^T by fitting the orientation-dependent yield stress to Eq. (6.2) for different temperatures.

Experimental data	$\dot{\varepsilon}$ (s^{-1})	T (K)	a_2^T	a_3^T	Stress measure
Spitzig and Keh [1]	5.6×10^{-4}	143	0.2564	0.6028	Proportional limit
		195	0.1590	0.4069	
		250	0.1595	0.3373	
		295	0.1601	0.3243	
Takeuchi [253]	4.0×10^{-3}	153	0.2422	0.6222	Lower yield
		195	0.1609	0.4673	
		298	0.2124	0.2822	

Table 7 gives the relative contributions of the Schmid and non-Schmid stress components to the critical resolved shear stress, τ_{cr}^T, as a function of temperature. Approximate loading orientations were estimated from the stereographic projections given in Ref. [1]. Experimental yield stress values were also taken from Ref. [1]. All calculations were performed for slip system β with the highest Schmid factor, assuming single slip at yield. As can be seen, the relative non-Schmid stress contributions to τ_{cr}^T decrease markedly with increase in temperature. They are each less than 7% of τ_{cr}^T at 295 K; although diminished, non-Schmid effects are still present at room temperature. More importantly, the calculated value of τ_{cr}^T (sum of the Schmid and the non-Schmid stress components) for different orientations at a given temperature is more or less invariant (all values are within 4% of the mean τ_{cr}^T calculated at a given temperature). Physically, τ_{cr}^T denotes the resistance to dislocation glide at yield; τ_{cr}^T is a material property and should be the same irrespective of the loading orientation. In our calculations, τ_{cr}^T is a function of the yield stress and the non-Schmid coefficients. While the yield stress values are taken from experiments, the non-Schmid coefficients are estimated here. This verifies that the estimated coefficients, a_1^T, a_2^T, and a_3^T, are indeed addressing the experimentally observed temperature-dependent non-Schmid yield behavior.

Table 7. Relative contributions of Schmid and non-Schmid stress components to τ_{cr}^{T} as a function of temperature.

T (K)	χ (°)	Loading orientation	σ_{Y} (MPa)	$\boldsymbol{m}^{\beta}\cdot\boldsymbol{\sigma}\cdot\boldsymbol{n}^{\beta}$ (MPa)	$a_{1}^{T}\boldsymbol{m}^{\beta}\cdot\boldsymbol{\sigma}\cdot\boldsymbol{n}_{ns}^{\beta}$ (MPa)	$a_{2}^{T}\left(\boldsymbol{n}^{\beta}\times\boldsymbol{m}^{\beta}\right)\cdot\boldsymbol{\sigma}\cdot\boldsymbol{n}^{\beta}$ (MPa)	$a_{3}^{T}\left(\boldsymbol{n}_{ns}^{\beta}\times\boldsymbol{m}^{\beta}\right)\cdot\boldsymbol{\sigma}\cdot\boldsymbol{n}_{ns}^{\beta}$ (MPa)	τ_{cr}^{T} (MPa)
143	-24	[1 2 20]	234.09	104.05	21.45	-13.83	45.38	157.05
	0	[$\bar{1}$ 3 7]	229.5	114.34	13.75	0	33.94	162.03
	20	[$\bar{3}$ 7 9]	263.93	120.93	4.85	13.85	15.19	154.82
195	-24	[1 2 20]	131.56	58.48	5.49	-5.30	17.27	75.94
	0	[$\bar{1}$ 3 7]	126.5	63.02	3.45	0	12.67	79.14
	20	[$\bar{3}$ 7 9]	136.62	62.60	1.14	4.89	5.33	73.96
250	-24	[1 2 20]	58.10	25.83	1.13	-2.26	5.99	30.69
	0	[$\bar{1}$ 3 7]	53.8	26.80	0.69	0	4.23	31.72
	20	[$\bar{3}$ 7 9]	56.76	26.01	0.22	1.96	1.74	29.93
295	-24	[1 2 20]	32.51	14.45	0.37	-1.26	3.02	16.58
	0	[$\bar{1}$ 3 7]	30.10	14.99	0.23	0	2.12	17.34
	20	[$\bar{3}$ 7 9]	31.30	14.34	0.07	1.08	0.86	16.35

Using atomistic simulations of a ½ <111> screw dislocation in bcc-Fe [233], the yield stress criterion given in Eq. (6.2) may be extended to account for the effect of tension/compression perpendicular to the glide direction and also account for the fact that hydrostatic stress does not contribute to dislocation glide. This leads to three additional terms in the expression for the critical yield stress [233]. For simplicity, the effect of these additional non-Schmid stresses on yield behavior is not considered the present work.

6.4   Crystal plasticity framework

The finite deformation crystal plasticity model is based on the multiplicative deformation of the deformation gradient, $\boldsymbol{F}$, into elastic, $\boldsymbol{F}^e$, and inelastic, $\boldsymbol{F}^i$, parts [49,50]. The inelastic velocity gradient, $\boldsymbol{L}^i$, given by $\boldsymbol{L}^i = \dot{\boldsymbol{F}}^i \cdot \boldsymbol{F}^{i-1}$, is the tensor sum of the crystallographic shearing rate, $\dot{\gamma}^\alpha$, over all slip systems, N_s, i.e.,

$$\boldsymbol{L}^i = \sum_{\alpha=1}^{N_s} \dot{\gamma}^\alpha \boldsymbol{m}_0^\alpha \otimes \boldsymbol{n}_0^\alpha \qquad (6.7)$$

where $\boldsymbol{m}_0^\alpha$ and $\boldsymbol{n}_0^\alpha$ are unit vectors corresponding to the slip and slip plane normal directions in the reference (or intermediate) configuration. Shearing rate, $\dot{\gamma}^\alpha$, is a function of the resolved shear stress, τ^α, and the internal state variables (ISVs) on each slip system α. The slip system dislocation density, ρ^α, given as the additive sum of mobile, ρ_M^α, and immobile dislocations, ρ_I^α, i.e., $\rho^\alpha = \rho_M^\alpha + \rho_I^\alpha$, is used as an ISV in this framework.

6.4.1 Dislocation glide kinetics

Thermally activated glide of ½ <111> screw dislocations by kink-pair nucleation is the rate controlling mechanism governing inelastic deformation in bcc metals at low temperatures (cf. [254]). In continuum constitutive formulations, the crystallographic shearing rate due to thermally activated dislocation glide is generally represented using a phenomenological Kocks-type activation enthalpy driven flow rule [52], i.e.,

$$\dot{\gamma}^\alpha = \begin{cases} \dot{\gamma}_0 \exp\left(-\dfrac{\Delta F_g}{kT}\left(1-\left(\dfrac{\tau_f^\alpha - s^\alpha}{s_0^\alpha}\right)^p\right)^q\right); & for \ \ \tau_f^\alpha > s^\alpha \\ 0; \ for \ \ \tau_f^\alpha \leq s^\alpha \end{cases} \tag{6.8}$$

where $\dot{\gamma}_0$ is the pre-exponential factor, ΔF_g is the activation energy for dislocation glide in the absence of external stress, k is Boltzmann constant, T is absolute temperature, τ_f^α is the driving stress for dislocation glide, s^α is the lattice resistance to dislocation glide, s_0^α is the lattice resistance at 0 K, and p and q are parameters used to model the shape of the activation enthalpy function. Note that the double-kink nucleation mechanism in bcc metals is governed by two different temperature regimes (cf. [254]). For simplicity, these two regimes are not explicitly considered in the present work.

The purpose of this work is to demonstrate a top-down approach for modeling non-Schmid effects in bcc metals at finite temperatures. It should be noted that while the coarse-grained constitutive models developed/used in this work are phenomenological in nature, we still consider the screw dislocation movement by kink-pair formation as the rate-controlling mechanism. In more (atomistically-derived) physical formulations, the crystallographic shearing rate is generally expressed as [246]

$$\dot{\gamma}^{\alpha} = \dot{\gamma}_0 \exp\left(-\frac{H_{\text{kp}}(\tau_f^{\alpha}, T)}{kT}\right) \qquad (6.9)$$

where $H_{\text{kp}}(\tau_f^{\alpha}, T)$ is the stress- and temperature-dependent activation free energy of kink-pair formation. We have recently used the nudged elastic band method to calculate the kink-pair formation energy from the approximate 0 K potential energy landscape (i.e., $H_{\text{kp}}(\tau_f^{\alpha}, T) \approx H_{\text{kp}}(\tau_f^{\alpha}, T = 0)$) [246]. However, to fully account for the effect of activation *entropy* and the associated Meyer-Neldel compensation rule [255], one should calculate the activation free energy as a function of all the stress components at various temperatures. At the moment, it is a very difficult task from the atomistic modeling standpoint. Hence, the present work represents an empirical characterization of the temperature effect on activation free energy of kink-pair formation in terms of the temperature dependent a_1, a_2, and a_3. The enthalpy function in its present form is simple enough for the parameters to be estimated directly from available experimental data. As will be shown later, this Kocks-type flow rule replicates the inelastic flow response fairly well.

In Eq. (6.8), s^{α} may be expressed as the additive sum of contributions from the lattice frictional resistance, s_{fric}^{T}, and the obstacle resistance, s_{obs}^{α}, i.e.,

$$s^{\alpha} = s_{fric}^{T} + s_{obs}^{\alpha} \qquad (6.10)$$

s_{fric}^{T} is the short range lattice resistance and is generally a function of the temperature-dependent Peierls stress in bcc metals. The long range resistance, s_{obs}^{α}, due to other defects, may be expressed as a function of the dislocation density using a Taylor hardening model, i.e.,

$$s_{obs}^{\alpha} = Gb\sqrt{\sum_{\zeta=1}^{N_s} q_{\rho} A^{\alpha\zeta} \rho^{\zeta}} \qquad (6.11)$$

where G is the shear modulus, b is the Burgers vector magnitude, q^{ρ} is the dislocation barrier strength, and, $A^{\alpha\zeta}$ is the matrix of slip system dislocation interaction coefficients. Ideally, s^{α} should be equal to τ_{cr}^{T} at yield, since τ_{cr}^{T} represents the total slip system resistance to glide initiation.

Strictly speaking, the driving stress for dislocation glide, τ_f^{α}, is just the resolved shear stress, τ^{α}, on slip system α; this must hold whether yield (i.e., initiation of glide at a threshold) follows Schmid's law or not. Further, crystal viscoplastic formulations do not generally model yield and inelastic flow separately. Yield is implicitly modeled in the flow rule using the lattice resistance, s^{α}, or a similar threshold-like term.

In the present formulation, we assume the initial (threshold) driving stress to be the additive sum of the resolved shear stress, τ^{α}, and the contribution from non-Schmid stresses, σ_{ns}^{α}, i.e.,

$$\tau_f^{\alpha}\Big|_{initial} = \tau^{\alpha} + \sigma_{ns}^{\alpha} \qquad (6.12)$$

From Eq. (6.2), σ_{ns}^{α} has the following form:

$$\sigma_{ns}^{\alpha} = a_1^T \boldsymbol{m}^{\alpha} \cdot \boldsymbol{\sigma} \cdot \boldsymbol{n}_{ns}^{\alpha} + a_2^T \left(\boldsymbol{n}^{\alpha} \times \boldsymbol{m}^{\alpha} \right) \cdot \boldsymbol{\sigma} \cdot \boldsymbol{n}^{\alpha} + a_3^T \left(\boldsymbol{n}_{ns}^{\alpha} \times \boldsymbol{m}^{\alpha} \right) \cdot \boldsymbol{\sigma} \cdot \boldsymbol{n}_{ns}^{\alpha} \qquad (6.13)$$

Eq. (6.12) thus satisfies the yield relation given in Eq. (6.2). However, in view of the foregoing statement that resolved shear stress drives dislocation glide, Eq. (6.12) should be modified beyond the point of yield such that the contribution from non-Schmid stresses diminishes with inelastic deformation. From a physical standpoint, it is unlikely that the non-Schmid effects would suddenly disappear; not all dislocations start gliding at

the point of initial yield, meaning that not all dislocation cores get constricted simultaneously at yield. Further, long range interaction fields with other dislocations may be expected to affect the extent of dislocation core spreading and its subsequent constriction. We propose to model this decay of the non-Schmid contribution to the driving stress as an exponential function of the effective inelastic strain, ε_{eff}^i, i.e.,

$$\tau_f^\alpha = \tau^\alpha + \sigma_{ns}^\alpha \exp\left(-\frac{\varepsilon_{eff}^i}{\varepsilon_0^i}\right) \tag{6.14}$$

where ε_0^i is a material constant. As the contribution of non-Schmid stresses decays with increasing inelastic strain, the resolved shear stress, τ^α, dominates the driving force for dislocation glide.

Note that the non-Schmid stresses may be assumed to decay as a function of the dislocation density, ρ^α, or some other state variable. For simplicity we choose the constitutive form given in Eq. (6.14). Detailed experimental studies, for example, of the orientation dependence of yield in pre-strained crystals, are needed to determine the exact nature of the decay of non-Schmid stresses with applied strain.

6.4.2 Dislocation evolution

We have developed constitutive equations for the evolution of mobile and immobile dislocations in bcc metals subjected to radiation damage in Chapter 2. Neglecting terms representing the interaction of dislocations with irradiation-induced defects, the rate of evolution of mobile and immobile dislocations, as a function of the crystallographic shearing rate, $\dot{\gamma}^\alpha$, is given as [16]

$$\dot{\rho}_M^\alpha = \frac{k_{mul}}{b}\sqrt{\sum_\varsigma \rho^\varsigma}\left|\dot{\gamma}^\alpha\right| - k_{cs}\exp\left(-\frac{\left(\tau^* - \left|\tau^\chi\right|\right)V_a}{kT}\right)\rho_M^\alpha\left|\dot{\gamma}^\alpha\right| - \frac{2R_c}{b}\rho_M^\alpha\left|\dot{\gamma}^\alpha\right| - \frac{1}{b\lambda^\alpha}\left|\dot{\gamma}^\alpha\right| \qquad (6.15)$$

$$\dot{\rho}_I^\alpha = \frac{1}{b\lambda^\alpha}\left|\dot{\gamma}^\alpha\right| - k_{dyn}\rho_I^\alpha\left|\dot{\gamma}^\alpha\right| \qquad (6.16)$$

The first term in Eq. (6.15) represents the rate of formation of new mobile dislocations by multiplication at existing dislocation segments, the second term represents the rate of migration of mobile dislocations by cross-slip (from slip plane α to slip plane χ), the third term represents the rate of mutual annihilation of mobile dislocation segments with opposite Burgers vectors within a critical capture radius R_c, and the fourth term represents the rate of immobilization of mobile dislocation segments by trapping at barriers, given as a function of the effective mean free path, $\lambda^\alpha = 1/\beta_\rho\sqrt{\rho^\alpha}$, of the glide dislocations. The corresponding rate of addition of immobile dislocations due to trapping of mobile dislocations is reflected in the first term of Eq. (6.16), while the second term represents the rate of annihilation of immobile dislocations by dynamic recovery. In these equations, k_{mul}, k_{cs}, and k_{dyn} are material constants corresponding to mobile dislocation multiplication, mobile dislocation cross-slip, and dynamic recovery of immobile dislocations, respectively. τ^* is the activation stress for cross-slip over an activation volume, V_a, and β_ρ is a constant associated with dislocation trapping. These equations are assumed to principally reflect the dislocation mechanisms governing inelastic deformation in bcc-Fe. Reference [16] provides a detailed description of the physical mechanisms modeled and the assumptions involved.

6.5   Model parameters

Temperature dependent elastic constants for bcc-Fe are adopted from [256]. As mentioned earlier, the material is assumed to have 24 {110} <111> slip systems, considering both positive and negative slip. These slip systems are listed in [230]. Based on bcc crystallography, the Burgers vector magnitude of Fe is given as $b = \left(\sqrt{3}/2\right)a_0$, where $a_0 = 0.2866$ nm is the lattice parameter of bcc-iron [83].

Experimental studies [250,251,257,258] have suggested that the activation energy for dislocation glide at zero stress, ΔF_g, is in the range 0.65-0.9 eV. We have assumed that $\Delta F_g = 0.7$ eV at all temperatures. Values of the shape function parameters, $p = 0.28$ and $q = 1.34$, are taken from [51], where they were used to model the tensile behavior of bcc-Ta. Note that p and q were fit to the atomistically calculated stress-dependent activation energies of kink-pair formation in Ref. [246] and it was found that p and q are not very sensitive to the detailed variation of stress dependent activation energies. The pre-exponential factor in the flow rule, $\dot{\gamma}_0$, is assumed to be have a constant value of 5.0×10^4 s^{-1}.

Temperature dependence of the non-Schmid coefficients, a_1^T, a_2^T and a_3^T, was discussed in Section 6.3. The non-Schmid contribution to the driving stress has been modeled to decay as an exponential function of the effective inelastic strain in Eq. (6.14). The value of the associated material constant, ε_0^i, is assumed to be 0.02, meaning that the non-Schmid contribution at $\varepsilon_{eff}^i = 0.02$ decreases to $\approx 37\%$ of the contribution at initial yield ($\varepsilon_{eff}^i = 0$). Systematic experiments/atomistic simulations are needed to further refine

this phenomenological relation. Parametric study of the effect of ε_0^i on the simulated stress-strain curves is shown in Section 6.6.3.

From [85], the lattice resistance at 0 K, $s_0^\alpha = 390$ MPa. From experiments [259], temperature-dependent values of the lattice frictional resistance, s_{fric}^T, are: $s_{fric}^{295\text{K}} \approx 10$ MPa, $s_{fric}^{250\text{K}} \approx 25$ MPa, $s_{fric}^{195\text{K}} \approx 60$ MPa, and $s_{fric}^{143\text{K}} \approx 115$ MPa. These values were again fit to a polynomial expression to obtain the temperature dependence of s_{fric}^T, i.e.,

$$s_{fric}^T = 361.7426 - 2.2311T[\text{K}] + 0.0035T[\text{K}]^2 \text{ MPa} \qquad (6.17)$$

Further, s_{fric}^T is assumed to be independent of the loading orientation. The dislocation barrier strength, q^ρ, is assumed to be 0.3 in the expression for obstacle resistance, s_{obs}^α. A similar value was used in Arsenlis et al. [12] to model the dislocation barrier resistance in irradiated Cu. The values of the dislocation interaction coefficients were assumed to be $A^{\alpha\alpha} = 1.0$ (self-interaction) and $A^{\alpha\varsigma}\left(\varsigma \neq \alpha\right) = 0.2$ (latent interaction). From experiments [257,259], $s_{obs}^\alpha \approx 5-8$ MPa at initial yield. Putting in values of the above mentioned parameters in Eq. (6.11), the initial value of dislocation density, $\rho^0 \approx 4.0-10.0 \times 10^4$ mm^{-2}. We have assumed that an equal population of mobile and immobile dislocations exists initially, and $\rho_M^0 = \rho_I^0 = 4.0 \times 10^4$ mm^{-2} on all slip systems.

Parameters associated with the dislocation evolution equations include: k_{mul}, k_{cs}, k_{dyn}, τ^*, V_a, R_c, and β_ρ. Since this work focusses on modeling the mechanical behavior of bcc-Fe at low and ambient temperatures, dislocation migration due to thermally

activated cross-slip may be neglected at these temperatures, i.e., $k_{cs} = 0$ (see [16] for values of the parameters, τ^* and V_a, when k_{cs} is non-zero). The critical capture radius, R_c, for mutual annihilation of dislocation dipoles is assumed to be $6b$ (≈ 1.5 nm). This is of the same order as that used in Ref. [12] for mutual dislocation dipole annihilation in irradiated Cu. The remaining parameters, k_{mul}, k_{dyn} and β_ρ, were used to fit simulation results to the experimental single crystal stress-strain curves of bcc-Fe [4] for different loading orientations at 298 K. Based on the fit (discussed in Section 6.6.1), $k_{mul} = 3.45 \times 10^{-2}$, $k_{dyn} = 2.75 \times 10^2$, and $\beta_\rho = 7.40 \times 10^{-2}$. Further, these parameters are assumed to be temperature invariant. Table 8 lists the values of the complete set of parameters.

Table 8. Model parameters for bcc-Fe.

Parameter	Value	Meaning
$C_{11}, C_{12}, C_{44},$ ν	$239260 - 24520 \big/ \big(\exp\big(392.03/T[\text{K}]\big) - 1\big)$ MPa, $135780 - 6550 \big/ \big(\exp\big(469.65/T[\text{K}]\big) - 1\big)$ MPa, $120720 - 3500 \big/ \big(\exp\big(162.9/T[\text{K}]\big) - 1\big)$ MPa, 0.29	Elastic constants (from [256])
G	$87600 - 17T[\text{K}]$ MPa	Shear modulus (from [260])
a_0	0.2866 nm	Lattice parameter (from [83])
ΔF_g, p, q, $\dot{\gamma}_0$	0.7 eV, 0.28, 1.34, 5.0×10^4 s^{-1}	Flow rule parameters
a_1^T, a_2^T, a_3^T	$a_1^T = 0.0106 + 2.3311\exp\big(-0.0162T\big),$ $a_2^T = 0.1727 + 108.9126\exp\big(-0.0496T\big),$ $a_3^T = 0.2699 + 3.5454\exp\big(-0.0160T\big)$; for $143\text{ K} \le T \le 298\text{ K}$	Non-Schmid parameters
s_{fric}^α, q^ρ, $A^{\alpha\alpha}$, $A^{\alpha\varsigma}\,\big(\varsigma \ne \alpha\big)$, s_0^α	$s_{fric}^T = 361.7426 - 2.2311T[\text{K}] + 0.0035T[\text{K}]^2$ MPa, 0.3, 1.0, 0.2, 390 MPa	Hardening parameters
ε_0^i	0.02	Parameter for decay of non-Schmid stresses
k_{mul}, k_{cs}, k_{dyn}, R_c, β_ρ	3.45×10^{-2}, 0, 2.75×10^2, $5b$, 7.40×10^{-2}	Dislocation evolution parameters

6.6   Results and discussion

6.6.1   Orientation-dependent stress-strain curves at 298 K

Three-dimensional (3D) finite element simulations were performed using the finite element program ABAQUS [91]. Periodic boundary conditions were enforced in all directions on a cubic simulation cell of size 100 μm on each side. The material was loaded in uniaxial tension using displacement-controlled boundary conditions at a strain rate of 10^{-4} s^{-1} (unless specified otherwise), with net traction free sides. The constitutive equations were implemented using the user material subroutine (UMAT) in ABAQUS.

The constitutive model was fit to the experimental initial hardening response (up to ≈ 5% strain) of single crystal Fe loaded in three different orientations, [0 0 1], [0 1 1] and [$\bar{1}$ 1 1], at 298 K. Figure 41 compares the simulated stress-strain curves with the experimental data [4,240]. A reasonable fit was obtained for the stress-strain response in all three orientations. However, the simulated yield stress for the [$\bar{1}$ 1 1] orientation differed slightly from the experimental value. Note that the non-Schmid parameters were calculated from a different set of experiments [1,253]. Small differences in material composition might have resulted in different values of yield stress. For example, it has been shown [261] that ppm level carbon concentration difference can result in non-negligible difference in the yield stress of Fe single crystals, especially at low temperatures. If the experimental data from Ref. [4] were used for calculating the non-Schmid parameters, $a_1^{298K} = 0.0363$, $a_2^{298K} = -0.0333$, $a_3^{298K} = 0.1417$, and $\tau_{cr}^{298K} = 17.87$ MPa. Due to the lack of systematic data regarding the variation of orientation-dependent yield stress with temperature in Ref. [4], these experimental results

187

were not used to develop the constitutive equations for non-Schmid parameters. Nevertheless, the overall stress-strain response of the simulated material is in qualitative agreement with experiments.
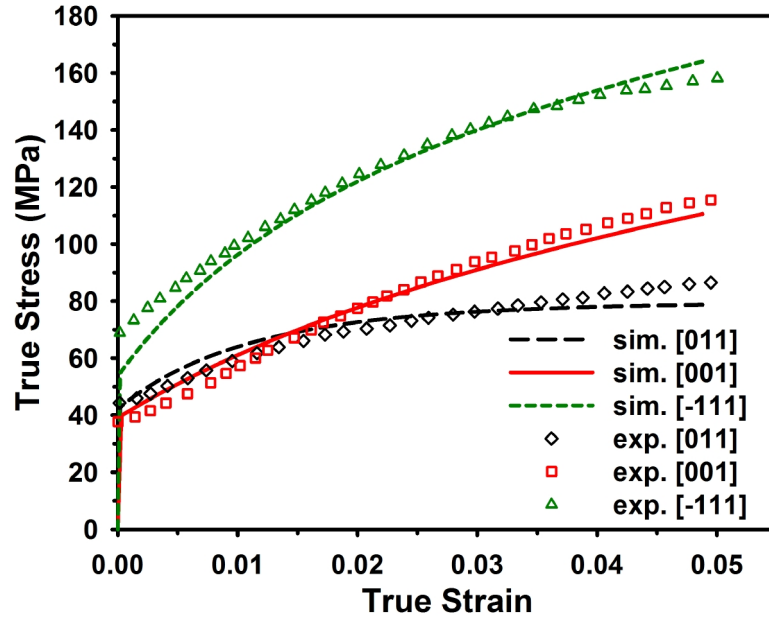
Figure 41. Comparison of simulations (solid and dotted lines) calibrated to the experimental stress-strain curves (open symbols) for three different orientations at $298\,\mathrm{K}$**. Experimental data from [4].**

Figure 42 shows the evolution of average mobile and immobile dislocation density as a function of strain for the three loading orientations. These dislocation densities are averaged over all slip systems. While the dislocation densities (both mobile and immobile) saturate for the [0 1 1] loading case, this is not the case for [0 0 1] and [$\bar{1}$ 1 1] loading. The hardening behavior in the stress-strain curves in Fig. 41 suggest the same (obstacle hardening is a function of dislocation density). Further, the mobile dislocation density for the [0 0 1] and [$\bar{1}$ 1 1] loading cases increases asymptotically.

This dislocation evolution behavior is qualitatively similar to that seen in experiments [4]; the nature of dislocation evolution, asymptotic or saturating, is a function of the loading orientation and active slip systems.
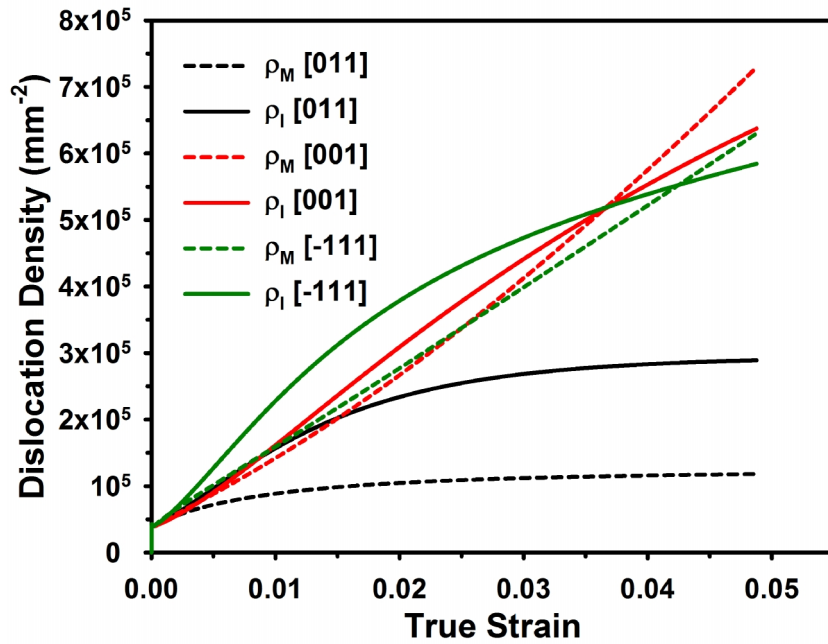
Figure 42. Evolution of average dislocation density as a function of strain for different loading orientations.

6.6.2 Temperature-dependent yield stress

The constitutive equations were used to predict the yield stress of single crystal Fe for various temperatures and loading orientations. The model predictions were compared to the experimental data [1] for the material loaded in $[1\,1\,16]$, $[\bar{1}\,3\,7]$, and $[\bar{4}\,9\,9]$ orientations at 143 K, 195 K, 250 K, and 295 K. Figure 43 compares the 0.2% yield stress measured from simulations to the corresponding experimental data as a function of angle, χ, which the MRSSP makes with the reference (110) slip plane. Angles, $\chi = -30°$,

$\chi = 0°$, and $\chi = 30°$, in Ref. [1] roughly correspond to the $[1\ 1\ 16]$, $[\overline{1}\ 3\ 7]$, and $[\overline{4}\ 9\ 9]$ loading orientations, respectively. Except for the $[\overline{4}\ 9\ 9]$ loading, the predicted orientation-dependent yield behavior was fairly accurate at all temperatures. The yield stress for $[\overline{4}\ 9\ 9]$ orientation was over-predicted at all temperatures. As mentioned earlier in Section 6.3, the experimental yield stress for this orientation, $\chi = 30°$, was not used to estimate the non-Schmid coefficients; a higher order stress term may be necessary to capture the yield behavior for this orientation. Generally, this orientation is also excluded in estimation of non-Schmid parameters from atomistic simulations (cf. [232]).
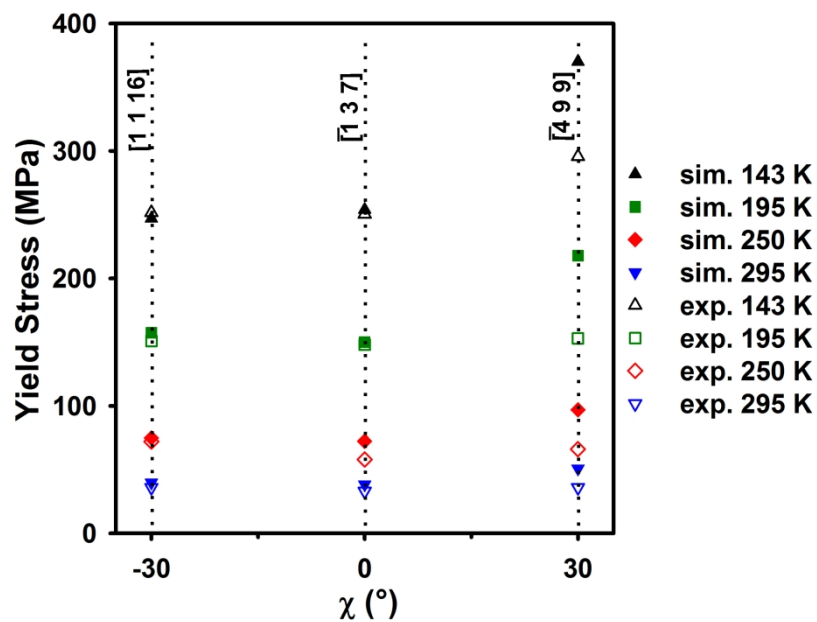
Figure 43. Comparison of yield stress measured from simulations (closed symbols) with experiments (open symbols) for different loading orientations and temperatures.

The yield stress, in the present case, is a function of the non-Schmid stresses, as well as the lattice frictional and obstacle resistances. Of these, the non-Schmid stresses

are orientation and temperature dependent (Eqs. (6.4)-(6.6)), while the lattice frictional resistance is assumed to depend only on temperature (Eq. (6.17)). Temperature dependence of the obstacle resistance was ignored in the present work; the simulated hardening response was, in many cases, not in agreement with the experimental hardening response at lower temperatures. Moreover, the hardening response was calibrated using a different set of experiments [4] at 298 K. The simulated hardening may not be expected to fit the experimental results from Ref. [1] at lower temperatures.

A ratio of the total resolved stress, including non-Schmid terms, to the Schmid stress (on slip system β with the highest Schmid factor) given as

$$R_{ns}^T = \frac{\boldsymbol{m}^\beta \cdot \boldsymbol{\sigma} \cdot \boldsymbol{n}^\beta + a_1^T \boldsymbol{m}^\beta \cdot \boldsymbol{\sigma} \cdot \boldsymbol{n}_{ns}^\beta + a_2^T \left(\boldsymbol{n}^\beta \times \boldsymbol{m}^\beta \right) \cdot \boldsymbol{\sigma} \cdot \boldsymbol{n}^\beta + a_3^T \left(\boldsymbol{n}_{ns}^\beta \times \boldsymbol{m}^\beta \right) \cdot \boldsymbol{\sigma} \cdot \boldsymbol{n}_{ns}^\beta}{\boldsymbol{m}^\beta \cdot \boldsymbol{\sigma} \cdot \boldsymbol{n}^\beta} \quad (6.18)$$

This ratio may be used for estimating the deviation from 'conventional' Schmid behavior at temperature T. Ratio R_{ns}^T is plotted for different temperatures in the standard stereographic triangle in Figs. 44(a)-(d). These values are calculated at the point of initial yield. The corresponding Schmid factor is plotted in Fig. 44(e). The deviation from Schmid behavior increases with decrease in temperature. The value of R_{ns}^T, although relatively lower, is slightly greater than unity at 250 K and 295 K. This suggests that non-Schmid effects are non-negligible at room temperature. Furthermore, R_{ns}^T is higher for crystallographic orientations between the [0 0 1] and [$\bar{1}$ 1 1] poles in the stereographic triangle. As one approaches the [0 1 1] pole, R_{ns}^T decreases gradually to unity at all temperatures.
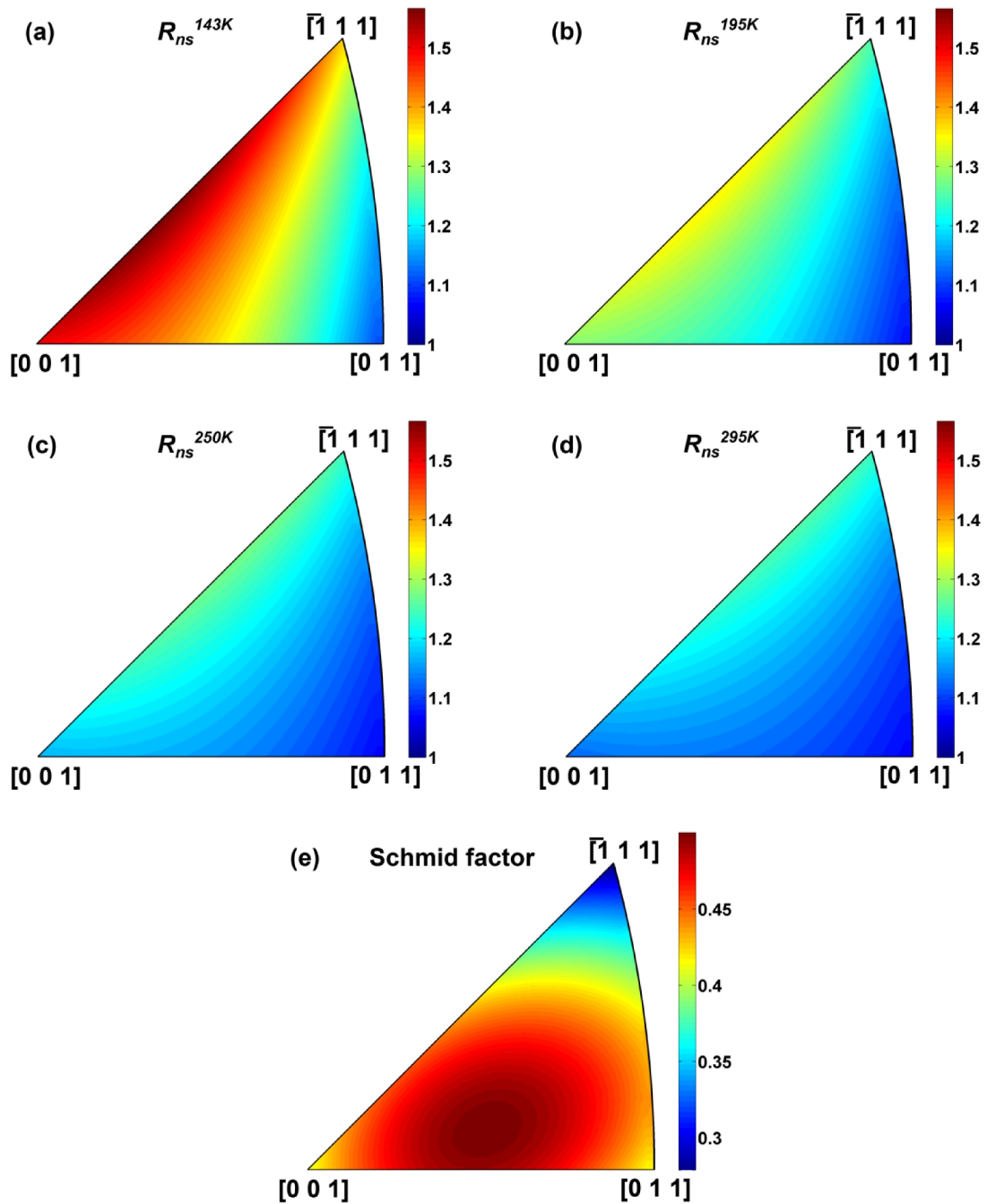
Figure 44. R_{ns}^{T} **for uniaxial tension plotted in the standard stereographic triangle at (a):** $143\,\text{K}$**, (b):** $195\,\text{K}$**, (c):** $250\,\text{K}$**, and (d):** $295\,\text{K}$**. (e): Schmid factor for bcc metals.**

6.6.3 Parametric study of ε_0^i

The effect of ε_0^i on the mechanical response of the specimen loaded in [1 1 16] orientation was explored at 195 K. The stress-strain response without non-Schmid effects, i.e., associative flow was also simulated. Figure 45 shows the stress-strain curves for all these cases compared to the experimental data. The 'associative' legend represents no non-Schmid effects/associative flow, and the open symbols show the experimental stress-strain curve from Ref. [1] for [1 1 16] loading at 195 K.

As ε_0^i is increased from 0.005 to 0.05, the initial flow stress decreases monotonically. The initial flow stress of the associative flow case is higher than those with non-Schmid stresses. Note that relaxation of the stress-strain response to a quasi-equilibrium state is observed at higher applied strains; this is more prominent for the material with lower ε_0^i. It might seem counter-intuitive that the material with higher non-Schmid stresses has a lower initial flow stress. Note that for glide to occur, the driving stress, τ_f^α, must overcome the lattice frictional and obstacle resistance. τ_f^α has contributions from the resolved shear stress, τ^α, and the non-Schmid stresses (both components of the macroscopic stress state). When non-Schmid stresses are present, they complement τ^α in overcoming the lattice resistance. However, for the case of associative flow, τ^α must have a higher relative contribution to τ_f^α; τ^α, and hence the macroscopic stress, has to increase to overcome the lattice resistance initially.
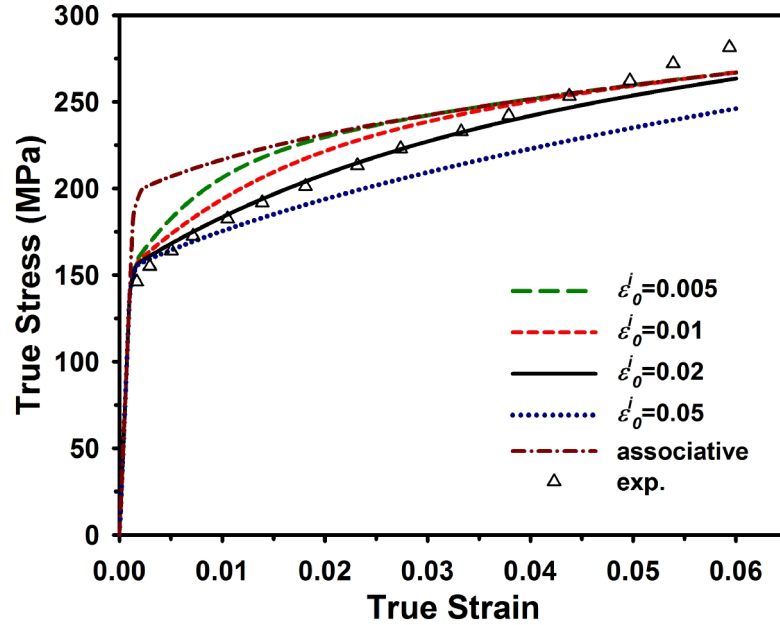
Figure 45. Parametric effect of ε_0^i **on the true stress-strain response of the material loaded in** $[1\,1\,16]$ **orientation at** $195\,\text{K}$ **compared to the associative flow behavior. Open symbols show the corresponding experimental data from [1].**

Comparison to experiments [1] shows that the material with $\varepsilon_0^i = 0.02$ best fits the experimental stress-strain data, all other parameters remaining unchanged. Accordingly, we have used $\varepsilon_0^i = 0.02$ in all our simulations. Systematic experiments, for example, uniaxial loading of single crystals with different levels of pre-strain, may be used to obtain a better estimate of this parameter (higher pre-strain would relate to lower contribution of non-Schmid effects).

6.6.4   Tension-compression asymmetry

The constitutive model was used to predict the tension-compression (TC) asymmetry of single crystal Fe loaded in different orientations. This asymmetry measured in terms of the strength differential, SD, is given by [125]

$$SD = \frac{\left(\sigma_Y^t - \sigma_Y^c\right)}{\left(\sigma_Y^t + \sigma_Y^c\right)/2} \qquad (6.19)$$

where σ_Y^t is the yield stress in tension, and σ_Y^c is the yield stress in compression. The yield stress measured at 0.2% strain was used in these calculations. Figure 46 shows the variation of SD with temperature for various loading orientations. A negative value of SD indicates higher yield stress in compression.

As can be seen, the tension-compression asymmetry is highly orientation and temperature dependent. Loading orientations [0 0 1] and [1 1 16] are stereographically close by, hence the overlap in their TC asymmetry behavior, especially at 250 K and 295 K. A qualitatively similar, but higher, degree of TC asymmetry is also seen for the [$\bar{1}$ 1 1] orientation. The yield stress is generally higher in compression, except for the [0 1 1] orientation at 143 K. Similar predictions were also made for the TC asymmetry of single crystal Mo in Ref. [243] using a constitutive model with non-Schmid considerations. Also note that the TC asymmetry is generally lower at 250 K and 295 K, though not zero. This again shows that TC asymmetry due to the non-Schmid effects is still present at room temperature.

This asymmetry arises from activation of different slip systems in tension and compression. A comparison of the possible activated slip systems in tension versus compression is given in Ref. [242] for different loading orientations. There is no

systematic experimental data available to compare to our model predictions. However, experiments [262,263] have shown that tension-compression asymmetry is indeed prevalent in similar Fe-Si alloys.
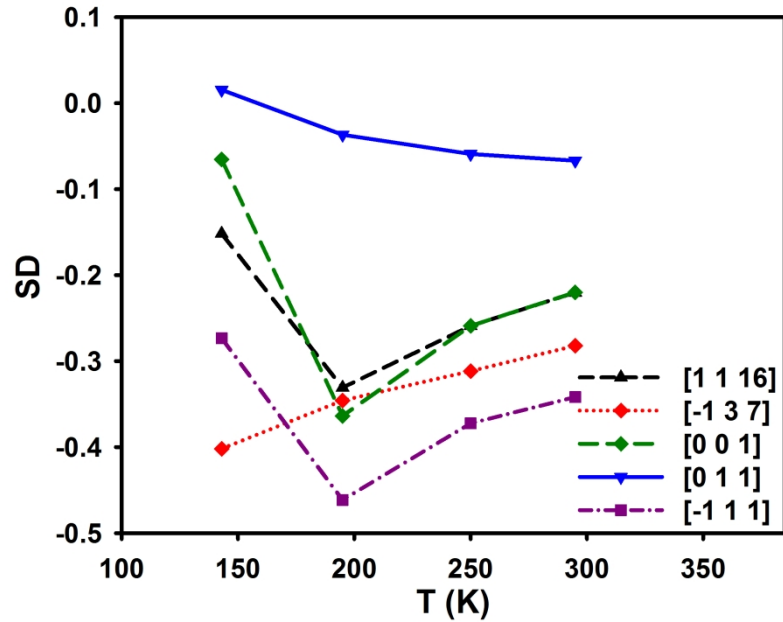
Figure 46. Variation of the strength differential, *SD*, with temperature for different loading orientations.

6.6.5   Strain rate dependence

The model was used to simulate the strain rate dependence of single crystal Fe loaded in the [0 0 1] orientation at 298 K by applying strain rates in the range 10^{-4} to 10^{0} s^{-1}, with the resulting stress-strain responses shown in Fig. 47(a). As expected, the flow stress increases at higher strain rates. Figure 47(b) plots the ratio of yield stress measured at a given strain rate to the corresponding yield stress at 10^{-4} s^{-1} for different loading rates. Simulation results of single crystal Fe at 298 K are compared with

experimental data for polycrystalline Fe [5]; a test temperature of 288 K was used in the experiments. Although a one-to-one correspondence may not be expected, the simulated increase in yield stress with applied strain rate is in general agreement with experiments, at least up to a strain rate of 10^{-1} s^{-1}. Beyond this, the simulations have slightly higher rate sensitivity than the experiments. Note that the experimental yield stress reported here is for polycrystalline Fe. The pre-exponential factor, $\dot{\gamma}_0$, may be used to calibrate the strain rate dependence in terms of the yield and flow stress. In the present simulations, $\dot{\gamma}_0 = 5.0 \times 10^4$ s^{-1} was used. A higher value of $\dot{\gamma}_0$ would result in lower yield and flow stress.
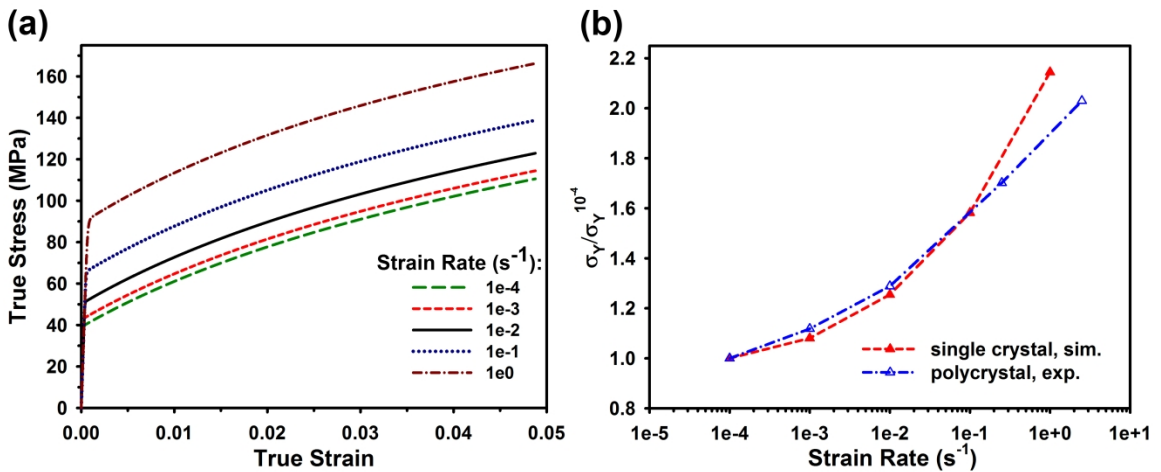
Figure 47. (a): Simulated strain rate sensitivity of single crystal Fe loaded in the [0 0 1] orientation at 298 K. (b): Comparison of simulated 0.2% yield stress of single crystal Fe with experimentally measured lower yield stress of polycrystal Fe as a function of strain rate. Experimental data from [5].

6.6.6 Implications for radiation damage

The models discussed in this Chapter have not addressed any issues relating to radiation damage at low temperatures so far. This is in part due to the complicated nature of non-Schmid effects by itself, and also due to the lack of relevant experimental data for single crystal Fe to compare our model predictions. Moreover, delineating the irradiation effects from the non-Schmid effects presents an added challenge. While irradiation hardening and flow localization due interactions of dislocations with interstitial loops may be modeled using the constitutive equations developed in Chapters 2 and 3, interaction of dislocations with the irradiation-induced point defects is expected to affect their mobility and the unit processes of dislocation kink pair formation.

Dr. Ting Zhu and Sankar Narayanan at Georgia Tech are presently studying these interactions and their effect on the deformation mechanism using atomistic simulations. Based on personal communication, the following summarizes some of their recent findings. While the far-field dislocation-interstitial interaction is still governed by the elastic strain field of these defects, screw dislocation migration is controlled by cross-kink nucleation on secondary slip planes (as opposed to double kink nucleation) once the interstitial approaches the screw dislocation core. Further, the spatial orientation of interstitials around the dislocation core also affects the Peierls stress for dislocation kink nucleation. These effects would manifest themselves in a modified form of the enthalpy shape function for screw dislocation mobility in Eq. (6.8).

While the above mentioned studies are for the unit process of kink-pair formation, we expect that the presence of a distribution of interstitials around a screw dislocation core would further hinder its glide by preventing core constriction on secondary slip

planes. From a statistical viewpoint, these effects may be accounted in the present framework by modeling the non-Schmid coefficients as a function of the mean field interstitial concentration, i.e.,

$$a_j^T = a_j^T\big|_0 + f_j(c_i) \qquad (6.20)$$

where a_j^T is the jth non-Schmid coefficient, $a_j^T\big|_0$ is the value of the corresponding non-Schmid coefficient in the absence of any irradiation (as modeled in the present simulations), and $f_j(c_i)$ is the functional dependence of the non-Schmid coefficient on the interstitial concentration, c_i, around the dislocation core. This last term needs to be determined from relevant atomistic calculations.

6.7   Summary

Constitutive equations have been developed for modeling orientation dependence and tension-compression asymmetry of single crystal bcc-Fe at low and ambient temperatures by attributing these effects to non-Schmid stresses that have been shown in previous 2D atomistic simulations to correlate with screw dislocation core spreading. Constitutive equations are also introduced for the decay of the non-Schmid contribution to the yield stress as a function of inelastic strain. These non-Schmid contributions are coupled with an existing dislocation density crystal plasticity framework to simulate the mechanical behavior of single crystal Fe. The model is fit to the experimental hardening response at 298 K. The yield stress and tension-compression asymmetry for different loading orientations and temperatures is also modeled. Model predictions are compared to available experimental data, including strain rate dependence of flow stress.

Temperature dependence of the non-Schmid parameters has not been previously examined. Furthermore, previous continuum constitutive models generally use the non-Schmid parameters measured from atomistic simulations at 0 K. This might not be physically accurate, as experiments suggest that the non-Schmid effects decay with increase in temperature. In this work, the non-Schmid parameters and their temperature dependence are inferred entirely from available experimental data for Fe. The methodology adopted in this work may also be used to estimate the temperature dependence of non-Schmid parameters for other bcc metals, such as Mo and Ta.

This work demonstrates a top-down approach to crystal plasticity modeling of temperature-dependent non-Schmid yield behavior in bcc metals. While a bottom-up approach employing atomistics (for example, [245]) may be more physically based with regard to dislocation line level processes involved in kink-pair formation, these models are presently of largely qualitative character. They predict significantly higher Peierls stress values than seen in experiments and do not account for many body defect interactions. The top-down approach taken here can be used to model mesoscopic (polycrystal) and macroscopic deformation behavior in applications.

It will clearly take more time and effort to rectify and fully understand the applicability of the kind of non-Schmid type formulation of crystal plasticity pursued here relative to approaches that consider in more detail the processes of kink pair formation at lower stress levels and finite temperatures typically of thermally activated flow in bcc crystals. The latter approaches do not resort to the core spreading argument and associated non-Schmid stress effects in Eq. (6.2) (i.e., $a_1 = a_2 = a_3 = 0$) [246]. However, tension-compression asymmetry is a challenge to be resolved in models that do

not incorporate non-Schmid stresses. Ultimately, it is likely necessary to rectify and adopt combined bottom-up and top-down modeling approaches to address the complexity of screw/edge dislocation activities in bcc crystals to make connections between the length scale hierarchy of atomistics, discrete dislocation dynamics, and crystal plasticity.

CHAPTER 7

SUMMARY AND CONCLUSIONS

7.1 Summary and novel contributions

7.1.1 Constitutive model development

A continuum crystal plasticity framework has been developed for modeling the mechanical behavior of irradiated bcc materials. The framework models the deformation behavior over a range of loading and radiation histories. Climb enhanced glide of dislocations is the principal inelastic deformation mechanism in this crystal plasticity framework. While the conventional glide component of deformation dominates during quasi-static loading, dislocation climb by stress-induced preferential absorption (SIPA) is more prevalent during creep loading of the irradiated materials.

A continuum damage framework has also been developed to model failure initiation at the interfaces of dislocation channels and grain boundaries (GBs) in irradiated bcc materials. Void nucleation and growth by condensation of supersaturated vacancies (generated during inelastic deformation) is the main failure mechanism in this damage framework.

Dislocation densities (mobile and immobile), size and number density of the irradiation-induced interstitial loops, and point defect concentrations are used as state variables in this crystal plasticity framework. The damage framework also uses the number density and size of voids as state variables, in addition to those used in the crystal plasticity framework.

Physically-based constitutive equations have been developed to model the evolution of these state variables by creation, exchange, interaction, and annihilation type mechanisms. Rate theory based equations for the evolution of point defects have also been integrated in this crystal plasticity framework. This is a unique feature of the present framework and has not been done previously. Rate theory calculations are usually performed for mean field material points and have not been correlated to the mechanical behavior previously. Radiation damage in metals is generally manifested in terms of point defect generation and their subsequent evolution. Correlation of the spatial point defect evolution to the deformation behavior is therefore fundamental to modeling radiation damage, more so in the case of irradiation creep. While irradiation hardening and subsequent flow localization can be modeled by simply considering the interstitial loops (in bcc metals), modeling irradiation creep requires consideration for the radiation-induced point defects, as well. Consideration of point defects also allows us to model void nucleation and growth by condensation of supersaturated vacancies generated during inelastic deformation.

In addition to modifying some of the existing models available in the literature, constitutive equations for the following physical mechanisms have been developed in this work:

- Inelastic deformation by climb enhanced glide of dislocations.
- Climb of mobile edge dislocations by absorbing point defect clusters and their transformation to interstitial loops.
- Growth of planar interstitial loops by absorbing point defects.
- Cross-slip of mobile screw dislocations.

- Annihilation of interstitial loops when they are within a critical capture radius of the interacting mobile dislocations, thus clearing pathways for easy dislocation glide.

- Temperature dependence of non-Schmid yield behavior.

- Decay of non-Schmid stresses with inelastic deformation.

- Diffusion-mediated growth of voids in a supersaturated field of vacancies under tensile hydrostatic stresses.

Integration of these models in the crystal plasticity framework not only provides a more physically-based representation of the deformation behavior, but also allows us to delineate the effect of each of these separate mechanisms on the overall macroscopic mechanical response and microstructure evolution. Parametric study of these models also offers guidance for tailoring properties for the design of 'radiation-resistant' materials.

7.1.2   Model application

The framework has been used to model the following major features of inelastic deformation in irradiated bcc materials:

- Increase in yield stress due irradiation hardening and the initial dislocation evolution due to interaction with irradiation-induced defects.

- Flow localization along narrow dislocation channels due to annihilation of irradiation-induced interstitial loops by the interacting mobile dislocations.

- Failure initiation at the interfaces of these dislocation channels and GBs by void nucleation and growth processes.

- Irradiation creep deformation by dislocation climb enhanced glide.

- Temperature-dependent non-Schmid yield behavior in bcc metals.

Prior to this work, there existed several constitutive crystal plasticity frameworks [12–15] to model the mechanical behavior of irradiated polycrystals. A distinct feature of our framework in comparison to these previous works is that we have explicitly modeled irradiation creep; none of these existing frameworks consider irradiation creep deformation. Moreover, microstructure evolution due to dislocation channel formation is not addressed explicitly in most of these frameworks. In contrast, we have modeled both the deformed microstructure evolution and the resulting mechanical behavior due to dislocation channel formation; correlating the deformed microstructure with the mechanical properties is essential to understanding the mechanics of these deformation processes.

Another novel contribution of this research is the void nucleation and growth based damage framework. While this framework was applied to model failure initiation at the dislocation channel interfaces in irradiated metals, the underlying physics of the framework is general enough for modeling void nucleation and growth mediated failure in virgin metals, as well.

Finally, constitutive modeling of the temperature dependence of non-Schmid stresses is another novel contribution of this research. While atomistically informed constitutive frameworks for modeling non-Schmid effects were developed previously (e.g. [233,242]), temperature dependence of the non-Schmid stresses was never studied systematically. Relevant findings of the present research pose the necessity for exploring these temperature effects in other bcc metals as well, in order to develop physically accurate constitutive models.

The constitutive crystal plasticity framework described in Chapter 2 has been published in Ref. [16]. Major findings of Chapter 3 relating to flow localization and dislocation channel formation have been published in Ref. [17]. The void nucleation and growth based damage framework used to model failure initiation in the regions of stress concentration in Chapter 4 has been submitted for publication [18]. Significant parts of Chapter 6 relating to the top-down modeling of temperature-dependent non-Schmid effects in bcc-Fe have also been submitted for publication [19].

This coarse-grained constitutive framework is suited for modeling the mechanical behavior at the meso- and macroscales, while addressing the physics of the underlying deformation phenomena. Atomistic and dislocation dynamics simulations are indeed essential for understanding the defect evolution unit processes, but they are unfeasible for simulating polycrystalline ensembles at the scale of microns and over large timescales. Using information (of the physical deformation mechanisms) gained from these lower scale simulations, the present continuum framework may be used to model their effect on the macroscopic mechanical properties and microstructural evolution.

A shortcoming of this body of work is neglect of the non-local character of transport relations for point defects (Eqs. (5.3)-(5.4)), as well as non-local relations for dislocation-interstitial loop interactions. Such relations are necessary to achieve FE mesh insensitive results. As a consequence of the local approximation, the mesh sizes used here must be regarded as the assigned material length scales for localization.

7.2   Conclusions

Based on application of the constitutive framework to model different loading conditions, the following major conclusions are drawn from the present research:

Flow localization along dislocation channels

- The constitutive framework is able to qualitatively capture the microstructural and mechanical aspects of inelastic flow localization due to dislocation channel formation in irradiated bcc materials.

- Flow localization in our simulations is a result of 'constitutive' material softening effects due to interstitial loop annihilation along preferred crystallographic planes, triggered by intergranular heterogeneity.

- Cross-slip promotes the formation of wider and more diffuse dislocation channels.

- Maximum localized inelastic strain in the channels is a linear function of the radiation dpa dose for the same initial crystallographic orientation distribution of grains.

- There are two dominant length scales governing the localization phenomena. The dislocation channel width is governed by the greater of the mean free path of mobile dislocations, l_d, and the mesh size, while the dislocation channel spacing is governed by the grain size.

Failure initiation along dislocation channel interfaces and GBs ahead of a notch

- The density of dislocation channels is much higher in the vicinity of a notch, as compared to the homogeneously deformed bulk.

- The void nucleation and growth based damage framework is able to model ductile 'zigzag' fracture and limited ductility 'channel' fracture in irradiated metals at elevated temperatures.

- Failure initiation is strongly sensitive to the interfacial energy change, $\Delta \Upsilon_{het}$, associated with heterogeneous void nucleation at the dislocation channel interfaces and GBs. This parameter may be used for calibrating our model predictions to experiments.

- The crack growth resistance of irradiated specimens is lower than that of the virgin specimens.

- The extent of localization and failure initiation is inhibited at higher strain rates.

Irradiation creep deformation

- Dislocation climb by stress-induced preferential absorption (SIPA) and subsequent dislocation glide is the primary irradiation creep mechanism in our framework. Using this mechanism, model predictions of creep rates and irradiation creep compliance are of the same order of magnitude as in experiments.

- The interstitial loop density was found to increase monotonically with ongoing radiation, while mean the loop size saturates following the initial transients.

- The in-situ radiation rate was measured in terms of $dpa \cdot s^{-1}$ using a phenomenological relationship that correlates the interstitial loop density with the radiation dpa damage. Using this correlation, the measured dpa rate was found to increase linearly with time. This asserts that the present framework is modeling

trends of irradiation creep qualitatively, as linear dpa rate is expected for a constant defect pair production rate.

- The creep strain rate decreases with decreasing grain size and higher GB sink strengths. This is because point defect sinks inhibit the inelastic deformation near GBs. Decrease in irradiation creep rate with decreasing grain size was also observed in experiments during in-reactor stress relaxation of Zr alloys [223,224].

Non-Schmid yield behavior of bcc-iron at low and ambient temperatures

- A top-down approach is used for modeling the temperature dependence of non-Schmid effects in bcc-Fe, using data entirely from experiments.

- Using the atomistically measured 0 K non-Schmid coefficients for modeling the mechanical behavior of bcc metals at finite temperatures is physically inaccurate.

- The contribution of non-Schmid stresses required to constrict the screw dislocation cores (for them to glide) decreases with increasing temperature and increasing inelastic deformation.

- Based on fit to experiments, the decay of non-Schmid coefficients with respect to temperature starts saturating at ~ 250 K in bcc-iron.

- Non-Schmid yield behavior and resulting tension-compression asymmetry though reduced, is still non-negligible at room temperatures in bcc-iron. At room temperature, the contribution of non-Schmid stresses to the critical resolved shear stress, τ_{cr}^{T}, is less than 7% of the total τ_{cr}^{T}.

7.3   Recommendations for future work

As with any model development, we have made numerous assumptions to simplify the constitutive equations and their numerical implementation. Most importantly, we have assumed a local material in all the model applications demonstrated in this research. This framework may be updated in future work to consider the non-local nature of dislocation-interstitial loop interactions by incorporating higher order gradient terms (of inelastic strain/dislocation density) in the evolution of flow stress. The work of Aifantis and co-authors [146–151] may be used as a starting point for this non-local approach. A non-local model would regularize the width of localized dislocation channels according to an intrinsic material length scale (as opposed to a mesh size-dependent channel width). Further, point defect spatial diffusion may be present at the timescales of irradiation creep deformation, as well. Point defect gradients are also expected to be non-negligible during slow strain rate in-reactor tension tests with concurrent irradiation. These defect gradients may be modeled in future work using the constitutive equations (5.3) and (5.4). In terms of numerical implementation, continuity of the point defect concentrations needs to be considered in a finite element framework in addition to the continuity of displacement. Alternatively, a numerical scheme may be developed where the point defect concentrations are mapped using a separate finite difference mesh, thus decoupling mechanical deformation and point defect diffusion.

As mentioned above, in-reactor tension tests (concurrent irradiation and deformation) may be simulated using this model framework in future work. This would be particularly interesting for exploring the effect of radiation dose on the dislocation channel formation behavior; Arsenlis et al. [47] showed that a threshold radiation dose

exists below which channel formation does not take place. It would also be informative to perform combined loading simulations, e.g., in-reactor tensile loading followed by stress hold and study its effect on the irradiation creep rates.

While the framework has been applied to model different deformation histories, detailed parametric exploration (within the window of physical feasibility) of the various constitutive models has not been performed in the present research. This should be addressed in future work in order to quantify the individual effect of each of these models on the measured mechanical properties and/or microstructural evolution characteristics, and the associated uncertainties.

Finally, validation of the constitutive models with relevant experiments, atomistic simulations, theoretical calculations, etc. is fundamental for the applicability of this framework to practical engineering problems. For example, the interfacial energy change parameter, $\Delta\Upsilon_{het}$, associated with heterogeneous void nucleation may be estimated from atomistic simulations of the nucleation of voids at interfaces performed for different stress triaxialities and temperatures. This parameter would affect the accurate measurement of fracture toughness in our simulations. As another example, the material constant associated with the decay of non-Schmid stresses as a function of inelastic strain (in Eq. (6.14)) may be estimated by pre-straining iron single crystals and studying its effect on the yield stress and flow stress at different temperatures. The presence of interstitials near the screw dislocation core is also expected to affect the non-Schmid yield behavior. Relevant atomistic studies may be performed to determine the functional dependence of non-Schmid coefficients on the interstitial concentration (cf. Eq. (6.20)) in future work.

REFERENCES

[1]　W.A. Spitzig, A.S. Keh, Orientation and temperature dependence of slip in iron single crystals, Metall. Trans. 1 (1970) 2751–2757.

[2]　S.A. Maloy, M.R. James, G. Willcutt, W.F. Sommer, M. Sokolov, L.L. Snead, et al., The mechanical properties of 316L/304L stainless steels, Alloy 718 and Mod 9Cr-1Mo after irradiation in a spallation environment, J. Nucl. Mater. 296 (2001) 119–128.

[3]　X. Jia, Y. Dai, The change of fracture toughness of martensitic steels after irradiation in SINQ target-3, J. Nucl. Mater. 356 (2006) 50–55.

[4]　A.S. Keh, Work hardening and deformation sub-structure in iron single crystals deformed in tension at 298°k, Philos. Mag. 12 (1965) 9–30.

[5]　J. Harding, The effect of grain size and strain rate on the lower yield stress of pure iron at 288°K, Acta Metall. 17 (1969) 949–958.

[6]　G.S. Was, Fundamentals of Radiation Material Science: Metals and Alloys, Springer, Berlin, 2007.

[7]　S.J. Zinkle, G.E. Lucas, Deformation and fracture mechanisms in irradiated FCC and BCC metals, Fusion Mater. Semi-Annu. Prog. Rep. Period End. June 30 2003 DOEER-031334 Oak Ridge Natl. Lab. (2003) 101–125.

[8]　S.J. Zinkle, G.S. Was, Materials challenges in nuclear energy, Acta Mater. 61 (2013) 735–758.

[9]　F.. Garner, M.. Toloczko, B.. Sencer, Comparison of swelling and irradiation creep behavior of fcc-austenitic and bcc-ferritic/martensitic alloys at high neutron exposure, J. Nucl. Mater. 276 (2000) 123–142.

[10]　L.K. Mansur, A.F. Rowcliffe, R.K. Nanstad, S.J. Zinkle, W.R. Corwin, R.E. Stoller, Materials needs for fusion, Generation IV fission reactors and spallation neutron sources - similarities and differences, J. Nucl. Mater. 329-333 (2004) 166–172.

[11]　O. Anderoglu, T.S. Byun, M. Toloczko, S.A. Maloy, Mechanical Performance of Ferritic Martensitic Steels for High Dose Applications in Advanced Nuclear Reactors, Metall. Mater. Trans. A. 44 (2013) 70–83.

[12]　A. Arsenlis, B.D. Wirth, M. Rhee, Dislocation density-based constitutive model for the mechanical behaviour of irradiated Cu, Philos. Mag. 84 (2004) 3617–3635.

[13] S. Krishna, A. Zamiri, S. De, Dislocation and defect density-based micromechanical modeling of the mechanical behavior of fcc metals under neutron irradiation, Philos. Mag. 90 (2010) 4013–4025.

[14] D. Li, H. Zbib, H. Garmestani, X. Sun, M. Khaleel, Modeling of irradiation hardening of polycrystalline materials, Comput. Mater. Sci. 50 (2011) 2496–2501.

[15] N.R. Barton, A. Arsenlis, J. Marian, A polycrystal plasticity model of strain localization in irradiated iron, J. Mech. Phys. Solids. 61 (2013) 341–351.

[16] A. Patra, D.L. McDowell, Crystal plasticity-based constitutive modelling of irradiated bcc structures, Philos. Mag. 92 (2012) 861–887.

[17] A. Patra, D.L. McDowell, Continuum modeling of localized deformation in irradiated bcc materials, J. Nucl. Mater. 432 (2013) 414–427.

[18] A. Patra, D.L. McDowell, A void nucleation and growth based damage framework to model failure initiation ahead of a sharp notch in irradiated bcc materials, under review (2013).

[19] A. Patra, T. Zhu, D.L. McDowell, Constitutive equations for modeling non-Schmid effects in single crystal bcc-Fe at low and ambient temperatures, under review (2013).

[20] G.R. Odette, B.D. Wirth, D.J. Bacon, N.M. Ghoniem, Multiscale-multiphysics modeling of radiation-damaged materials: embrittlement of pressure-vessel steels, MRS Bull. 26 (2001) 176–181.

[21] G.R. Odette, G.E. Lucas, Embrittlement of nuclear reactor pressure vessels, JOM J. Miner. Met. Mater. Soc. 53 (2001) 18–22.

[22] B.D. Wirth, G.R. Odette, D. Maroudas, G.E. Lucas, Energetics of formation and migration of self-interstitials and self-interstitial clusters in [alpha]-iron, J. Nucl. Mater. 244 (1997) 185–194.

[23] J. Marian, B.D. Wirth, J.M. Perlado, Mechanism of formation and growth of <100> interstitial loops in ferritic materials, Phys. Rev. Lett. 88 (2002) 255507.

[24] B.D. Wirth, G.R. Odette, D. Maroudas, G.E. Lucas, Dislocation loop structure, energy and mobility of self-interstitial atom clusters in bcc iron, J. Nucl. Mater. 276 (2000) 33–40.

[25] T. Diaz de la Rubia, H.M. Zbib, T.A. Khraishi, B.D. Wirth, M. Victoria, M.J. Caturla, Multiscale modelling of plastic flow localization in irradiated materials, Nature. 406 (2000) 871–874.

[26] B.D. Wirth, V. Bulatov, T. Diaz de la Rubia, Atomistic simulation of stacking fault tetrahedra formation in Cu, J. Nucl. Mater. 283-287 (2000) 773–777.

213

[27] S.J. Zinkle, Y. Matsukawa, Observation and analysis of defect cluster production and interactions with dislocations, J. Nucl. Mater. 329-333 (2004) 88–96.

[28] S.J. Zinkle, P.J. Maziasz, R.E. Stoller, Dose dependence of the microstructural evolution in neutron-irradiated austenitic stainless steel, J. Nucl. Mater. 206 (1993) 266–286.

[29] M.I. Luppo, C. Bailat, R. Schäublin, M. Victoria, Tensile properties and microstructure of 590 MeV proton-irradiated pure Fe and a Fe-Cr alloy, J. Nucl. Mater. 283-287 (2000) 483–487.

[30] N.M. Ghoniem, G.L. Kulcinski, The effect of pulsed irradiation on the swelling of 316 stainless steel in fusion reactors, Nucl. Eng. Des. 52 (1979) 111–125.

[31] L.K. Mansur, T.C. Reiley, Irradiation creep by dislocation glide enabled by preferred absorption of point defects -- theory and experiment, J. Nucl. Mater. 90 (1980) 60–67.

[32] H. Rauh, R. Bullough, J.R. Matthews, The dislocation bias during irradiation: Effects of climb motion and rate limitation, Philos. Mag. A. 65 (1992) 53–70.

[33] H.J. Frost, M.F. Ashby, Deformation-Mechanism Maps, Permagon Press, Oxford, 1982.

[34] J. Weertman, Theory of steady-state creep based on dislocation climb, J. Appl. Phys. 26 (1955) 1213–1217.

[35] R. Bullough, M.H. Wood, Mechanisms of radiation induced creep and growth, J. Nucl. Mater. 90 (1980) 1–21.

[36] J.R. Matthews, M.W. Finnis, Irradiation creep models -- an overview, J. Nucl. Mater. 159 (1988) 257–285.

[37] A.D. Brailsford, R. Bullough, Irradiation creep due to the growth of interstitial loops, Philos. Mag. 27 (1973) 49.

[38] P.T. Heald, M.V. Speight, Steady-state irradiation creep, Philos. Mag. 29 (1974) 1075–1080.

[39] R. Bullough, J.R. Willis, The stress-induced point defect-dislocation interaction and its relevance to irradiation creep, Philos. Mag. 31 (1975) 855–861.

[40] R. Bullough, M.R. Hayns, Irradiation-creep due to point defect absorption, J. Nucl. Mater. 57 (1975) 348–352.

[41] L.K. Mansur, Irradiation creep by climb-enabled glide of dislocations resulting from preferred absorption of point defects, Philos. Mag. A. 39 (1979) 497–506.

[42]   N.M. Ghoniem, J.R. Matthews, R.J. Amodeo, A dislocation model for creep in engineering materials, Res Mech. 29 (1990) 197–219.

[43]   G.R. Odette, D. Frey, Development of mechanical property correlation methodology for fusion environments, J. Nucl. Mater. 85-86 (1979) 817–822.

[44]   G.E. Lucas, The evolution of mechanical property change in irradiated austenitic stainless steels, J. Nucl. Mater. 206 (1993) 287–305.

[45]   B.N. Singh, A.J.E. Foreman, H. Trinkaus, Radiation hardening revisited: role of intracascade clustering, J. Nucl. Mater. 249 (1997) 103–115.

[46]   N.M. Ghoniem, B.N. Singh, L.Z. Sun, T. Díaz de la Rubia, Interaction and accumulation of glissile defect clusters near dislocations, J. Nucl. Mater. 276 (2000) 166–177.

[47]   A. Arsenlis, M. Rhee, G. Hommes, R. Cook, J. Marian, A dislocation dynamics study of the transition from homogeneous to heterogeneous deformation in irradiated body-centered cubic iron, Acta Mater. 60 (2012) 3748–3757.

[48]   Y. Estrin, L.P. Kubin, Local strain hardening and nonuniformity of plastic deformation, Acta Metall. 34 (1986) 2455–2464.

[49]   R.J. Asaro, J.R. Rice, Strain localization in ductile single crystals, J. Mech. Phys. Solids. 25 (1977) 309–338.

[50]   R.J. Asaro, Micromechanics of crystals and polycrystals, Adv. Appl. Mech. 23 (1983) 1–115.

[51]   M. Kothari, L. Anand, Elasto-viscoplastic constitutive equations for polycrystalline metals: Application to tantalum, J. Mech. Phys. Solids. 46 (1998) 51–67.

[52]   U.F. Kocks, A.S. Argon, M.F. Ashby, Thermodynamics and kinetics of slip, Permagon Press, 1975.

[53]   C. Deo, C. Tomé, R. Lebensohn, S. Maloy, Modeling and simulation of irradiation hardening in structural ferritic steels for advanced nuclear reactors, J. Nucl. Mater. 377 (2008) 136–140.

[54]   D.L. McDowell, Viscoplasticity of heterogeneous metallic materials, Mater. Sci. Eng. R Rep. 62 (2008) 67–123.

[55]   M.S. Duesbery, V. Vitek, D.K. Bowen, The Effect of Shear Stress on the Screw Dislocation Core Structure in Body-Centred Cubic Lattices, Proc. R. Soc. Lond. Math. Phys. Sci. 332 (1973) 85–111.

[56] M.S. Duesbery, On Non-Glide Stresses and Their Influence on the Screw Dislocation Core in Body-Centred Cubic Metals. I. The Peierls Stress, Proc. R. Soc. Lond. Ser. Math. Phys. Sci. 392 (1984) 145–173.

[57] Q. Qin, J.L. Bassani, Non-schmid yield behavior in single crystals, J. Mech. Phys. Solids. 40 (1992) 813–833.

[58] Q. Qin, J.L. Bassani, Non-associated plastic flow in single crystals, J. Mech. Phys. Solids. 40 (1992) 835–862.

[59] V. Racherla, J.L. Bassani, Strain burst phenomena in the necking of a sheet that deforms by non-associated plastic flow, Model. Simul. Mater. Sci. Eng. 15 (2007) S297–S311.

[60] V. Vitek, V. Paidar, Chapter 87 Non-planar dislocation cores: a ubiquitous phenomenon affecting mechanical properties of crystalline materials, in: J.P. Hirth (Ed.), Dislocations Solids Tribute FRN Nabarro, Elsevier, 2008: pp. 439–514.

[61] M. Peach, J.S. Koehler, The Forces Exerted on Dislocations and the Stress Fields Produced by Them, Phys. Rev. 80 (1950) 436.

[62] E. Orowan, Problems of plastic gliding, Proc. Phys. Soc. 52 (1940) 8–22.

[63] R. Sizmann, The effect of radiation upon diffusion in metals, J. Nucl. Mater. 69-70 (1978) 386–412.

[64] A.D. Brailsford, R. Bullough, The rate theory of swelling due to void growth in irradiated metals, J. Nucl. Mater. 44 (1972) 121–135.

[65] R.E. Stoller, G.R. Odette, Microstructural evolution in an austenitic stainless steel fusion reactor first wall, J. Nucl. Mater. 141-143 (1986) 647–653.

[66] R.E. Stoller, Modeling dislocation evolution in irradiated alloys, Metall. Trans. A. 21 (1990) 1829–1837.

[67] A.A. Semenov, C.H. Woo, Stochastic effects on dislocation structure development under cascade-damage irradiation, Appl. Phys. Mater. Sci. Process. 67 (1998) 193–207.

[68] U. Essmann, H. Mughrabi, Annihilation of dislocations during tensile and cyclic deformation and limits of dislocation densities, Philos. Mag. A. 40 (1979) 731–756.

[69] J.P. Hirth, J. Lothe, Theory of dislocations, 2nd ed., John Wiley and Sons, New York, 1982.

[70] M. Rhee, H.M. Zbib, J.P. Hirth, H. Huang, T.D. de la Rubia, Models for long-/short-range interactions and cross slip in 3D dislocation simulation of BCC single crystals, Model. Simul. Mater. Sci. Eng. 6 (1998) 467–492.

[71] A. Arsenlis, D.M. Parks, Modeling the evolution of crystallographic dislocation density in crystal plasticity, J. Mech. Phys. Solids. 50 (2002) 1979–2009.

[72] U.F. Kocks, A statistical theory of flow stress and work-hardening, Philos. Mag. 13 (1966) 541–566.

[73] R.A. Austin, D.L. McDowell, A dislocation-based constitutive model for viscoplastic deformation of fcc metals at very high strain rates, Int. J. Plast. 27 (2011) 1–24.

[74] Y. Estrin, Dislocation density-related constitutive modeling, in: Unified Const. Laws Plast. Deform., Academic Press, San Diego, 1996: pp. 69–106.

[75] Y. Estrin, H. Mecking, A unified phenomenological description of work hardening and creep based on one-parameter models, Acta Metall. 32 (1984) 57–70.

[76] N. Hashimoto, S.J. Zinkle, R.L. Klueh, A.F. Rowcliffe, K. Shiba, Deformation Mechanisms in Ferritic/Martensitic Steels Irradiated in HFIR, Mater. Res. Soc. Symp. Proc. 650 (2001) R1.10.

[77] K. Farrell, T.S. Byun, N. Hashimoto, Deformation mode maps for tensile deformation of neutron-irradiated structural alloys, J. Nucl. Mater. 335 (2004) 471–486.

[78] S.J. Zinkle, B.N. Singh, Microstructure of neutron-irradiated iron before and after tensile deformation, J. Nucl. Mater. 351 (2006) 269–284.

[79] M. Ashrafi-Nik, Thermo hydraulic optimisation of the EURISOL DS target, EURISOL-DS/TASK2/TN-02-25-2008-0016, 2006.

[80] V.M. Schastlivtsev, D.P. Rodionov, Y.V. Khlebnikova, I.L. Yakovleva, Peculiarity of structure and crystallography of plastic deformation of lath martensite in structural steels, Mater. Sci. Eng. A. 273-275 (1999) 437–442.

[81] W.B. Jones, C.R. Hills, D.H. Polonis, Microstructural evolution of modified 9Cr-1Mo steel, Metall. Trans. A. 22 (1991) 1049–1058.

[82] K. Sawada, K. Miyahara, H. Kushima, K. Kimura, S. Matsuoka, Contribution of Microstructural Factors to Hardness Change During Creep Exposure in Mod.9Cr-1Mo Steel, ISIJ Int. 45 (2005) 1934–1939.

[83] R.A. Johnson, D.J. Oh, Analytic embedded atom method model for bcc metals, J. Mater. Res. 4 (1989) 1195–1201.

[84] M.F. Ashby, Mechanisms of deformation and fracture, Adv. Appl. Mech. 23 (1983) 117–177.

[85]   T. Suzuki, H. Koizumi, H.O.K. Kirchner, Plastic flow stress of b.c.c. transition metals and the Peierls potential, Acta Metall. Mater. 43 (1995) 2177–2187.

[86]   S. Queyreau, G. Monnet, B. Devincre, Slip systems interactions in [alpha]-iron determined by dislocation dynamics simulations, Int. J. Plast. 25 (2009) 361–377.

[87]   M.I. Mendelev, Y. Mishin, Molecular dynamics study of self-diffusion in bcc Fe, Phys. Rev. B. 80 (2009) 144111.

[88]   R.E. Stoller, S.I. Golubov, C. Domain, C.S. Becquart, Mean field rate theory and object kinetic Monte Carlo: A comparison of kinetic models, J. Nucl. Mater. 382 (2008) 77–90.

[89]   J. Marian, B.D. Wirth, R. Schäublin, J.M. Perlado, T. Díaz de la Rubia, <1 0 0>-Loop characterization in [alpha]-Fe: comparison between experiments and modeling, J. Nucl. Mater. 307-311 (2002) 871–875.

[90]   L.P. Evers, W.A.M. Brekelmans, M.G.D. Geers, Scale dependent crystal plasticity framework with dislocation density and grain boundary effects, Int. J. Solids Struct. 41 (2004) 5209–5230.

[91]   ABAQUS, Simulia, Dassault Systemes, Providence, RI, 2007.

[92]   O. van der Sluis, P.J.G. Schreurs, W.A.M. Brekelmans, H.E.H. Meijer, Overall behaviour of heterogeneous elastoviscoplastic materials: effect of microstructural modelling, Mech. Mater. 32 (2000) 449–462.

[93]   M. Matijasevic, E. Lucon, A. Almazouzi, Behavior of ferritic/martensitic steels after n-irradiation at 200 and 300 °C, J. Nucl. Mater. 377 (2008) 101–108.

[94]   H. Magnusson, R. Sandström, Creep Strain Modeling of 9 to 12 Pct Cr Steels Based on Microstructure Evolution, Metall. Mater. Trans. A. 38 (2007) 2033–2039.

[95]   R.L. Klueh, J.M. Vitek, Fluence and helium effects on the tensile properties of ferritic steels at low temperatures, J. Nucl. Mater. 161 (1989) 13–23.

[96]   A.F. Rowcliffe, J.P. Robertson, R.L. Klueh, K. Shiba, D.J. Alexander, M.L. Grossbeck, et al., Fracture toughness and tensile behavior of ferritic-martensitic steels irradiated at low temperatures, J. Nucl. Mater. 258-263 (1998) 1275–1279.

[97]   P. Spätig, R. Schäublin, S. Gyger, M. Victoria, Evolution of the mechanical properties of the F82H ferritic/martensitic steel after 590 MeV proton irradiation, J. Nucl. Mater. 258-263 (1998) 1345–1349.

[98]   S.A. Maloy, M.B. Toloczko, K.J. McClellan, T. Romero, Y. Kohno, F.A. Garner, et al., The effects of fast reactor irradiation conditions on the tensile properties of two ferritic/martensitic steels, J. Nucl. Mater. 356 (2006) 62–69.

[99] R.P. Tucker, M.S. Wechsler, S.M. Ohr, Dislocation Channeling in Neutron-Irradiated Niobium, J. Appl. Phys. 40 (1969) 400–408.

[100] D.J. Edwards, B.N. Singh, Evolution of cleared channels in neutron-irradiated pure copper as a function of tensile strain, J. Nucl. Mater. 329-333, Part B (2004) 1072–1077.

[101] D.J. Edwards, B.N. Singh, J.B. Bilde-Sørensen, Initiation and propagation of cleared channels in neutron-irradiated pure copper and a precipitation hardened CuCrZr alloy, J. Nucl. Mater. 342 (2005) 164–178.

[102] Z. Jiao, J.T. Busby, G.S. Was, Deformation microstructure of proton-irradiated stainless steels, J. Nucl. Mater. 361 (2007) 218–227.

[103] B.L. Eyre, A.F. Bartlett, An electron microscope study of neutron irradiation damage in alpha-iron, Philos. Mag. 12 (1965) 261–272.

[104] M. Victoria, N. Baluc, C. Bailat, Y. Dai, M.I. Luppo, R. Schäublin, et al., The microstructure and associated tensile properties of irradiated fcc and bcc metals, J. Nucl. Mater. 276 (2000) 114–122.

[105] F.A. Smidt, B. Mastel, Some observations of dislocation channelling in irradiated iron, Philos. Mag. 20 (1969) 651–656.

[106] E.H. Lee, T.S. Byun, J.D. Hunn, M.H. Yoo, K. Farrell, L.K. Mansur, On the origin of deformation microstructures in austenitic stainless steel: part I-microstructures, Acta Mater. 49 (2001) 3269–3276.

[107] J.S. Robach, I.M. Robertson, B.D. Wirth, A. Arsenlis, In-situ transmission electron microscopy observations and molecular dynamics simulations of dislocation-defect interactions in ion-irradiated copper, Philos. Mag. 83 (2003) 955–967.

[108] Z. Jiao, G.S. Was, The role of irradiated microstructure in the localized deformation of austenitic stainless steels, J. Nucl. Mater. 407 (2010) 34–43.

[109] B.L. Eyre, Direct observations of neutron irradiation damage in [alpha]-iron, Philos. Mag. 7 (1962) 2107–2113.

[110] P.M. Rice, S.J. Zinkle, Temperature dependence of the radiation damage microstructure in V-4Cr-4Ti neutron irradiated to low dose, J. Nucl. Mater. 258-263 (1998) 1414–1419.

[111] A. Luft, Microstructural processes of plastic instabilities in strengthened metals, Prog. Mater. Sci. 35 (1991) 97–204.

[112]   R. Chaouadi, Effect of irradiation-induced plastic flow localization on ductile crack resistance behavior of a 9%Cr tempered martensitic steel, J. Nucl. Mater. 372 (2008) 379–390.

[113]   J.S. Robach, I.M. Robertson, H.-J. Lee, B.D. Wirth, Dynamic observations and atomistic simulations of dislocation–defect interactions in rapidly quenched copper and gold, Acta Mater. 54 (2006) 1679–1690.

[114]   B.D. Wirth, V.V. Bulatov, T.D. de la Rubia, Dislocation-Stacking Fault Tetrahedron Interactions in Cu, J. Eng. Mater. Technol. 124 (2002) 329–334.

[115]   Y.N. Osetsky, R.E. Stoller, D. Rodney, D.J. Bacon, Atomic-scale details of dislocation–stacking fault tetrahedra interaction, Mater. Sci. Eng. A. 400–401 (2005) 370–373.

[116]   Y. Matsukawa, Y.N. Osetsky, R.E. Stoller, S.J. Zinkle, Destruction processes of large stacking fault tetrahedra induced by direct interaction with gliding dislocations, J. Nucl. Mater. 351 (2006) 285–294.

[117]   D. Rodney, Atomic modeling of irradiation-induced hardening, Comptes Rendus Phys. 9 (2008) 418–426.

[118]   H.-J. Lee, B.D. Wirth, Molecular dynamics simulation of the interaction between a mixed dislocation and a stacking fault tetrahedron, Philos. Mag. 89 (2009) 821–841.

[119]   H.J. Lee, J.H. Shim, B.D. Wirth, Molecular dynamics simulation of screw dislocation interaction with stacking fault tetrahedron in face-centered cubic Cu, J. Mater. Res. 22 (2007) 2758–2769.

[120]   T. Nogaret, D. Rodney, M. Fivel, C. Robertson, Clear band formation simulated by dislocation dynamics: Role of helical turns and pile-ups, J. Nucl. Mater. 380 (2008) 22–29.

[121]   T. Nogaret, D. Rodney, M. Fivel, C. Robertson, Clear Band formation simulated by dislocation dynamics, Probl. At. Sci. Technol. 4 (2009) 97–108.

[122]   J.L. Bassani, K. Ito, V. Vitek, Complex macroscopic plastic flow arising from non-planar dislocation core structures, Mater. Sci. Eng. A. 319-321 (2001) 97–101.

[123]   A. Seeger, Why anomalous slip in body-centred cubic metals?, Mater. Sci. Eng. A. 319-321 (2001) 254–260.

[124]   R. Gröger, V. Vitek, Multiscale modeling of plastic deformation of molybdenum and tungsten. III. Effects of temperature and plastic strain rate, Acta Mater. 56 (2008) 5426–5439.

[125] J.L. Bassani, V. Racherla, From non-planar dislocation cores to non-associated plasticity and strain bursts, Prog. Mater. Sci. 56 (2011) 852–863.

[126] D.S. Gelles, R.E. Schäublin, Post-irradiation deformation in a Fe-9%Cr alloy, Mater. Sci. Eng. A. 309–310 (2001) 82–86.

[127] D. Terentyev, D.J. Bacon, Y.N. Osetsky, Reactions between a 1/2⟨111⟩ screw dislocation and ⟨100⟩ interstitial dislocation loops in alpha-iron modelled at atomic scale, Philos. Mag. 90 (2010) 1019–1033.

[128] A. Nomoto, N. Soneda, A. Takahashi, S. Ishino, Interaction analysis between edge dislocation and self interstitial type dislocation loop in BCC iron using molecular dynamics, Mater. Trans. 46 (2005) 463–468.

[129] D.J. Bacon, Y.N. Osetsky, Z. Rong, Computer simulation of reactions between an edge dislocation and glissile self-interstitial clusters in iron, Philos. Mag. 86 (2006) 3921–3936.

[130] L.Z. Sun, N.M. Ghoniem, S.-H. Tong, B.N. Singh, 3D dislocation dynamics study of plastic instability in irradiated copper, J. Nucl. Mater. 283-287, Part 2 (2000) 741–745.

[131] N.M. Ghoniem, S.-H. Tong, B.N. Singh, L.Z. Sun, On dislocation interaction with radiation-induced defect clusters and plastic flow localization in fcc metals, Philos. Mag. A. 81 (2001) 2743–2764.

[132] T.A. Khraishi, H.M. Zbib, T.D. de la Rubia, M. Victoria, Localized deformation and hardening in irradiated metals: Three-dimensional discrete dislocation dynamics simulations, Metall. Mater. Trans. B. 33 (2002) 285–296.

[133] D. Rodney, G. Martin, Y. Bréchet, Irradiation hardening by interstitial loops: atomistic study and micromechanical model, Mater. Sci. Eng. A. 309-310 (2001) 198–202.

[134] B.N. Singh, X. Huang, S. Tahtinen, P. Moilanen, P. Jacquet, J. Dekeyser, Final report on in-reactor tensile deformation of pure iron and Fe-Cr alloy, Riso National Laboratory, Technical University of Denmark, Roskilde, Denmark, 2007.

[135] B.N. Singh, D.J. Edwards, S. Tahtinen, P. Moilanen, P. Jacquet, J. Dekeyser, Final report on in-reactor tensile tests on OFHC-copper and CuCrZr alloy, Riso National Laboratory, Technical University of Denmark, Roskilde, Denmark, 2004.

[136] R. LeSar, J.M. Rickman, Coarse Graining of Dislocation Structure and Dynamics, in: D. Raabe, F. Roters, F. Barlat, L.-Q. Chen (Eds.), Contin. Scale Simul. Eng. Mater., Wiley-VCH Verlag GmbH & Co. KGaA, 2005: pp. 429–444.

[137] J.V. Sharp, Deformation of neutron-irradiated copper single crystals, Philos. Mag. 16 (1967) 77–96.

[138]   V.V. Bulatov, M. Tang, H.M. Zbib, Crystal Plasticity from Dislocation Dynamics, MRS Bull. 26 (2001) 191–195.

[139]   M. Zhang, F. Bridier, P. Villechaise, J. Mendez, D.L. McDowell, Simulation of slip band evolution in duplex Ti–6Al–4V, Acta Mater. 58 (2010) 1087–1096.

[140]   T.S. Byun, N. Hashimoto, K. Farrell, E.H. Lee, Characteristics of microscopic strain localization in irradiated 316 stainless steels and pure vanadium, J. Nucl. Mater. 349 (2006) 251–264.

[141]   M. Briceno, J. Fenske, M. Dadfarnia, P. Sofronis, I.M. Robertson, Effect of ion irradiation-produced defects on the mobility of dislocations in 304 stainless steel, J. Nucl. Mater. 409 (2011) 18–26.

[142]   J.V. Sharp, Correlation between cleared channels and surface slip steps in neutron irradiated copper crystals, Radiat. Eff. 14 (1972) 71–75.

[143]   J.L. Brimhall, B. Mastel, Deformation structure of neutron-irradiated copper-aluminum alloy, Appl. Phys. Lett. 9 (1966) 127–128.

[144]   J.V. Sharp, Deformation of neutron irradiated copper alloys, Acta Metall. 22 (1974) 449–457.

[145]   N. Hashimoto, T.S. Byun, K. Farrell, S.J. Zinkle, Deformation microstructure of neutron-irradiated pure polycrystalline vanadium, J. Nucl. Mater. 336 (2005) 225–232.

[146]   H.M. Zbib, E.C. Aifantis, On the gradient-dependent theory of plasticity and shear banding, Acta Mech. 92 (1992) 209–225.

[147]   E.C. Aifantis, On the microstructural origin of certain inelastic models, J. Eng. Mater. Technol. 106 (1984) 326–330.

[148]   H.M. Zbib, E.C. Aifantis, A Gradient-Dependent Flow Theory of Plasticity: Application to Metal and Soil Instabilities, Appl. Mech. Rev. 42 (1989) S295.

[149]   H.. Zbib, E.. Aifantis, Size effects and length scales in gradient plasticity and dislocation dynamics, Scr. Mater. 48 (2003) 155–160.

[150]   J. Pontes, D. Walgraef, E.C. Aifantis, On dislocation patterning: Multiple slip effects in the rate equation approach, Int. J. Plast. 22 (2006) 1486–1505.

[151]   D. Walgraef, E.C. Aifantis, On certain problems of deformation-induced material instabilities, Int. J. Eng. Sci. 59 (2012) 140–155.

[152]   G. Po, N. Ghoniem, Continuum modeling of plastic flow localization in irradiated fcc metals, J. Nucl. Mater. 442 (2013) S607–S611.

[153]   G.R. Odette, M.Y. He, E.G. Donahue, P. Spätig, T. Yamamoto, Modeling the multiscale mechanics of flow localization-ductility loss in irradiation damaged bcc alloys, J. Nucl. Mater. 307-311 (2002) 171–178.

[154]   M. Sauzay, K. Bavard, W. Karlsen, TEM observations and finite element modelling of channel deformation in pre-irradiated austenitic stainless steels - Interactions with free surfaces and grain boundaries, J. Nucl. Mater. 406 (2010) 152–165.

[155]   P. Evrard, M. Sauzay, Modelling of the effect of dislocation channel on intergranular microcrack nucleation in pre-irradiated austenitic stainless steels during low strain rate tensile loading, J. Nucl. Mater. 405 (2010) 83–94.

[156]   E.A. Little, Fracture mechanics evaluations of neutron irradiated Type 321 austenitic steel, J. Nucl. Mater. 139 (1986) 261–276.

[157]   R. Fish, C. Hunter, Tensile Properties of Fast Reactor Irradiated Type 304 Stainless Steel, in: F. Shober (Ed.), Irradiat. Eff. Microstruct. Prop. Met., ASTM International, West Conshohocken, PA, 1976: pp. 119–138.

[158]   E. West, M. McMurtrey, Z. Jiao, G. Was, Role of Localized Deformation in Irradiation-Assisted Stress Corrosion Cracking Initiation, Metall. Mater. Trans. A. 43 (2012) 136–146.

[159]   M.D. McMurtrey, G.S. Was, L. Patrick, D. Farkas, Relationship between localized strain and irradiation assisted stress corrosion cracking in an austenitic alloy, Mater. Sci. Eng. A. 528 (2011) 3730–3740.

[160]   J. Henry, X. Averty, Y. Dai, P. Lamagnère, J.P. Pizzanelli, J.J. Espinas, et al., Tensile properties of 9Cr–1Mo martensitic steel irradiated with high energy protons and neutrons, J. Nucl. Mater. 318 (2003) 215–227.

[161]   D.J. Michel, R.A. Gray, Effects of irradiation on the fracture toughness of fbr structural materials, J. Nucl. Mater. 148 (1987) 194–203.

[162]   Y. Dai, X.J. Jia, K. Farrell, Mechanical properties of modified 9Cr-1Mo (T91) irradiated at [less-than-or-equals, slant]300 °C in SINQ Target-3, J. Nucl. Mater. 318 (2003) 192–199.

[163]   E. Wakai, S. Jitsukawa, H. Tomita, K. Furuya, M. Sato, K. Oka, et al., Radiation hardening and -embrittlement due to He production in F82H steel irradiated at 250 °C in JMTR, J. Nucl. Mater. 343 (2005) 285–296.

[164]   T.S. Byun, M.B. Toloczko, T.A. Saleh, S.A. Maloy, Irradiation dose and temperature dependence of fracture toughness in high dose HT9 steel from the fuel duct of FFTF, J. Nucl. Mater. 432 (2013) 1–8.

223

[165]   T.L. Anderson, Fracture mechanics: fundamentals and applications, CRC Press, Boca Raton, FL, 2005.

[166]   A.M. Cuitiño, M. Ortiz, Ductile fracture by vacancy condensation in f.c.c. single crystals, Acta Mater. 44 (1996) 427–436.

[167]   R. Raj, M.. Ashby, Intergranular fracture at elevated temperature, Acta Metall. 23 (1975) 653–666.

[168]   R. Raj, Nucleation of cavities at second phase particles in grain boundaries, Acta Metall. 26 (1978) 995–1006.

[169]   M. Yoo, H. Trinkaus, Crack and cavity nucleation at interfaces during creep, Metall. Mater. Trans. A. 14 (1983) 547–561.

[170]   J.P. Hirth, W.D. Nix, Analysis of cavity nucleation in solids subjected to external and internal stresses, Acta Metall. 33 (1985) 359–368.

[171]   I.-W. Chen, A.S. Argon, Creep cavitation in 304 stainless steel, Acta Metall. 29 (1981) 1321–1333.

[172]   J.S. Wang, J.J. Stephens, W.D. Nix, A statistical analysis of cavity nucleation at particles in grain boundaries, Acta Metall. 33 (1985) 1009–1021.

[173]   H.R. Brager, F.A. Garner, G.L. Guthrie, The effect of stress on the microstructure of neutron irradiated type 316 stainless steel, J. Nucl. Mater. 66 (1977) 301–321.

[174]   F.A. McClintock, A criterion for ductile fracture by the growth of holes, J. Appl. Mech. 35 (1968) 363.

[175]   J.R. Rice, D.M. Tracey, On the ductile enlargement of voids in triaxial stress fields, J. Mech. Phys. Solids. 17 (1969) 201–217.

[176]   A.L. Gurson, Continuum theory of ductile rupture by void nucleation and growth: Part I-Yield criteria and flow rules for porous ductile media, J. Eng. Mater. Technol. 99 (1977) 2–15.

[177]   V. Tvergaard, Influence of voids on shear band instabilities under plane strain conditions, Int. J. Fract. 17 (1981) 389–407.

[178]   V. Tvergaard, On localization in ductile materials containing spherical voids, Int. J. Fract. 18 (1982) 237–252.

[179]   V. Tvergaard, A. Needleman, Analysis of the cup-cone fracture in a round tensile bar, Acta Metall. 32 (1984) 157–169.

[180]   A.A. Benzerga, J.-B. Leblond, Ductile Fracture by Void Growth to Coalescence, in: Adv. Appl. Mech., Elsevier, 2010: pp. 169–305.

[181]   A.A. Benzerga, Micromechanics of coalescence in ductile fracture, J. Mech. Phys. Solids. 50 (2002) 1331–1362.

[182]   A.A. Benzerga, J. Besson, A. Pineau, Anisotropic ductile fracture: Part II: theory, Acta Mater. 52 (2004) 4639–4650.

[183]   J. Besson, Continuum Models of Ductile Fracture: A Review, Int. J. Damage Mech. 19 (2010) 3–52.

[184]   D. Hull, D.E. Rimmer, The growth of grain-boundary voids under stress, Philos. Mag. 4 (1959) 673–687.

[185]   M.V. Speight, J.E. Harris, The Kinetics of Stress-Induced Growth of Grain-Boundary Voids, Met. Sci. 1 (1967) 83–85.

[186]   J. Weertman, Theory of high temperature intercrystalline fracture under static or fatigue loads, with or without irradiation damage, Metall. Mater. Trans. B. 5 (1974) 1743–1751.

[187]   I.-W. Chen, A.S. Argon, Diffusive growth of grain-boundary cavities, Acta Metall. 29 (1981) 1759–1768.

[188]   A.C.F. Cocks, M.F. Ashby, On creep fracture by void growth, Prog. Mater. Sci. 27 (1982) 189–244.

[189]   A. Needleman, J.. Rice, Plastic creep flow effects in the diffusive cavitation of grain boundaries, Acta Metall. 28 (1980) 1315–1332.

[190]   R.E. Stoller, G.R. Odette, A model based fission-fusion correlation of cavity swelling in stainless steel, J. Nucl. Mater. 104 (1981) 1361–1365.

[191]   F.D. Fischer, J. Svoboda, Void growth due to vacancy supersaturation – A non-equilibrium thermodynamics study, Scr. Mater. 58 (2008) 93–95.

[192]   E.A. Repetto, M. Ortiz, A micromechanical model of cyclic deformation and fatigue-crack nucleation in f.c.c. single crystals, Acta Mater. 45 (1997) 2577–2595.

[193]   J. Lemaitre, A course on damage mechanics, Springer-Verlag, Berlin, 1992.

[194]   L.K. Mansur, Theory and experimental background on dimensional changes in irradiated alloys, J. Nucl. Mater. 216 (1994) 97–123.

[195]   R.W. Balluffi, A.V. Granato, F. R. N. Nabarro, Editor, Dislocations in Solids, Vol. 4, North Holland, Amsterdam, 1979.

[196]   M. Gologanu, J.-B. Leblond, J. Devaux, Approximate models for ductile metals containing non-spherical voids—Case of axisymmetric prolate ellipsoidal cavities, J. Mech. Phys. Solids. 41 (1993) 1723–1754.

[197]   V.P. Bennett, D.L. McDowell, Crack tip displacements of microstructurally small surface cracks in single phase ductile polycrystals, Eng. Fract. Mech. 70 (2003) 185–207.

[198]   G.M. Castelluccio, D.L. McDowell, Assessment of small fatigue crack growth driving forces in single crystals with and without slip bands, Int. J. Fract. 176 (2012) 49–64.

[199]   C.F. Shih, Relationships between the J-integral and the crack opening displacement for stationary and extending cracks, J. Mech. Phys. Solids. 29 (1981) 305–326.

[200]   E.E. Underwood, The mathematical foundations of quantitative stereology, in: Stereol. Quant. Metallogr. ASTM STP 504, American Soceity for Testing and Materials, Atlantic City, NJ, 1971: pp. 3–38.

[201]   H. Mehrer, M. Lübbehusen, Self-Diffusion along Dislocations and in the Lattice of alpha-Iron, in: Defect Diffus. Forum, Trans Tech Publ, 1991: pp. 591–604.

[202]   Y. Shima, Y. Ishikawa, H. Nitta, Y. Yamazaki, K. Mimura, M. Isshiki, et al., Self-diffusion along dislocations in ultra high purity iron, Mater. Trans. 43 (2002) 173–177.

[203]   F.A. McClintock, Plasticity aspects of fracture, in: Fract. Adv. Treatise, Academic Press, New York, 1971: pp. 47–225.

[204]   Z. Li, W. Guo, The influence of plasticity mismatch on the growth and coalescence of spheroidal voids on the bimaterial interface, Int. J. Plast. 18 (2002) 249–279.

[205]   R. Becker, Effects of strain localization on surface roughening during sheet forming, Acta Mater. 46 (1998) 1385–1401.

[206]   O. Akourri, M. Louah, A. Kifani, G. Gilgert, G. Pluvinage, The effect of notch radius on fracture toughness JIc, Eng. Fract. Mech. 65 (2000) 491–505.

[207]   R.O. Ritchie, R.M. Horn, Further considerations on the inconsistency in toughness evaluation of AISI 4340 steel austenitized at increasing temperatures, Metall. Trans. A. 9 (1978) 331–341.

[208]   M. Yoda, The effect of the notch root radius on the J-integral fracture toughness under modes I, II and III loadings, Eng. Fract. Mech. 26 (1987) 425–431.

[209]   R. Damani, R. Gstrein, R. Danzer, Critical notch-root radius effect in SENB-S fracture toughness testing, J. Eur. Ceram. Soc. 16 (1996) 695–702.

[210]   T. Fett, Influence of a finite notch root radius on fracture toughness, J. Eur. Ceram. Soc. 25 (2005) 543–547.

[211] T. Nishida, Y. Hanaki, G. Pezzotti, Effect of Notch-Root Radius on the Fracture Toughness of a Fine-Grained Alumina, J. Am. Ceram. Soc. 77 (1994) 606–608.

[212] R.O. Ritchie, B. Francis, W.L. Server, Evaluation of toughness in AISI 4340 alloy steel austenitized at low and high temperatures, Metall. Trans. A. 7 (1976) 831–838.

[213] T.R. Wilshaw, C.A. Rau, A.S. Tetelman, A general model to predict the elastic-plastic stress distribution and fracture strength of notched bars in plane strain bending, Eng. Fract. Mech. 1 (1968) 191–211.

[214] G.R. Odette, T. Yamamoto, H.J. Rathbun, M.Y. He, M.L. Hribernik, J.W. Rensman, Cleavage fracture and irradiation embrittlement of fusion reactor alloys: mechanisms, multiscale models, toughness measurements and implications to structural integrity assessment, J. Nucl. Mater. 323 (2003) 313–340.

[215] J. Garnier, Y. Bréchet, M. Delnondedieu, C. Pokor, P. Dubuisson, A. Renault, et al., Irradiation creep of SA 304L and CW 316 stainless steels: Mechanical behaviour and microstructural aspects. Part I: Experimental results, J. Nucl. Mater. 413 (2011) 63–69.

[216] C. Xu, G.S. Was, In situ proton irradiation creep of ferritic–martensitic steel T91, J. Nucl. Mater. 441 (2013) 681–687.

[217] J. Garnier, Y. Bréchet, M. Delnondedieu, A. Renault, C. Pokor, P. Dubuisson, et al., Irradiation creep of SA 304L and CW 316 stainless steels: Mechanical behaviour and microstructural aspects. Part II: Numerical simulation and test of SIPA model, J. Nucl. Mater. 413 (2011) 70–75.

[218] J. Chen, P. Jung, J. Henry, Y. de Carlan, T. Sauvage, F. Duval, et al., Irradiation creep and microstructural changes of ODS steels of different Cr-contents during helium implantation under stress, J. Nucl. Mater. 437 (2013) 432–437.

[219] M. Toloczko, F. Garner, Stress and Temperature Dependence of Irradiation Creep of Selected FCC and BCC Steels at Low Swelling, J. ASTM Int. 1 (2004) 73–85.

[220] S.. Bruemmer, E.. Simonen, P.. Scott, P.. Andresen, G.. Was, J.. Nelson, Radiation-induced material changes and susceptibility to intergranular failure of light-water-reactor core internals, J. Nucl. Mater. 274 (1999) 299–314.

[221] P.T. Heald, J.E. Harbottle, Irradiation creep due to dislocation climb and glide, J. Nucl. Mater. 67 (1977) 229–233.

[222] J.P. Foster, K. Bunde, D.L. Porter, Irradiation creep of annealed 304L stainless steel at low dose levels, J. Nucl. Mater. 317 (2003) 167–174.

[223]   A. Causey, In-Reactor Stress Relaxation of Zirconium Alloys, in: J. Schemel, H. Rosenbaum (Eds.), Zircon. Nucl. Appl., ASTM International, 100 Barr Harbor Drive, PO Box C700, West Conshohocken, PA 19428-2959, 1974: pp. 263–263–11.

[224]   A.R. Causey, F.J. Butcher, S.A. Donohue, Measurement of irradiation creep of zirconium alloys using stress relaxation, J. Nucl. Mater. 159 (1988) 101–113.

[225]   J. Chen, P. Jung, W. Hoffelner, Irradiation creep of candidate materials for advanced nuclear plants, J. Nucl. Mater. 441 (2013) 688–694.

[226]   V. Vitek, Structure of dislocation cores in metallic materials and its impact on their plastic behaviour, Prog. Mater. Sci. 36 (1992) 1–27.

[227]   M.S. Duesbery, V. Vitek, Plastic anisotropy in b.c.c. transition metals, Acta Mater. 46 (1998) 1481–1492.

[228]   V. Vitek, Core structure of screw dislocations in body-centred cubic metals: relation to symmetry and interatomic bonding, Philos. Mag. 84 (2004) 415–428.

[229]   V. Vitek, M. Mrovec, J.L. Bassani, Influence of non-glide stresses on plastic flow: from atomistic to continuum modeling, Mater. Sci. Eng. A. 365 (2004) 31–37.

[230]   R. Gröger, V. Racherla, J.L. Bassani, V. Vitek, Multiscale modeling of plastic deformation of molybdenum and tungsten: II. Yield criterion for single crystals based on atomistic studies of glide of screw dislocations, Acta Mater. 56 (2008) 5412–5425.

[231]   V. Vitek, M. Mrovec, R. Gröger, J.L. Bassani, V. Racherla, L. Yin, Effects of non-glide stresses on the plastic flow of single and polycrystals of molybdenum, Mater. Sci. Eng. A. 387-389 (2004) 138–142.

[232]   J. Chaussidon, M. Fivel, D. Rodney, The glide of screw dislocations in bcc Fe: Atomistic static and dynamic simulations, Acta Mater. 54 (2006) 3407–3416.

[233]   A. Koester, A. Ma, A. Hartmaier, Atomistically informed crystal plasticity model for body-centered cubic iron, Acta Mater. 60 (2012) 3894–3901.

[234]   G.J. Irwin, F. Guiu, P.L. Pratt, The influence of orientation on slip and strain hardening of molybdenum single crystals, Phys. Status Solidi A. 22 (1974) 685–698.

[235]   R. Gröger, A.G. Bailey, V. Vitek, Multiscale modeling of plastic deformation of molybdenum and tungsten: I. Atomistic studies of the core structure and glide of 1/2<1 1 1> screw dislocations at 0 K, Acta Mater. 56 (2008) 5401–5411.

[236]   C.. Statham, D. Vesely, J.. Christian, Slip in single crystals of niobium-molybdenum alloys deformed in compression, Acta Metall. 18 (1970) 1243–1252.

[237] C.J. Bolton, G. Taylor, Anomalous slip in high-purity niobium single crystals deformed at 77°K in tension, Philos. Mag. 26 (1972) 1359–1376.

[238] J. Christian, Some surprising features of the plastic deformation of body-centered cubic metals and alloys, Metall. Mater. Trans. A. 14 (1983) 1237–1256.

[239] M.H.A. Nawaz, B.L. Mordike, Slip Geometry of Tantalum and Tantalum Alloys, Phys. Status Solidi A. 32 (1975) 449–458.

[240] T. Yalcinkaya, W.A.M. Brekelmans, M.G.D. Geers, BCC single crystal plasticity modeling and its experimental identification, Model. Simul. Mater. Sci. Eng. 16 (2008) 085007.

[241] T. Buchheit, C. Battaile, C. Weinberger, E. Holm, Multi-scale modeling of low-temperature deformation in b.c.c. metals, JOM J. Miner. Met. Mater. Soc. 63 (2011) 33–36.

[242] C.R. Weinberger, C.C. Battaile, T.E. Buchheit, E.A. Holm, Incorporating atomistic data of lattice friction into BCC crystal plasticity models, Int. J. Plast. 37 (2012) 16–30.

[243] H. Lim, C.R. Weinberger, C.C. Battaile, T.E. Buchheit, Application of generalized non-Schmid yield law to low-temperature plasticity in bcc transition metals, Model. Simul. Mater. Sci. Eng. 21 (2013) 045015.

[244] Z.M. Chen, M. Mrovec, P. Gumbsch, Atomistic aspects of $\case{1}{2}\langle 1\,1\,1 \rangle$ screw dislocation behavior in α-iron and the derivation of microscopic yield criterion, Model. Simul. Mater. Sci. Eng. 21 (2013) 055023.

[245] Z. Chen, Modelling the plastic deformation of iron, KIT Scientific Publishing, Karlsruhe, 2013.

[246] S. Narayanan, D.L. McDowell, T. Zhu, Crystal plasticity model for bcc iron atomistically informed by kinetics of correlated kinkpair nucleation on screw dislocations, in review (2013).

[247] D. Caillard, Kinetics of dislocations in pure Fe. Part I. In situ straining experiments at room temperature, Acta Mater. 58 (2010) 3493–3503.

[248] D. Caillard, Kinetics of dislocations in pure Fe. Part II. In situ straining experiments at low temperature, Acta Mater. 58 (2010) 3504–3515.

[249] M.R. Gilbert, S. Queyreau, J. Marian, Stress and temperature dependence of screw dislocation mobility in α-Fe by molecular dynamics, Phys. Rev. B. 84 (2011) 174103.

[250] D. Brunner, J. Diehl, Strain-Rate and Temperature Dependence of the Tensile Flow Stress of High-Purity α-Iron above 250 K (Regime I) Studied by Means of Stress-Relaxation Tests, Phys. Status Solidi A. 124 (1991) 155–170.

[251] D. Brunner, J. Diehl, Temperature and Strain-Rate Dependence of the Tensile Flow Stress of High-Purity α-Iron below 250 K. I. Stress/Temperature Regime III, Phys. Status Solidi A. 124 (1991) 455–464.

[252] C. Marichal, H. Van Swygenhoven, S. Van Petegem, C. Borca, {110} Slip with {112} slip traces in bcc Tungsten, Sci. Rep. 3 (2013).

[253] T. Takeuchi, Orientation Dependence of Work-Hardening in Iron Single Crystals, Jpn. J. Appl. Phys. 8 (1969) 320–328.

[254] A.S. Argon, Strengthening mechanisms in crystal plasticity, Oxford University Press Oxford, 2008.

[255] T. Zhu, J. Li, S. Yip, Atomistic Reaction Pathway Sampling: The Nudged Elastic Band Method and Nanomechanics Applications, in: Nano Cell Mech. Fundam. Front. Ed. Horacio Espinosa Gang Bao, 1st ed., John Wiley & Sons, Chichester UK, 2013: pp. 313–338.

[256] J.J. Adams, D.S. Agosta, R.G. Leisure, H. Ledbetter, Elastic constants of monocrystal iron from 3 to 500 K, J. Appl. Phys. 100 (2006) 113530.

[257] W.. Spitzig, A.. Keh, Orientation dependence of the strain-rate sensitivity and thermally activated flow in iron single crystals, Acta Metall. 18 (1970) 1021–1033.

[258] D. Brunner, J. Diehl, Temperature and Strain-Rate Dependence of the Tensile Flow Stress of High-Purity α-Iron below 250 K II. Stress/Temperature Regime II and Its Transitions to Regimes I and III, Phys. Status Solidi A. 125 (1991) 203–216.

[259] W. Spitzig, A. Keh, The role of internal and effective stresses in the plastic flow of iron single crystals, Metall. Mater. Trans. B. 1 (1970) 3325–3331.

[260] S. Naamane, G. Monnet, B. Devincre, Low temperature deformation in iron studied with dislocation dynamics simulations, Int. J. Plast. 26 (2010) 84–92.

[261] D.. Stein, J.. Low Jr., Effects of orientation and carbon on the mechanical properties of iron single crystals, Acta Metall. 14 (1966) 1183–1194.

[262] B. Šesták, N. Zárubová, Asymmetry of Slip in Fe-Si Alloy Single Crystals, Phys. Status Solidi B. 10 (1965) 239–250.

[263] S. Takeuchi, E. Furubayashi, T. Taoka, Orientation dependence of yield stress in 4.4% silicon iron single crystals, Acta Metall. 15 (1967) 1179–1191.